High Field Phenomenology in Linear Accelerators for the Compact Linear Collider

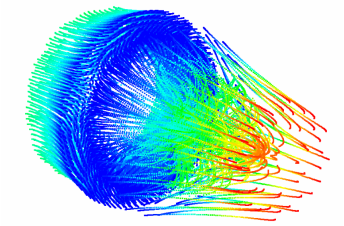

Thomas Geoffrey Lucas, BSc, MSc.

(ORCID: 0000-0002-6700-0481)

Submitted in total fulfillment
of the requirements of the degree of
Doctor of Philosophy

December 2018

School of Physics,
University of Melbourne

Abstract

The Compact Linear Collider (CLIC) is a 3 TeV linear electron-positron collider which is proposed to operate with loaded accelerating gradients up to 100 MV/m. These high gradients are accompanied by high field phenomena which limit the operation of the accelerating structures. Achieving reliable operation at these accelerating gradients requires an in-depth understanding of these phenomena and their effects on CLIC. This thesis investigates the phenomenology of high fields in CLIC accelerating structures through tests performed at the CERN's high gradient testing facilities.

The commissioning of a novel RF test stand will be presented. Using a unique RF pulse weaving method in combination with RF pulse compression, the new test stand offered the ability to test multiple accelerating structures in situ and at repetition rates up to 200 Hz. This offered a significant increase in the high gradient testing capacity at CERN. Using the new test stand, as well as existing infrastructure, four unique accelerating structures underwent conditioning to high gradients. These accelerating structures included a CLIC baseline design prototype, a structure with high order mode damping material, and two structures fabricated through novel machining and joining technologies. Three of the four structures were able to reliably operate at unloaded accelerating gradients of at least 100 MV/m with low breakdown rates.

Concurrent to the high gradient testing of accelerating structure, was an investigation into the radiation within the testing facilities, which was known to be the result of field emission capture. A series of measurements and simulations characterised the radiation produced during high power testing. A particular focus for the investigation was how the field emission capture varies with phase velocity. A model to describe the dependence of the capture of field emitted electrons on the phase velocity is presented. Measurements on the X-band test stands at CERN demonstrated that the capture increased $\sim 20\%$ for a 1 MHz increase in the RF driver frequency. These results were corroborated using a three dimensional RF and particle simulation.

Declaration

This is to certify that:

- The thesis comprises of only my original work towards the PhD except where indicated in the preface.
- Due acknowledgement has been made in the text to all other material used.
- The thesis is less than 100 000 words in length, exclusive of tables, maps, bibliographies and appendices.

Thomas Geoffrey Lucas

Preface

This thesis outlines the work performed by the author on the development of high gradient technology for a normal conducting linear collider. The text begins with a literature review which describes the Compact Linear Collider and the physics of high gradient linear accelerators, with due acknowledgement of all references.
In Chapter 5, the commissioning of a new test stand is presented. The work in this chapter was performed collaboratively by the author along with several colleagues at CERN. This work was presented at the 2018 International Particle Accelerator Conference (non peer-reviewed) in Vancouver where it was published in the conference's proceedings [56, 57]. The phrasing and work in reference [57] is completely that of the author and therefore the description from this publication was used in Section 5.3.3. The conference proceedings of references [56] and [57] are included in Appendix C.
Chapter 6 presents a description of a capture mechanism of field-emitted electrons in CLIC structures. This work describes the dependence of the field-emitted electron capture on the phase velocity was published in *Nuclear Inst. and Methods in Physics Research, A 914 (2019)* 4652 on 27 October 2018. The simulations, theory and measurements were performed primarily by author with helpful contributions from colleagues. Some phrasing used in Sections 6.4 to 6.8 has been taken from reference [69] and the full journal article has been included in Appendix C.
Finally, Chapter 7 presents the high gradient testing of four unique CLIC prototype accelerating structures. The high power testing results for the TD26CCR05 N3 structure was published as a *CLIC note* (not peer-reviewed) on 19 September 2018 and was written by the author of this thesis [66]. The high power testing and analysis of the structure were performed by the author while the postmortem was performed by the Rolf Wegner (CERN) with contributions by the author. The text from this publication has been used in this thesis in Sections 7.2 and 7.8. Following is a description of the operation of a structure built from milled halves. The high power testing and analysis in this article was performed by the author of this

thesis with contributions by Theodoros Argyropoulous (CERN). The postmortem analysis was performed collaboratively by Enrique Rodriguez-Castro (CERN), Rolf Wegner, and the author of this thesis. This work has been published in *Physical Review Accelerators and Beams 21, 061001 (2018)* on 7 June 2018 and was written primarily by the author. Phrasing and work from this publication are included in Sections 7.3 and 7.8. Concluding Chapter 7 is a description of the concepts which could be used for a large-scale RF conditioning programme. This work was also presented in the conference proceedings of the 2018 International Particle Accelerator Conference in [57], mentioned previously, and the some phrasing from this publication was included in Section 7.7 and 7.8.

Acknowledgements

During the journey of finishing this thesis, I have been lucky enough to have numerous wonderful people supporting me throughout my studies and challenge me academically. I would like to thank these people sincerely for all they've done throughout my PhD. Firstly I'd like to begin with my base at University of Melbourne. Mark Boland and Roger Rassool, you have been my supervisors for several years now and have given me opportunities that I could only have been able to dream of when beginning university. Roger, thank you for the emotional and academic support you have provided throughout my academic life. Mark, you have challenged me to think and encourage every idea I had, whether or not the ideas were any good. This is more than I could have asked for. Matteo Volpi, what an incredible experience this has been! Working with you over the last few years has been absolutely amazing. We've had endless fun inside and outside of the lab. Looking forward to many years to come. Paul Giansiracusa, thank you for the years of comradery. We've had many adventures around the world and I hope we can continue to work together in the future. Geoff Taylor, I'd like to thank you for the support and opportunities which you've provided over the years. Always enjoyed our conversations whether they're physics or cycling related. Kent, Bryn, Dave, Jim, and Kev thanks for warmly welcoming me into the group from day one. Our interesting discussions over the years have definitely livened up the basement.

To my CERN mentors and colleagues. Walter Wuensch, I am forever grateful that you took me on as a student and gave me unrestricted access to such amazing hardware. Thank you for pushing me to think and teaching me so much about the wonderful field of high gradient physics. Thibaut Lefevre, hard to believe it's been 6 years since we first met in Prevessin. I'd like to tell you how much I appreciate your endless enthusiasm and support during my time at CERN. To the Xbox team of Nuria, Gerry, Igor, Alexej, Theo, Ben, Jorge, Anna, Jan, Claudio, Veronica, Rolf, Daniel, Xavier and Sam. I could not have asked for a better group of people to work with. I enjoyed every moment the running and commissioning the Xboxes, and look

forward to continuing to collaborate in the future.
To those I met along the way. Valery, thanks for you encouragement and help in the work involving the halves structure. Look forward to seeing and possibly working with you in coming years. Riccardo and Paolo of PSI, thanks for the warm reception and allowing me to run your accelerating structure.
Finally and most significantly I would like to thank my family and partner. To my mother, Merrilyn, thank you for your devotion and sacrifice to ensure that I received the best education and opportunities throughout my life. To my brother, Benjamin, you've always encouraged me in my studies and have been the one person I can speak to about physics and maths. To my grandmother, Linda, I am grateful for you taking me in when I decided to move down to Melbourne. We always have a good laugh together. To my partner, Susi, I am forever grateful for the love, support, understanding, and encouragement that you've provided throughout my studies. I would not have been able to get through this without you.

Dedicated to my Mother and Father.

"The important thing is not to stop questioning. Curiosity has its own reason for existing. One cannot help but be in awe when he contemplates the mysteries of eternity, of life, of the marvellous structure of reality. It is enough if one tries merely to comprehend a little of this mystery every day."

- Albert Einstein

Contents

List of Figures

List of Tables

Acronyms

ADC	Analog-to-Digital Converter
BDR	Breakdown Rate
BLM	Beam-Loss Monitor
BSM	Beyond the Standard Model
CLIC	Compact Linear Collider
CERN	European Organisation for Nuclear Research
COM	Centre-of-Mass
CTF3	CLIC Test Facility 3
FCC	Future Circular Collider
FCCee	Electron-Positron Future Circular Collider
FE	Field-Emitted
HL-LHC	High-Luminosity Large Hadron Collider
HPRF	High Power Radio-Frequency
HOM	Higher Order Mode
ILC	International Linear Collider
KEK	Kō Enerugī Kasokuki Kenkyū Kikō
LHC	Large Hadron Collider
LLRF	Low-Level Radio-Frequency
LEP	Large Electron-Positron Collider
NEG	Non-Evaporative Getter
NLC	Next Linear Collider
RF	Radio-Frequency
SEM	Scanning Electron Microscope
SLAC	Stanford Linear Accelerator Center
SM	Standard Model
TE	Transverse Electric
TM	Transverse Magnetic
VNA	Vector Network Analyser

Chapter 1

Introduction

Experiments delving deep into the fundamentals of the Standard Model (SM), and searching for hints of beyond the Standard Model (BSM) physics, have so far heavily relied on circular colliders. In such accelerators, particles make numerous turns of the accelerator gaining a small amount of energy on each turn, in accordance with the synchrotron principle [1]. Circular colliders have produced collisions at centre-of-mass (COM) energies up to 13 Teraelectronvolts (TeV) for hadrons, at the Large Hadron Collider (LHC), and 209 Gigaelectronvolts (GeV) for leptons, at Large Electron-Positron Collider (LEP) [2, 3]. The emission of synchrotron radiation limits the achievable COM energy in circular accelerators. The power lost to synchrotron radiation has a fourth power dependence on the particle energy and also goes with the inverse fourth power of the particle mass and inverse square of the bending radius [4, 5, 7]. Consequently, high energy electron-positron circular colliders require a large circumference to reach the energy regimes of interest. An example of such an accelerator was LEP with a $\sim$27 km circumference. In the TeV COM energy regime, a linear electron-positron collider proves to be by far the most cost effective scheme (Figure 1.1) and for this reason, it has been proposed as the next generation electron-positron collider at the European Organisation for Nuclear Research (CERN) in Geneva, Switzerland [8]. The Compact Linear Collider (CLIC) will use accelerating structures with loaded accelerating gradients between 72 and 100 MV/m [9]. Such accelerating gradients will allow the ultimate COM energy of 3 TeV to be achieved in 50 km, once accounting for non-accelerating sections such as focussing magnets.

1.1 Statement of Problem

The effects of certain phenomena, such as RF breakdown and field emission, become more prevalent at higher accelerating gradients, due to an increase in surface fields, and consequently limit the achievable gradients. Understanding the behaviour of these phenomena within accelerating structures is key to operating at the desired gradients of CLIC.

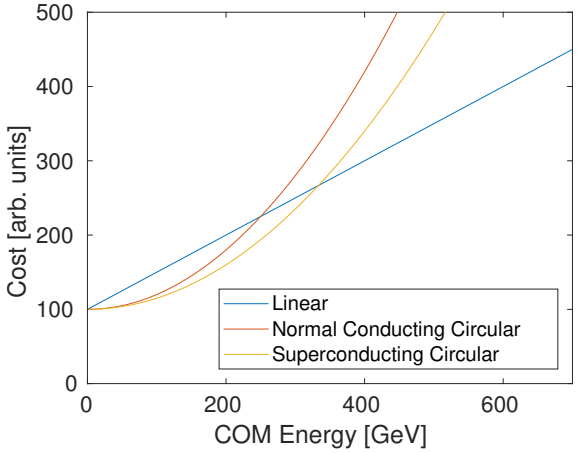

Figure 1.1: A comparison of the relative cost of a linear electron-positron collider versus a circular electron-positron collider in arbitrary units plotted with respect to the COM energy of the machine in GeV [12].

1.2 Contention

The aim of this thesis is to present and describe the high field phenomenology within high gradient X-band accelerating structures through the testing of four unique structure prototypes. The objective of this testing is to improve the understanding of how certain phenomena limit or impede high gradient operation, and present solutions to minimise their effects. Ultimately, the thesis will demonstrate the accelerating gradients achieved in the four CLIC prototypes.

1.3 Motivation of a Linear Lepton Collider

Modern particle physics predicts that the answers to many of the open questions, including electroweak symmetry breaking, dark matter, and other physics beyond the Standard Model, lie in the terascale energy regime [6, 10]. Collisions of protons within the LHC have allowed the particle physics community to probe for answers within this energy regime. However these collisions have large uncertainties in the COM energy and produce a significant background event rate resulting from the composite nature of the protons. Collisions in lepton colliders are between fundamental particles resulting in cleaner interactions and considerably less energy uncertainty [11]. Previously, LEP was able to collide electrons and positrons at COM energies up to 209 GeV, which hindsight tells us was only several GeV below the threshold for Higgs production [2].

Synchrotron radiation emission introduces a significant road block to achieving the goal of producing higher energy electron/positron beams with a circular collider. Power emission due to synchrotron radiation from a charged particle in a homoge-

neous magnetic field, and travelling perpendicular to the field, is given by [4, 5, 7]:

$$P_\gamma = \frac{2}{3}\frac{e^2 c}{\rho^2}\frac{\beta^4 E^4}{m^4}, \tag{1.1}$$

where e is the charge of the electron, c is the speed of light, ρ is the bending radius, β is the particle velocity, E is the particle energy and m is the particle mass. High energy electron-positron circular accelerators are the most affected by this phenomenon. However, in light of the constraints imposed by Equation 1.1, there are a few solutions to reach the terascale level with a lepton collider. These are discussed below:

1. **A very large radius circular collider:** One such solution is to increase the radius of the circular collider. The most recent proposals for future accelerators included the electron-positron Future Circular Collider (FCCee) [13]. The proposed 100 km circumference of FCCee would reduce its power emission by a factor of nine in comparison to LEP[1] although this option still fights with the strong E^4 and m^4 dependencies. Due to civil engineering costs, this option only becomes feasible if the tunnel is later re-used for a high energy hadron collider (for example the Future Circular Collider (FCC), a 100 TeV proton-proton collider).

2. **A circular collider with heavy leptons**: Alternatively, some in the physics community have proposed switching constituent particles to a heavier lepton. A muon collider has been proposed with a collision energy of approximately 10 TeV, though this still requires a study into muon cooling after their production [14].

3. **A linear collider**: Two linear colliders have been proposed each based on different accelerator technologies. The first is the International Linear Collider (ILC) which is based on superconducting accelerating structures and will operate with a loaded accelerating gradient of 30 MV/m. With a proposed COM energy of 250 GeV, ILC's main goal will be to study the Higgs boson. A potential upgrade to 500 GeV will allow for top quark production and BSM searches [87]. Such superconducting linacs have high power efficiency but they are limited to accelerating gradient of less than 50 MV/m [86]. The alternative linear collider is the Compact Linear Collider which will use normal conducting accelerating structures to push the boundaries of accelerating gradients. CLIC aims to be also constructed in three stages starting at 380 GeV to investigate the Standard Model, before an increase to 1.5 TeV and 3 TeV

[1] If the FCCee were operating at the COM energy of LEP.

will allow BSM searches. CLIC's design has the requirement of loaded accelerating gradients of 72 MV/m for the 380 GeV stage before being increased to 100 MV/m for the latter TeV stages. Such accelerating gradients are well above past achievements of linear accelerators (linacs) and as such the ability to reliably achieve them is one of the major goals of the CLIC research and development programme [9].

Having presented the alternate designs, the remainder of this thesis is directed towards investigating the accelerator technology of the Compact Linear Collider. Chapter 2 will overview CLIC's design which has been reported in references [9] and [15]. The design parameters of the machine will be overviewed particularly looking at the main linac and the COM energy stages. From the three COM energy stages, the physics potential will be explained. The discussion will emphasise details of the precision measurements of the properties of the top quark and Higgs boson, which other proposed machines also aim to investigate.

1.4 High Gradient Linear Accelerators

High accelerating gradients come at the cost of high surface electric and magnetic fields that are known to lead to several phenomena which impact upon the nominal operation of the accelerating structures. Particularly crucial for CLIC are the phenomena of RF breakdown and the capture of field-emitted electrons. An RF breakdown within an accelerating structure causes a transverse kick to the CLIC beam rendering it useless for that pulse. For this reason CLIC aims for an RF breakdown to occur in less than one of every 100 pulses, or a breakdown rate (BDR) of less than 3×10^{-7} breakdowns/pulse/metre (bpp/m) [9]. Chapter 4 will review the physics of high surface fields with a description of the phenomena expected to influence high gradient operation. Although not as catastrophic as RF breakdown, the capture of field-emitted electrons leads to several effects which can limit the performance of CLIC. Chapter 6 will investigate the capture dynamics of field-emitted electrons in high gradient, high frequency accelerating structures using a series of measurements and simulations.

1.5 CLIC Test Facilities at CERN

As expected with any project as ambitious and novel as CLIC, the design and development of the unique concepts need to be investigated on a small scale before the approval of construction. One such investigation is being undertaken by a collaboration between CERN, SLAC in Stanford (USA) and KEK in Tsukuba (Japan) who together are testing several CLIC design concepts. These include the generation

of high power RF, which will be explained in greater detail in Section 2.1.3, and the testing of high gradient accelerating structures. The following will discuss the efforts and testing facilities at CERN, which occurred prior to the beginning of this work [26, 27].

1.5.1 CLIC Test Facility

The CLIC Test Facility, called CTF3[2], provided the first tests of several key CLIC concepts at CERN. Illustrated in Figure 1.2, CTF3 begins with an injector and 3 GHz linac which accelerates a high current (4.5 A) drive beam up to 130 MeV. To create the required bunch separation of ∼83 ps, four bunch trains from the drive beam are progressively delayed and interleaved in the combiner ring to produce the 12 GHz beam. This beam is then guided into the CLIC Experimental Area (CLEX), where it passes through a set of Power Extraction Transfer Structures (PETS) which are used to efficiently generate the 12 GHz RF pulses for the CLIC accelerating structures[3]. These RF pulses are delivered through a waveguide network into a CLIC super-structure (two CLIC accelerating structures) running parallel to the drive beam. The Two-Beam Test Stand (TBTS) has provided the proof of concept for the CLIC drive beam model and been able to test the superstructure at a peak power of up to 135 MW [17, 16, 18]. Unfortunately, given its low pulse repetition rate

[2]CTF has undergone two major upgrades since its initial design therefore the current set-up is considered the third iteration and consequently it is referred to as CTF3.

[3]The reader should note that the 12 GHz value, used throughout this thesis, is actually 11.9942 GHz. The rounded number is used for brevity.

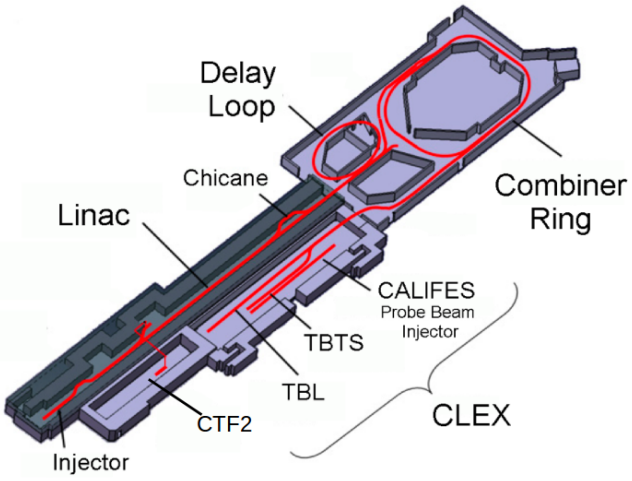

Figure 1.2: Diagram of the CTF3 Layout [19]. The linac, delay loop and combiner ring each participate in the creation of a 12 GHz bunch train. This bunch train is input into the TBTS where the power extraction transfer structures are located. The CTF2 bunker is included at the bottom of the diagram and is the location for current high gradient tests for the reconfigured Xbox 1.

of 5 Hz, CTF3 is unable to condition accelerating structures efficiently and therefore is unable to achieve the low BDRs required for CLIC. In the past, achieving these BDRs had been observed to take several hundred million high power RF pulses [58]. This would amount to approximately 4.5 years of continuous operation at 5 Hz. To efficiently test accelerating structures at low BDRs, CERN had commissioned two X-band[4] test stands. Each of these operates at 50 Hz and drive the accelerating structure with a high power klystron[5] and modulator[6].

1.5.2 X-band Test Stands 1

Commissioned in 2012, the first X-band test stand (Xbox 1) is used in the testing of CLIC structures at high power and at lower BDRs than CTF3. Xbox 1 powers a single CLIC structure using a 115 MW Scandinova modulator and 50 MW CPI X-band klystron. Together these produce 50 MW RF pulses at a pulse repetition rate up to 50 Hz with a maximum pulse length of 1.5 μs [23]. This offers an order of magnitude improvement of the repetition rate in comparison to CTF3. If more peak power is required, an RF pulse compressor can increase the peak power above 150 MW. With this set-up, Xbox 1 was able to be used in the testing of the effects of beam-loading on the CLIC beam [20]. Such beam-loading is the result of electromagnetic fields induced by the main beam reducing the accelerating gradient within the accelerating structures [21]. With the announcement of the upgrade of CTF3, the Xbox 1 test stand waveguide network was reconfigured to test structures without beam in the CTF2 bunker, located adjacent to the injector for CTF3 (Figure 1.2) [24]. Using this new set-up, the Xbox 1 test stand was used to test CLIC accelerating structures without beam-loading. Demonstrating the feasibility and reproducibility of achieving the high gradients and low BDRs required for CLIC [22].

1.5.3 X-band Test Stands 2

The second X-band test stand (Xbox 2) was commissioned in 2014, in a separate testing bunker, in order to expand CERN's high gradient testing capacity (Figure 1.3). Based on the same high power infrastructure as Xbox 1, Xbox 2 also operates with a pulse repetition rate of 50 Hz and each RF pulse can achieve a peak power up to 50 MW for a 1.5 μs pulse [22, 23]. Similar to Xbox 1, Xbox 2 also has a pulse compressor for an increase in the peak power. Xbox 2 is only able to power a single structure although future plans include the testing of CLIC superstructures [28].

[4] X-band is the frequency regime between 9 and 12 GHz. In the case of CLIC, the X-band frequency means 11.994 GHz.

[5] A klystron is a high power vacuum tube amplifier.

[6] A modulator provides high voltage pulses for the klystron.

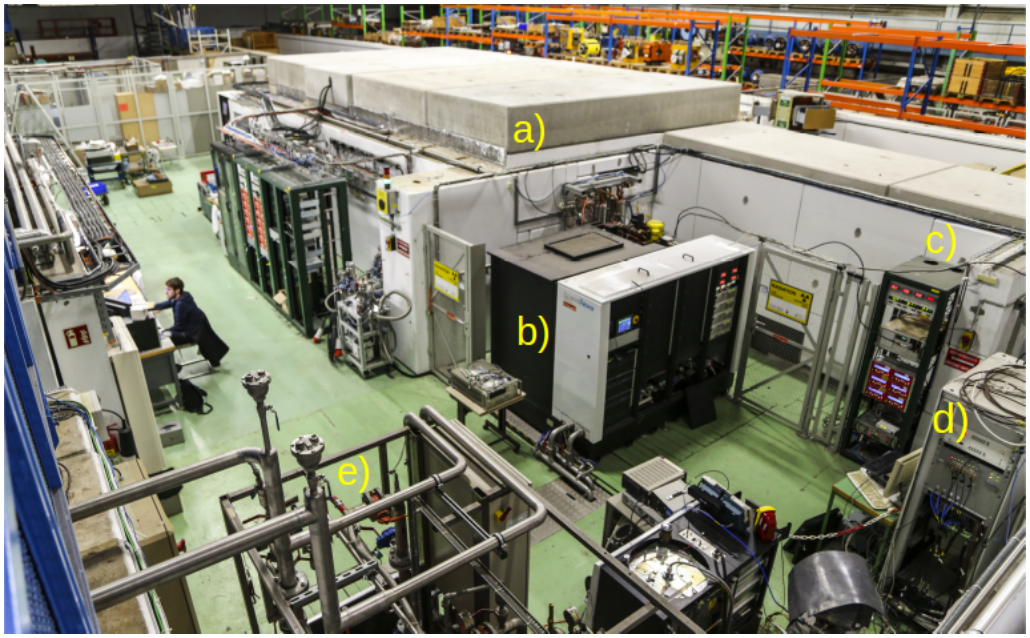

Figure 1.3: A photograph of the Xbox 2 test stand in Building 150 at CERN. The major components are labelled: a) is the test bunker, b) is the modulator with klystron positioned behind, c) is the vacuum rack with pre-amplifier, d) is the LLRF rack with acquisition crate, and e) is the low conductive water system.

1.5.4 Current Testing Capacity and the Case for a New Test Stand

For the next report on the feasibility of CLIC, which is due in 2019, it is the aim of the CLIC collaboration to have approximately 40 structures tested to high gradients. Given the current testing capacity, this would require another decade to complete and therefore another test stand is necessary to meet the demand. The new test stand needs to significantly increase the testing capacity of CERN in order to test the 40 accelerating structures required. In Chapter 5, the commissioning of a new test stand will be described in detail beginning with its final design, through the assembly and calibration and concluding with the high power conditioning of the system with first structure installation.

1.6 Structure Nomenclature

Before discussing the results of previous tests, the nomenclature used for the naming of CLIC structures will be introduced. Structures aim to test unique aspects of CLIC separately to understand how each of the features affect the high gradient capabilities of the structure. Common to the majority of structures' names is to start with 'T' and possibly followed by a 'D'. These indicate that the structure has tapered irises (T) and/or contains higher order mode damping waveguides (D). Tapering is included to produce a constant accelerating gradient throughout the structure

(explained in Section 3.5) while higher order mode (HOM) damping aims to remove higher frequency induced in the structure by the presence of a beam [36, 20]. Following the 'T' or 'TD' is a number which represents the number of accelerating cells in the structure which is commonly 18, 24, or 26. Another feature commonly referred to is the rounding profile's radius used in the machining of the disks expressed as 'R05' for 0.5 mm rounding or 'R1' for 1 mm rounding. The reader should note that it is common that the R05 is omitted in the name. A more recent addition to the CLIC structures is the compact coupler, represented in the name as 'CC'. This compact coupler replaced a mode launcher design and aims to increase the effective accelerating gradient by reducing the length of non-accelerating sections [91]. In order to damp HOM fields induced by the beam, CLIC aims to use Silicon Carbide damping material inside the HOM dampers. Structures with this damping material have 'SiC' included at the end of their names. Finally, most accelerating structure prototypes have been produced several times to understand the reproducibility. A serial number follows the structure name to distinguish identical prototypes, written as an 'N' followed by a number[7].
In this thesis, the results from the high power testing of four unique structure prototypes will be presented and some new nomenclature will be explained in detail in Chapters 7.

1.7 Previous High Gradient Results

By 2015, CERN had tested four CLIC structure prototypes and were about to commence the conditioning of two others. The results of these structures are presented in Table 1.1. Only a TD26CC and crab cavity were tested successfully without developing a hot-cell. While CERN was commissioning its first two X-band test stands, Xbox 1 and Xbox 2, work on the development of achieving high gradients in CLIC structures had begun at two other facilities although using the American

[7]CLIC's accelerator does not only consist of structures which accelerate longitudinally. The final focus of the CLIC will use a deflecting cavity to increase the machine's luminosity. Indicative of the shape of the intersecting bunches after the deflection, the structure is commonly referred to as a Crab Cavity.

Table 1.1: CLIC structure results from high power testing up to 2015, at CERN.* Developed a hot-cell where the conditioning state deteriorated. †Crab Cavity displayed as the surface field given the structure is a deflecting cavity [20, 25, 24].

Test Stand	Structure	Gradient [MV/m]	Pulse Length [ns]	BDR [bpp/m]
Xbox 1	TD24R05	94*	200	2×10^{-5}
	T24	80*	190	1×10^{-6}
	TD26CC N1	100	250	3×10^{-6}
Xbox 2	Crab	154†	200	3×10^{-5}

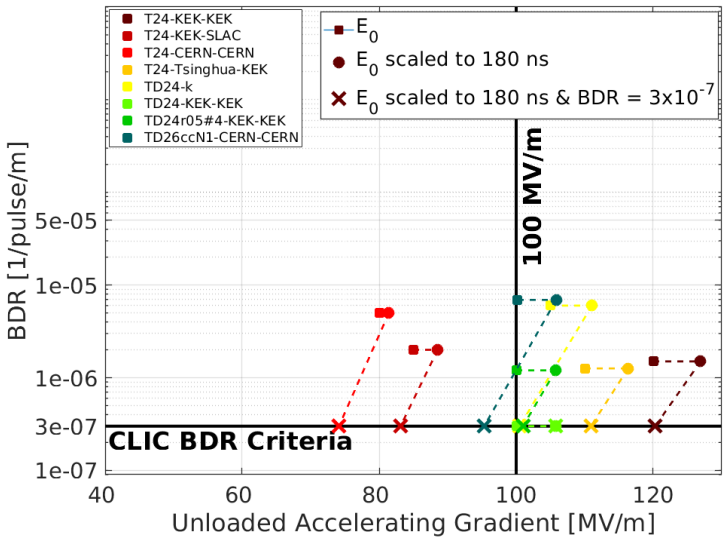

Figure 1.4: Testing results up to 2015 for CERN, SLAC and KEK. On the y-axis is the breakdown rate, in bpp/m, plotted against the achieved unloaded accelerating gradient in MV/m. The three marker types are the operational gradient (square), operational gradient normalised to nominal pulse length (circle) and operational gradient normalised to nominal pulse length and breakdown rate (cross). Each colour represents a different prototype structure with the legend indicating the "Prototype name-Fabricated by-Tested by".

X-band frequency of 11.4 GHz [26, 27]. Figure 1.4 displays the achieved unloaded gradient as raw values as well as gradients scaled to CLIC nominal RF pulse length and BDR parameters. Results from KEK had demonstrated to have tested the early CLIC designs of the T24 and TD24 to beyond an unloaded gradient of 100 MV/m. Simple and shorter structures, such as the T24 and TD24, have lower surface electric and magnetic fields for a given accelerating gradient and therefore less influenced by RF breakdown and other high gradient phenomena [29]. Achieving these results with a structure design more like that proposed for CLIC, with more cells and Higher Order Mode (HOM) damping waveguides, had only been achieved once on the TD26CCR05 N1 (also known as the CLIC-G* N1) [24]. The most recent high power testing results using Xbox 2 and the newly commissioned Xbox 3 will be presented in Chapter 7. These will illustrate the high power testing results for four structures including: a CLIC baseline design structure, a structure with higher order mode (HOM) damping material and two novel design structures aimed at reducing the cost of production.

1.8 Summary

A linear collider proves to be a cost-effective means of reaching the terascale COM energy regime with a lepton-lepton collider. The Compact Linear Collider is a

concept design aiming to have an ultimate COM energy of 3 TeV, with 380 GeV and 1.5 TeV stages. Achieving these COM energies in an accelerator of reasonable length requires high accelerating gradients up to 100 MV/m which is well beyond that of current linear accelerator technology. Generating these accelerating gradients in a reliable fashion is under investigation with significant efforts currently being made by CERN and other organisations around the world. The latter chapters of this thesis will describe the commissioning of a novel RF test stand. This new RF test stand will be shown to be able to test CLIC accelerating structures to the nominal gradient of 100 MV/m in a more cost and time effective manner than previous test stands. The high gradient testing of four unique accelerating structures, conducted using the new test stands and its predecessors, will illustrate the reproducibility of achieving these high gradients. Finally, another phenomenon related to the capture of field-emitted electrons will be reported on through a series of measurements and simulations.

Chapter 2

Compact Linear Collider

The Compact Linear Collider is a multi-TeV electron-positron linear collider proposed to be located at CERN on the French-Swiss Border. In order to understand the motivation of the work in this thesis, this chapter will outline the design of CLIC and look at possible physics which may be investigated.

2.1 Overview

To investigate a wide variety of energy regimes, CLIC will be built in three stages. The first stage of 380 GeV, known as CLIC-380, aims to probe the Standard Model in great detail. Afterwards CLIC will become the first lepton-lepton collider to reach the terascale with a penultimate COM energy stage of 1.5 TeV before implementing its ultimate COM energy of 3 TeV. A map of the proposed site for the three tunnel lengths corresponding to the three stages of CLIC is illustrated in Figure 2.1, where the LHC and Lake Geneva (Lac Léman) set the scale. Achieving the proposed beam parameters requires developments in numerous areas of accelerator physics including high gradient linear accelerators. In this section, the injector and main linac will be described along with the methods conceived to drive the large power requirements of the main linac.

2.1.1 Injector System

Prior to the main X-band linac of CLIC, the main beam undergoes several stages of acceleration in the injector system. Initiating the positron source is an electron gun, followed by a 5 GeV linac. Collision of these electrons into a fixed target will produce high energy photons through bremsstrahlung radiation and subsequently, converted through pair production, electrons and positrons. The positrons are isolated using a bending magnet. Two pre-injector linacs, powered by 2 GHz RF, accelerate the main beam electrons, produced in a separate process, and the aforementioned positrons up to 200 MeV where they are injected into a single 2.66 GeV linac. A vital parameter

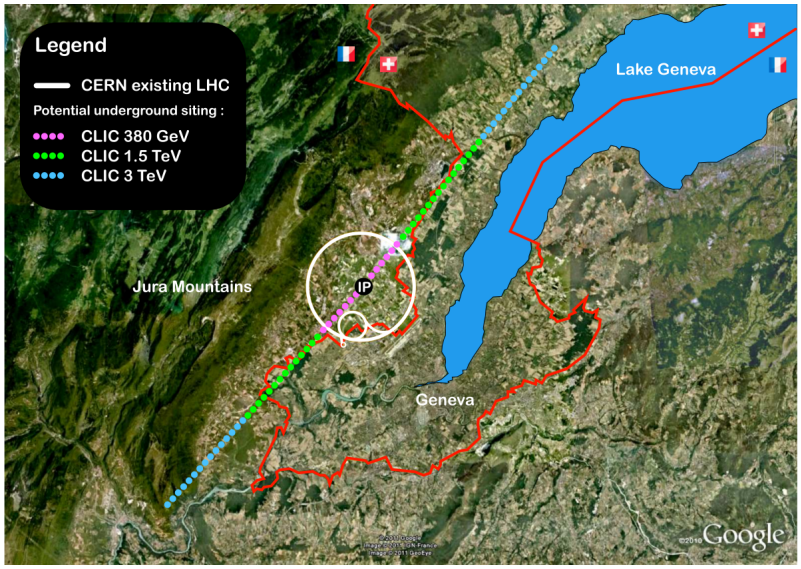

Figure 2.1: A map of the CLIC sites for each COM stage proposed. The LHC, with a 8.5 km diameter, sets the scale for the map and the interaction point (IP) of CLIC is located directly at the centre of the LHC [15].

to define the number of events at the interaction point is the luminosity which is defined as:

$$\mathcal{L} = H_D \frac{N^2}{4\pi\sigma_x\sigma_y} n_b f_r, \tag{2.1}$$

where N is the number of particles per bunch, $\sigma_{x,y}$ is the horizontal/vertical bunch size, n_b is the number of bunches, and f_r is the bunch frequency [30]. This illustrates that the luminosity is inversely proportional to the transverse bunch size (σ). At 2.86 GeV, the positrons and electrons undergo a stage of damping, which is repeated for the "hot" positrons, to reduce the transverse size of the bunches and therefore increasing the luminosity (Figure 2.2).
Compression in the buncher compressor (BC1) prepares the electron and positrons for the booster linac which adds an additional 6.14 GeV. After reaching 9 GeV, the electrons and positrons are ready for injection into their respective main X-band linacs.

2.1.2 Staged Baseline Main Linac

The Conceptual Design Report (CDR) for CLIC outlined the design of the 3 TeV COM energy machine, along with 500 GeV and 1.4/1.5 TeV stages [9]. Recently, the design was rebaselined to reduce the first stage to 380 GeV and the second stage was chosen to be 1.5 TeV. The first stage has a proposed loaded accelerating gradient of 72 MV/m, leading to a total length of 11.4 km. For Stages 2 and 3, the loaded

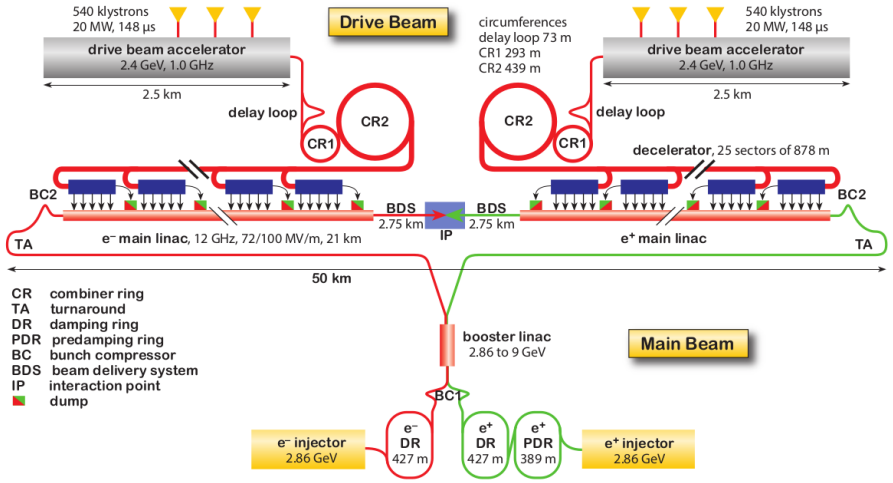

Figure 2.2: An outline of the design of CLIC for the ultimate energy of 3 TeV [9].

accelerating gradient will be increased to 100 MV/m with a doubling of luminosity in each stage. Further parameters of the main linac for the three stages of CLIC are summarised in Table 2.1.

2.1.3 High Power RF System

With an estimated average wall-plug power consumption of 252 MW, it is important that each component of CLIC is designed to operate as energy efficiently as possible. For this reason, several investigations into methods for the generation of the high power RF are being conducted [15]. Two schemes for driving CLIC have been proposed:

Table 2.1: Beam parameters for the three COM energy stages of the rebaselined design of CLIC [15].

Parameter	Symbol	Unit	Stage 1	Stage 2	Stage 3
COM Energy	$\sqrt{s}$	GeV	380	1500	3000
Repetition Rate	f_{rep}	Hz	50	50	50
Number of Bunches per Train		n_b	352	312	312
Bunch Separation	Δt	ns	0.5	0.5	0.5
Pulse Length	τ_{RF}	ns	244	244	244
Loaded Accelerating gradient	G	MV/m	72	72/100	72/100
Total Luminosity	$\mathcal{L}$	10^{34} cm^{-2} s^{-1}	1.5	3.7	5.9
Luminosity Above 99% of $\sqrt{s}$	$\mathcal{L}_{0.01}$	10^{34} cm^{-2} s^{-1}	0.9	1.4	2
Main Tunnel Length		km	11.4	29.0	50.1
Number of Particles per Bunch	N	10^9	5.2	3.7	3.7
Bunch Length	σ_z	μm	70	44	44
IP Beam Size	σ_x/σ_y	nm	149/2.9	60/1.5	40/1
Normalised Emittance (end of linac)	ϵ_x/ϵ_y	nm	920/20	660/20	660/20
Normalised Emittance (at IP)	ϵ_x/ϵ_y	nm	950/30	-	-
Estimated Power Consumption	P_{wall}	MW	252	364	589

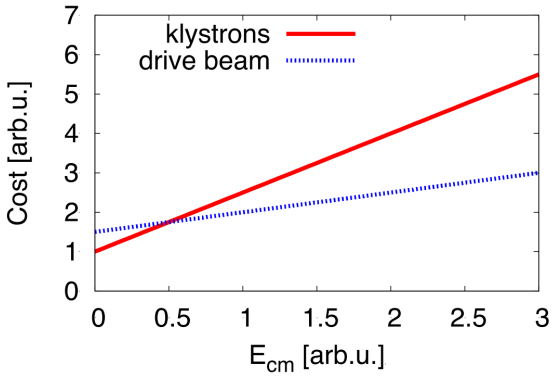

Figure 2.3: A cost comparison, in arbitrary units, for using a drive beam versus using klystrons to power CLIC, plotted against the COM energy in arbitrary units [31].

1. A two beam acceleration scheme, and

2. a klystron driven scheme.

Figure 2.3 displays the cost analysis of the two schemes and demonstrates that the most cost effective solution differs depending on the COM energy. For lower COM energy linear colliders, the most efficient means to power it is through a gallery of klystrons. This klystron gallery is used in the vast majority linear accelerators. For higher COM energy linear colliders, it is found that using klystrons is inefficient due to the total number of klystrons necessary. CLIC aims to be the first such accelerator to use the new drive-beam acceleration technique.

Two-Beam Acceleration Scheme

Generating the nominal accelerating gradient of CLIC will require a peak input power of 270 MW per metre [9]. If the 3 TeV stage of CLIC were to operate with a klystrons it would require ∼100 000 units. Such a scheme is infeasible as klystrons have a product lifetime less than that of the machine and therefore would require replacement within CLIC's lifetime. On top of this they require continual maintenance. The two factors would lead to an unreasonable machine down-time. Proposed to drive the main beam is a two-beam accelerating scheme where a high current, lower energy drive-beam powered by fewer klystrons uses its beam power to generate 11.994 GHz RF at high power for the CLIC beam. This scheme is by far the most efficient method for the long baseline 1.5 and 3 TeV stages.

A diagram of a CLIC module with drive beam is shown in Figure 2.4. Running parallel to the main beam, the CLIC drive beam operates at 2.4 GeV with 100 A of beam current. The PETS takes power within the high current beam and converts it into RF power. This RF power is then transferred along approximately 60 cm of waveguide to drive the main beam modules. Numerous sections of PETS would be required for CLIC with each just 878 m in length and only able to drive 3000

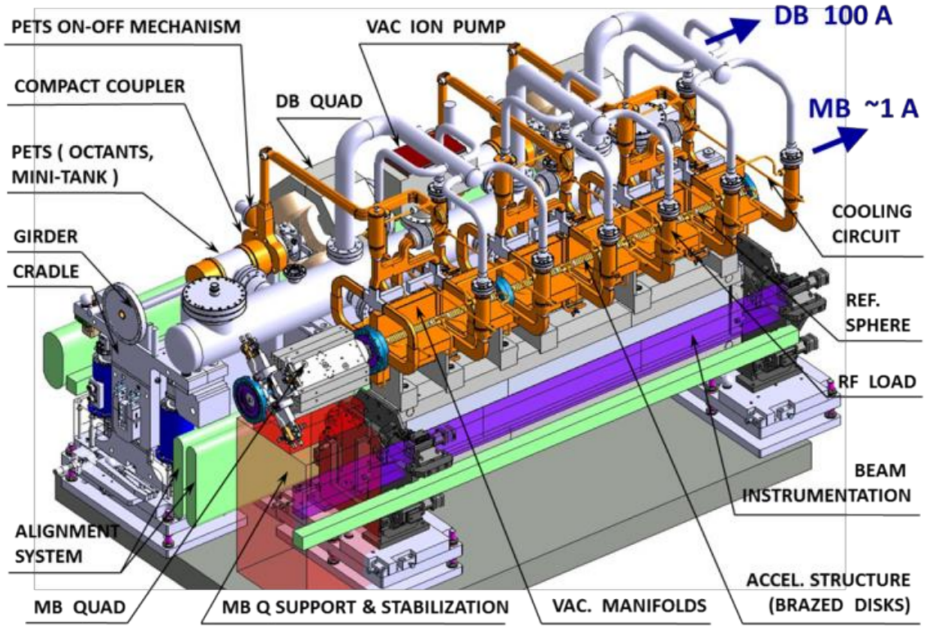

Figure 2.4: A complete CLIC module with the drive beam adjacent to the main linac. Six accelerating structures are found in the module [9].

accelerating structures. Such a design is highly efficient for long linear accelerators as the lifetime of the drive beam facility is comparable to the main-beam facility.

Klystron-Based CLIC-380

Klystrons have recently undergone a rapid evolution in their efficiency through a development in their bunching cavities. Defining the efficiency as the ratio of the output RF power to the input power, new klystron designs are aiming for efficiencies of over 80% in comparison to around 40% for current designs [32]. If this can be achieved then this would reduce the number of klystrons by a factor of two and enhance the feasibility of a klystron driven CLIC-380. For the upgrade to the 1.5 and 3 TeV, it has been proposed that the remainder of the machine could use the two beam acceleration scheme (TBAS) [9, 15].

2.2 CLIC Physics

An accelerator like CLIC will permit the exploration of a wide variety of physics, from high precision measurements of the Standard Model to direct and indirect searches for BSM physics. Exploring all these regimes will be done through the staged construction, discussed in previous sections, where the collision energy of CLIC will increased with each stage. The 380 GeV stage is a Standard Model physics probe used to gain access to Higgs boson and top quark physics. At 1.5 and

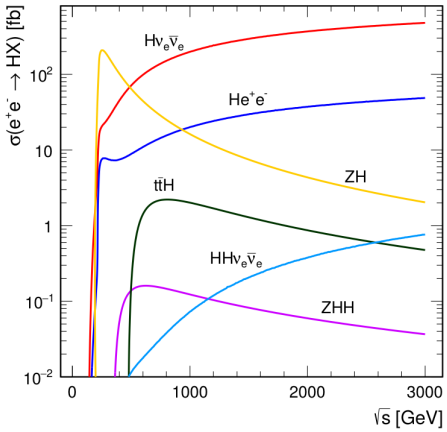

Figure 2.5: The cross-sections, in femtobarns, for various Higgs boson events expected to occur at CLIC plotted against the COM energy in GeV [15].

3 TeV, the second and third stages start the exploration for BSM physics. Along with BSM searches these high COM energy stages begin to search for rare Higgs physics including self-coupling, quartic coupling, double Higgs boson production, and rare Higgs boson decay [9].

2.2.1 Higgs Boson

A lepton collider provides the cleanest environment for Higgs boson studies. Figure 2.5 displays the calculated cross-section for the several Higgs processes expected from CLIC up to 3 TeV. At the lower COM energy ($\sqrt{s}$) stage of $\sqrt{s} = 380$ GeV, Higgsstrahlung ($e^+e^- \rightarrow ZH$) proves to be the most common Higgs boson producing process, although with a significant contribution from vector-boson fusion ($e^+e^- \rightarrow H\nu_e\bar{\nu}_e$) [33]. At higher COM energies, $\sqrt{s} \rightarrow 3$ TeV, the Higgsstrahlung cross-section is suppressed and other processes such as vector-boson fusion and ZZ fusion ($e^+e^- \rightarrow He^+e^-$) begin to dominate as the energy is increased towards 3 TeV.

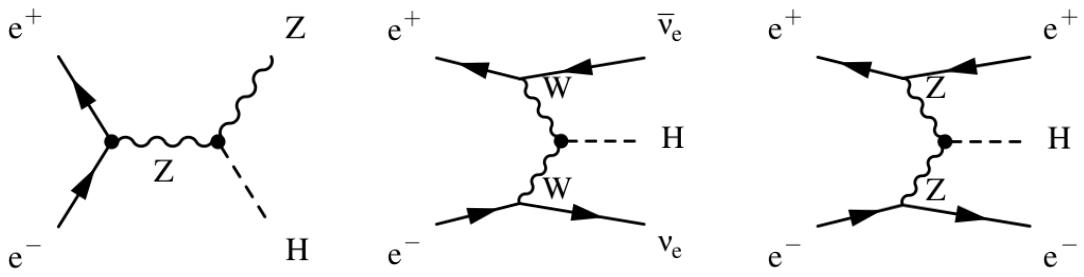

(a) Higgsstrahlung. (b) Vector Boson Fusion. (c) Z Boson Fusion.

Figure 2.6: Feynman diagrams for the three most prominent Higgs boson events expected to occur in CLIC [15].

Table 2.2: Leading-order Higgs boson cross-sections for an unpolarised CLIC beam. The expected number of events are listed at the bottom after accounting for initial state radiation and beamstrahlung [15].

$\sqrt{s}$	350 GeV	1.4 TeV	3 TeV
$\mathcal{L}_{int}$	500 fb^{-1}	1.5 ab^{-1}	2 ab^{-1}
$\sigma(e^+e^- \to ZH)$	133 fb	8 fb	2 fb
$\sigma(e^+e^- \to H\nu_e\bar{\nu}_e)$	34 fb	276 fb	477 fb
$\sigma(e^+e^- \to He^+e^-)$	7 fb	28 fb	48 fb
$\#HZ$ events	68 000	20 000	11 000
$\#H\nu_e\bar{\nu}_e$ events	17 000	370 000	830 000
$\#He^+e^-$ events	3,700	37 000	84 000

The three main Higgs boson related events expected in CLIC are illustrated using Feynman diagrams in Figure 2.6. Table 2.2 details the expected cross-section of Higgs boson events with unpolarised beams. Taking into account the expected beam physics, such as initial state radiation and beamstrahlung, the expected number of events are listed at the bottom of the table [15, 33].

2.2.2 Top Quark

Along with Higgs physics, a lepton collider based on CLIC would provide an opportunity to measure the top quark's properties with unprecedented precision. With the heaviest mass of any particle in the Standard Model, the top quark is of great interest for SM and BSM physics. The top quark has the strongest coupling to the

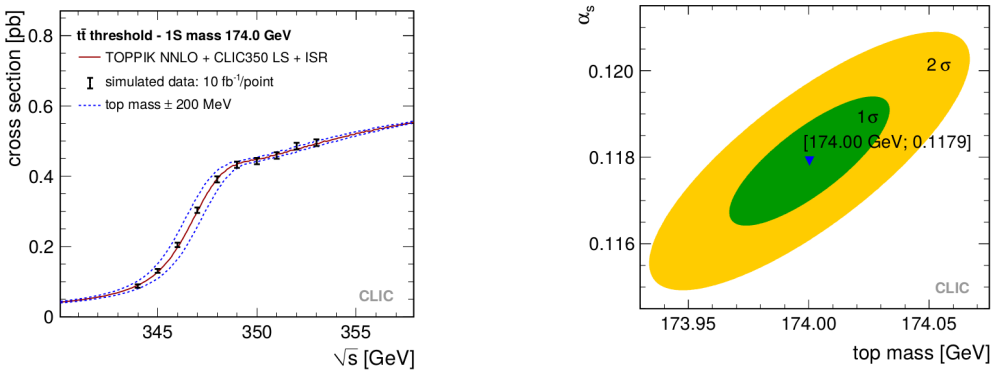

(a) Threshold scan.

(b) Mass reconstruction.

Figure 2.7: The two techniques of determining the Top quark mass at CLIC [9]. The left-hand figure depicts a simulated threshold scan where the cross-section in picobarns is plotted against the COM energy of the machine in GeV. The right-hand figure illustrates a simulation of the data from a mass reconstruction where the strong coupling constant is plotted against the Top quark mass in GeV. The colours represent one (green) and two sigma (yellow) standard deviations from the mean.

Higgs field and is currently the leading uncertainty in SM vacuum tests [34]. In the proposed High-Luminosity LHC (HL-LHC), the statistical error expected for the top quark mass is ∼10 MeV although it is afflicted with significant systematic uncertainties of around 600 MeV. Investigating the top quark mass at CLIC can be done through two complementary methods. The first is a threshold scan which is the most accurate method known [9]. This method involves measuring the $t\bar{t}$ production rate which will rise greatly as the $\sqrt{s}$ passes the pair production energy of the top quark, as demonstrated in Figure 2.7a. Secondly, the mass can be reconstructed from the decay products. The advantage of this method is that it can be performed at any energy. Using this method, the mass can be reconstructed to a statistical precision of 80 MeV (Figure 2.7b) [9].

2.2.3 Beyond the Standard Model

Searches for BSM physics at CLIC will be possible through two different methods. The first is a direct search which can reach energy scales up to $\sqrt{s}/2$ and $\sqrt{s}$ for pair and single-production, respectively. Results from the LHC have so far been unable to find any hints of particles above the top quark mass which makes such a search not overly promising. A more likely scenario where BSM physics may be found is through an indirect detection of couplings to Standard Model physics. Searches for indirect detection of BSM physics are expected to be sensitive up to tens of TeV at CLIC [15].

2.3 Summary

The unique strengths of an accelerator like CLIC make it a viable and attractive option for the next generation electron-positron collider. A staged design, beginning at 380 GeV, will allow CLIC to act as a Higgs boson and top quark factory with latter stages searching for BSM physics. The CLIC approach of using high accelerating gradients up to 100 MV/m overcomes the limitations of conventional linac technology, allowing a TeV linear collider of viable length to be built. Methods on driving the beam for each energy stage are under investigation with ideas of using klystrons for the 380 GeV stage and a drive beam for the 1.5 and 3 GeV stages. CLIC will offer unprecedented accuracy for measuring the properties of the Higgs boson and top quark, with almost an order of magnitude greater statistical precision in comparison to the HL-LHC.

Chapter 3

Physics of Linear Accelerators

In preparation for the discussion of the high gradient results of several accelerating structure prototypes, which will occur later in this thesis, this chapter will describe the concepts of accelerating structure operation. Below is an introduction to a common accelerating structure design for relativistic electrons known as an iris-loaded waveguide.

3.1 Lorentz Force Equation

In the presence of electric and magnetic fields, charged particles undergo acceleration. The force applied is described by the Lorentz force equation:

$$\vec{F} = q(\vec{E} + \vec{v} \times \vec{B}), \tag{3.1}$$

where $\vec{E}$ is the electric field, $\vec{v}$ and q are the velocity and charge of the particle, and $\vec{B}$ is the magnetic field [35]. For acceleration in the direction of motion, only the electric field component is useful and therefore the force applied for acceleration can be written simply as $\vec{F} = q\vec{E}$. Using this equation the first condition for continuous acceleration can be defined, which is that: *the electric field must have a component in the direction of acceleration.* For this reason free-space electromagnetic fields are not be used for continuous acceleration of a propagting beam.

3.2 Acceleration in an Iris-Loaded Waveguide

To generate a longitudinal component in an electric field, one must impose boundary conditions. This section begins by investigating the properties of an oscillating electric field inside a uniform cylindrical waveguide.

3.2.1 A Cylindrical Waveguide

In order for an RF wave to propagate within a waveguide it must satisfy the wave equations. These are given as:

$$\nabla^2 \vec{E} - \frac{1}{c^2}\frac{\partial \vec{E}}{\partial t^2} = 0, \tag{3.2}$$

and

$$\nabla^2 \vec{B} - \frac{1}{c^2}\frac{\partial \vec{B}}{\partial t^2} = 0, \tag{3.3}$$

where $\vec{E}$ and $\vec{B}$ are the electric and magnetic field vectors, respectively, and c is the speed of light [36]. As previously stated, any electric field used needs to have a z component and therefore only the transverse magnetic (TM) modes can accelerate particles as transverse electric (TE) modes have $E_z = 0$ as their name suggests. The TM_{01} mode has the longitudinal electric field required and has no azimuthal dependence, referred to as monopole-like. These two features make it a popular mode for acceleration and commonly this mode is referred to as the accelerating mode. For a uniform waveguide with azimuthal symmetry, the wave equation gives the longitudinal electric field for the TM_{01} mode as:

$$E_z(r, z, t) = EJ_0(Kr)\exp[i(\omega t - k_0 z)], \tag{3.4}$$

where E is the electric field amplitude, J_0 is a Bessel function, K is the cutoff wavenumber of the TM_{01} mode, k_0 is the wavenumber, and ω is the frequency [36]. For this mode, $B_z = 0$ and is therefore omitted from the remainder of this derivation of the longitudinal field properties. The dispersion relation can be shown to be of the form:

$$\omega^2 = (Kc)^2 + (k_0 c)^2. \tag{3.5}$$

Rearranging the dispersion relation, the phase velocity, defined as $v_p = \omega/k_0$, is found to be [36]:

$$v_p = \frac{\omega}{k_0} = \frac{c}{\sqrt{1 - (Kc)^2/\omega^2}} > c. \tag{3.6}$$

A common graphical representation for understanding the dispersion relation is the Brillouin diagram which depicts the frequency (ω) plotted against the wavenumber (k_0). Figure 3.1 illustrates the dispersion relation for a uniform waveguide with the $v_p = c$ line depicted. At this point, the second condition for continuous acceleration can be defined which is that *the particle and RF wave must travel at the same velocity to remain synchronous (synchronism condition).* A uniform waveguide always has $v_p > c$ and as a result particles are unable to remain synchronous with

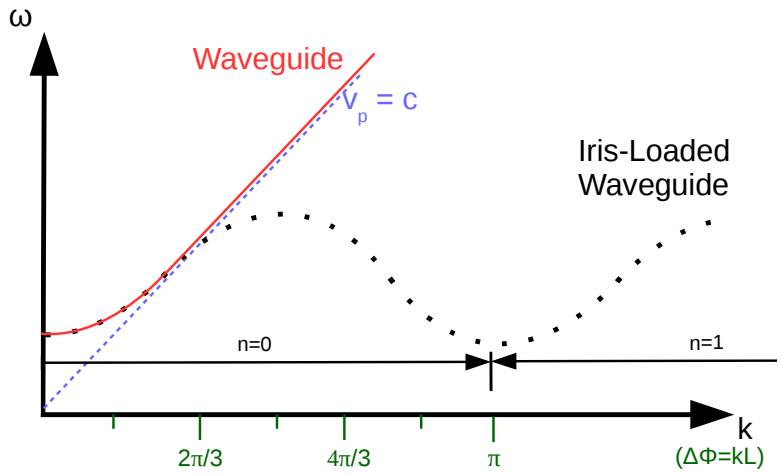

Figure 3.1: Brillouin diagram, which plots frequency against the phase advance, illustrating the dispersion relations for a uniform waveguide (red) and for an iris-loaded waveguide (black dots). The speed of light line is depicted in blue.

the RF wave as they travel along the waveguide. The solution to this is to load the waveguide with periodic obstructions. A common solution is an iris although this is not the only solution [40]. Irises allow a reduction of the phase velocity of the RF wave to $v_p \leq c$ and therefore particles can travel at the same velocity as the wave, making the synchronism condition possible. For the main linac of CLIC the design aims for a phase velocity of c, as the electrons and positrons are highly relativistic [36].

3.2.2 Periodic Boundary Conditions and Floquet's Theorem

When constructing the solution to the wave equation within a periodically loaded waveguide, it must not only satisfy the wave equation but also the Floquet theorem. This theorem states: *In a given mode of an infinite periodic structure, the fields at two different cross-sections that are separated by one period differ only by a constant factor which in general is a complex number.* This can be written as:

$$E(r, z + L, t) = E(r, z, t) \exp(\pm i k_0 L). \tag{3.7}$$

The introduction of a set of periodic irises each equally separated by a length, L, will perturb the electric field in the longitudinal plane (z). An equation satisfying this can be written as [36]:

$$E(r, z, t) = E_L(r, z) \exp[i(\omega t - k_0 z)], \tag{3.8}$$

where $E_L(r, z)$ is a periodic function of period length L and $\exp[i(\omega t - k_0 z)]$ is the wave component. As with any periodic formula, $E_L(r, z)$ can be expanded as a

Fourier series and be written as [36]:

$$E_L(r,z) = \sum_{n=-\infty}^{\infty} a_n(r)\exp(-i2\pi nz/L), \tag{3.9}$$

where a_n are the Fourier coefficients [36]. Solving the cylindrical wave equation (Equation 3.3) using Equation 3.9, it is found that:

$$a_n''(r) + \frac{a_n'(r)}{r} - K_n^2 a_n(r) = 0, \tag{3.10}$$

where the differentiation terms are with respect to r and $K_n^2 = (\omega/c)^2 - (k_0 + 2\pi n/L)^2$. For $K_n^2 > 0$, this is found to be a propagating wave whose solution is:

$$E_z(r,z,t) = \sum_{n=-\infty}^{\infty} E_n J_0(K_n r)\exp[i(\omega t - k_n z)]. \tag{3.11}$$

Interpreting this equation it is found that there are an infinite number of waves, known as space harmonics, each of which is represented by the index n (Figure 3.1) [36]. Taking this wave solution, the phase velocity can be written as [36]:

$$v_{p,n} = \frac{\omega}{k_n} = \frac{\omega}{k_0 + 2\pi n/L}. \tag{3.12}$$

The result is that to reduce the phase velocity of a periodic structure, one can simply choose a sufficiently large space harmonic.
At this point one can define a component of an iris-loaded waveguide. The region between two irises is known as an *accelerating cell*. RF power injected into the accelerating structure will begin to fill these accelerating cells. An important quality of the periodic structure is the group velocity which defines the velocity at which the RF power moves through the structure. Referring back to Figure 3.1, the group velocity is found from the slope of the dispersion curve, which can be written as [36]:

$$v_g = \frac{d\omega}{dk} = 2\pi L\frac{df}{d(\Delta\phi)}. \tag{3.13}$$

Figure 3.1 also illustrates that all space harmonic components have the same group velocity. The group velocity affects the stored power in the periodic structures by modifying the time it takes for the wave to move throughout the structure. The group velocity can be varied through a change in the iris radius and thickness. In Section 3.5, this will be shown to be a technique to increase the efficiency of energy transfer to the beam. The fill time (t_{fill}) is the total time for the accelerating

structure to fill with RF power and is given by an integration over the group velocity profile of the structure, written as [36]:

$$t_{fill} = \int \frac{dz}{v_g(z)}. \tag{3.14}$$

In Chapter 7, the fill time will be used to understand the high gradient performance of accelerating structures.

3.3 Energy Gain in an RF Cell

Considering a structure filled with RF power, one can now define the energy gain per accelerating cell, using a simplified single RF gap model. The real component of the longitudinal and on-axis electric field, for the TM_{01} mode, in an RF cell is defined as:

$$E_z(z,t) = E(z)\cos(\omega t + \phi_s), \tag{3.15}$$

where ω is the frequency of the RF field in rad/s and ϕ_s is the synchronous phase [36]. For a particle travelling at velocity v in the field, described in Equation 3.15, the energy gain for a particle crossing the RF gap is given by the Panofsky equation. It states that for an input particle of charge q the change in energy is given as an integration over the field experienced by the particle, which can be written as:

$$\Delta W = q\int_{-L/2}^{L/2} E_z \cos\left(\omega\frac{z}{v} + \phi_s\right)dz, \tag{3.16}$$

where L is the cell length [39, 36]. Solving this integral, the energy gain can be simply expressed as:

$$\Delta W = qV_0T\cos(\phi_s), \tag{3.17}$$

where T is the transit-time factor and V_0 is the gap voltage. A definition for the *accelerating gradient* of an accelerating cell can now be defined as:

$$G = \frac{V_0T}{L}, \tag{3.18}$$

which has a unit of V/m[1][2] [96]. The transit-time factor (T) accounts for the difference in energy gain for an oscillating electric field compared to a constant DC

[1]The accelerating gradient is sometimes defined in the units MeV/m.

[2]Beam-loading reduces the effective gradient therefore gradients can be referred to as *loaded* or *unloaded*. In this thesis all accelerating gradients are unloaded unless states otherwise.

electric field and, for a simple pillbox cavity, is approximately defined as:

$$T \approx \frac{\sin \frac{\omega L}{2v}}{\frac{\omega L}{2v}}. \tag{3.19}$$

This demonstrates that acceleration in RF fields is not as effective as acceleration in a DC field as $T < 1$ for $\frac{\omega L}{2v} > 0$. The surface electric field can be written as proportional to the accelerating gradient such that:

$$E_s = cG, \tag{3.20}$$

where c is the proportionality constant. The value of c is dependent on the geometry of the cell and is generally found to be between 1.8 and 2.6 for CLIC structures.

3.4 Accelerating Structure Properties

As iris-loaded waveguides are commonly referred to as accelerating structures, this term will be used for the remainder of this text. In this section, the relation between the input power, stored energy and accelerating gradient will be described.

3.4.1 Figures of Merit

Each accelerating cell in an accelerating structure acts as an RF resonator. For a resonator, the ratio of the stored energy to power loss per cycle is known as the quality factor (Q), which is defined as:

$$Q = \frac{\omega U}{P}, \tag{3.21}$$

where U is the stored energy, ω is the frequency, and P is the average dissipated power [36]. Having a high Q ensures that a large amount of power can be stored within the cavity. The quality factor for accelerating structure cells is $Q \approx 5700$. Another important parameter is the shunt impedance (r) which describes the effectiveness of generating an accelerating voltage for a given power loss and is defined as [92]:

$$r = \frac{(GL)^2}{P}. \tag{3.22}$$

In order to achieve a high accelerating gradient, accelerating structures are designed with a high shunt impedance [36]. Finally, an important parameter to take

into account is the ratio of the shunt impedance to the quality factor, commonly called r over Q. Described by the equation:

$$\frac{r}{Q} = \frac{(GL)^2}{U\omega}, \tag{3.23}$$

r over Q describes the efficiency of acceleration per unit stored energy at a given frequency [92]. With these important parameters, the power propagation through an accelerating structure can be described.

3.5 Travelling Wave Accelerators

The accelerating structures of the main linac of CLIC will operate with a travelling wave mode where the RF power is input at one end of the structure and dissipated in a matched RF load at the other end [37]. The choice in using a travelling wave mode rather than a standing wave mode is due to two reasons: (1) standing-wave structures are very sensitive to mechanical tolerances and (2) travelling waves are much more energy efficient for short beam pulses [36] [3]. Below are descriptions of the mode choice and a structure feature unique to travelling wave structure, employed to increase r/Q.

3.5.1 Operating Mode

The operational modes available in an accelerating structure are dependent on the number of cells. Referring back to Figure 3.1, the dispersion curve for the accelerating structure is observed to be made up of discrete points rather than a straight line. This is because the conditions for resonance must be satisfied. The phase advance per cell ($\Delta\phi$) needs to satisfy the condition:

$$\Delta\phi = kL = \frac{p\pi}{N}, \tag{3.24}$$

where $p = 0, 1, ..., N$ are the operational modes given a total number of cells N [36]. In practice, to achieve a flat field distribution across the structure a detuning of the end cells is required. The amount of detuning differs for the 0 and π modes and therefore one must choose which is present. As a consequence, a single cell structure can only operate with the standing wave modes $\Delta\phi = 0$ or π. While for a 3-cell structure, the travelling wave modes $\Delta\phi = \pi/3$ and $2\pi/3$ are available and one of the standing wave modes $\Delta\phi = 0$ or π [38]. When calculating the mode to use for CLIC, it is found that the $\Delta\phi = 2\pi/3$ has a large shunt impedance and therefore is

[3] In order to achieve a pure travelling wave mode, the structure and the waveguide network must be impedance matched to prevent reflections.

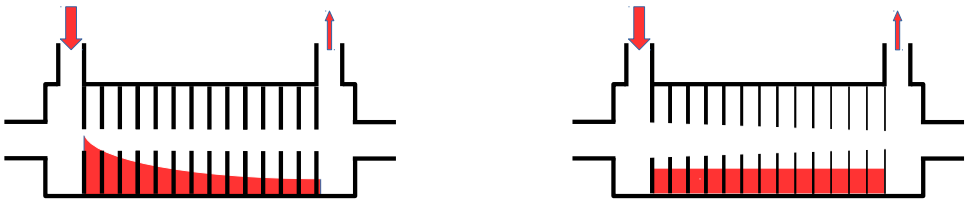

(a) Constant Impedance. (b) Constant Gradient.

Figure 3.2: A pictorial description of the ratio of the power dissipation along the structure, depicted in red, for constant impedance structure in comparison to a constant gradient structure. A constant impedance structure has the largest stored power in the cell at the beginning of the structure, with the stored power reducing exponentially along the structure. The constant gradient design, as its name suggests, keeps a constant stored power in each cell along the structure.

used in all CLIC structure designs. Past RF designs for predecessor high gradient colliders have trialled using the $5\pi/6$ mode [51].

3.5.2 Constant Impedance vs Constant Gradient Structure

When considering the geometric design of a travelling wave accelerating structure, especially the iris radius and thickness, it is important to consider how to maximise r/Q for each cell. If one is to couple identical cavities together, to create the accelerating structure, it is found that the power dissipation (P_w) follows differential equation [36]:

$$\frac{dP_w}{dz} = -\frac{\omega P_w}{Qv_g}. \tag{3.25}$$

The solution to this differential equation shows that the power dissipates along the structure in an exponential fashion, according to:

$$P_w(z) = P_0 e^{-\frac{\omega z}{Qv_g}}. \tag{3.26}$$

where P_0 is the peak input power [36]. Illustrated in Figure 3.2a is the power dissipation for a constant impedance structure, where the red depicts the power loss across the structure. Such a design results in the greatest surface fields occurring at the beginning of the structure due to the stored RF power being greatest in this region. In order to reduce peak surface fields with respect to the accelerating gradient over the structure, it is more effective to even out the stored power distribution over the structure. By reducing the group velocity, the stored power can be increased. A reduction in the group velocity is achieved through a reduction of the iris radius

and thickness. This technique is known as iris tapering and allows for a reduction in the peak E_s of the structure as all of the accelerating cells share the work rather than the first cell applying the greatest gradient. For a constant power dissipation along the structure, the group velocity variation over the structure must have the form [36]:

$$v_g(z) = \frac{\omega L}{Q} \frac{1 - (z/L)(1 - e^{-\frac{\omega L}{Q v_g}})}{1 - e^{-\frac{\omega L}{Q v_g}}}. \tag{3.27}$$

Figure 3.2b demonstrates the power dissipation across the constant gradient structure. The irises' radii can be observed to reduce along with the iris thickness over the structure.

3.6 Summary

For continuous acceleration to occur within an oscillating electric field, two conditions must be satisfied: (1) The electric field must have a component in the direction of acceleration and (2) its phase must remain synchronous with the beam. Confining the electric fields within an iris-loaded waveguide generates the longitudinal electric field component and reduces the phase velocity to $v_p \leq c$ creating the conditions suitable for acceleration. For CLIC structures, the design aims for a phase velocity equal to c given the ultra-relativistic energies of the electrons/positrons. Travelling wave structures are found to be the most efficient option, given CLIC's short pulse lengths, with the $2\pi/3$ mode chosen due to its large shunt impedance.

Chapter 4

Phenomenology of High Gradient Acceleration

In the previous chapter, it was shown that an increase in the accelerating gradient led to an increase in the surface electric fields. Along with this increase in E_s, a large accelerating gradient also leads to larger surface magnetic fields (H_s). Naïvely one might think that to generate an arbitrarily high accelerating gradient, it would be possible to simply input more power, in accordance with Equation 3.22. Unfortunately, other phenomena begin to come into play in regions where high surface electric and magnetic fields are present. In this chapter, these phenomena will be described and found to be the limiting factors in achieving arbitrarily high accelerating gradients.

4.1 Field-Induced Electron Emission

In the presence of large surface electric fields, electrons from the surface of a material can be liberated into the free-space above the surface. Known as field emission (FE), this phenomenon is thought to be central to initiating RF breakdowns (vacuum arcs), which will be discussed in Section 4.2.2. In Chapter 6, it will be shown that these FE electrons can also become captured in the RF fields and affect the performance of an accelerating structure. To understand the mechanism of field emission, one begins on the surface of an accelerating structure where electric fields are present. These surface electric fields reduce and narrow the potential barrier holding electrons in the conductive layer. Such an effect increases the probability of electrons in this conduction layer tunnelling through to the vacuum. To describe this, Fowler and Nordheim in reference [41] started with a clean, flat metallic surface and defined a potential barrier as:

$$V(z) = \begin{cases} -W_a & \text{if } z > 0 \\ -eE_s z - e^2/4z & \text{if } z < 0 \end{cases}, \tag{4.1}$$

where $-e^2/4z$ is the contribution by the emitted electron and its image charge in the surface, W_a is the potential energy of the charge inside the metal and $-eE_sz$ is the surface electric field [42]. Figure 4.1a demonstrates the potential barrier proposed for two different surface electric field levels where a narrowing of the barrier is visible for a greater electric field strength. Using the Wentzel, Kramers, and Brillouin (WKB) approximation, a time-independent Schrödinger equation ($D(W_z)$) can be formed to describe the probability of the electrons tunnelling through the barrier. This probability, along with the number of electrons ($N(W_z)$), gives the current density of the tunnelling electrons as:

$$j_F = e\int_{-\infty}^{\zeta} D(W_z)N(W_z)dW_z, \tag{4.2}$$

where ζ is the Fermi energy [42]. Integrating Equation 4.2 over z and accounting for an RF field rather than a DC field, it is found that the total current emitted by an area (A_e) is given by:

$$\bar{I}_{FN} = \frac{5.7\times10^{-12}10^{-4.52\phi^{-0,5}}A_e(\beta E_s)^2}{\phi^{1.75}}\exp\left(-\frac{6.53\times10^9\phi^{1.5}}{\beta E_s}\right), \tag{4.3}$$

where ϕ is the work function of the surface material, β is an enhancement factor

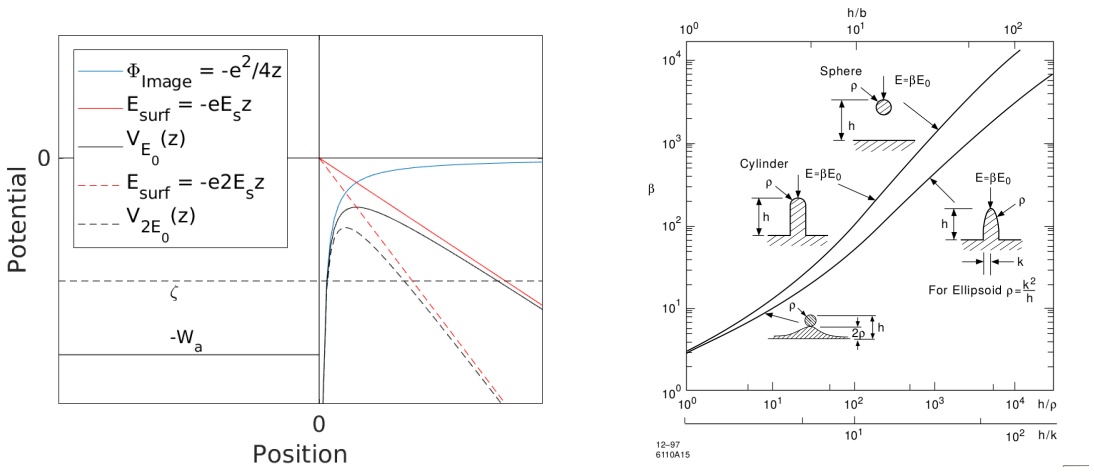

(a) Field emission potential barrier.

(b) Emitter geometry dependence.

Figure 4.1: A description of the field emission of electrons for given a potential barrier and emitter geometry. The left-hand diagram plots the potential of the barrier against the distance from the atom. The potential due to the image charge is plotted in blue. Two strengths of surface electric field are illustrated in solid red for lower field and dashed red for higher field. The barriers which results from these two field strengths are plotted in solid black for the lower field and dashed black for the higher field. The horizontal line, labelled ζ, illustrates the fermi energy and W_a is the potential energy of the electron. The right-hand figure plots the field enhancement factor (β) against a geometric factor (h/k or h/rho). This geometric factor is the ratio of the height of the emitter to its radius [42].

for the surface fields, and E_s is the surface electric field [42]. From this one will notice that an increase in the electric field significantly increases the emitted current. For field emission measurements, it has been found that the emitted current is significantly greater than the excepted emission given the calculated E_s. It has been found that E_s appears to be enhanced and therefore when writing the Fowler-Nordheim equation a factor β, known as the field enhancement factor, is added and defined as:

$$\beta = \frac{E_{\text{effective}}}{E_s}, \tag{4.4}$$

which is the ratio of the effective surface electric field, taken from field emission measurements, to the surface electric field expected from RF simulations [42]. The cause of this apparent field enhancement is not yet understood but is expected to be related to the geometry of surface features among other things [36]. The value of β can be measured by scanning the input power, which can be converted into a surface electric field, and measuring the field emission intensity (I_f). This is usually done by measuring the field-emitted current which reach the end of the accelerating structure. To extract the value of beta, one can plot $\log_{10} I_f/E_s^{2.5}$ against $1/E_s$ and find that the gradient as [42]:

$$\frac{d(\log_{10} I_f/E_s^{2.5})}{d(1/E_s)} = -\frac{2.84 \times 10^9 \phi^{1.5}}{\beta}. \tag{4.5}$$

This allows the effective β value to be extracted[1]. Typically these beta values are found to be between 30 and 100 although advancements in surface treatments and cleanliness of the accelerating structure preparation environment continue to reduce this factor [42]. Given the emitted electrons have the possibility of entering the RF buckets[2], field-emitted electrons can be captured and propagate along the structure. These captured FE electrons will be reviewed in great detail in Chapter 6.

4.2 RF Breakdown

Limitations in achieving arbitrarily high accelerating gradients in normal conducting linacs fall almost entirely on a single phenomenon. RF breakdown, also known as vacuum arcing, is a process where a large amount of current is spontaneously emitted from a surface region within the accelerating structure. RF breakdown currently has no known mechanism although significant progress has been made in the understanding of the process over the last decade. The following is a description

[1]The effective β of the structure is an average over many emission sites throughout the whole structure. Actual β values are a microscopic quantity which can not be measured as of yet.

[2]An RF bucket is a region where electrons can undergo continuous acceleration

of RF breakdown and the phenomena expected to contribute to an increase in the likelihood of a breakdown event. To begin, the effects of RF breakdown and why they are undesirable for CLIC will be detailed.

4.2.1 Effect of RF breakdowns on CLIC and RF Test Stands

RF breakdown is considered to be the primary limiting factor in achieving the high gradients necessary for CLIC. In Section 1.4 it was described that each RF breakdown causes a destructive transverse kick to the bunches, within that RF pulse, leading to a total loss of luminosity. For CLIC's main goal of producing high energy collisions, this is the driving factor behind the aim of reducing the likelihood of RF breakdowns. Although RF breakdowns can also lead to other problems which must be addressed in the design and operation of high gradient testing facilities. Such effects include: Reflection of RF power towards RF driver, potential damage of accelerating structures, and increased radiation dosage received by local instrumentation. Although the effects of these are expected to be minor for CLIC they can affect nominal operation of testing facilities, like the X-band test stands. Such effects will also prove useful later in the determination of the location of a breakdown event [43].

4.2.2 Stages of an RF Breakdown

Investigations into RF breakdown have been ongoing for several decades, with significant progress towards understanding the mechanism occurring within the last decade. Despite this, an exact mechanism is yet to be defined. Below is a description of the stages of RF breakdown expected to contribute to the phenomenon [44], along with a diagram for each stage in Figure 4.2.

1. **Field Emission:** Expected to initiate RF breakdowns is the emission of electrons due to large surface electric fields (Figure 4.2a), as discussed in Section 4.1.

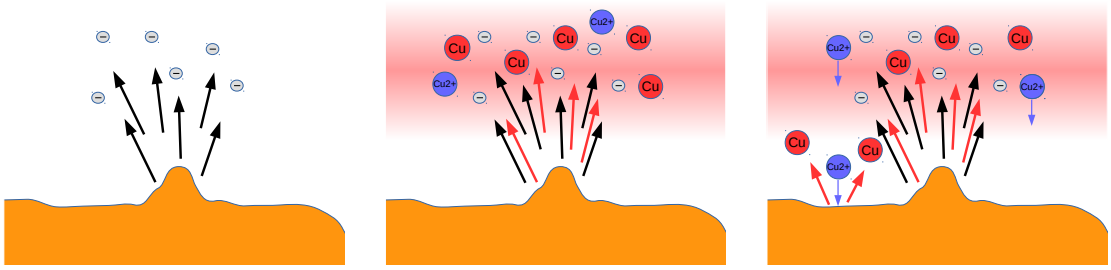

(a) Field Emission. (b) Neutrals evaporate. (c) Bombardment.

Figure 4.2: A description of three main stages of an RF breakdown cycle which are expected to repeat given certain conditions allowing the breakdown to grow [44].

2. **Neutrals evaporate**: Neutral atoms begin to evaporate from the surface where the FE electrons ionise these gaseous particles (Figure 4.2b).

3. **Bombardment**: These ions are accelerated across the plasma sheath and bombard the surface. If the bombardment sputters more atoms than the number of ions which hit the surface, the arc can grow through a continuation of this process (Figure 4.2c).

Advanced microscopy techniques have allowed these breakdown sites to be observed in great detail. Using a scanning electron microscope (SEM), the RF breakdown sites can be visualised and characterised. A microgram of RF breakdown sites is depicted in Figure 4.3, where individual sites are visible next to a breakdown cluster.

4.2.3 Surface Electric Fields

With the assumption that field emission is the precursor for RF breakdown, investigations into the dependence of RF breakdown on surface electric fields have been ongoing for many decades [97].

A Power-Law Dependence for Breakdowns

Understanding the rate of breakdown events is important for optimising the performance of accelerating structures. In reference [45], an attempt to develop a scaling law took data from 21 separate structure tests, where Figure 4.4a displays the fits produced on a log-log scale. Without searching for an underlying mechanism but

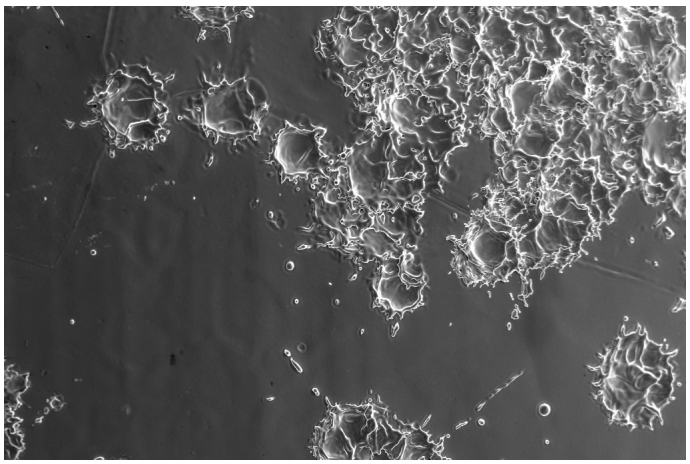

Figure 4.3: An SEM image of the RF breakdown sites on the CLIC-G Open structure. Numerous RF breakdown sites are visible on the sample and the overlapping of sites is commonly observed.

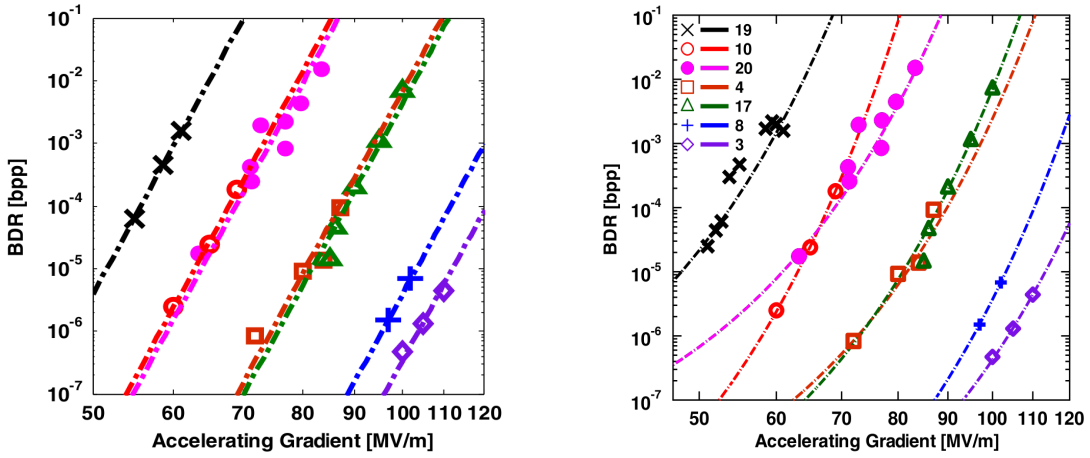

(a) Power-Law Fit (b) Dislocation Model

Figure 4.4: Models proposed to predict and understand the depedence of the BDR on the accelerating gradient. Each figure plots the BDR in bpp against the accelerating gradient in MV/m. Various markers illustrate data taken from different structures. The left-hand model is empirical (Power-Law Fit) while the right-hand mode is a theory-based model (Dislocation Model) [47, 45].

rather simply aiming to fit the data with an empirical formula, a strong dependence of the BDR on the surface electric field was found as:

$$E_s^{30}\tau_p^5 \propto \text{BDR}, \tag{4.6}$$

where τ_p is the pulse length and BDR is the breakdown rate in breakdowns/pulse (bpp) [45]. A power-law fit was adopted in preference to an exponential due to the non-zero BDR value for the exponential at zero field strength. The pulse length dependence was taken from reference [46] and confirmed with the same data.

A Dislocation Model for RF Breakdowns

Despite being useful for scaling the BDR to operational parameters, the power law fit has no underlying physical mechanism, and therefore can not explain this apparent dependence on the surface electric field. To further understand the relationship between the increase in surface electric field and BDR, a model where breakdowns are assumed to be induced as a result of vacancies formed by external stresses was developed in reference [47]. For this model, the rate of breakdown events is expected to be proportional to the rate of vacancy formations which was written as:

$$BDR \propto e^{\epsilon_0 E^2 \Delta V / k_B T}, \tag{4.7}$$

where ϵ_0 is the dielectric constant of vacuum, ΔV is the relaxation volume of the defect, k_B is Boltzmanns constant, and T is the temperature. Fitting this model to

the set of data used in the empirical model of reference [45], Figure 4.4b demonstrates the fit for the vacancy formation model.

4.2.4 Pulsed Surface Heating

Investigations into past results of high gradient tests demonstrated that the peak surface electric field, achieved by different accelerating structures, varied significantly [45]. For this reason it is expected that RF breakdowns do not exclusively depend on the surface electric field. Surface magnetic fields are expected to play an indirect role in RF breakdown. Surface magnetic fields induce surface currents which run through the structure. Such currents suffer Ohmic losses leading to surface heating. The change in temperature for a square pulse of length τ_p is given approximately by:

$$\Delta T(t) \approx \frac{R_s H_s^2 \sqrt{\tau_p}}{\rho c_s \sqrt{\pi \alpha_D}}, \tag{4.8}$$

where R_s is the surface resistance, ρ is the material density, c_s is the specific heat, and α_D is thermal diffusivity [48]. Continuous cycling of the magnetic fields causes thermal stresses on the surface material and has been observed to result in an increase in surface roughness [49]. The increased surface roughness introduces imperfects which can undergo field emission and RF breakdown.

4.2.5 Power Flow

It was previously stated that the limitation in the achievable gradient of an accelerating structure does not appear to rely strictly on the surface electric field. Along with surface electric fields investigations, into the effects of power flow have also been undertaken. During testing of CLIC and Next Linear Collider (NLC) structures, it was found that larger aperture, and therefore high group velocity, structures supported greater power flows. Using data from the high power testing of these structures, a relation for the power flow through a structure of minimum iris circumference (C) was defined as:

$$P\tau_p^{1/3} \propto C, \tag{4.9}$$

where P is the total power flow for a given breakdown rate and τ_p is the pulse length. This equation was able to explain the achievable peak power flowing through the structures. Although this model faced difficulties to explain the concept of RF breakdown in standing wave structures, which experience no net power flow through the structure [50].

The authors of reference [45] investigated the idea that power flowing through field emitters may be the cause of RF breakdown. Due to the low resistivity of copper,

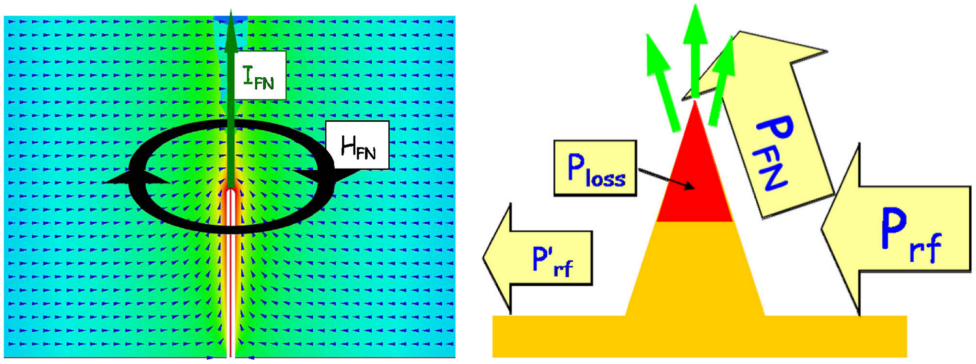

(a) Induced local magnetic field.

(b) Power flow diagram.

Figure 4.5: Diagram for the concept of local power flow [45]. The current within a field emitter created by surface electric fields induces a local magnetic field and therefore a power flow occurs. The power within the field emission can be up to the power within the RF.

the amount of power required to achieve a relevant change in temperature is quite significant. Inside the accelerating structure, there is only one source of power that being the RF source (P_{RF}). For an RF source the power flow density (Poynting vector) is well defined as:

$$\vec{S} = \vec{E} \times \vec{H}, \tag{4.10}$$

where $\vec{E}$ is the electric field and $\vec{H}$ is the magnetic field. For the mechanism to describe the flow of power within the field emitter tips, it is found that the induced current (I_{FN}), from the surface electric field, results in a local magnetic field (Figure 4.5a). For a microscopic cylindrical tip protruding from the surface of an iris, the induced magnetic field is given by:

$$H_{FN} = I_{FN}/2\pi d, \tag{4.11}$$

where d is the radial distance from the cylindrical tip's surface. The power flow due to the RF fields can be separated into two components [45]:

$$P_{RF} = E_0 \cdot H_{RF}^{TW} \sin^2 \omega t + E_0 \cdot H_{RF}^{SW} \sin \omega t \cos \omega t. \tag{4.12}$$

The left component is the active power flow which describes the transport of energy along the structure and therefore only occurs in travelling wave structures. The right component is the energy oscillating between the electric and magnetic field, known as the reactive power flow, and is expected for standing and travelling wave RF power.
For the power flow within the emitter one can take the Poynting vector and substi-

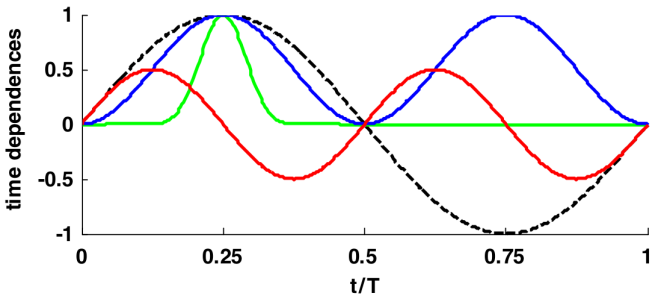

Figure 4.6: Evolution of the amplitude of the electric field (dashed black line), active power flow (blue line), reactive power flow (red line), and field emission power flow (green line) plotted over an RF period [45].

tute in equation 4.3 and 4.11, to give [45]:

$$P_{FN} = \oint_s S_{FN} ds \propto \oint_s (E(t))^3 \cdot \exp\left(- \frac{6.53 \times 10^9 \phi^{1.5}}{\beta E(t)} \right) ds. \tag{4.13}$$

In Figure 4.5b it is illustrated that the power flowing through the emitter originates from the RF. The power is lost to the electrons emitted from the tip and through ohmic losses (P_{Loss}). Power transferred to the field-emitted current can be up to the RF power entering the emitter such that [45]:

$$P_{Loss} \ll P_{FN} \leq P_{RF}. \tag{4.14}$$

Ohmic power losses are significantly lower than the field-emitted power loss, due to the low resistivity of copper. The I_{FN} component is in-phase with the active power flow whereas it is 90° out-of-phase with the reactive power (Figure 4.6). The result is that the active power flow is more efficient in providing power to the field-emitted electrons than the reactive power flow [45].
Adapting the power flow into a common RF parameter is done through the use of the Poynting vector $\vec{S}$. The active power flow is found to be the real component of the Poynting vector ($\mathrm{Re}(S)$) while the reactive component is the imaginary component of the Poynting vector ($\mathrm{Im}(S)$). The quantity S_c describes the localised power flow as [45]:

$$S_c = |Re(\vec{S})| + g_c \, |Im(\vec{S})|. \tag{4.15}$$

In the new quantity, g_c defines the affect of the active power versus the reactive power resulting from the phase shift, demonstrated in Figure 4.6. The value of g_c is found by:

$$g_c = \frac{\int_0^T |P_{RF}^{SW}| \cdot P_{FN} dt}{\int_0^T |P_{RF}^{TW}| \cdot P_{FN} dt}, \tag{4.16}$$

which is usually found to have a value between 0.15 and 0.2 [45]. This new factor has been used to describe the how power flow may limit both travelling and standing wave structures [45].

4.3 Conditioning

When operating high gradient structures, it has been observed that the systems begin operation at low gradients and are unable to begin operation at their nominal gradient. A gradual increase in the accelerating gradient is possible through a technique known as *conditioning*. This technique commonly takes ∼700 million high power RF pulses to achieve the ultimate high gradient [84]. The conditioning of four accelerating structures will be demonstrated in Chapter 7. Previous results have demonstrated that the progress of conditioning is dependent on the number of pulses [58]. Using the idea of dislocations and vacancy formation mentioned in reference [47], it has been postulated that conditioning is similar process to mechanical hardening [84, 20].

4.4 Summary

In the presence of high surface electric and magnetic fields, phenomena such as RF breakdown and field emission will impact nominal operation of accelerating structures. An RF breakdown leads to a destructive transverse kick to the bunches for that RF pulse, consequently reducing the luminosity. Decreasing the peak surface fields has been demonstrated to reduce the rate of RF breakdown. Therefore, CLIC structures are designed to minimise these surface fields for a given accelerating gradient. Operating at the nominal accelerating gradients of CLIC requires an extensive conditioning process which has been previously found to take ∼700 million pulses [20].

Chapter 5

A Novel X-band Test Stand

In previous chapters the three high gradient testing facilities at CERN were introduced, including the two X-band test stands dedicated to understanding the high gradient operation of CLIC structure prototypes. Xbox 1 and Xbox 2 each have the ability to test a single accelerating structure approximately every seven months, given a pulse repetition rate of 50 Hz. It is the aim of the CLIC collaboration to have approximately 40 structures tested to high gradients to determine the reproducibility of the 100 MV/m accelerating gradients. Given that only 13 CLIC prototype accelerating structures had been tested up to 2015, a significant increase in testing capacity was required. This chapter will review the commissioning of a novel test stand at CERN, Xbox 3, which offers the ability to test four structures concurrently at pulse repetition rates up to 200 Hz. Initiating this chapter is a review of the design of the test stand which was described in [22] and [20]. Following is a detailed account of the commissioning of this new test stand which was performed by the author in collaboration with others in the group. Two structures installed within weeks of one another were the first two structures to be tested on Xbox 3 and their conditioning histories will be detailed in Sections 7.4 and 7.5. During the testing of these structures, several operational challenges were faced by the author. These will be explained in detail with the aim of improving the design and operation of future test stands. Concluding the chapter are the operational parameters which were ultimately achieve by the end of this work.

5.1 Design Overview of Xbox 3

A peak power of ∼45 MW is required to generate an unloaded gradient of 100 MV/m within a typical CLIC structure [52]. This can be achieved using a single high power klystron, as was the case for Xbox 1 and Xbox 2, although this scheme had some limitations, which the new system aimed to overcome:

1. **Cost**: High power klystron and modulators are extremely expensive. The new test stand would need to reduce the cost of testing accelerating structures.

2. **Repetition Rate**: High power klystrons are limited to 50 Hz, due to their high average power. The new test stand would need to be able to achieve pulse repetition rates above 50 Hz while remaining on a harmonic of the mains power.

In order to increase the repetition rate and cost efficiency, any klystrons used in the new system would be required to operate at a reduced peak power. In order to reach the required input power with low power klystrons additional amplification would be necessary. For Xbox 3, two additional stages of amplification are proposed:

1. **RF pulse weaving**: Weaving of the klystrons' pulses allows the output peak power of klystrons to be combined where the output peak power is the sum of the input peak power.

2. **Pulse compression**: Using the combined RF pulse, a stage of pulse compression increases the peak power at the expense of pulse length.

Each of these stages are discussed in detail below.

5.1.1 RF Pulse Weaving

The first of its kind to be built, Xbox 3 begins with the weaving of the two RF pulses output from low power klystrons. Weaving the two RF pulses creates a single RF pulse at a power equal to the sum of the two input pulses, if the phases of the two signals are synchronous. Early in the design cycle of Xbox 3, several options were explored on how to achieve this. Using a T junction to combine two RF pulses was an option although there were concerns the average power at high repetition rates may be too high for the structure. Alternatively, a 90° hybrid allows the pulsing of two structures on alternate pulses through a manipulation of the trigger delay. This halves the average power dissipated in each structure while retaining the testing capacity. For the description of the RF pulse weaving, the four ports of the hybrid will be labelled. The two pairs of nominally isolated ports are the input and output pairs. The input pair are connected to the klystrons, and are labelled as such, and the output pair, which are connected to the accelerating structures, are labelled Lines 1 and 2. To begin the pulsing of Line 1, a 90° phase shift was added between the two input pulses. This can be described by a scatter matrix as:

$$\begin{bmatrix} S_1 \\ S_2 \\ S_3 \\ S_4 \end{bmatrix} = \frac{-1}{\sqrt{2}} \begin{bmatrix} 0 & i & 1 & 0 \\ i & 0 & 0 & 1 \\ 1 & 0 & 0 & i \\ 0 & 1 & i & 0 \end{bmatrix} \begin{bmatrix} 1 \\ 0 \\ 0 \\ i \end{bmatrix} = \frac{-1}{\sqrt{2}} \begin{bmatrix} 0 \\ 2i \\ 0 \\ 0 \end{bmatrix}. \tag{5.1}$$

During the following pulse, the trigger for Klystron B is delayed by half the RF period ($T/2$). The result is that now Line 2 is pulsed with double the power while Line 1 receives no power, written as:

$$\begin{bmatrix} S_1 \\ S_2 \\ S_3 \\ S_4 \end{bmatrix} = \frac{-1}{\sqrt{2}} \begin{bmatrix} 0 & i & 1 & 0 \\ i & 0 & 0 & 1 \\ 1 & 0 & 0 & i \\ 0 & 1 & i & 0 \end{bmatrix} \begin{bmatrix} 1 \\ 0 \\ 0 \\ -i \end{bmatrix} = \frac{-1}{\sqrt{2}} \begin{bmatrix} 0 \\ 0 \\ 2 \\ 0 \end{bmatrix}. \tag{5.2}$$

Switching the trigger delay on Klystron 2 between 0 and $T/2$ on each successive pulse allows each line to receive every second pulse. This scheme delivers double the klystron power (or $V = \sqrt{2}$) to the two lines at a repetition rate of half that output from the klystrons and therefore does not reduce the testing capacity, which would commonly result from a reduction in repetition rate. This weaving stage can be repeated multiple times to weave numerous klystron pulses which was considered in the design of Xbox 3. At this stage the pulse could be input into the structure, if the klystrons had a peak power of ∼22.5 MW, although another stage of amplification is possible through the use of a pulse compressor.

5.1.2 RF Pulse Compression

In Xboxes 1 and 2 a SLED type 1 RF pulse compressor is employed to increase the peak power at the expense of pulse length [22]. A description of how a SLED Type 1 RF pulse compressor operates is found in Appendix A. To summarise this description, an RF pulse compressor uses two high Q cavities operating at the $TE_{0,1,32}$ mode to store RF power which is extracted through a manipulation of the RF pulse phase profile. This phase profile involves a flip of ∼110° before a parabolic ramp to 180° creating an output pulse with a constant amplitude [53].
For pulse compressors there are primarily two qualities that define their operation, the definitions of which assume a flat-top pulse on the input and output pulse. Firstly the gain (G) is the ratio of the input peak power (P_{in}) to the output peak power (P_{out}), written as [54]:

$$G = \frac{P_{out}}{P_{in}}. \tag{5.3}$$

The second is the compression factor (C) which is defined as the ratio of the input pulse length (τ_{in}) to output pulse length (τ_{out}) written as [54]:

$$C = \frac{\tau_{in}}{\tau_{out}}. \tag{5.4}$$

From these two qualities, the efficiency (ε) is defined as the ratio of the input power to the output power, written as:

$$\varepsilon = \frac{P_{out}\tau_{out}}{P_{in}\tau_{in}} = \frac{G}{C}. \tag{5.5}$$

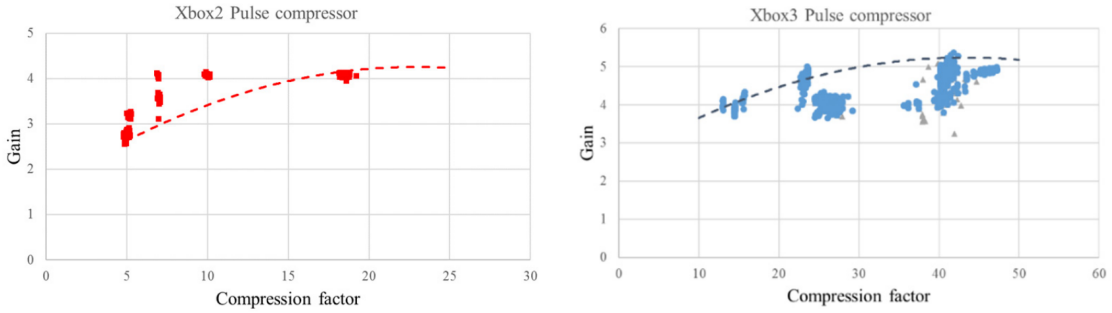

(a) Xbox 2.

(b) Xbox 3.

Figure 5.1: A comparison of the operation of the pulse compressors on Xbox 3 with that of Xbox 2. The two graphs plot the gain against the compression factor, each unitless. The dashed lines depict the expected gain to compression factor [54].

For Xbox 2 using a compression factor between 5 and 19, the achievable gain was between 3 and 4 which was deemed too low for Xbox 3 to achieve 56 MW (Figure 5.1a). To address this short coming, the compression factor was increased significantly to operate between 13 and 47. Consequently Xbox 3 could operate with a gain between 4 and 5 (Figure 5.1b). A ramification of this change in compression factor was a decrease in the power efficiency of Xbox 3 (10-25%) in comparison to Xbox 2 (15-60%). These measurements of the pulse compressor's operation on Xbox 3 were performed during commissioning which meant that extensive testing was required to achieve the optimal operating conditions. For this reason, the gain is not constant for a given compression factor and led to the noisy results observed in Figure 5.1b. The maximum gain for a given compression factor reflects the optimal results.

5.1.3 Xbox 3 Design

The final design for Xbox 3 was determined through the known gain factors available from the pulse weaving ($G = 2$) and pulse compression ($G = 4$). Early designs used the technique of weaving four klystrons each outputting a 6 MW, 5 μs RF pulse at 400 Hz [22]. Such klystrons were designed and manufactured by Toshiba who agreed to make six units in total. Initial testing of the first prototype klystron found that it could operate at 7 MW, with an increased gun voltage, as depicted in Figure 4.3 of reference [22]. This led to a revision of the Xbox 3 design which included only one stage of pulse weaving along with a stage of pulse compression. Such a design would aim to reach 56 MW, assuming a compression factor of 4.
Figure 5.2 depicts the conceptual set-up for Xbox 3 from the start of the pre-amplifier to the end of the RF line illustrating the peak power, pulse length and repetition rate after each component. The two lines aim to receive 56 MW, 200 ns pulses at 200 Hz. Weaving two klystrons on two identical set-ups, in comparison to weaving

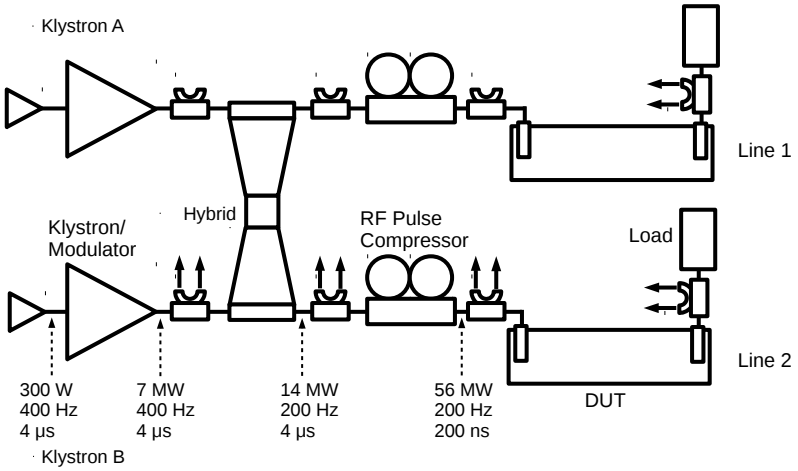

Figure 5.2: High Power RF set-up of one symmetric half of Xbox 3. An input of 300 W from the SSA drives the klystron which can output up to 7 MW. Weaving the two 7 MW klystrons and alternating the power between two lines generates a peak power of 14 MW at half the repetition rate. Pulse Compression increases the peak power at the expense of pulse length. At the end of the compression Xbox 3 aims to deliver 56 MW for 200 ns pulses at 200 Hz. The power achieved at the DUT is dependent on the waveguide length between the pulse compressor and the DUT with power losses of $\sim$0.1 dB/m.

four klystrons, doubled the achievable testing capacity through a doubling of the repetition rate. Ultimately, Xbox 3 has a potential testing capacity 16 times greater than Xbox 2 or Xbox 1[1].

Figure 5.3 illustrates a simplified diagram of a symmetric half of Xbox 3. Xbox 3 consists of four sections, each with a specific task. Initiating the RF signal is the low-level radio-frequency (LLRF) crate marked in yellow. Common to Xbox 2 and 3 is the idea of RF mixing and multiplying to generate and measure the 12 GHz RF signals required for the klystron and measured from the test stand [22]. This mixing involves starting with a lower frequency oscillator which for Xbox 3 is 2.4 GHz. This 2.4 GHz RF is split in two, with one signal multiplied to 9.6 GHz and the other modulated to the amplitude and phase programme required for the operation of the structure. These two signals are subsequently mixed together, where output generates a sum and difference of the input signals. The difference, a modulated 7.2 GHz signal, is removed using a 12 GHz bandpass filter and the modulated 12 GHz is sent towards the high power RF section, discussed further below. This technique is a much more cost effective option than using a 12 GHz oscillator as was used in Xbox 1 [22]. The direct measurement of 12 GHz RF is at the limit of modern ADCs making it an expensive task. A more cost efficient option is mixing the signals to a lower frequency which can then be sampled in a lower frequency ADC. For Xbox 3, this is performed in a similar means to the generation of the 12 GHz RF for the high power. Inside the LLRF crate is also a 2.9 GHz RF oscillator which is multiplied

[1]given a repetition rate four times higher and four times the testing slots.

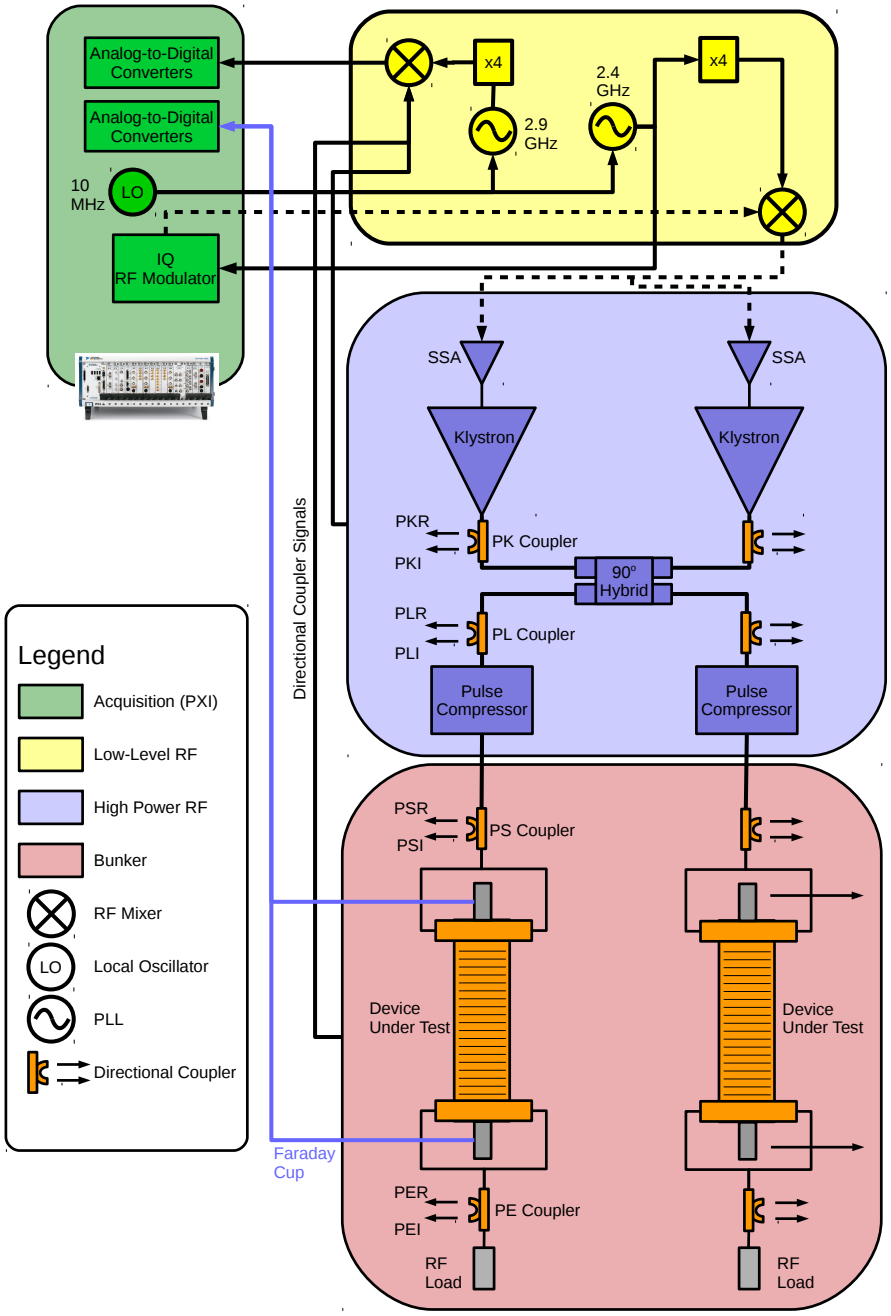

Figure 5.3: A simplified diagram of one symmetric half of Xbox 3. Locking to the 10 MHz local oscillator, a 2.4 GHz signal is multiplied, modulated and upmixed to create a 12 GHz RF driver for the pre-amplifier of Xbox 3 (SSA). A second signal at 2.9 GHz is multiplied to 11.6 GHz for the downmixing of signals sampled from the HPRF. The 12 GHz modulated signal enters the high power RF section, shown in purple, where the SSA prepares the pulse for the klystron, which outputs up to 7 MW of peak power. The combination of the hybrid and pulse compressor is used to generate a peak output power of 56 MW, as discussed in preceding sections. Signals are sampled by directional couplers and mixed with the 11.6 GHz signal to create 400 MHz samples of the RF signal, which are digitised in the PXI crate.

Table 5.1: Cable calibration of the first LLRF crate for Line 1 and Klystron A. The RF signal was 7.96 dBm at the input. Summing over the power loss from the coupler, splitter and cables allowed the attenuation which was required before the ADC to be calculated.

Name	Signal [dBm]	Atten. [dB]	Splitter Atten. [dB]	Approx. Coupling [dB]	Approx. Signal [dBm]	Req. Atten. [dB]
KLY	0.91	-7.05	-5.82	-39.32	56.00	4
PEI	-1.72	-9.63	-5.82	-60.00	100.00	25
PER	4.64	-3.32	-6.11	-60.00	100.00	31
PKI	-10.37	-18.28	-5.95	-60.00	99.00	15
PKR	1.28	-6.68	-5.56	-60.00	99.00	27
PLI	3.77	-4.19	-5.72	-60.00	99.00	29
PLR	3.82	-4.14	-5.73	-60.00	99.00	29
PSI	-2.14	-10.05	-6	-60.00	107.50	31
PSR	-1.57	-9.48	-5.67	-60.00	107.50	32
SSA	-12.00	-19.91	-6.43	0.00	27.00	1

to produce an 11.6 GHz RF signal. Mixing the 11.6 GHz with a 12 GHz RF signal, sampled from the test stand, produces a 400 MHz RF signal which is simpler and less costly to digitise.

Initiating the high power radio-frequency (HPRF) section is the modulated 12 GHz input signal, mentioned above, which is input into a solid state amplifier (SSA) amplifying it up to 300 W. Subsequently a klystron/modulator amplifies the 300 W modulated signals to 7 MW which is input into the waveguide network. After the weaving to achieve 14 MW and compression to achieve 56 MW, as described in the previous section, the pulse is input into the testing bunker. Located in the bunker is the device under test (DUT) which accepts the high power RF pulse allowing the testing of the DUT at high power. Extraneous power is routed to the RF load thereby minimising unwanted reflected power towards the DUT. System control and data acquisition is accomplished using a National Instruments PXI crate. This system also generates the reference 10 MHz local oscillator (LO) that controls the phase-lock loops (PLLs) within the LLRF (Figure 5.3) [94].

5.2 Commissioning of Xbox 3

With the design finalised, commissioning of Xbox 3 began in 2015. Commissioning commenced with the characterisation of the low power and high power RF components.

5.2.1 Characterisation of Low Power RF Component and Cables

Digitisers in the PXI have a full scale input power range of 10 dBm. Signals above this level may cause damage to the front-end circuitry. In light of this, a procedure was developed to determine the ideal attenuation levels to allow optimal use of the dynamic range of the system. Before pulsing could begin, the power level of the

RF signals from the directional couplers reaching the ADCs needed to be determined. Using an RF signal generator (Anritsu MG3692C), an 11.994 GHz signal at 10 dBm (7.96 dBm after the input cable) was sent through each of the expected signal paths[2]. At the end of the signal path, a power sensor (Rohde and Schwarz NRP-Z81) measured the received power which allowed the amount of signal loss throughout the LLRF network to be determined, an example of which is depicted in Table 5.1. Multiplying the cable attenuation with the expected coupling factor of the directional couplers and the splitters, the total line loss from directional coupler to ADC input was determined. Expected peak power levels at various points within the test stand were known from the RF designs. Using these values, the approximate peak power reaching each of the ADC channels was calculated. RF attenuators were added where necessary in the aim to have a maximum input power of 10 dBm, to ensure to use the entire dynamic range. A photograph of the calibration set-up is displayed in Figure 5.4. This procedure was used to calibrate all of the signal pathways within Xbox 3.

[2]The input was increased to 17 dBm when the losses were greater and the measured signal dropped below the noise floor.

(a) Calibration set-up.

(b) Xbox 3 LLRF and Acquisition.

Figure 5.4: Calibration of the LLRF components and cables in Xbox 3. The set-up depicts the RF signal generator (Anritsu MG3692C) measuring a part of the LLRF with the Rohde and Schwarz NRP-Z81 power sensor. A second power sensor confirms the stability of the output. The complete LLRF rack is shown for the two symmetric halves although the two halves shared a PLL for early operation of Xbox 3.

5.2.2 Characterisation of High Power RF Components

To gain a full understanding of the entire RF system it is also vital to understand the HPRF components. As all waveguide components were tested during manufacturing, it was reasonable to assume from that point on that they would not require re-testing. However for more complex components, such as the hybrids and pulse compressor cavities, each component was tested at low power using a vector network analyser (VNA).

90° Hybrid

The RF outputs from each klystron are routed to the 90° hybrid circuitry arranged to act as an RF combiner. To receive proper combination and cancellation within Lines 1 and 2, and minimise reflections towards the klystrons, the signals must be carefully balanced. In Xbox 3, there are six hybrids in total: four located in the four pulse compressors and two for the combination. All six hybrids underwent low power testing to ensure the transmission and reflection levels from each port were suitable (Figure 5.5). Figure 5.6 displays the results of the RF testing of one of the hybrids, using a four-channel VNA (Rohde and Schwarz ZVA 24). Illustrated in Figure 5.6a are the transmission level spectra for the four ports around the operational frequency (depicted by a vertical blue line). Transmission between each of the ports is within 0.05 dB of the expected -3.01 dB which was deemed to be an acceptable level. In Figure 5.6b, the data displaying the reflection from the four ports back towards the two klystrons is presented. From this it can be observed that the reflection is a maximum of -45 dB which equates to a 200 W reflection for an input power of 7 MW, similarly deemed to be acceptable. This procedure was repeated for all six hybrids.

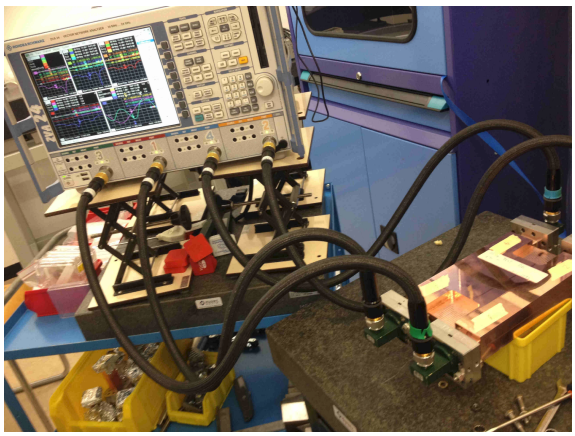

Figure 5.5: RF testing of the fourth hybrid used in Xbox 3. The testing was performed using a four channel VNA testing the S-parameters for the four port component.

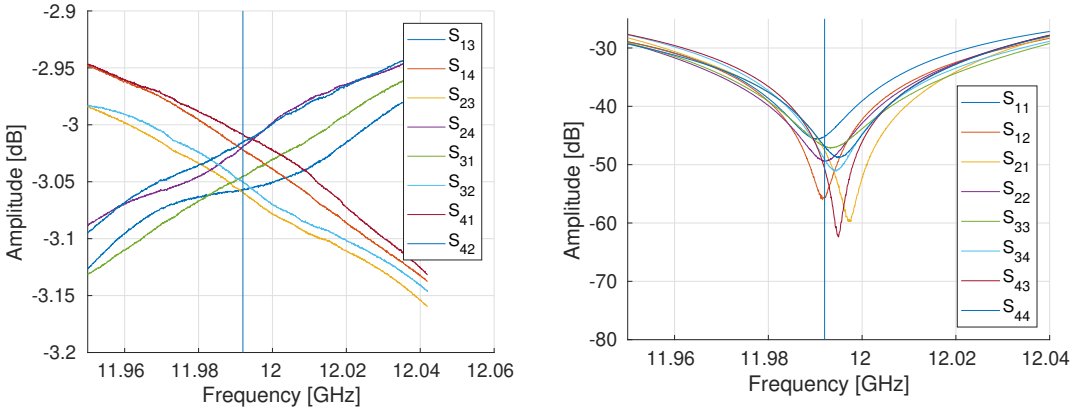

(a) Hybrid transmission spectra.

(b) Hybrid reflection spectra.

Figure 5.6: The S-parameters measured from the cold testing of one of the hybrids used in Xbox 3. The plots display the transmitted (left-hand figure) and reflected (right-hand figure) power, between ports 1 to 4, in dB plotted against the RF frequency in GHz. A vertical line illustrates the operational frequency of 11.994 GHz.

Pulse Compressor

Completing the pulse compressor are two high quality factor (Q = 180000) cavity resonators. Given the high Q, it is important to ensure that the cavities are tuned well to the desired RF frequency. Before their installation onto Xbox 3, each pulse compressor cavity underwent cold testing in the RF lab using a two channel VNA (Rohde and Schwarz ZVA 24) to determine whether each cavity was operating at the correct frequency (Figure 5.7). All initial tests were performed at 30°C with atmospheric pressure inside the cavities resulting in a shift of the resonant frequency to 11.992 GHz, 2.2 MHz lower than for vacuum. Each cavity was designed to operate at the European X-band frequency of 11.9942 GHz. Small discrepancies in the operational frequency were corrected through minor adjustments to the end caps of the cavities, where the cavity joins the hybrid, as illustrated in Figure 3.25 of reference [22]. Figure 5.8 demonstrates the SLED's frequency response after fine tuning and under a vacuum of 10^{-5} mbar. The resonant frequency of the cavities is observed to be in good agreement with desired frequency of 11.9942 GHz.

5.2.3 Waveguide Assembly and Evacuation

When the low power RF testing of the line was completed, the waveguide network was assembled with the hybrid and pulse compressor. Presented in Figure 5.9 is a photograph of Xbox 3 during the commissioning. Each waveguide was installed and each joint was checked for vacuum leaks.

For high power operation, the waveguide network required an ultra-high vacuum of $< 10^{-7}$ mbar. The NEXTorr vacuum system used in the test stand combines both

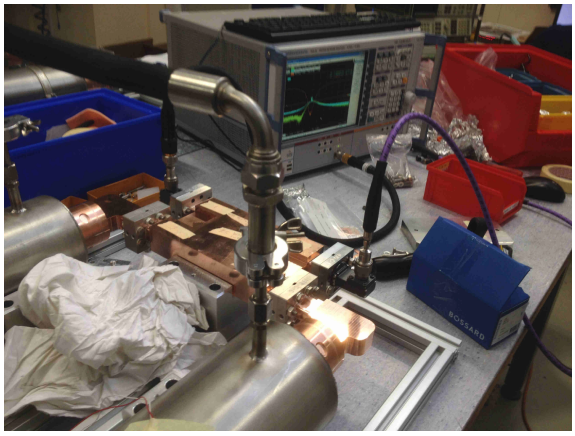

Figure 5.7: RF testing of the pulse compressor using the two channel VNA (Rohde and Schwarz ZVA 24). Testing was performed at a constant 30°C with atmospheric pressure before evacuating the pulse compressor after the cavities were deemed to be tuned to the correct frequency.

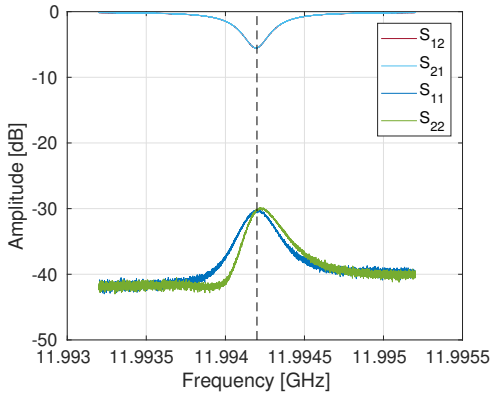

Figure 5.8: S-parameter measurements of one of the pulse compressors used on Xbox 3. The power loss in dB from the reflection (S_{22} and S_{11}) and transmission (S_{21} and S_{12}) from each port are plotted against the RF frequency in GHz. A vertical line illustrates the operational frequency of 11.994 GHz.

non-evaporative getter (NEG) and ion pumping technologies inside a small housing. A roughing pump attached to the bottom of the pulse compressor, approximately the middle of the waveguide network, was used to start the pumping process. This first stage of pumping brought the network down to 10^{-6} mbar. At this point, the NEG pumps were turned on while the roughing pump continued to operate. By heating the NEG unit to around 550 K, most gas molecules adhere to the pump through the process of sorption. The NEG pumps of the NEXTorr units furthest from roughing pump were turned on first to ensure the whole network was pumped down homogeneously. Once the NEG pumps had operated for 3-4 hours, the roughing pump valve was closed and the ion pumps were initiated. The ion pumps were to remain on for all high power testing ensuring adequate vacuum levels in the case of an RF breakdown. During the installation, the NEXTorr units were placed along

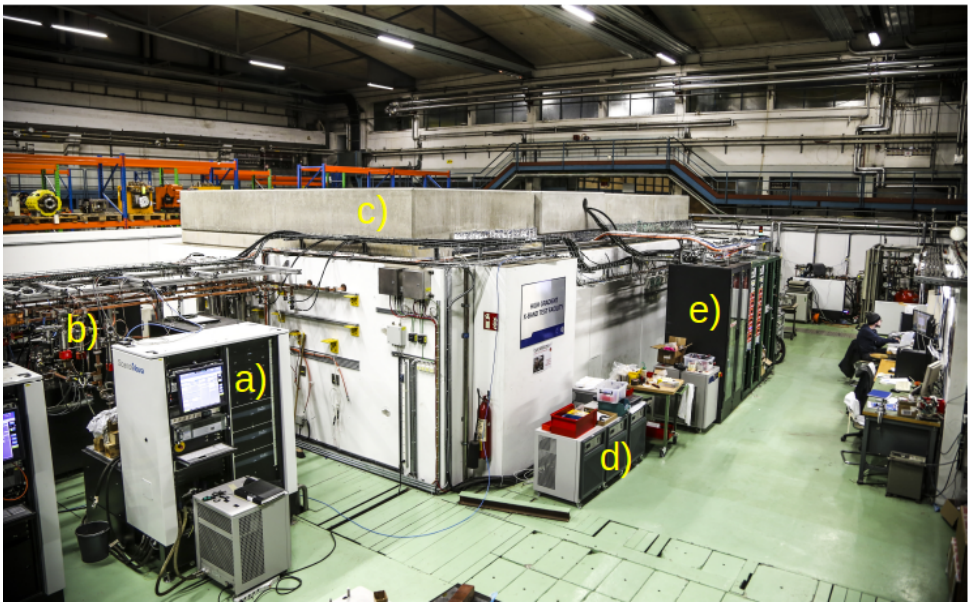

Figure 5.9: A photograph of Xbox 3 from inside the Experimental Hall during its commissioning. The major components are labelled: a) is one of the modulator/klystrons units, b) is the waveguide network, c) is the testing bunker, d) is a set of cooling units and, e) is the LLRF rack which also includes the acquisition units and vacuum controllers.

several sections of Xbox 3 to ensure of even distribution of pressure throughout the waveguide network [55].

5.2.4 Conditioning of the High Power Network

Following the waveguide evacuation, the conditioning of the high power RF network of Xbox 3 began. Initially setting the RF pulse length to 50 ns, the pressure conditioning strategy, described in [22], was used with an upper limit of 5×10^{-8} mbar. An algorithm was used to gradually increase the input power over a period of two months. Once 35 MW of peak power was reached, it was decided that a structure could be installed. On March 17 2017 the TD24 R05 SiC N1 was installed onto line 1 which was followed by the T24 PSI N1 on Line 2 one month later. A photograph of the two structures installed is displayed in Figure 5.10. The history of the conditioning for the TD24 R05 SiC N1 and T24 PSI N1 will be discussed in Sections 7.4 and 7.5, respectively.

5.3 Operational Challenges

During the test stand commissioning and subsequent high power testing of accelerating structures, several challenges were faced in the operation of this novel test stand. These challenges, and how they were overcome, will be discussed in this section.

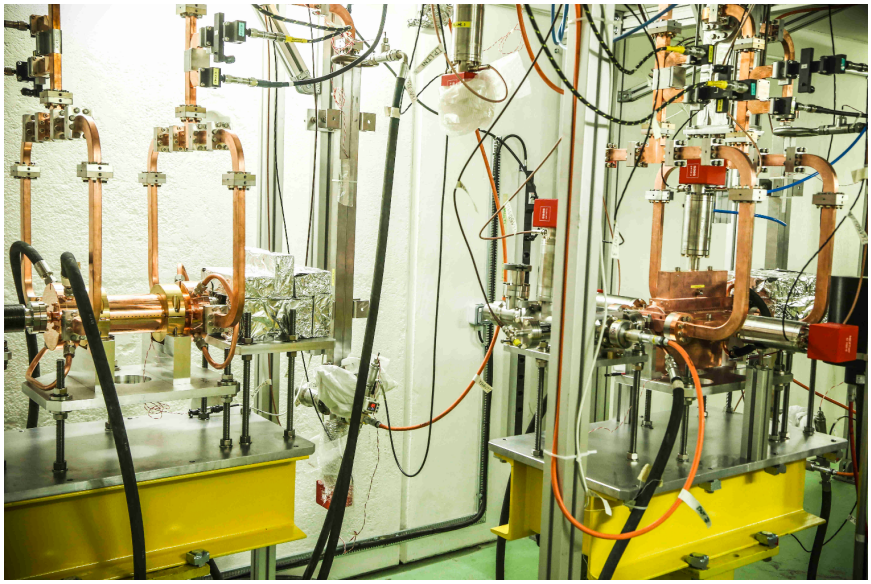

Figure 5.10: The first two structures to be installed on Xbox 3. The T24PSI is visible on the left and the TD24R05 SiC on the right.

5.3.1 Klystron Testing

After their delivery to the test stand area, each klystron was tested at CERN. It was found that the klystrons could operate at the nominal power of 6 MW but could not reliably operate at the 7 MW achieved by the first prototype [22] (Figure 5.11a). This resulted in a reduction of the expected power available to the DUT from 56 MW to 48 MW. This was still deemed sufficient for the purposes of high gradient testing. Along with testing of the peak power available, the klystron saturation curves were investigated for irregularities. Figure 5.11b illustrates a discontinuity in the phase profile of the klystron. The cause of this discontinuity was unable to be determined and given the need to power ramp during operation, this presented a challenge to the operators. During the operation of Xbox 3, the operators needed to ensure that the klystron in question was operating well away from this discontinuity through varying the RF driver power. It was later found that this discontinuity shifted through the power transfer curve over time.

5.3.2 RF Reflection and Interference with Klystron

In Section 4.2.1 it was explained that RF breakdown causes a reflection of RF power towards the RF source, which for the X-band test stands is the klystron(s). Klystrons are designed to absorb small reflections though large reflections are undesirable as they can cause damage to the cavities. During breakdown events where $\tau_p > 80$ ns, it was observed that the peak input power of a small portion of these events was increased by up to 40% for a portion of the RF pulse, an example of which is displayed in Figure 5.12a [54]. Investigations into this revealed that these break-

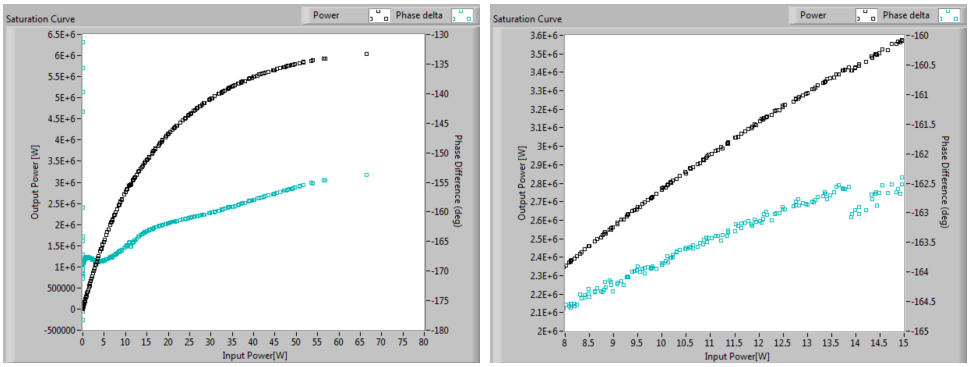

(a) Full saturation curve. (b) Zoom of phase discontinuity.

Figure 5.11: A power transfer curve produced during the testing of Klystron C in Xbox 3. The curves plot the peak input power from the solid state amplifier in Watts on the x-axis, and the peak output power in Watts (black) and output phase in degrees (cyan) from the klystron on the y-axis. The right-hand plot zooms around a phase discontinuity found in the klystron.

downs occurred at the start of the structure and delving deeper it was found that these breakdowns occurred towards the beginning of the RF pulse (Figure 5.12b). In Xbox 2 and 3, there is approximately 10 meters of waveguide network, between the klystron and the DUT, which equates to approximately 80 ns transit time for the return trip of the RF from the klystron to the DUT. When an RF breakdown occurs at the beginning of the RF pulse, the klystron continues to deliver power for the remainder of that pulse before being interlocked. During this time, it was observed that reflected component of the RF pulse could re-enter the klystron and constructively interfere with its own pulse. This same effect was also observed as a small amplitude spike on "non-breakdown" pulses in the incident RF pulse flat-top. A correction in the input phase profile allowed flattening of the pulse though this brought further challenges through a discontinuity in the incident RF phase. A more permanent solution to would be to have longer waveguides, where the time of flight is greater than the pulse length and therefore no interference can occur. This would require at least 30 meters for the CLIC pulse length of 240 ns. This will consequently lead to greater power loss, approximately 3 dB, compared to a shorter waveguide. No impact on the rate of RF breakdowns was observed despite the structure seeing more power [56].

5.3.3 Conditioning Retardation due to Algorithm

Conditioning in all of the X-band test stands is controlled by a PXI with similar software which contains the conditioning algorithm described in [22]. Key operator selectable parameters are N and M which represent the time delay between checking the BDR and the amplitude of the incremental power increase, respectively. Hence, the rate of power increase is dependent on the BDR limit, the loop length (N),

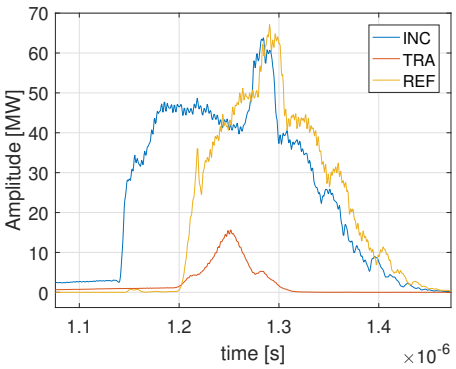

(a) Breakdown waveform with interference.

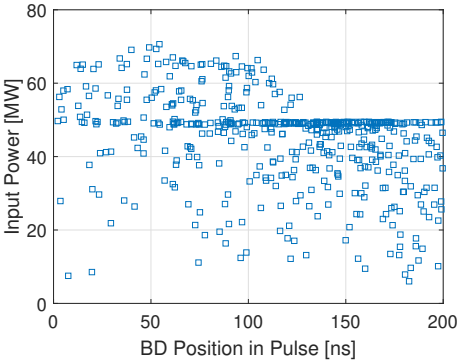

(b) Position in the pulse where interference occurs.

Figure 5.12: RF Breakdown leading to a reflection and interference of the RF signal. The left-hand plot displays the waveforms measured during a single interference event by plotting the amplitude in MW of the incoming (INC), transmitted (TRA) and reflected (REF) signals against time in seconds. The right-hand plot displays the peak input power in MW for several hundred breakdown events plotted against the location of the breakdown in ns [56].

and the power step size (M) [57]. During the conditioning of the first structure on Xbox 3, it was observed that the rate of conditioning was unusually slow and linear in comparison to past structure results [58]. Figure 5.13 displays a portion of the high power testing results of the TD24R05 SiC N1 structure. For the first 200 million pulses, which had an increment loop length of 30 000 pulses, power step of 10 kW, and BDR limit of 3×10^{-5} bpp, it was shown that the increase in power was only 7 MW over 200 million pulses. Accelerating structures commonly reach > 40 MW for a similar number of pulses. At 200 million pulses, the BDR limit was changed to 10^{-4} bpp and a loop length reduced to 7500 pulses. The choice of this breakdown rate was from previous experience with accelerating structures. Previous structures

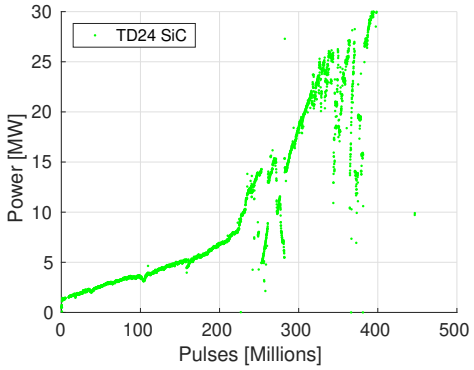

Figure 5.13: A portion of the high power testing history of the TD24 R05 SiC N1 illustrating the conditioning retardation due to the algorithm. The y-axis displays the peak input power in MW plotted against the number of pulses on the x-axis in millions of pulses [57].

have been successfully tested at BDRs of 8×10^{-5} bpp while damage was observed when breakdown rates reached 8×10^{-4} bpp [20, 22]. A clear increase in the rate of conditioning is visible with the distinct curvature of conditioning. This demonstrates the algorithms ability to retard the progress of the structure's conditioning [57]. The drops at 250 and 350 million pulses are the result of conditioning of the waveguide network and the klystron phase issue mentioned in Section 5.3.1.

5.3.4 High Power RF Cooling

Xbox 3 has been designed to operate at a repetition rate well beyond that of Xbox 1 and 2. For RF operating at 11.994 GHz, the power loss factor for the WR-90 waveguide used in the Xbox 3 set-up is ∼0.1 dB/m. Operating at the RF parameters of 40 MW peak for a 200 ns pulse at 200 Hz, the power loss to the waveguide is ∼30 W per metre of waveguide, which needs to be displaced. In Xbox 3 problems related to power displacement were solved with the addition of waveguide cooling pipes on the flanges.
Temperature stability is particularly important for the pulse compressor cavities as they need to remain at the resonant frequency of 11.9942 GHz for nominal operation. As discussed in Section 5.2.2, there is a large amount of power dissipation within the pulse compressors. Initially, the pulse compressors were cooled with a 2.4 kW chiller. This was deemed insufficient for 200 Hz operation after cases where the temperature was unable to remain stable at 30°C. At 200 Hz for a 12 MW input and 3μs pulse, the total power entering the pulse compressor is ∼5 kW, up to ∼4 kW of which will be dissipated in the pulse compressor (Figure 5.1b). Upgrading the chilling capacity to 5 kW displaced the excess heat adequately.

5.4 Xbox 3 Operational Parameters

The conceptual design of Xbox 3 aimed to produce 54 MW of input power though some unexpected challenges limited the power achievable at the structure. Klystrons operating below the expected peak power (although still to design specification), power losses in the waveguide network, and imperfections in the hybrids, all contributed to the reduction in the expected peak power received at the DUT. Despite this, Xbox 3 was still able to operate as the first RF test stand built through weaving low power klystrons. Using the compression factor and gain from Figure 5.1b along with the known input power and klystron pulse length, Figure 5.14 depicts the peak power and pulse length achieved by Xbox 3. For shortest pulse lengths used in high power testing ($\tau = 50$ ns), the peak power could reach ∼44 MW. While at a pulse length of $\tau \approx 200$ ns, the peak power output was reduce to ∼34 MW, due to the reduction in the compression ratio.

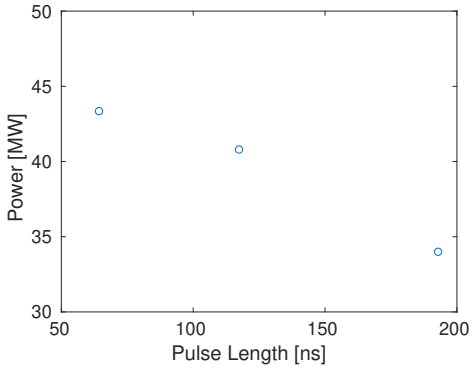

Figure 5.14: Operational parameters achieved by Xbox 3. The peak power in MW on the y-axis is plotted against the pulse length in ns on the x-axis.

5.5 Summary

The commissioning details of novel X-band test stand have been presented in this chapter. This test stand was commissioned at CERN for the purposes of high power testing of CLIC accelerating structures and other RF components. The new test stand uses two low power klystrons which are interweaved together, as discussed earlier through the use of a 90° hybrid and allow two lines to be pulsed on atlernate pulses. Using RF pulse compression, it was possible to achieve peak power outputs of 34 MW for a 200 ns pulses and a maximum of 44 MW for a 50 ns pulse. Although this is below the original target designed peak power of 56 MW, this has proven to be sufficient to test structures to an unloaded accelerating gradient of approximately 100 MV/m. The commissioning of Xbox 3 has demonstrated that it is possible to use low power klystrons and realise a set-up that is not only more cost effective but also operates at a pulse repetition rate of 200 Hz per line which significantly increases the testing capacity.

Chapter 6

Phenomenology of the Capture of Field-Emitted Electrons in CLIC Structures

Fowler and Nordheim first described that the application of surface electric fields led to the spontaneous emission of electrons from the conduction layer of materials [41]. Under certain field conditions, these electrons are captured and propagate through the accelerating structure with undesirable consequences for the beam and surrounding instrumentation. In this chapter, the capture of field-emitted electrons within CLIC structures will be characterised through a series of measurements and simulations. In particular the emphasis will be directed to the capture dependence on the RF phase velocity which was previously unreported.

6.1 Effects of Dark Current for the Operation of CLIC and the X-band Test Stands

In the previous sections it was reported that CLIC accelerating structures will be required to operate with peak surface electric fields in excess of 200 MV/m. Under these conditions, the high surface electric fields will lead to the spontaneous emission of electrons, the theory of which was summarised in Section 4.1. Given the correct field conditions, these field-emitted electrons may be captured by the oscillating RF fields and traverse the accelerating structure as a current. For this reason this phenomenon is commonly referred to as *dark current*. For high power testing of accelerating structures this propagating current collides with its surrounding environment resulting in background radiation. This background radiation dictates the personnel and instrumentation shielding requirements for experiments [59]. Furthermore dark current which remains within the structure can affect beam diagnostics and in extreme cases lead to transverse kicks on bunches [60].

6.2 Measuring Dark Current on the X-band Test Stands

To be able to further understand the phenomenology of dark current in CLIC accelerating structures, Xboxes 1 to 3 are equipped with several measurement devices suited for the purpose of current and radiation measurements. These devices include: Faraday cups, beam-loss monitors, ionisation chamber radiation monitors, dosimeters and a spectrometer.

6.2.1 Faraday Cups

To measure phenomena related to the field emission of electrons and RF breakdown, Faraday cups were installed upstream and downstream of the structure. Each cup is located at the end of each structure after a small section of beam pipe such that propagating electrons enter the cup, creating a measurable current. They were aligned to the axis of the structure to ensure the optimal measurement of propagating electrons.

6.2.2 Beam-Loss Monitor

It is highly likely field-emitted electrons created within the accelerating structures will not all be transmitted through to the Faraday cup. It is postulated that only a small proportion of the field-emitted electrons within the accelerating structure will reach the end of the structure and enter the Faraday cup, as the vast majority of them will most likely interact with the metallic walls. Electrons at higher energies have a greater penetrative ability which means the bremsstrahlung induced electromagnetic shower passes through the metallic walls of the accelerating structure easier than at lower energies. This shower is then expelled into the surrounding environment. A beam-loss monitor (BLM) was created by placing silica-based optical fibres along the side of the structure for the measurement of this shower. Measurements using this system were first performed by Kastriotou, et al. and subsequently tested at the Australian Synchrotron [63]. The principle of operation of these BLMs relies on the production of Cherenkov radiation which results from interactions of the high energy electrons with the medium within the fibre. Frank and Tamm found that electrons traversing a medium with a velocity above the phase velocity of light within the medium will produce a positive net dipole field which results in Cherenkov Radiation [64]. The threshold velocity is found by setting the characteristic angle $\theta_c = 0$ in

$$\cos\theta_c = \frac{c}{vn}. \tag{6.1}$$

where v is the velocity of the electron, n is the refractive index of the medium and c is the speed of light. Solving this gives a threshold velocity of 2.04×10^8 ms^{-1}

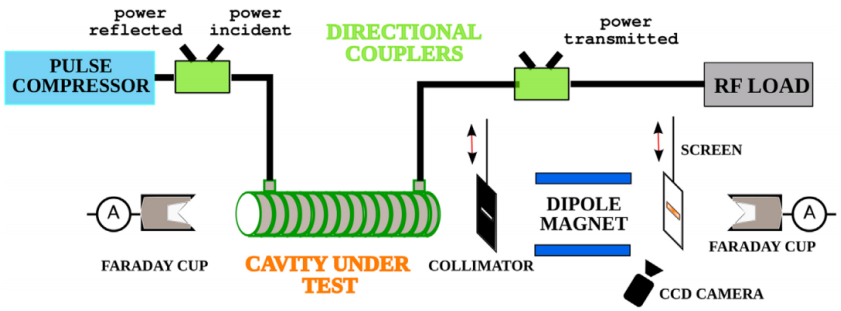

Figure 6.1: Schematic view of the Xbox 2 with the spectrometer [65].

or 186 keV. Given the fields within the structure are in the 100 MV/m regime, the electrons only need to travel ∼2 mm to reach these energies.

6.2.3 Ionisation Chamber Radiation Monitor

For each of the X-band test stands, the Radiation Protection Group monitors the radiation dose rate inside and outside the bunkers. During operation, the radiation monitoring logs allowed the radiation monitor to be used an offline diagnostic. Access to this data proved to be vital to improve the understanding of the dark current in structures.

6.2.4 Spectrometer

Xbox 2 has a spectrometer installed, for dedicated measurements of RF breakdown emission energy spectra and transverse location, controlled by X-band group at Uppsala University. A diagram of the spectrometer set-up is shown in Figure 6.1. Located before the downstream Faraday cup, the spectrometer begins with a tungsten slit which contains two slit patterns (a single 10×0.5 mm slit and a pin-hole of 0.5 mm in diameter) [65]. The beam from the slit passes through to a steering magnet which operates with an integrated magnetic field strength of 0.2 - 10 mTm [65]. The magnet separates the electrons based on their energy after which they are projected onto a scintillating screen. During operation it was possible to operate with the screen and collimator completely retracted, and with the magnet switched off [65]. Such a configuration allowed the downstream Faraday cup to be used, although it was important to account for the long section of beampipe when operating this way.

6.2.5 Dosimeter

At specific locations within the bunker, dosimeters sensitive to gamma, beta and neutron radiation were placed to monitor the dose. As these were film based dosimeters, it was imperative to plan all measurements and avoid oversaturation, as to avoid

the time-consuming manual reset procedure.

6.3 Measurements of Dark Current at Xbox 2 and Xbox 3

In order to characterise the dark current within the CLIC structures under test on Xbox 2 and Xbox 3, a series of measurements were performed. These measurements set out to understand the capture of dark current and the resultant emission of radiation throughout the conditioning process. All measurements were performed with a constant power and pulse length. This section details several measurements performed to further understand numerous unexpected variations in the radiation level within the bunker. More details of the conditioning of these structures will be presented in Chapter 7.

6.3.1 Radiation Emission from the X-band Test Stands

During the conditioning of the CLIC-G Open and TD26CC R05 N3 accelerating structures, it was found that radiation level within the bunker was much greater than expected. Such was the extent of the radiation that the two structures had their conditioning progress impeded and had to run at a reduced power for a portion of their high power testing. During conditioning, it was decided that the bunker containing the accelerating structure would have another 30 cm of concrete added to the roof, after it was found to be a weak spot in the shielding. Further lead bricks were added to shield other weak spots.

Continued radiation related machine down-time led to the decision to perform dedicated measurements of the radiation within the bunker for Xbox 2 and its spectrometer, and each of Xbox 3's individual test slots. Using dosimeters, assigned specifically for measurements, the radiation measurements were performed. The RF was switched on to the greatest achievable power, for the current state of conditioning of the structure, for 90 s. Stabilising the power took ∼3 s after starting the RF

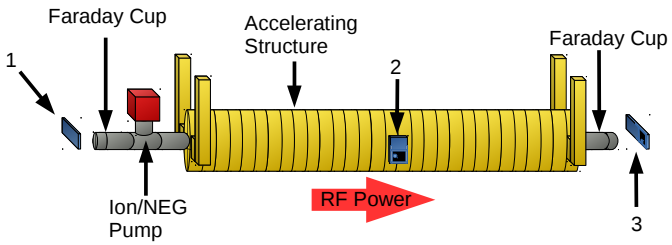

Figure 6.2: A diagram of the experiment performed to map the radiation output from the accelerating structures tested on Xbox 3. Dosimeters were placed outside the vacuum at the end of the upstream and downstream beampipe as well as a single dosimeter on the side of the structure.

Table 6.1: Radiation measurements from Xbox 3 for the two individual test slots. Figure 6.2 displays the location of the dosimeter with the distances listed below.

Location (Figure 6.2)	Distance [m]	Rad. Meas. [μSv/h]
1	0.4	15.3
2	0.34	11.8
3	0.6	5349.4
1	0.4	8.5
2	0.78	9.4
3	0.62	3461.3

power. Dosimeters were placed upstream, downstream, and one on the side of the structure for the two test slots of Xbox 3 (Figure 6.2). The details of the location and measured dose are demonstrated in Table 6.1. It was found that for the Xbox 3 structures, the measured doses downstream of the structure (3 in Figure 6.2) were 3 orders of magnitude greater than the side (2 in Figure 6.2) or upstream (1 in Figure 6.2). It is postulated that this may be the result of capture. This hypothesis will be investigated further later in the chapter through a series of simulations.

The test slot set-up for Xbox 2 differed from Xbox 3 by the addition of a spectrometer which measured the output current of RF breakdowns and captured field emission. The spectrometer operates by collimating the current using a tungsten slit. Similar dose measurements, to those previously discussed, were conducted on the Xbox 2 set-up (Figure 6.3), with additional dosimeters measuring the dose from the collimator. The greatest dose was found to be directly next to the tungsten collimator (Dosimeter 4, 5, 6, and 9), as presented in Table 6.2. Discussion arising from the analysis of these results identified the spectrometer as a likely contributor to the large background radiation dosages measured within the bunker and as it could not be shielded sufficiently a decision was made to remove the spectrometer from the set-up. Together with this, it was decided to increase the shielding around

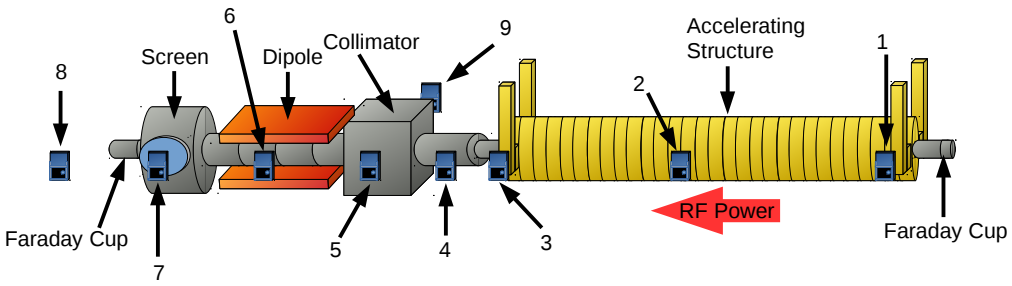

Figure 6.3: A diagram of the experiment performed to map the radiation output from the accelerating structure and spectrometer on Xbox 2. Dosimeters were placed along the length of the set-up to understand where shielding was required for the spectrometer set-up in comparison to the Xbox 3 test slot.

Table 6.2: Radiation measurements from Xbox 2 with its spectrometer. The set-up is illustrated in Figure 6.3.

Location (Figure 6.3)	Distance [m]	Rad. Meas. [μSv/h]
1	0.75	0
2	0.75	17.6
3	0.75	9
4	0.75	88.5
5	0.75	45.53
6	0.75	69
7	0.75	16
8	0.75	3.9
9	0.75	126

the downstream Faraday cups and to decrease the shielding near the structure itself. These simple changes led to an eight fold decrease in radiation within the bunker and allowed the conditioning to continue.

6.3.2 Observations of the Evolution of Dark Current during Conditioning in CLIC Structures

To gain a better understanding of the dark current levels which will be in an operational CLIC, one must investigate how the dark current varies as the structure continues to undergo conditioning. The measurements of such began on the TD26CC R05 N3 structure, once the structure had reached its ultimate gradient of 110 MV/m at a pulse length of 170 ns [66]. These results are presented and summarised in Figure 6.4. It is evident that the dark current, measured using the BLM system, encounters a net reduction over the 180 million pulses of conditioning with occasional transient jumps.

Investigations into the cause of these jumps found that they correlated with breakdown events. As a consequence, during the conditioning, the background radiation level within the bunker would instantaneously increase by almost an order of magnitude measured by the radiation monitor. To understand these changes in radiation level, measurements of the variation of dark current with input power were performed and are demonstrated in Figure 6.5. It was found that after the breakdown, the effective field enhancement factor (β) and effective emission area ($A_e \propto \alpha$) changed as a result of these breakdown events. It is postulated that the explosive expulsion of molten copper during a breakdown event produces new emitters within the structure. It was also observed that not all breakdowns caused such large increases and the variation in the baseline dark current level appeared sporadic in nature. These observations will be crucial for an operational CLIC or any high gradient accelerator. This is because they imply that the background dark current

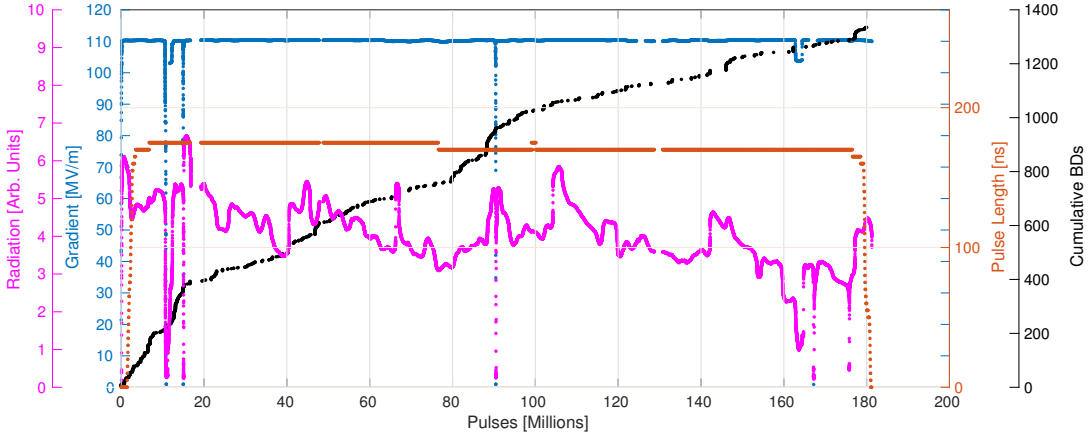

Figure 6.4: The dark current measured using the BLM system on the TD26CC R05 N3 (magenta) plotted on the y-axis against the number of pulses in millions of pulses. The gradient (blue), pulse length (red) and cumulative breakdowns (black) are also plotted against the number of pulses for completeness.

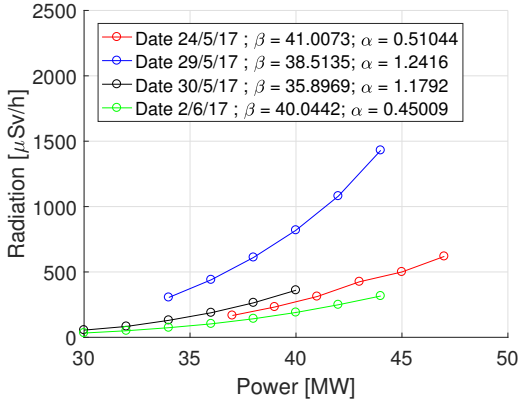

Figure 6.5: Four measurements of radiation, in μSv/h, plotted with respect to the input power, in MW, during different points in time before and after an RF breakdown event which caused a radiation increase. The measurements were taken: several days before the breakdown (red), directly after the breakdown (blue), and one (black) and four days (green) after the breakdown. β is the effective field enhancement factor and α is proportional to the emitter area A_e.

level, and therefore radiation, is highly likely to increase after an RF breakdown. Such behaviour will need to be taken into account for the radiation shielding of CLIC instrumentation, along with all future RF test stands or high gradient linacs.

6.4 Dependence of the Capture of Field-Emitted Electron on the Phase Velocity

During the operation of the CLIC-G Open structure, a radiation safety threshold was exceeded leading to an interlock of the machine. Shown in Figure 6.6a, the background radiation within the bunker gradually increased over ∼1 hour period [67].

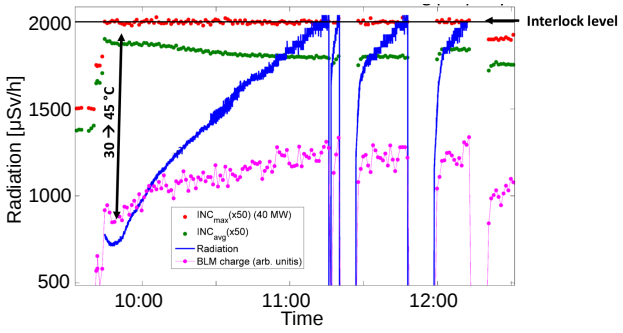

(a) First observation.

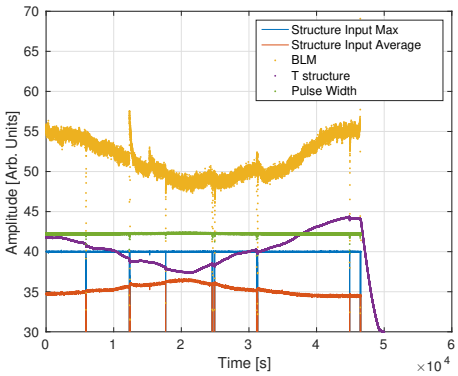

(b) Structure temperature vs radiation.

Figure 6.6: First observation and testing of the temperature dependence of radiation. The left-hand diagram displays: measured radiation within the bunker (blue) in μSv/h, the BLM signal (magenta) in arbitrary units , and the average (green) and peak (red) input power in MW. All of which are plotted against time. The interlock level is illustrated by a horizontal black line. The right-hand diagram displays the subsequent testing of the radiation dependence on temperature. The plot illustrates the structure temperature (purple), in degrees Celsius, and the BLM signal (yellow), in arbitrary units, along with the RF pulse parameters of the peak (blue) and average (red) input power, in MW, and pulse length (green), in ns. These are all plotted against time in seconds [68].

During this time it can be observed that there was no increase in the peak power and a decrease in the average power, therefore the radiation increase was not expected to be the result of a power variation. Investigations into the cause of this radiation increase found a correlation between the structure's operational temperature and the background radiation within the bunker. This was corroborated through systematic changes to the structure's operational temperature (Figure 6.6b). It was hypothesised that this variation resulted from a variation in the resonant frequency. The following section will detail the mechanism expected to be responsible for the enhanced dark current level. This work was published in reference [69] which can be found in its entirety in Appendix C.

6.4.1 A One-Dimensional Model

To understand the capture of field-emitted electrons for a varying structure temperature, one must begin by understanding the requirements of capture. Appendix B illustrates the derivation of the equation which defines the required gradient for electrons to stay synchronous with an RF wave with a phase velocity of c. A more general equation for capture can be written for the case of a varying phase velocity

(v_p) as

$$E_0 \geq \frac{\pi m_0 c^2}{\lambda e}\left(\frac{v_p - v_0}{v_p + v_0}\right)^{\frac{1}{2}}, \tag{6.2}$$

where m_0 is the mass of an electron, e is the electron charge magnitude, and v_0 is the velocity of the electrons [69, 70]. Such a relation demonstrates that a reduction in the phase velocity reduces the required gradient for capture of field-emitted electrons. To understand how the phase velocity varies with the operational parameters, one begins with the definitions of phase velocity and group velocity given by Equations 3.12 and 3.13. These show that the phase velocity can be varied through a change in ω. Differentiating Equation 3.12 against ω gives the variation in phase velocity with respect to RF driver frequency as [69]:

$$\frac{dv_p}{d\omega} = \frac{1}{k} - \frac{\omega}{k^2}\frac{dk}{d\omega} \tag{6.3}$$

$$= \frac{1}{k}\left(1 - \frac{\omega}{k}\frac{1}{v_g}\right) \tag{6.4}$$

$$= \frac{\lambda}{2\pi}\left(1 - \frac{v_p}{v_g}\right). \tag{6.5}$$

Setting the synchronicity condition as c, as used in CLIC structures, gives [69]:

$$dv_p = \frac{\lambda}{2\pi}\left(1 - \frac{c}{v_g}\right)d\omega. \tag{6.6}$$

This gives the relation between the variation in the phase velocity and RF driver frequency. Intepretting this relation, it found that an increase in the RF driver frequency results in a decrease in the phase velocity, given typical group velocity (v_g) values for structures are well below c and if the structure is a forward travelling wave design, where the group velocity travels in the same direction as the phase velocity. For a backward travelling wave structure, the group velocity travels in the opposite direction of the phase velocity therefore a increase in the RF driver frequency results in an increase in the phase velocity, according to equation 6.6.
Equivalent to a variation in the RF driver frequency, a shift in the resonant frequency (ω_r) can also vary the phase velocity. Such a shift in ω_r can be achieved through a variation in the operating temperature of the structure which causes thermal expansion/contraction of the structure, and therefore changes the radius of the accelerating cells of the structure. The variation in the resonant frequency for a given temperature change is given as [69]:

$$\frac{d\omega_r}{dT} = -\alpha\omega_r, \tag{6.7}$$

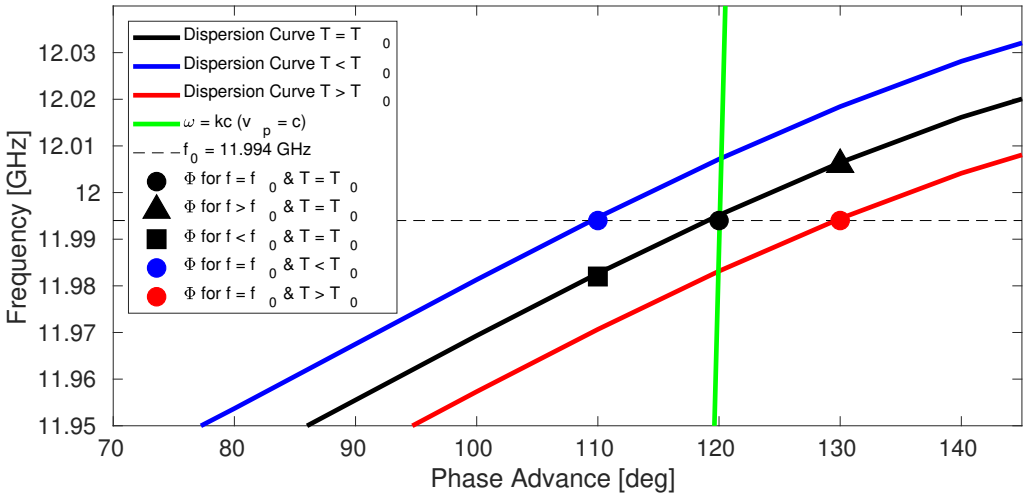

Figure 6.7: Variation in the phase advance per cell with changes in the structure temperature (T) and the RF driver frequency (f). The three curves represent the dispersion curves of a structure at three different temperatures. Five operational points on these dispersion curves are marked: Nominal RF driver frequency and structure temperature (●), an increase in the structure temperature (●), an increase in the RF driver frequency (▲), a decrease in the structure temperature (●), and a decrease in the RF driver frequency (■). The green line represents the speed of light line [69].

where α is the thermal expansion coefficient which for copper is 17×10^{-6} K^{-1} and $\omega_r = 2\pi f_r$ is the resonant frequency ($f_r = 11.994$ GHz) in rad/s [69]. A 1°C increase in the structure temperature results in a 203 kHz decrease in f_r. In Equation 6.7 it is observed that the change in temperature varies ω_r rather than ω. To demonstrate how the $d\omega_r$ is related to a $d\omega$, Figure 6.7 displays the dispersion curve for three operating temperatures and three RF driver frequencies. It is found that an increase in the structure temperature, which Equation 6.7 explains is a decrease in the resonant frequency, is equivalent to an increase in the RF driver frequency for the phase velocity. From this diagram, it can be shown that an increase in ω_r is equal to a reduction in ω such that [69]:

$$d\omega = -d\omega_r. \tag{6.8}$$

Substituting Equations 6.7 and 6.8 into Equation 6.6 gives the change in the phase velocity with respect to the structure temperature change as:

$$dv_p = \frac{\lambda}{2\pi}\left(1 - \frac{c}{v_g}\right)\alpha\omega_r dT. \tag{6.9}$$

It is found that an increase in the structure temperature similarly increases the phase velocity.

To understand the scales required for a noticeable variation in v_p, the phase velocity normalised to the speed of light is plotted against the structure temperature

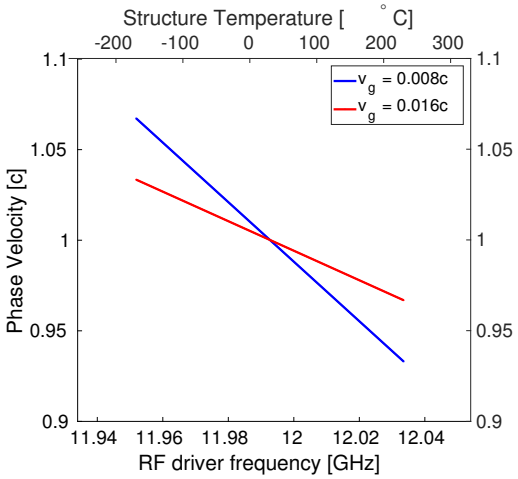

Figure 6.8: A graph demonstrating the variation in the phase velocity, plotted on the y-axis, for a change in the RF driver frequency, plotted on the bottom x-axis, for two difference group velocity (v_g) cells. The top x-axis demonstrates the temperature change required for the equivalent frequency shift [69].

Table 6.3: RF pulse parameters for three structures during dark current measurements on the two test stands [69].

Test Stand	Structure	Power [MW]	Gradient [MV/m]	Pulse Length [ns]	Rep. Rate [Hz]
Xbox 2	TD26CC R05 N3	43	100	170	50
Xbox 3	TD24 R05 SiC N1	17	64	50	50
Xbox 3	T24 PSI N1	33	94	200	50

and RF driver frequency in Figure 6.8 for a group velocity of 0.008 c and 0.016 c. These group velocity values are the maximum and minimum values within the iris-tapered CLIC baseline structure design [9]. The change in the phase velocity is 0.082 %c/MHz and 0.164 %c/MHz for a group velocity of 0.016 c and 0.008 c, respectively. In Equation 6.2 it was previously shown that a decrease in the phase velocity reduces the required gradient for the capture of field-emitted electrons. In summary it can be stated that:
The capture likelihood of field-emitted electrons will increase when there is an increase in RF driver frequency or an increase in structure temperature due to a reduction in phase velocity, and vice versa [69].

6.4.2 Measurements of Field Emission Capture Changes with Phase Velocity

Measurements of the dark current capture dependence on the phase velocity through changes to ω and ω_r were performed on the X-band test stands at CERN. Such measurements were performed using three accelerating structures that were under high power testing at the time. The RF driver frequency and structure temperature were varied for a constant peak power, pulse length and pulse repetition rate to measure

the variation of steady state dark current [59]. Table 6.3 depicts the RF pulse parameters used for the measurements on the three structures. The experimental set-up of the dark current measurements for the structures installed on Xbox 2 and Xbox 3 are illustrated in Figures 6.9a and 6.9b, respectively [69]. The dark current measurements were performed indirectly using an ionisation chamber radiation monitor which tracked the radiation dose at the end of the structure, known to be caused by dark current incident with the Faraday cup [59]. Between the measurements of each structure, the radiation monitor was aligned to be directly downstream of the structure under test and approximately 1 m from the end of the beam line. The spectrometer set up on Xbox 2 had its collimator and screen completely retracted during the measurement [65]. The choice of using the radiation monitor to measure dark current was due a poorly aligned Faraday cup in Xbox 2, after the spectrometer, consequently leading to poor signal strength. The change in structure temperature will be referred to as a shift in resonant frequency from here onwards, calculating the equivalent frequency shift using Equation 6.7. This will allow an easy comparison for the two operational parameter changes. Radiation measurements were performed at structure resonant frequency shifts of -3 MHz (-2 MHz for TD24 R05 SiC N1), 0 MHz, and +1 MHz. Likewise, radiation measurements were performed for a variation in the klystron driver frequency. Such variations in the RF driver frequency were restricted to ±1 MHz due to the bandwidth limitation of the klystron. Presented in Figure 6.10 are the radiation measurements for a given RF driver or resonant frequency shift, and each fit with a linear regression. For an increase in the RF driver and equal magnitude decrease in resonant frequency (structure temper-

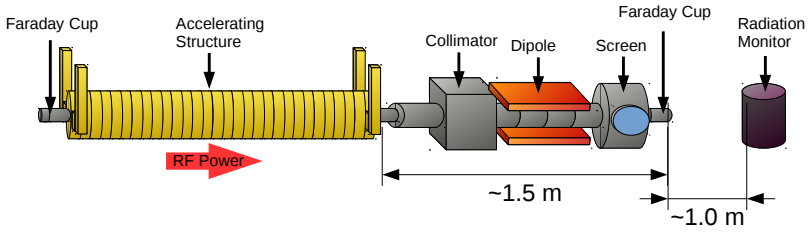

(a) Xbox 2 and spectrometer.

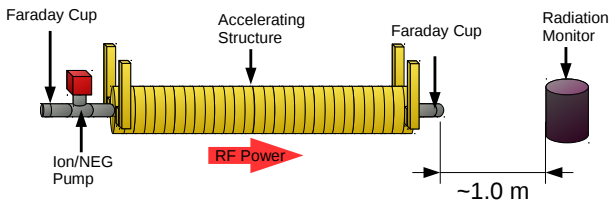

(b) Xbox 3.

Figure 6.9: Experimental set-up for the measurement of the dependence of dark current on the RF driver frequency and structure temperature using a radiation monitor [69].

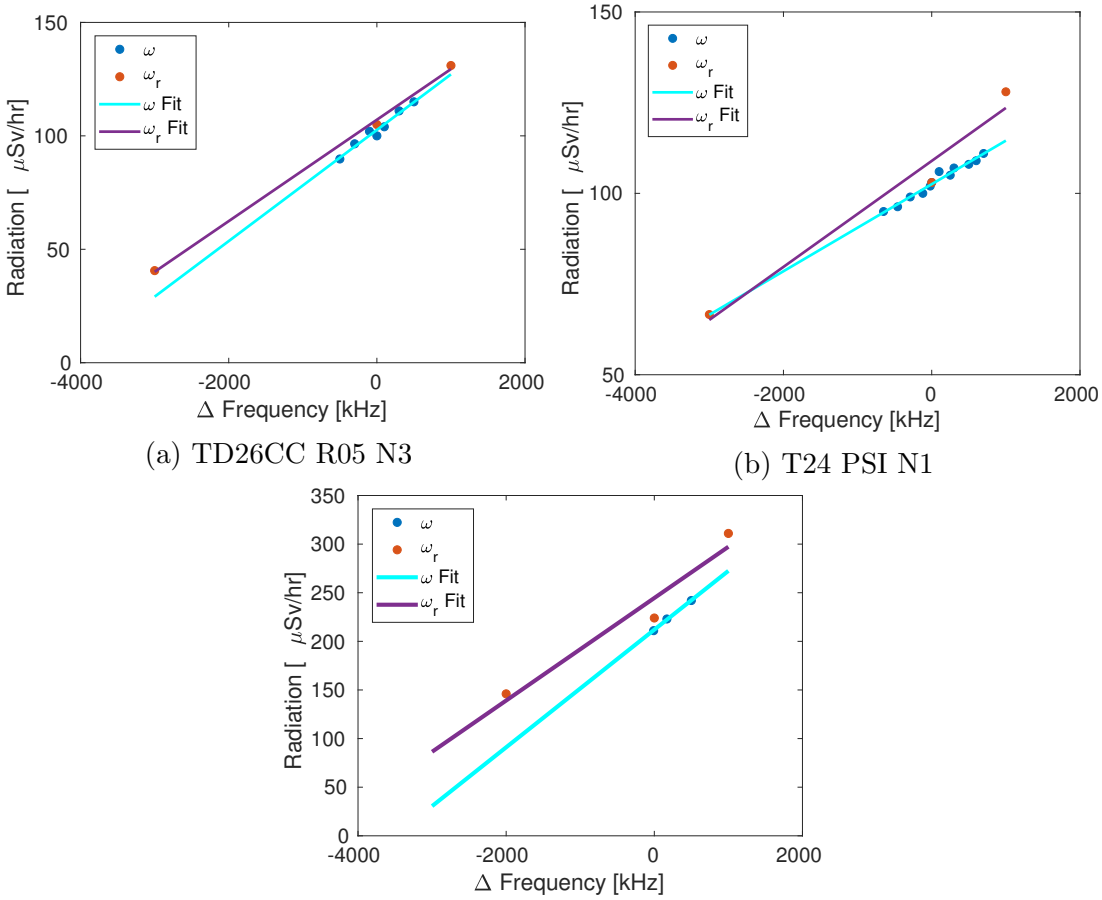

(a) TD26CC R05 N3

(b) T24 PSI N1

(c) TD24 R05 SiC N1

Figure 6.10: Measurements of the change in dark current induced radiation in μSv/h plotted against a change in the RF driver (blue) or equivalent change in the resonant frequency (red) in kHz. The linear fits display the average rate of change for the resonant frequency (purple) and the driver frequency (cyan). [69].

ature increase), an increase in the radiation level within the bunker was measured. The vertical offset between the temperature and frequency measurements resulted from RF breakdowns causing new baseline dark current levels. When taking the RF driver frequency (ω) fit values a 24.5%/MHz, 28.67%/MHz, and 12.64%/MHz shift in the radiation levels is found for the TD26CC R05, TD24 R05 SiC N1, and T24PSI, respectively. This increase in dark current for an increase in RF driver frequency and decrease in resonant frequency (increase in structure temperature) is what is expected from Equations 6.6 and 6.9 supporting the change in phase velocity as the mechanism for the dark current variation [69].

6.5 Three Dimensional RF and Particle Simulation

To further study the capture and propagation of field-emitted electrons, a simulation was assembled using CST Microwave and Particle Studio [71]. To begin, attempts to calculate the entire geometry of the structure were performed. It was determined that calculating the entire structure geometry for RF fields and particle simulations required too much computational power to make it feasible. Instead, to obtain the electric and magnetic field distributions, simulations began with the eigenmode solver for a single cell geometry. The middle cell from the TD26CC R05 structure, currently the CLIC baseline structure, was used for the single cell geometry [72]. In this cell, the iris radius is 2.75 mm resulting in a group velocity of around $0.012c$. The boundary conditions on the single cell started with $\Delta\phi = 2\pi/3$ (120°) mode, as used in the CLIC design, then solved the E and H fields for a single cell (Figure 6.11).

Previously a frequency dependence on the capture of field-emitted electrons within the structure was discussed. Running the eigenmode solver for various $\Delta\phi$ values allowed a change in the RF driver frequency of the cell. In Figure 6.12, the five points on the dispersion curve are plotted for different $\Delta\phi$ values on the single cell geometry. The phase and group velocity is found using equations 3.12 and 3.13, setting $k = \Delta\phi/L_{cell}$ where L_{cell} is the cell length. These give the phase velocity and group velocity as $v_p = c$ and $v_g = 0.011998c$, respectively, which agrees well with the expected value. Low power testing of the structure, using a non-perturbative bead-pull measurement, demonstrated good agreement with the simulation [73, 74].

After the electromagnetic field conditions had been established, they were imported into the particle-in-cell (PIC) module of CST. For the particle simulation, a 48 cell model was assembled to understand the upstream and downstream behaviour

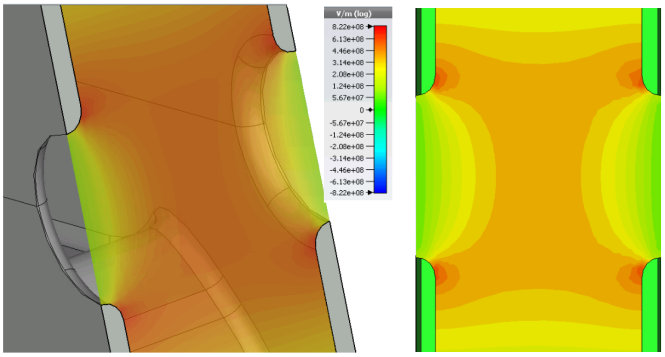

Figure 6.11: The electric field profile of the eigenmode solution of the middle cell for the TD26CC R05 single cell design. The three dimensional model demonstrates the geometry of the cell with a cross-section of the electric field profile illustrated. The colour map displays the field strengths with respect to the position on the cross section [69].

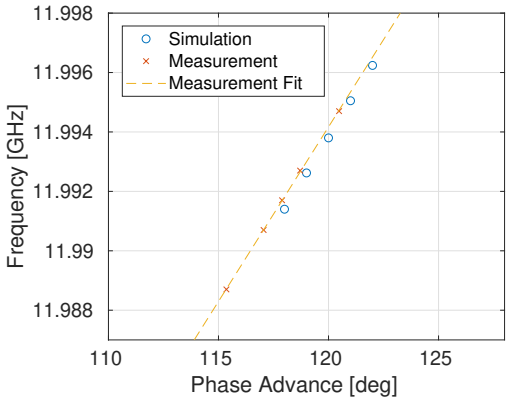

Figure 6.12: A Brillouin diagram, which plots the resonant frequency of the structure against the phase advance, demonstrates points on a dispersion curve created in the simulation (blue circle) and compares them to the measured values (red cross). A dashed yellow line illustrates a linear fit of the measurement data [69].

of a 24 cell structure [60]. Floquet's theorem, discussed in Section 3.2, stated that for infinitely repeating coupled cells the electromagnetic fields in each cell differ by only a phase difference [70]. Based on this, the single cell electromagnetic fields were imported into each of the adjacent cells with the appropriate phase advance for the given RF driver frequency. The result was a full accelerating structure with the appropriate phase advance per cell and field conditions for a structure completely filled with RF power. The limitation of this method is that the cells are all identical in nature without the iris tapering present in constant gradient structures. Despite this, the RF simulation acts as a constant gradient structure as required due to the same field being imported into the adjacent cells.

Two dimensional monitors at each iris measured the properties of particles emitted from the centre of the 48 cells. The idea of using this symmetry for upstream and downstream behaviour of a full structure model was exploited in reference [60]. The iris is set as the source of the particles (Figure 6.13) because the surface electric fields are greatest, as was shown in Figure 6.11, and therefore the field-emitted current

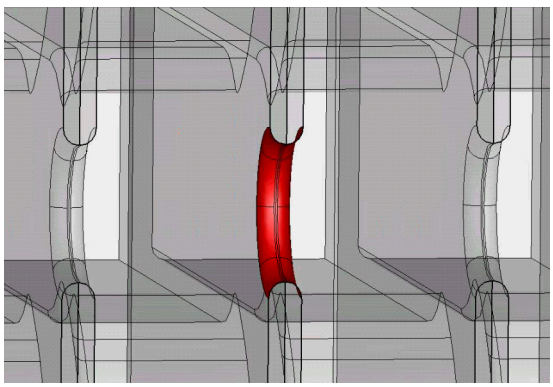

Figure 6.13: Depicted in red is the area of the iris used in the particle simulation. [69].

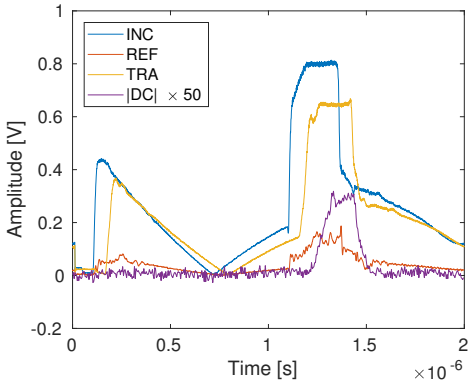

Figure 6.14: An example of the primary RF waveforms used for the analysis. The amplitude of the incoming (INC), reflected (REF), and transmitted (TRA) RF signals, along with the downstream Faraday cup (DC), are plotted in volts against time, in seconds [69].

density is greatest. To find the density of field-emitted electrons, the emission area used the Fowler-Nordheim model described in Equation 4.3. By setting the total area of the iris as the emitter, early simulations found that the simulated downstream current was well beyond that measured. Emitters in structures are known to be microscopic in nature and therefore their area is vastly smaller than the total area of the iris [42]. For the model an emitter density factor is added to determine the effective area of the emitter(s). Measurements in X-band test stands at CERN demonstrate downstream current in the hundreds of microamp to milliamp regime (Figure 6.14). Figure 6.15 depicts the downstream current plotted against the effective area of the emitter and shows that the effective area size is from 0.01 to 1 μm^2. The upper limit of the effective emitter area obtained was spread homogeneously across the entire iris as it is not yet known how the position of the emitter on the iris affected the capture of field emitted electrons. The scaled emission current density

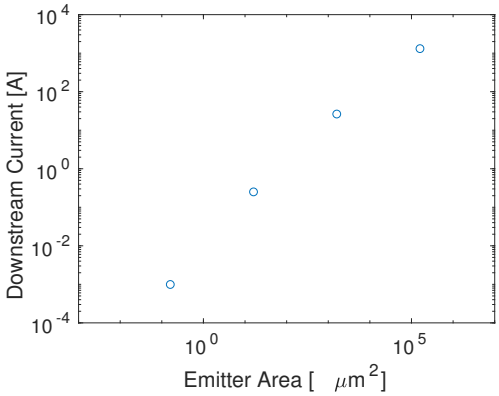

Figure 6.15: The downstream current, in amperes, on the y-axis is plotted against the effective emitter area, in μm^2, on the x-axis [69].

(j'_F) used for the final simulation is given by multiplying the current density (j_F) by the ratio of the effective emitter area to the iris area such that:

$$j'_F = \frac{A_{emitter}}{A_{iris}} j_F, \tag{6.10}$$

where $A_{emitter}$ is the effective area of the emitter and A_{iris} is the area of the iris. For the emission model a field enhancement factor of $\beta = 30$ was chosen, as it is a typical value measured in experiments, and the work function for copper set to be 4.5 eV [75]. Changes in the work function are expected to be negligible for these relatively small changes in operational temperature [61, 62]. To investigate the relation between RF driver frequency and the capture of field-emitted electrons, as discussed in section 6.4.1, the RF model was repeated with a variation of the boundary condition. For a variation in the RF driver frequency, the fields from the various $\Delta\phi$ eigenmode solutions were imported into the model with the appropriate phase advance per cell.

6.6 Results of Simulation

Running the simulations in CST's PIC solver, the properties of the macroparticles were extracted from each two dimensional monitor and the emission surface as ASCII files, and analysed in Matlab. It was decided that the results would be taken from the time when the system reached its steady state solution, which was when the input of particles to the system through field emission was equal to the loss of particles from the system. This point was found to be after approximately 4 RF oscillations which is ∼333 ps. Simulation results for current emitted and current transmission were averaged from 333 ps to 1 ns.

6.6.1 Capture Efficiency per Cell

Taking the ratio of emitted current from the iris to the current passing through each of the 2D monitors at each iris interface, the capture and transport efficiency was calculated for each cell using an accelerating gradient of 100 MV/m. Figure 6.16a depicts the transmission ratio from each cell, normalised to the emitted current. The transmission ratio is defined as the ratio of particles which reach the end of the structure with respect to the total emitted from a given cell. Figure 6.16b illustrates the total dark current reaching an iris. This is calculated by simply summing the current at each cell from one end of the structure towards the upstream or downstream output. The value at cells 1 and 24 for the upstream and downstream current, respectively, will represent the relative output current. This can be seen to be significantly greater for the downstream. It is clear that the downstream output can be separated into two regions: cells 1 to 20 (Region 1) and cells 20 to 24 (Region

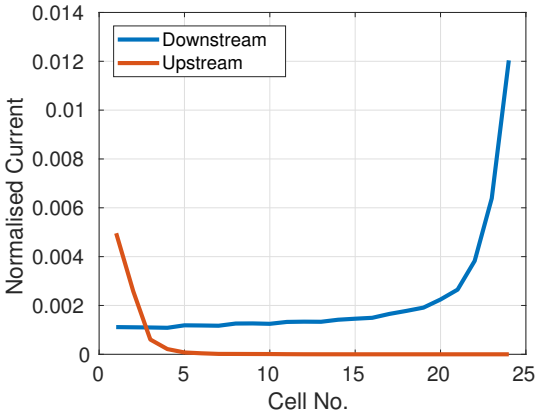

(a) Normalised to Emitted Current

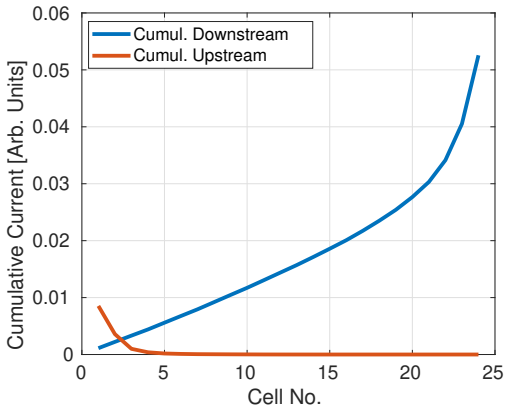

(b) Total dark current reaching cell.

Figure 6.16: Simulation results depicting the amount of dark current reaching the upstream/downstream beam input/output of the structure. The left-hand plot illustrates the current reaching the downstream (blue) or upstream (red) of the structure normalised to the total emission from the iris plotted against the cell number of the emitters. On the right-hand plot, the values from the left-hand plot are summed towards their respective output displaying total current arriving at the cell, in arbitrary units, plotted against the cell number.

2). Overwhelmingly the downstream dark current is found to result from Region 2. For this region, the solid angle between the downstream output and the irises is greatest, and therefore has the most direct path to the output. Additionally, the field-emitted currents in Region 2 do not have as many RF fields to contend with to exit the structure. For field-emitted particles in Region 1, a steady decrease in the transmitted current as the emitter moves away from the downstream output is visible. It was determined through the simulations that current output from Region 1 required capture by the RF fields to be transmitted through to the downstream output and the steady decrease observed between cells 20 to 1 resulted from these captured electrons being lost from the traversing RF buckets. Between 0.1% and 0.2% of the particles are captured and reach the downstream output for gradients of 100 MV/m. In Figures 6 and 8 of reference [60], it was determined that a large fraction of field-emitted electrons in Region 2 would not make it to the downstream Faraday cup, due to their large divergence and low energy.

In the case of the upstream dark current, it was observed that only the irises at the beginning of the structure are able to generate electrons which reach the upstream output. This is understood to be the case due to the preference for the acceleration direction which propagates from upstream to downstream. For electrons further downstream, these were observed to be deflected by the forward travelling RF bucket and therefore could not reach the upstream output.

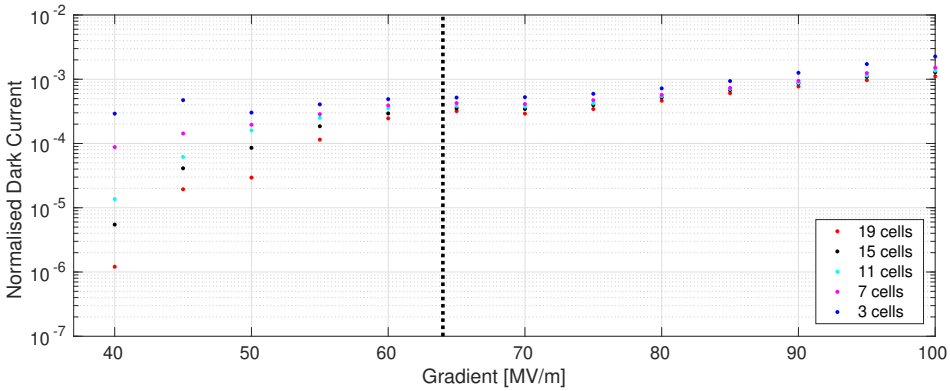

Figure 6.17: Normalised dark current transmitted to the downstream output of the structure, for five irises distributed across the structure, plotted against the accelerating gradient in MV/m. The emitters are located 19 cells (red), 15 cells (black), 11 cells (cyan), 7 cells (magenta) and 3 cells (blue) from the downstream output.

6.6.2 Capture Efficiency versus Gradient

It is expected that the capture and transport of the field emitted electrons will vary with accelerating gradient. Assuming a phase velocity equal to the speed of light, the electrons need to be at relativistic velocities to stay synchronous with the RF phase, as dictated by the second condition of continuous acceleration. Using Equation 6.2 and setting the phase velocity to c and the particles to be stationary ($v = 0$), the gradient for capture in MV/m is given simply as:

$$E \geq \frac{1.6[\mathrm{MV}]}{\lambda}, \tag{6.11}$$

where λ is the RF wavelength in metres. In the case of CLIC structures, the frequency is 11.994 GHz (25 mm) which results in a capture gradient of 64 MV/m. Figure 6.17 illustrates the fraction of field-emitted current transmitted downstream from five cells evenly distributed across the structure for gradients between 40 and 100 MV/m. A vertical dashed line depicts the capture threshold value of 64 MV/m which separates two regions of capture behaviour. As the gradient is reduced to below the capture threshold it is found that the ratio of emitted electrons reaching the end of the structure which need to travel more than 3 cells, drops significantly. This is because the capture of the field-emitted electrons becomes less likely. It is found that for the emitters which are only 3 cells away, the ratio reaching the end varies only slightly as the gradient drops to 40 MV/m. On the other hand, above the capture threshold at ∼70 MV/m to ∼100 MV/m, it can be found that the ratio of emitted current reaching the downstream output increases exponentially. This is postulated to be the result of better capture of electrons from the iris section which would usually be lost.

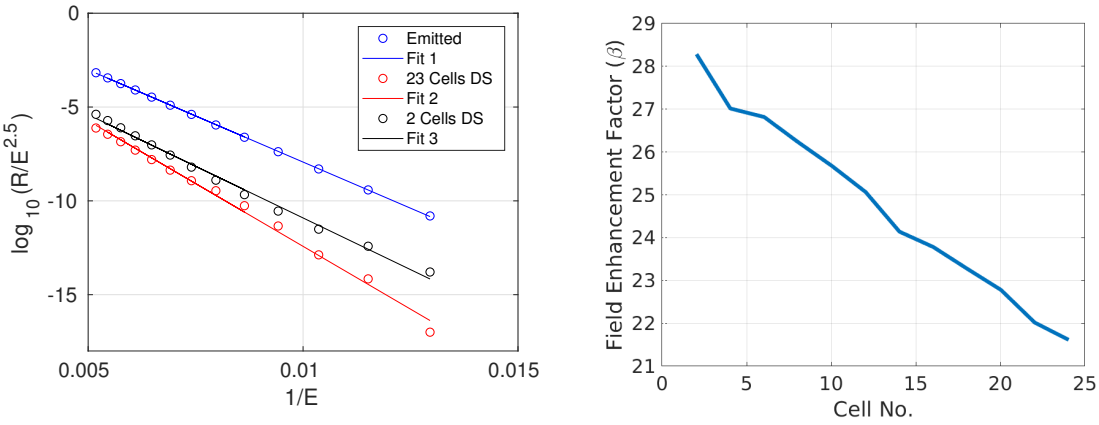

(a) Example β Scans

(b) β vs Cell No.

Figure 6.18: Simulation of power scans which are used to measure the field enhancement factor. The left-hand plot illustrates three power scans where the log of the current normalised to the electric field to the power of 2.5 is plotted against the inverse of the electric field. The current is measured at the emitter (blue), two cells downstream (black) and 23 cells downstream (red). The fits illustrate the gradient which is used to obtain the field enhancement factor. On the right-hand plot, the calculated field enhancement factor (β) is plotted against the number of cells traversed before measurement.

6.6.3 Effect of Capture on the measurement of the Field Enhancement Factor

Earlier in Section 4.1, the idea of field emission was explored and a field enhancement factor (β) described. This β factor is an apparent surface field enhancement and can be measured through a variation in the gradient, as described in Equation 4.5. It was described in the previous section that a variation in gradient also varied the transport of the current downstream towards the measurement device. Measuring β is performed using the Faraday cups, BLMs or radiation monitors. As all of these are located completely or partially downstream of the structure, therefore it is anticipated that the measured β is affected by both the intensity of field emitted electrons and their capture and transport, given these are both gradient dependent. To illustrate how transport affects the measurements of the enhancement factor, β was measured along the structure at each iris for a set value in the emission model equal to $\beta = 30$. Three examples of the data taken from the scan are presented in Figure 6.18a, where it can be found that the measured emission is greatest at the point of emission and drops significantly as the detector moves away from the emission area. The three fits to the data have a differing slope and therefore β, as it was shown in Equation 4.5 that the slope is inversely proportional to β. Repeating this for each cell and extracting the measured β, Figure 6.18b illustrates the beta value across the structure. It is found as the distance between the emission site and the measuring device is increased, the measured β drops linearly. Therefore the way to measure an accurate β is to measure as close to the region of emission as possible.

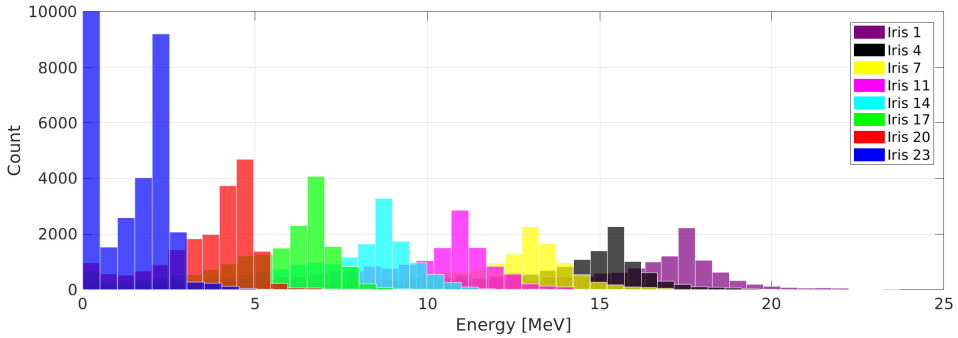

Figure 6.19: A histogram of the energy spectra of dark current to reach the downstream output when emitted from various irises. The macroparticle count is plotted against the energy of the macroparticles in MeV. The colours represent the iris where the particles were emitted.

6.6.4 Dark Current Energy Spectrum

After becoming captured within the electromagnetic fields, the field-emitted electrons begin to undergo acceleration. This not only influences their likelihood of reaching the end of the structure but also results in them gaining energy. The amount of energy they gain is expected to be dependent on the iris from where the electrons were emitted. Radiation within the bunker is also related to the energy of the dark current. This is the result of the higher energy electrons creating more secondary electrons when colliding with the walls, as well as having a greater penetration strength to pass through the structure walls into the local environment. In order to minimise the effects of captured dark current, a broader understanding of its energy spectrum is required.

The energy spectra for the electrons exiting the structure downstream are presented in Figure 6.19. These were emitted from irises equally spaced along the structure for an accelerating gradient of 100 MV/m. It is found that for the field emitted electrons from Iris 23, which is 1 cell away from the downstream output, two peaks occur in the energy spectrum. The higher energy peak at ∼2 MeV is produced by the electrons which have been captured and accelerated. The peak at low energies $E_k < 0.5$ MeV occurs from electrons which are emitted from the iris but have not been captured, therefore do not undergo continuous acceleration. These electrons can propagate a few cells away from their emission point as illustrated in Figure 6.16a, but are then removed due to their asynchronism with the RF phase. For the field-emitted electrons emitted from Iris 20, the peak shifts to 5 MeV as the captured electrons are accelerated, a large loss of these captured electron occurs as these electrons slip from their RF bucket during transport. This trend continues for electrons from Irises 20 to 1 as the captured electrons increase in kinetic energy while also continuing to be lost. Electrons traversing the entire structure, emitted from the first iris, reach a mean kinetic energy of 17 MeV in the 20 cm of accelerating structure.

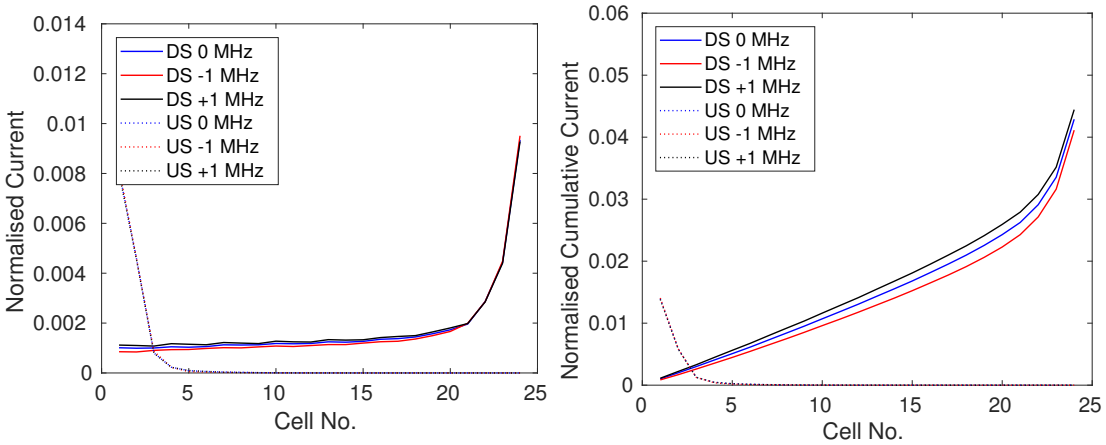

(a) Normalised to the Emitted Current.

(b) Total dark current reaching cell.

Figure 6.20: A repetition of the scan performed in Figure 6.16 for a variation in driver frequency. The left-hand plot illustrates the current reaching the downstream or upstream of the structure normalised to the total emission from the iris plotted against the cell number of the emitters. On the right-hand plot, the values from the left-hand plot are summed towards their respective output displaying total current arriving at the cell (arbitrary units) plotted against the cell number [69].

6.6.5 Variation of Field Emission Capture with Operating Frequency

Measurements presented in Section 6.4.1 illustrated the change in the measured dark current through a variation of the RF driver frequency or structure operational temperature. This variation was described using a one dimensional approximation demonstrating that the phase velocity would decrease due to an increase in structure temperature or increase in RF driver frequency. This reduction in phase velocity resulted in better capture of the field-emitted electrons and therefore a greater dark current level. To corroborate the measurements and the one-dimensional model, the simulation developed in CST was used to further understand the changes in dark current capture given a variation in the RF driver frequency. Figure 6.20 displays the capture efficiency from each cell where the capture is plotted as a fraction of the emission for each cell (Figure 6.20a), and as an accumulation towards each respective output (Figure 6.20b). The capture efficiency is shown to increase for a greater frequency RF driver as found in measurements. Simulations demonstrated that electrons emitted later in the RF oscillation are captured for higher RF driver frequencies whereas they slip from the RF bucket at lower RF driver frequencies. This effect is therefore observed for the field-emitted electrons which have undergone capture, which is important for the analysis of the simulations. Figures 6 and 8 of reference [60] depicted that the low energy particles emitted from the irises far downstream predominantly were not measured in the Faraday cups. This was understood to be caused by the poor capture of these electrons which prevented them from passing through the small section of beam pipe at the end of the structure and

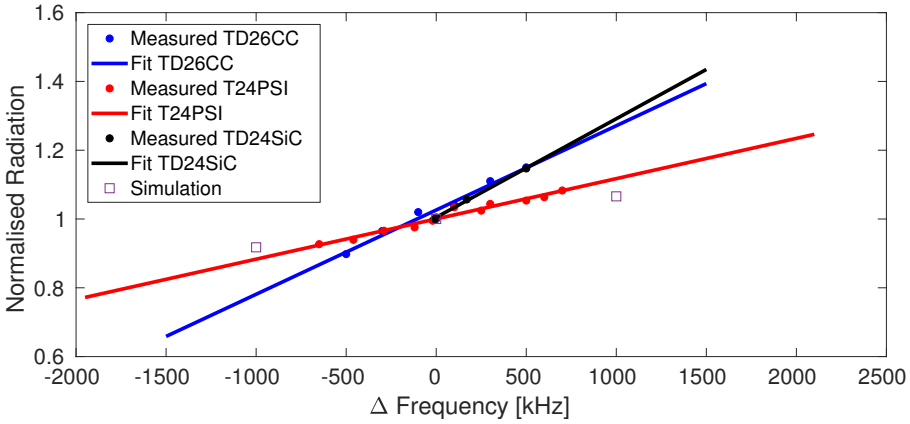

Figure 6.21: A comparison of the simulated and measured variation in the radiation due to a change in the driver frequency. Plotted on the y-axis is the radiation level, normalised to that measured at the nominal frequency. This is plotted against the change in driver frequency in kHz. The solid points represent the measured data from the TD26CC (blue), the TD24SiC (black) and T24 PSI structures with a linear fit. The unfilled squares depict the results from the simulations [69].

on to the Faraday cup. These low energy particles are observed as the jump in transmission downstream in cells 21 to 24 of Figure 6.16a. Taking this into account, the analysis used particles arriving downstream of the structure which were known to have been captured (cells 1 to 20), and therefore likely to arrive at the Faraday cup due to their lower emittance and greater longitudinal momentum. From cells 1 to 20, the cumulative capture for the nominal RF driver frequency is 0.0243 compared to 0.0259 for +1 MHz and 0.0223 for -1 MHz. This accounts for an average of 8.05%/MHz change in the capture of the dark current with respect to the RF driver frequency. With these simulations the results were compared to the measured data. To calculate the expected radiation from the simulations, a simple model which assumed the power deposited in the Faraday cup was proportional to the radiation produced was used. This approximation does not account for the complexities of Bremsstrahlung and pair production which are expected when the particles interact with the Faraday cup. Calculations of the power dissipation were performed by measuring the power of the macro-particles at the most downstream two-dimensional monitor. The power transmitted through the monitor was taken once the simulation had reached an equilibrium in the power flow. Figure 6.21 compares these simulation results to the measurement results from Figure 6.10 where the change in RF driver frequency was used. A similar magnitude change in the dark current between the simulation and measured results for the T24 PSI N1 structure was found. The large difference between the T24 PSI N1 structure and the other two structures is yet to be understood and will be studied in future investigations.

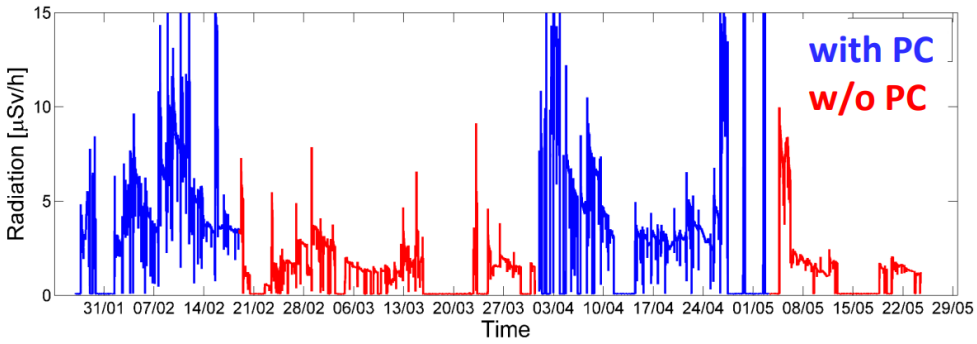

Figure 6.22: Radiation within the bunker during high power testing of the CLIC-G Open for operation with and without the pulse compressor. The plot illustrates the measured radiation, in μSv/h, on the y-axis plotted against the time of operation. Blue lines represent when operation occurred with a pulse compressor while red represents operation without the pulse compressor [68].

6.7 Field Emission Capture Enhancement Due to Pulse Compressor Phase Profile

The pulse flattening was performed through a phase ramp after an ~110° flip. This allowed the power to be extracted from the pulse compressor in a controlled manner. For the operation of the X-band test stands, it was previously believed that the phase could simply be ramped, and due to the lack of beam, the structure would operate as desired. During operation of Xbox 2, it was observed that the undesired radiation output from the structure was greater during operation with the SLED than during operation using only the klystron as illustrated in Figure 6.22. This is also demonstrated for a single pulse in Figure 6.23. From this it was determined that the phase ramp was in fact affecting the operation through shifting the RF

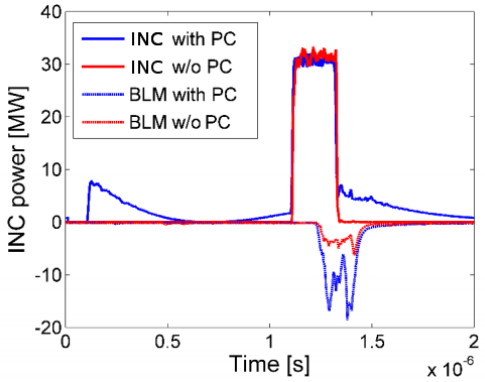

Figure 6.23: An example of the RF pulse, in MW, and BLM, in arbitrary units, plotted against time in seconds. The blue illustrates operation with a pulse compressor while the reds displays the operation without a pulse compressor [68].

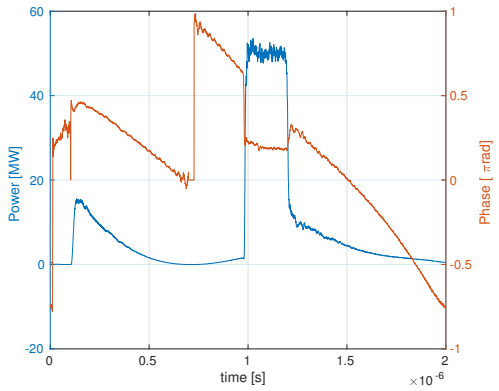

Figure 6.24: The phase and resultant amplitude profiles for the operation of the pulse compressor with a flat phase programme. The power in MW (blue) and phase in pi-radians (red) of a pulse is displayed on the left and right y axes, respectively, and plotted against time in seconds.

driver frequency. The change in the RF driver frequency is given:

$$\Delta f = \frac{1}{2\pi}\frac{d\phi}{dt} \tag{6.12}$$

where $d\phi$ is the change in phase and dt is the duration of the phase ramp in seconds. From this equation, it was found that for the shortest pulse length used in operation (50 ns), there was up to a $\sim$4 MHz shift of the RF driver frequency. While for the longest pulse length used (200 ns), the frequency shift reduced to $\sim$1 MHz, given the larger dt. This particular case was attributed to a frequency increase, during the phase ramp, which resulted in an increase in radiation during operation with the SLED. Fixing this issue was simple as it was well known for operation with beam. By adding a constant phase shift throughout the filling and extraction cycle of the SLED, equivalent to driving at a reduced frequency, one can achieve the necessary flat phase and flat amplitude required for the pulse at the nominal frequency (Figure 6.24).

6.8 Summary

For high gradient applications, high surface electric fields lead to the emission of electrons from the metallic surface of the accelerating structure. Under certain field conditions, these field-emitted electrons can be captured in traversing RF fields and become a captured dark current propagating throughout the accelerator. Such dark current leads to: a background radiation level for experiments (possibly damaging local instrumentation and increasing the shielding requirements), can cause an increase in the background level of beam diagnostics, and in extreme cases lead to transverse kicks on present beam. Measurements demonstrated that the dark cur-

rent level within the structure decreases with conditioning though can experience transient increases after RF breakdown when new emission tips are formed. Further measurements demonstrated that radiation, resulting from dark current, was predominantly found downstream. Shielding of the Faraday cup, rather than the structure, was found to be more effective in reducing the radiation emitted into the surrounding environment.

A significant variation in the dark current was observed and found to be the result of a dependence of the capture of field-emitted electrons on the RF driver frequency and the structure resonant frequency. A one-dimensional model was used to demonstrate that an increase in the RF driver frequency or a decrease in the resonant frequency resulted in an increase in the capture of field-emitted electrons. This was shown to be the result of a reduction in the phase velocity leading to better capture of electrons which would usually slip from the RF bucket.

A three dimensional RF and particle simulation was assembled to better understand the dynamics of field emission capture. The model demonstrated that approximately 0.1-0.2% of the dark current, emitted from the iris of a structure, undergoes capture. When emitted from the first iris, this dark current could reach upwards of 17 MeV over the length of the structure. Varying the RF driver frequency in the simulation demonstrated similar results to those found in measurements.

Chapter 7

Analysis of the High Gradient Performance of CLIC Structure Prototypes

In this chapter the high power testing of four CLIC prototype accelerating structures, performed by the author, on the newly commissioned Xbox 3 and its predecessor Xbox 2, will be presented demonstrating the reproducibility of achieving unloaded gradients above 100 MV/m. Each structure has a unique design and testing objective, which will be outlined before summarising the high power results. A postmortem analysis of two of the structures was performed with contributions by the author. These will demonstrate the effects of high power on the RF properties of the structures. Using the results from these high power tests, the effects of conditioning at greater repetition rates will be investigated and used to explore cost effective strategies for the conditioning of the ∼28 000 structures required for CLIC-380. Initiating the discussion is an overview of the analytical techniques and signal processing tools used by the author to develop an analysis code which was written to understand the behaviour of the structures at high accelerating gradients.

7.1 Signal Processing and Analytical Techniques

During testing of the accelerating structures, the PXI (acquisition crate) stored the waveform data on a local hard drive from each of the channels of the ADCs. Waveforms were saved given the following two cases:

1. Every 40/60 s for Xbox 3/Xbox 2 tagged as Type 3 when stored, and

2. Breakdown event tagged as Type 0 and the pulse before the breakdown tagged as Type 2 when stored. Xbox 2 also stores the penultimate pulse before the breakdown, tagged as Type 1.

This tagging of the waveform types was found to be vital for separating them in the analysis code. Table 7.1 displays a list of the ADC channels which were saved during the two cases listed above. Three particularly important channels for the analysis were PSI (or INC for incoming), PEI (or TRA for transmitted), and PSR (or REF for reflected).

7.1.1 IQ Demodulation

For the purpose of digitising the RF signals sampled from the directional couplers, the PXI has four 1.6 GSPS, 12-bit ADCs each of which measured the In-Phase (I) and Quadrant (Q) components of the RF signals. To understand the purpose of sampling the I and Q components of the RF signal, one can think of the measured RF voltage at time t as:

$$V_m(t) = \mathcal{R}[(I + iQ)\exp(i\omega t)], \tag{7.1}$$

where ω is the operating frequency. In Section 5.1.3 it was discussed that the RF signals from the high power network were downmixed to 400 MHz. Sampling these RF signals at 1.6 GSPS obtained the pure I and Q components in the sequential order I,Q,-i,-Q [22]. Taking the value of the I and Q at time t, the amplitude (A) was defined as:

$$A(t) = \sqrt{I(t)^2 + Q(t)^2}. \tag{7.2}$$

Table 7.1: Nomenclature for waveguide couplers. The ADC channels measured the forward and reflected signals from each directional waveguide coupler. Some couplers have alternative names which are considered more descriptive of the waveform at that location. * Xbox 2 only.

ADC Channel Name (Alternative)	Description
PKI (KLY)	Klystron Output
PKR	Reflection to Klystron
PLI	Pulse Compressor Input
PLR	Pulse Compressor Reflection
PSI (INC)	Input to Structure
PSR (REF)	Reflection from Structure
PEI (TRA)	Output of Structure
PER	Reflection from Load
DCUp	Faraday Cup Upstream
DCDown	Faraday Cup Downstream
BLM*	Cherenkov Fibre Monitor Upstream
BLM TIA*	Cherenkov Fibre Monitor Downstream

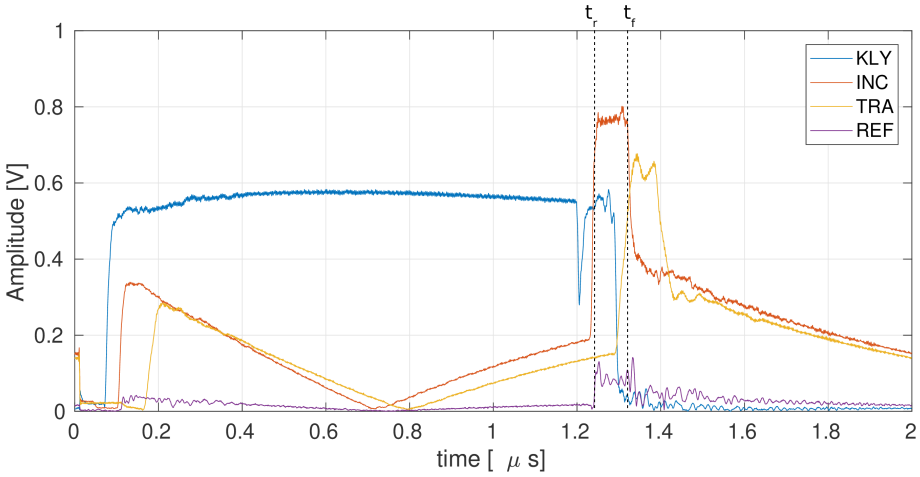

Figure 7.1: The raw ADC signals of the waveforms, in Volts, sampled from the output of the klystron (blue), the input of the structure (red), transmitted through the structure (yellow) and reflected from the structure (purple), each plotted against time in μs. The annotations define start (t_r) and end (t_f) of the useable RF pulse.

Given I and Q are separated by 90°, the phase of the RF is given as:

$$\phi(t) = \tan^{-1}\left(\frac{Q(t)}{I(t)}\right). \tag{7.3}$$

Thus the IQ demodulators allowed the amplitude and phase to be measured. This will be demonstrated to be vital for the diagnosis of the location of RF breakdowns in the coming sections.

7.1.2 RF Gradient and Pulse Length

The first step was to define the accelerating gradient and pulse length of the RF pulse input into the DUT (INC), as this defines the operational conditions within the structure. In Figure 7.1 the raw signals from the ADCs are displayed for the KLY, INC, TRA, and REF channels for a normal (Type 3) pulse. It was previously discussed that all of the X-band test stands at CERN use a RF pulse compressor. It can be observed that INC is not square in nature, the result of using a pulse compressor, and therefore the pulse has no clear start and finish. A strong rise in the INC waveform at ∼1.25 μs initiates the RF pulse which continues with a constant amplitude before dropping significantly at ∼1.32 μs. This region ($t_r < t < t_f$) is defined as the useable RF pulse where beam could be injected. After the pulse passes ($t_f < t$), the waveform continues with a distinct decaying profile. This part of the waveform is the discharge of the remaining energy stored within the pulse compressor. Returning to the useable RF pulse region ($t_r < t < t_f$), the pulse

length (τ) is defined as:

$$\tau = t_{\mathrm{f}} - t_{\mathrm{r}}, \tag{7.4}$$

where the t_{f} is the 10% falling edge of the pulse and t_{r} is the 90% rising edge of the pulse. Using these values, the mean pulse amplitude is defined as:

$$\bar{\mathrm{A}}_{\mathrm{INC}} = \frac{\int_{t_{\mathrm{r}}}^{t_{\mathrm{f}}} \mathrm{A}_{INC}(t)dt}{t_{\mathrm{f}} - t_{\mathrm{r}}}. \tag{7.5}$$

Through a calibration procedure, the ADC data value was converted into an accelerating gradient. Fitting the ADC counts to the input power from a known RF source, using a quadratic equation, produced a calibration curve. This gave the input power in terms of the mean pulse amplitude, such that:

$$P_{INC} = 10^{P_{loss}/10}(C_2\bar{A}_{INC}^2 + C_1\bar{A}_{INC} + C_0), \tag{7.6}$$

where C_0, C_1, and C_2 are the second-order polynomial fit coefficients and P_{loss} accounts for power losses between the directional coupler and ADC. Converting the power into a gradient required information from the RF design [36]. The gradient was calculated using the following equation:

$$G[\mathrm{MV/m}] = 100\sqrt{\frac{P_{\mathrm{INC}}}{P_{\mathrm{INC\ at\ 100\ MV/m}}}}, \tag{7.7}$$

where $P_{\mathrm{INC\ at\ 100\ MV/m}}$ is the power required to generate a 100 MV/m unloaded accelerating gradient within the structure. This factor is proportional to the shunt impedance found in Equation 3.22 and is dependent on the cell geometry.

7.1.3 RF Breakdown Analysis

Identifying the location and properties of RF breakdowns was key to understanding the behaviour of the accelerating structures and their test stands. The analysis of the structure behaviour was only interested in breakdowns which occurred within the structure though not all saved events were of this nature. Events which could be saved by the Xbox system included:

- RF breakdowns within the structure.
- RF breakdowns within the waveguide network including pulse compressor and load.
- False breakdowns caused by operator setting an incorrect interlock threshold, or a new baseline dark current level caused by a breakdown event.

Before the analysis of the precise location of the breakdowns within the structure could be performed, the breakdowns were filtered into events inside and outside of the structure. Taking the breakdowns within the structure, false breakdowns were removed using a missing energy procedure which will be discussed further below.

Breakdown Filtering from Hardware Flags

Finding the approximate location of a breakdown within the waveguide network was performed through investigating the interlock flags tripped during the event. A breakdown flag is a logic value which describes whether a threshold had been exceeded during the event. When the event data was saved, a list of possible breakdown flags was included in the file with a binary on/off description of their status. In Section 4.2 it was discussed that during a breakdown event the RF power is reflected from the location of the breakdown. This results in the reflected signal in directional couplers upstream of the breakdown event (towards the klystron) increasing in comparison to non-breakdown events. Table 7.2 describes the location of a breakdown identified by the furthest downstream breakdown flag to be tripped. As an example a breakdown between the waveguide couplers PS and PL will reflect the RF power towards the PL and PK which is further upstream (refer to Figure 5.3 for the directional coupler locations).
For breakdowns within the accelerating structure, a large transient current can be expelled during the breakdown event for $\sim 1\mu$s which subsequently arrives at the upstream and downstream Faraday cups [76]. Such an increase in current was used as another trigger for identifying RF breakdown events and therefore was included in the filtering process. It was found that this trigger was important to identify RF breakdowns at the end of the RF pulse where reflected power diminishes to the point where it can not be used to trip a threshold. Given these two factors, a breakdown was considered to be within the structure given the condition that there was a triggering of the breakdown flags of the Faraday cups or PSR, and there was no trigger for PER. This can be written as:

$$\mathrm{BD}_{structure} = (DCDown_{flag} \vee DCUp_{flag} \vee PSR_{flag}) \wedge \neg PER_{flag}, \tag{7.8}$$

Table 7.2: Breakdown location identification through the furthest downstream breakdown flag tripped.

Furthest Downstream Flag tripped	Breakdown Location Between:
PSR_{flag}	PS and PE coupler
PLR_{flag}	PL and PS coupler
PKR_{flag}	PK and PL coupler
PER_{flag}	PE coupler and RF load

where $DCDown_{flag}$ and $DCUp_{flag}$ are the downstream and upstream Faraday cup breakdown flags, PSR_{flag} and PER_{flag} are the reflected power breakdown flags for the PS and PE directional couplers, and $\vee$ and $\wedge\neg$ are the boolean logical operators 'or' and 'and not', respectively. This condition however was not able to identify whether a breakdown was caused by a false trigger, therefore further filtering was required.

Breakdown Filtering through Missing Energy

As previously discussed, an RF breakdown causes a reflection of the RF power. Given this, it was anticipated that there will be energy missing from the transmitted RF pulse during a breakdown event and more energy present in the reflected signal. This was used to identify normal pulses misidentified as breakdown pulses. As a first step, the energy within each waveform was defined. The RF pulse energy was given as:

$$E = \int P \; dt, \tag{7.9}$$

where P is the signal power. A subscript was used to denote the channel name. Using the waveform energy, two metrics were defined to describe energy transmission (E_{TRA}) and reflection (E_{REF}) during a breakdown event, each of which are normalised to the input energy (E_{INC}). The first metric, which defines the normalised energy reflected from the structure, was defined as:

$$E_{Norm.REF} = \frac{E_{INC} - E_{REF}}{E_{INC} + E_{REF}}. \tag{7.10}$$

Similarly the second metric, which defines the normalised transmitted energy through the structure, was defined as:

$$E_{Norm.TRA} = \frac{E_{INC} - E_{TRA}}{E_{INC} + E_{TRA}}. \tag{7.11}$$

These two metrics were used to identify false breakdowns. Figure 7.2 demonstrates the two metrics plotted against each other for a single day of high power operation, although the values have not been calibrated. If the normalised reflected and transmitted pulse energy was similar to that of a Type 3 pulse, the event was tagged as a possible false breakdown and analysed manually.

Time-of-Propagation Method

Locating the position of RF breakdowns within the structure was crucial in understanding the performance of an accelerating structure. The most popular method for locating breakdowns involves measuring the difference in the time of arrival of

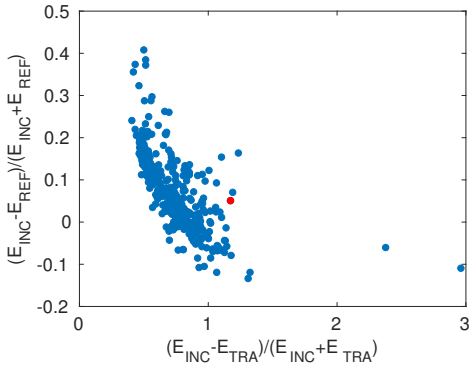

Figure 7.2: The normalised reflected energy (Equation 7.10) plotted against the normalised transmitted energy (Equation 7.11) for many breakdown events taken from a day of conditioning.

the rise and fall of reflected RF signals and transmitted signals, respectively during a breakdown event, which can be written as:

$$t_{TOP} = t_{R10} - t_{T90}. \tag{7.12}$$

In the case of the reflected signal, this is taken as the 10% deviation of the reflected signal (t_{R10}). Similarly, in the case of the transmitted signal, this signal is the 10% fall of the transmitted signal (t_{T90}). The 10% deviation value was chosen for two reasons. Firstly, this deviation level keeps the analysis in line with established conventions for using this analytical technique and secondly to prevent the misidentification of deviation points due to pulse-to-pulse variation in the RF signal. The method of identifying the location of a breakdown, using this time-of-propagation (TOP) difference, is illustrated in Figure 7.3 [77]. For the case of a breakdown at the beginning of the structure, the reflection would be measured almost instanta-

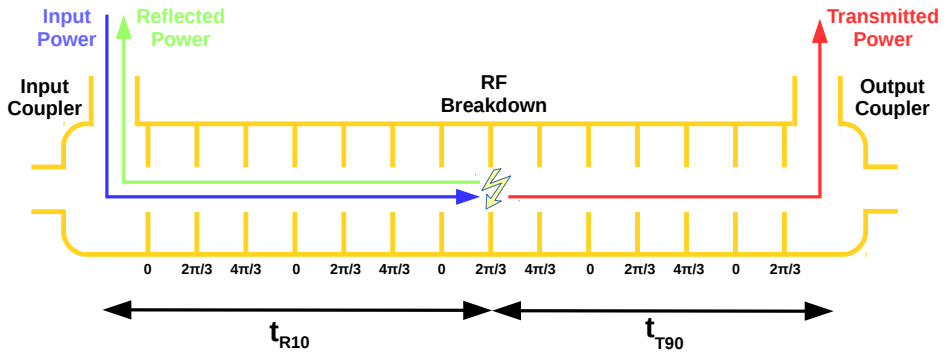

Figure 7.3: An illustration of the method of measuring the breakdown location. Two methods are used to accurately determine the breakdown location. The first measures the time-of-propagation difference of t_{R10} and t_{T90}. With the values of t_{R10} and t_{T90}, the phase advance of the reflected RF signals indicates the relative position of a breakdown to a repetitive cell region (three cells for CLIC).

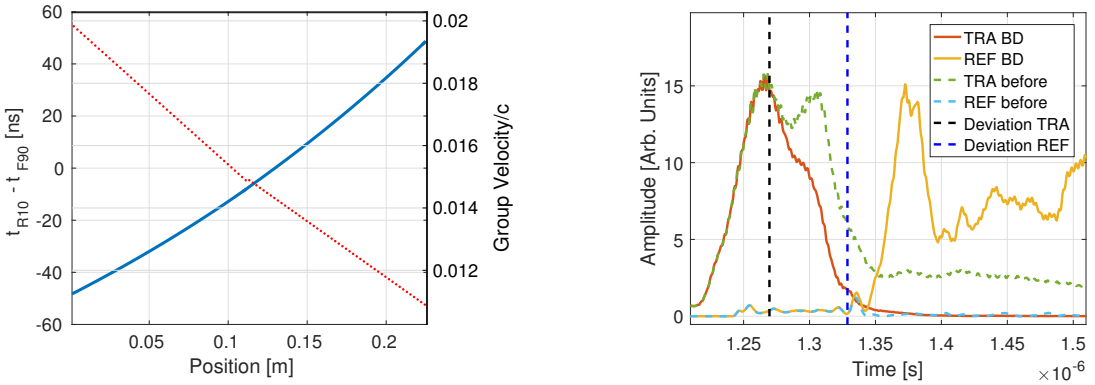

(a) Translation function.

(b) Deviation point.

Figure 7.4: Breakdown location methodology used in the analysis. The left-hand plot illustrates the translation function (blue, left y-axis) for finding the position in the structure (x-axis). This is calculated using the group velocity profile (red dashed, right y-axis) similarly plotted against the position in the structure. The right-hand diagram displays the reflected (solid, red) and transmitted (solid, yellow) RF signals for a breakdown pulse and reflected (dashed, green) and transmitted (dashed, cyan) RF signals for the pulse prior. These are plotted against time on the x-axis. The two dashed vertical lines illustrate the points where the reflected (blue) and transmitted (black) deviated from the RF signal of the previous pulse, as calculated by the analysis code.

neously while the transmitted signal would take the t_{fill} to propagate through the structure. For the contrast situation of a breakdown at the end of the structure, the transmitted signal in this case would be measured with minimal delay while the reflection would take t_{fill} to propagate back to the beginning of the structure. The time taken to propagate between the structure and the waveguide is ∼1 ns and disappears from Equation 7.13, given that it is a differential. Therefore t_{TOP} is found to have the boundary conditions of $t_{TOP} = [-t_{fill}, t_{fill}]$. The tapering of the irises is used to create a constant gradient in accelerating structures, as had been discussed in Section 3.5, but as a result the group velocity varies along the structure. The structure profile of the group velocity was well known through RF simulations and this allowed the measured time-of-propagation differential to be converted into a location within the structure (Figure 7.4a). The translation from time-of-propagation difference to a location within the structure was found by integrating over the group velocity profile, written as:

$$t_{R10} - t_{T90} = l_{cell}\left(\sum_{0}^{n_{BD}} \frac{1}{v_g(n)} - \sum_{n_{BD}}^{N} \frac{1}{v_g(n)}\right), \tag{7.13}$$

where l_{cell} is the cell length, $v_g(n)$ is the group velocity in cell n, N is the total number of cells in the structure, and n_{BD} is the number of cells between the start of the structure and the breakdown event [78]. The relation to translate the time-

of-propagation difference into a physical location within the structure is presented in blue in Figure 7.4a.

Accurately determining the location of the falling/rising edge was key to precisely locating the breakdown location. During normal pulsing without a breakdown, imperfections in the reflected and transmitted RF signals were present in the measured signals. An example of which is found in the REF signal at $\sim 1.25 \times 10^{-6}$ s in Figure 7.4b. There was a concern that these imperfections may be misidentified as a rise or drop in power caused by a breakdown, and lead to an incorrect calculation of the breakdown location. Using the pulse prior to the breakdown (Type 2) the steady-state reflections were able to be accounted for. The location of the breakdown was therefore determined from where the RF signal of the breakdown pulse deviated from the RF signal of the prior pulse (Figure 7.4b). A simple algorithm fitting the rising edge of the transmitted pulse allowed the time jitter between the pulses to be minimised.

Phase Differential

A means to improve the accuracy of locating breakdowns was to measure the phase information of the input RF signal and reflected signal during the breakdown event. By measuring the difference in RF phase of the INC (ϕ_{INC}) and REF (ϕ_{REF}) signals at the rising edge of breakdown signal, and aligning the signals accounting for expected delays (t_d), a relative breakdown location (ϕ_{BD}) is given by [78]:

$$\phi_{BD} = \langle \phi_{REF}(t + t_d) - \phi_{INC}(t) \rangle. \tag{7.14}$$

As the RF propagates through the structure, there is a phase advance of $\Delta\varphi$ for each cell. Consequently the phase difference of the RF signal, for the return trip

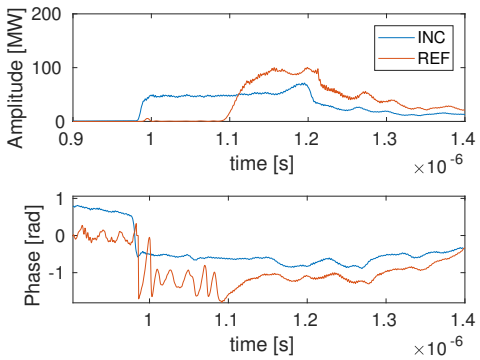

Figure 7.5: The waveforms for the amplitude in MW and the phase in radians of the incoming (solid, blue) and reflected (solid, red) RF signals plotted against time for a breakdown event.

from the input coupler to the breakdown site, can be written as:

$$\phi_{BD} = 2\Delta\varphi \cdot n_{BD} + \phi_0. \tag{7.15}$$

where n_{BD} is the number of cells between the start of the structure and breakdown event, and ϕ_0 is the initial phase [78]. For CLIC structures, which have a phase advance per cell value of $\Delta\varphi = 2\pi/3$, the measured value of ϕ_{BD} is periodic in nature, repeating every three cells. An example of this is illustrated in Figure 7.3. In Figure 7.5 the amplitude and phase of the INC and REF signals are illustrated for a breakdown event, accounting for time delays. At the rising edge of the REF amplitude, $t \approx 1.1\mu$s, it can be observed that the difference between ϕ_{INC} and ϕ_{REF} asymptotes to the value of $\Delta\varphi$. This demonstrates that the amplitude of the RF signal modulates the phase signal which was accounted for when measuring ϕ_{BD}.

Phase Difference vs Time-of-Propagation

Achieving cell-by-cell resolution was performed through combining the time-of-propagation method with the phase difference method. Plotting these two variables against one another expanded the certainty boundaries for a breakdown's location from one cell to a three cell region [78]. This method also gave insight into the phase advance for each cell within the structure, which was used to understand the tuning of the accelerating cells.

7.1.4 Code Development

Using the analytical and signal processing tools presented in the preceding sections, a programme was developed for the analysis of structures tested on Xbox 2 whilst Xbox 3 was undergoing commissioning. This programme was subsequently generalised to be used on Xbox 3. Early versions of the programme repeated the analysis on each compilation which was deemed inefficient. It was decided that the programme would be more efficient if the waveform analysis was performed only once and created an analysed file which could be used subsequently by a separate plotting programme. The final analysis consisted of three separate programmes, each of which are briefly explained below and detailed in a diagram in Figure 7.6:

1. **Make Matfiles**: Converted the TDMS files output from the labview software controlling the PXI crate to a Matlab binary file (MAT-file).

2. **Day Analysis**: Analysed the data from the date(s) selected by performing the analytical techniques discussed in this section. This analysis could be chosen to operate in automatic mode or manual mode. The manual mode allowed the user to verify the deviation points, discussed in Figure 7.4b, for each breakdown waveform and also examine the phase difference. After the

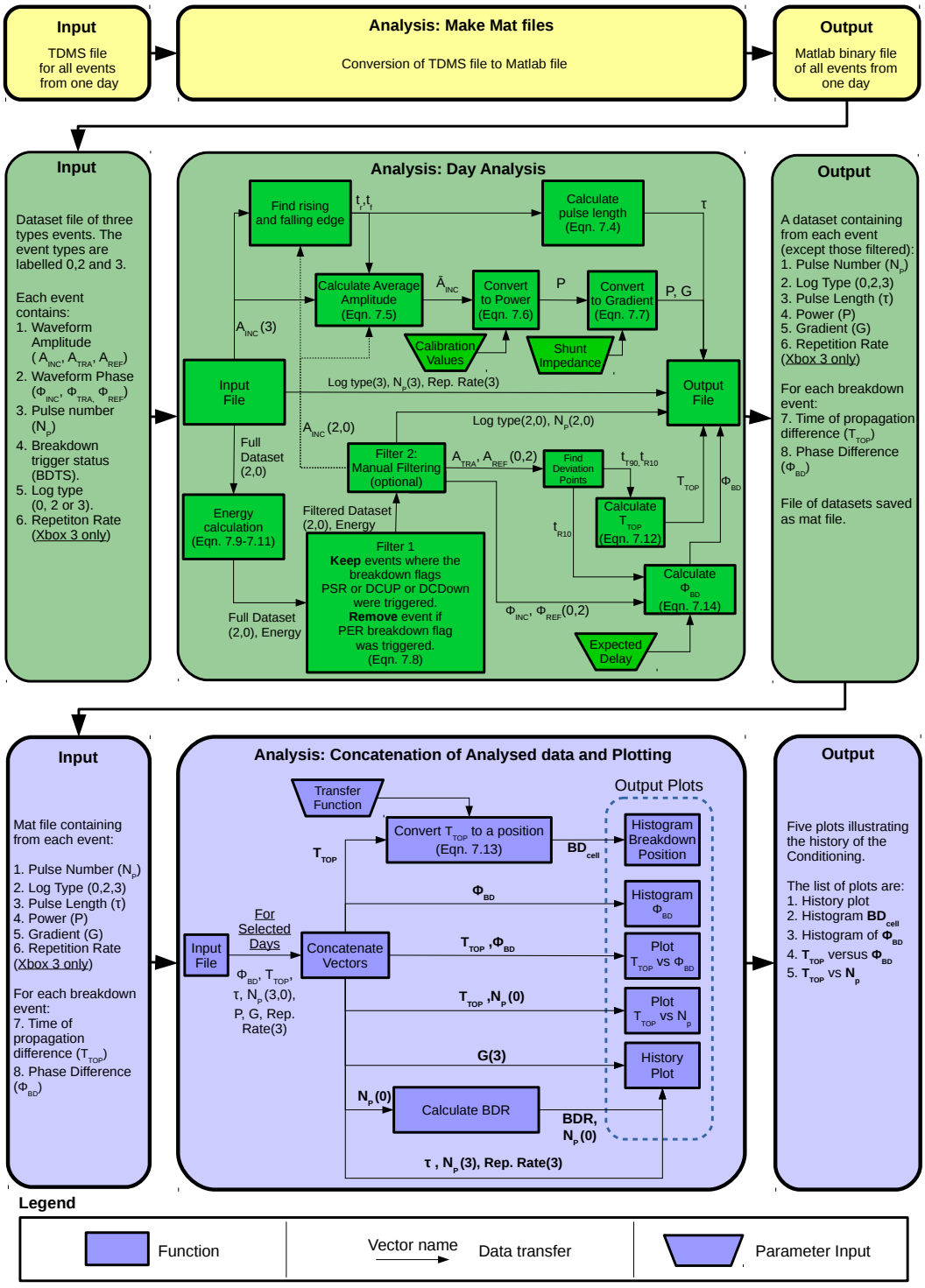

Figure 7.6: A diagram summarising the analysis codes written for Xbox 2 and 3. The analysis consisted of three codes: Make Matfiles (yellow), Day Analysis (green), and Concatenation of analysed data and plotting (blue). Each analysis code is split into three boxes. The left-hand boxes represent the input files, the middle boxes are the analysis code and the right-hand boxes are the output. Bolded vector names indicate a concatenation of numerous days and bracketed numbers indicate a subset based on log types.

automatic or manual analysis was performed, this programme produced a file for that day of high power testing which contained the time-of-propagation and ϕ_{BD} values for each breakdown which occurred during the day. The gradient and pulse length measurements for all waveforms were also included.

3. **Concatenation of analysed data and plotting**: Connected the data from the file output from the Day Analysis code and plotted the selected variables against one another. The time-of-propagation values were converted into physical position using a transformation function created uniquely for each accelerating structure design (refer to Equation 7.13).

These programmes were used for the analysis of the high power performance of several accelerating structures between 2015 and 2018. The following sections summarise the results from the testing performed on four structures. The high power testing in Sections 7.2 and 7.3 were performed using Xbox 2 while the high power testing in Sections 7.4 and 7.5 were performed on the newly commissioned Xbox 3.

7.2 CLIC Base-Line Design

In the CLIC rebaseline design, an RF design for the CLIC baseline structure was included in the submission [15]. With 26 regular cells and two coupling cells, this design is longer than its predecessors. The TD26CC R05 N3 has the tapered iris profile present in all 12 GHz CLIC designs though the mode launcher input couplers had been replaced with a compact coupler (CC) design. The aim of which was to reduce the length of the non-accelerating section of the structure [79, 91]. TD26CC R05 has the addition of HOM damping waveguides although the three prototypes were not built with the silicon carbide (SiC) HOM damping material. For the purpose of the machining, the cell edge has a rounding profile with a 0.5 mm diameter (R05). The aim of testing this prototype was to determine the effects of the compact couplers and investigate whether this longer and more complex RF design could reach 100 MV/m. This section is a review of the high power testing and subsequent postmortem analysis of the TD26CC R05 N3. This work was published in reference [66] which is included in its entirety in Appendix C.

7.2.1 Conditioning History

The TD26CC R05 N3 structure was installed on the Xbox 2 test stand (Figure 7.7). The conditioning history is depicted in Figure 7.8 which will be referred to throughout the entire high power testing history described below. Conditioning began with a short RF pulse length (red) of 70 ns, the BDR limit of the conditioning algorithm

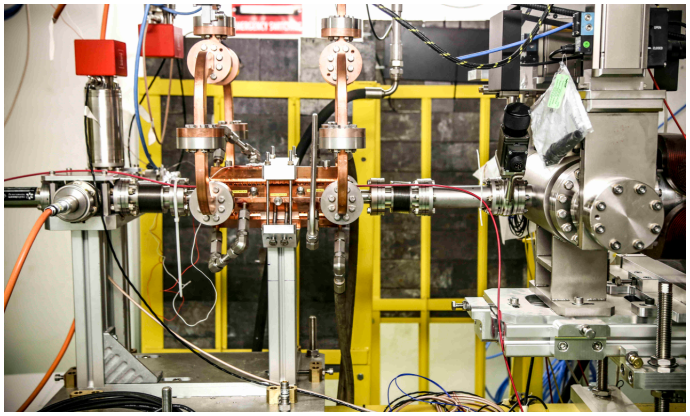

Figure 7.7: Photograph of the TD26CC R05 N3 installed on Xbox 2 [66].

was set to 8×10^{-5} breakdowns per pulse (bpp) for 50 million pulses after which the structure had reached an unloaded accelerating gradient (blue) of 60 MV/m. It was found that this BDR limit led a large variance in the BDR (magenta). This was assumed to be undesirable for the accelerating structure and the BDR limit was reduced to 3×10^{-5} bpp, clearly visible as a reduction in the slope of the cumulative breakdowns (black). Continuing to condition, the structure reached 105 MV/m after 300 million pulses. Investigations into the rate of conditioning revealed an uncharacteristically linear behaviour which was later found to be the result of the conditioning algorithm retarding the structure's progress [57].

At 105 MV/m, and just above 300 million pulses, the safe limit of radiation outside the test bunker was exceeded and temporarily prevented further increases to the power. This radiation resulted from dark current in the structure, discussed thoroughly in Chapter 6. During these periods where the gradient was limited, a

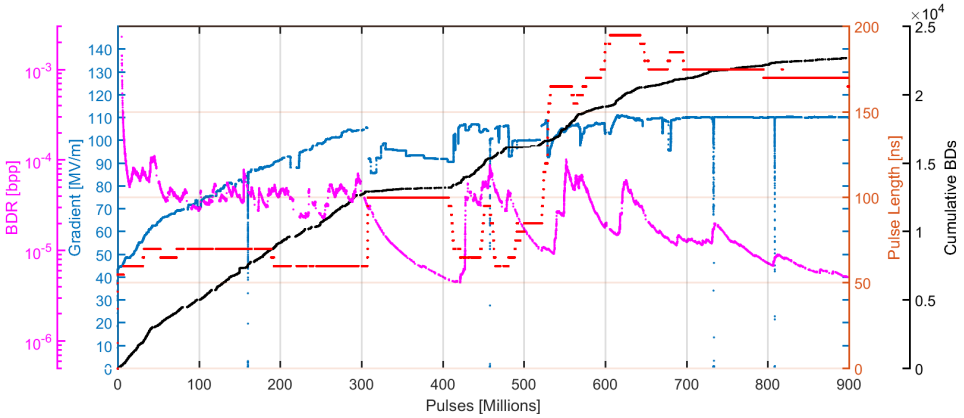

Figure 7.8: The entire high power conditioning history of the TD26CC R05 N3 tested using Xbox 2. The plot depicts the gradient in MV/m (blue), the pulse length in ns (red), the cumulative breakdowns (black) and the breakdown rate in bpp (magenta) plotted against the total number of pulses [66].

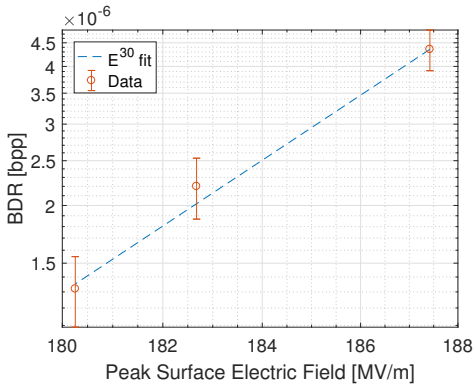

Figure 7.9: Measurements of the breakdown rate in bpp plotted against the peak surface electric field in MV/m. The theoretical dependence of BDR $\propto E^{30}$ is included (blue, dashed) [66].

measurement of the BDR's dependence on the surface electric fields, proportional to the accelerating gradient, was performed. During these measurements, the pulse length was increased to 100 ns which in accordance with Equation 4.6 should increase the BDR therefore improving statistics. Scanning through peak surface electric field values of 187.5 MV/m followed by 182.6 MV/m and 180.25 MV/m, the measured BDR dependence is displayed in Figure 7.9. Previous tests had found a dependence of E^{30} which fits well within the error bars of the measured values [45, 66].

At 415 million pulses into the high power testing, the radiation shielding was reconfigured as to better shield the Faraday Cup, as was discussed in Section 6.3.1. This reconfiguration of the shielding allowed the structure to resume its conditioning towards higher accelerating gradients with the RF pulse parameters set to those used at ∼300 million pulses. Between 415 and 500 million pulses, the structure was conditioned up to an unloaded gradient of 107 MV/m, at which it was found that a reflection from the structure caused an undesirable peak in the flat top of the RF pulse. As was discussed in Section 5.3.2, this peak was caused by a reflection of the RF power into the klystron while it was still generating the pulse. Therefore this phenomenon only occurred once the pulse length was greater than the RF propagation time from the klystron to the structure, and back. The power also had to be great enough that the reflected power was comparable to that generated by the klystron. A change to the phase profile allowed the pulse amplitude to be flattened. At 540 million pulses, a new pulse length and shape were established to flatten the pulse by reducing the reflection from the start of the accelerating structure. Up to 600 million pulses, the structure operated with a "CLIC-like" pulse shape which featured a power ramp of 60 ns at the start of the pulse and a 160 ns pulse flat top [80].

At 600 million pulses, the structure was increased to a 200 ns pulse length and operated with the undesirable peak in the otherwise flat pulse. Further conditioning

of the structure allowed it to be operated at up to 113 MV/m although an excess of breakdowns at the beginning of the structure was observed. This will be discussed further in the breakdown distribution analysis in the next section [66]. From 650 to 700 million pulses, the pulse shape was reconfigured to a CLIC pulse. Detailed in [80], this RF pulse shape configuration has a total pulse length of 240 ns made up of a 180 ns flat-top and 60 ns power ramp at the beginning of the RF pulse. For an accelerating structure with a high beam current, the CLIC pulse acts as a 240 ns flat pulse which has the gradient of that at the beginning of the 60 ns ramp. This results from beam-loading where the total RF power is reduced by fields induced by the beam [80]. The ramp in the RF power at the start of the CLIC pulse aims to compensate for a reduced beam-loading experienced by the structure when the bunch train first enters the structure. For a structure without beam, such as that on Xbox 3, the CLIC pulse will act similar to an RF pulse of 180 ns in length with a gradient equal to the flat-top of the CLIC pulse. This is expected because the BDR has a strong dependence on the field strength (Equation 4.6) and therefore the contribution to the BDR caused by the lower gradient initial ramp is expected to be minor. This allowed testing with the nominal CLIC pulse shape and also removed the undesirable peak in the pulse caused by the reflection. Setting the unloaded gradient to a constant 110 MV/m, the structure's conditioning was continued with the intention of reducing the BDR for the last 200 million pulses. A small change in the pulse length occurred at 800 million pulses as a consequence of a reconfiguration of the phase control after a power outage. At the end of conditioning, the TD26CC R05 N3 had reached 110 MV/m with 170 flat top and a BDR of 2×10^{-5} bpp/m, which is the highest gradient achieved on a HOM damped CLIC structure.

7.2.2 Breakdown Distribution

An analysis of the breakdown distributions revealed further information about the performance of the accelerating structure. Found using the time-of-propagation method and transformation formula given by the group velocity profile, Figure 7.10a depicts the normalised breakdown distribution within the structure plotted against the cell number. A distribution with an almost homogeneous spread of breakdowns demonstrated the field flatness of the structure, as the breakdowns are expected to occur more frequently in regions of greater surface electric field strength [47, 45]. A small excess of breakdowns was measured at the start of the structure requiring further investigation. To understand this excess of breakdowns at the start of the structure, the time-of-propagation distribution was plotted against the number of pulses of conditioning (Figure 7.10b). For the first 300 million pulses of conditioning, the breakdowns were evenly distributed across the structure. From 300 to 415 million pulses, the structure operated at a reduced power due to the radiation constraint consequently few breakdowns occurred. After 415 million pulses, the

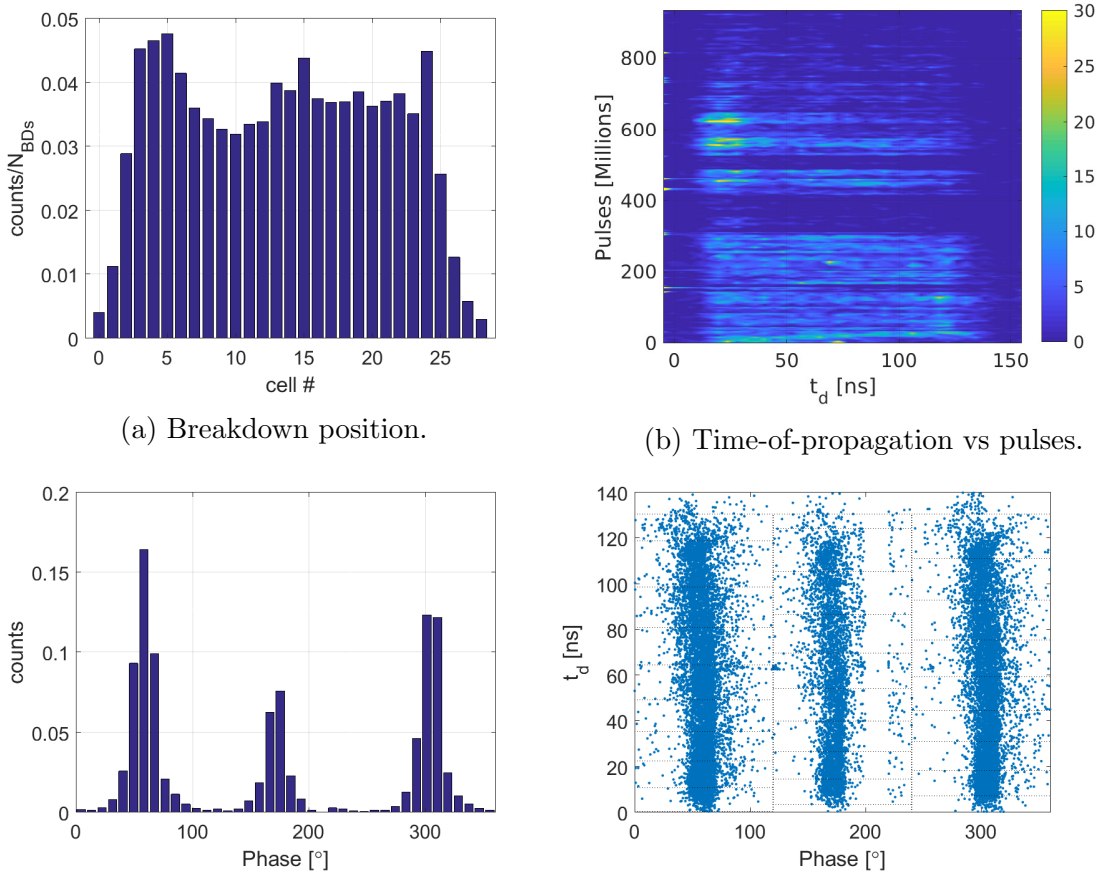

(a) Breakdown position.

(b) Time-of-propagation vs pulses.

(c) ϕ_{BD}.

(d) Time-of-propagation vs ϕ_{BD}.

Figure 7.10: Breakdown distributions for the TD26CC R05 N3 structure for the conditioning on Xbox 2. The top-left figure depicts a histogram of the breakdown locations across the structure where the ratio of breakdowns is plotted against the cell number. The top-right figure illustrates the evolution of these breakdowns' locations over the conditioning by plotting the time-of-propagation value, in ns, against the number of pulses, and displaying it as a density map. The colour map illustrates the density of breakdowns in the area during that period of conditioning. The bottom-left figure displays a histogram of the phase difference for the breakdowns during the conditioning by plotting the ratio of breakdowns against the phase difference, in degrees. The bottom-right figure plots the breakdown position within the structure, expressed as a time-of-propagation in ns, against the phase difference of the breakdown in degrees [66].

structure continued conditioning, along another power reduction was required at 475 million pulses. Resuming the conditioning after 540 million pulses, the gradient was increased to the 113 MV/m which resulted in an excess of breakdowns at the start of the structure. A reduction in gradient reduced the total number of breakdowns though they continued to predominantly occur at the input of the structure. These results led to the conclusion that once the input gradient affected the breakdown distribution, the previous distribution is unlikely to be recovered even with a field reduction.

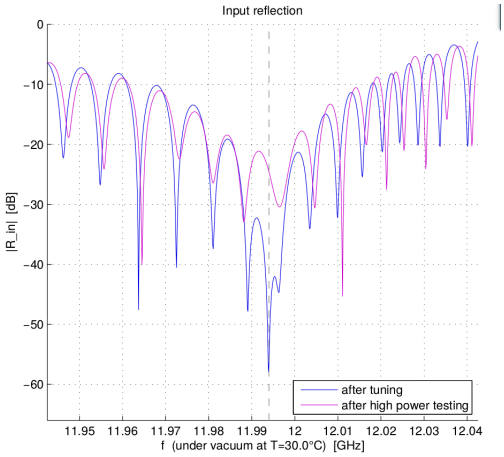

(a) S11 from input coupler.

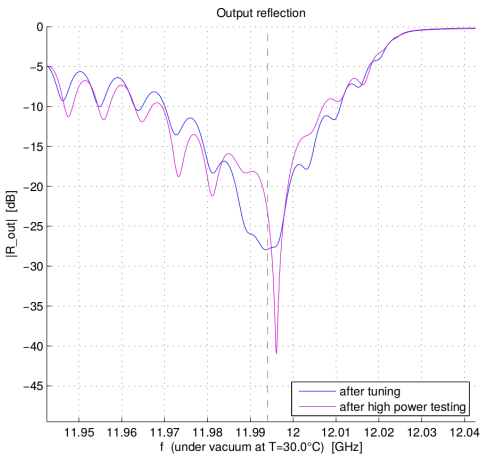

(b) S11 from output coupler.

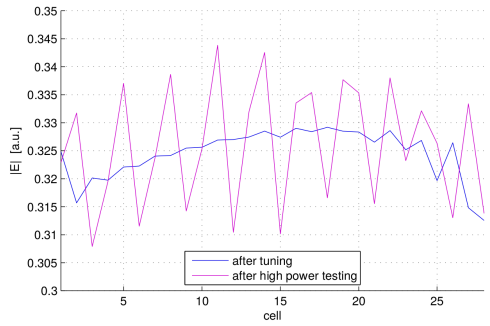

(c) Electric field amplitude distribution.

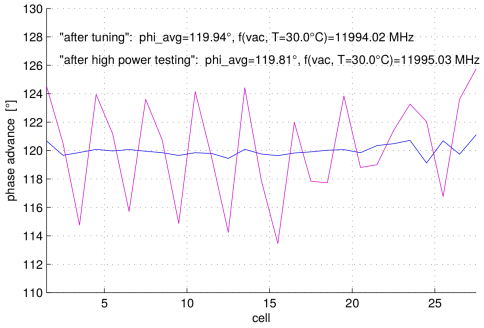

(d) Electric field phase distribution.

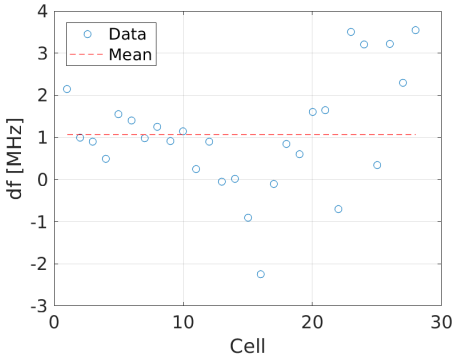

(e) Detuning per cell.

Figure 7.11: RF testing of the structure before and after high power testing on Xbox 2. The top two plots illustrate the reflection from the input and output couplers in dB plotted against the RF driver frequency in GHz, for before (blue) and after (magenta) high power testing. The middle two plots depict the amplitude, in arbitrary units, and phase advance, in degrees, of the electric field along the structure plotted against the cell number for before (blue) and after (magenta) high power testing. The bottom plot illustrates the frequency detuning of each cell due to high power testing by plotting the change in frequency, in MHz, against the cell number. The mean detuning for the structure is illustrated with a horizontal dashed red line [66].

Investigations into the ϕ_{BD} distribution found the three peaks separated by $\sim 120°$. This is commonly observed for CLIC accelerating structures and is indicative of breakdowns occurring predominantly on the iris of each cell (Figure 7.10c) [77]. Figure 7.10d displays the time-of-propagation plotted against ϕ_{BD} where three vertical clusters are visible which feature a small curvature. Three perfectly vertical clusters separated by 120° are indicative of a perfectly tuned structure and therefore this curvature is associated with cell detuning, which may occur from high power operation [77].

7.2.3 Post-Test Analysis

For long term operation of the accelerating structures, it is important to understand changes in the RF properties which may result from high power operation. After the structure had completed its high power testing it was removed from the test stand and taken for testing of its RF properties. In Figures 7.11a and 7.11b, the reflection from the input and output ports, respectively, are displayed before (labelled "after tuning") and after high power testing. Before high power testing, the structure was observed to be well tuned to the operational frequency of 11.994 GHz with a reflection from the input coupler of -58 dB. After the high power testing, the reflection at the operational frequency can be found to increase significantly to -26 dB. Using a non-perturbative bead-pull method, the cell detuning due to high power could be determined. Figure 7.11e illustrates an average frequency change of $\sim$1 MHz (corresponding to $\sim 1°$ in phase advance) [73]. Such significant detuning resulted in a clear change in amplitude and phase of the electric field profile, presented in Figures 7.11c and 7.11d. The variance of the field amplitude and phase was observed to increase after high power testing. It has been previously observed that field profiles of structures have changed after high power testing and this provides further evidence supporting the detuning of structures due to high power operation.

7.3 Structure Fabricated From Milled Halves

Based on the RF design of the CLIC-G (T24), which had been tested at high gradients and low BDR [9], the CLIC-G Open was designed and manufactured to investigate novel fabrication techniques. As an alternative to individual disks, which uses precision turning and milling, the CLIC-G Open was fabricated through the milling of two structure halves (Figure 7.12). This novel accelerating structure design built upon previous work of an accelerating structure made from quadrants [81], as well as the PETSs for CLIC's drive beam facility which are constructed from octants [9, 67]. The new assembly technique offered a number of advantages in comparison to traditional disk-based structures which were the motivation of this study. Particularly notable are: a reduction of the number of precision pieces, freedom of choice in

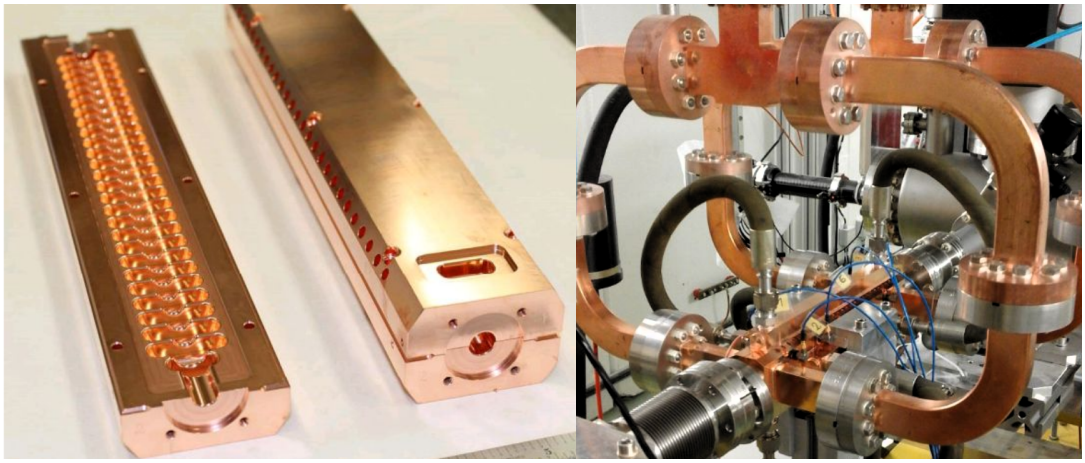

(a) Prototype Fabricated. (b) Installed on Xbox 2.

Figure 7.12: Photographs of the CLIC-G Open structure [67].

joining since there are no RF currents flowing through the metal-to-metal joint, the use of the unique geometry for higher order mode damping, and an overall reduction of the total manufacturing cost. The following high power conditioning and postmortem analysis was published as part of reference [67] which can be found in its entirety in Appendix C.

7.3.1 High Power Testing

Figure 7.13 summarises the history of the structure's high power testing. At the beginning of the conditioning process, the BDR (magenta) was kept at a constant 5×10^{-5} breakdowns per pulse (bpp). Once reaching an unloaded gradient of 95 MV/m (blue) at 150 million pulses, radiation emitted from the structure exceeded the

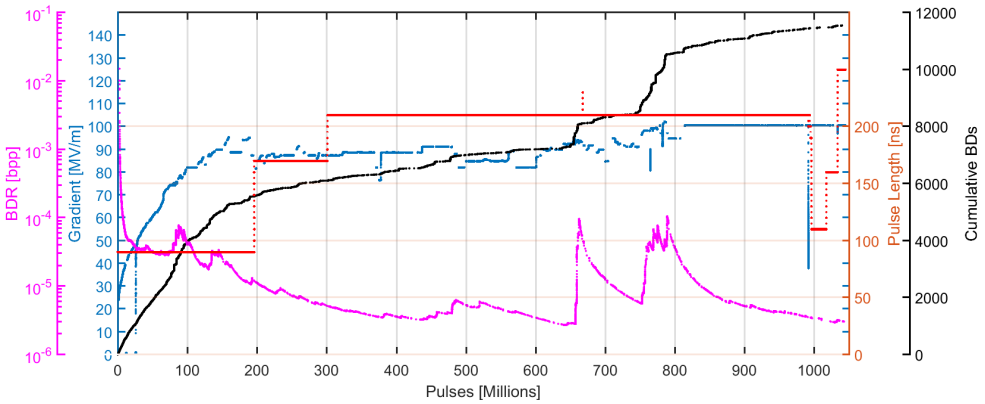

Figure 7.13: Conditioning history of the CLIC-G Open structure on Xbox 2. The plot depicts the gradient in MV/m (blue), the pulse length in ns (red), the cumulative breakdowns (black) and the breakdown rate in bpp (magenta) plotted against the number of pulses [67].

maximum safety limit outside the bunker. This was the first observation of radiation issues related to dark current and was the initial motivation for the work performed in Chapter 6. As the input power to the structure could not be increased until this issue was solved, the structure was pulsed with a reduced and constant gradient of 90 MV/m. This began at 150 million pulses with the first pulse length of 90 ns. During this period the structure continued to condition, demonstrated by the decreasing trend in the BDR visible up to 200 million pulses. Conditioning of the structure led to a reduction in radiation and allowed the pulse length to be increased to 160 ns at 200 million pulses, without surpassing the maximum radiation safety limit. From 300 million pulses onwards the final pulse length of 200 ns was set. Various experiments were performed investigating the relation between accelerating

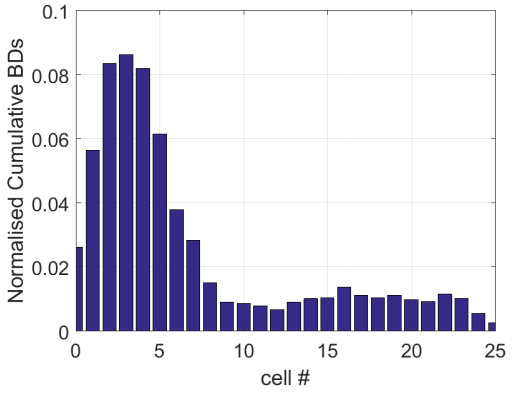

(a) Breakdown distribution.

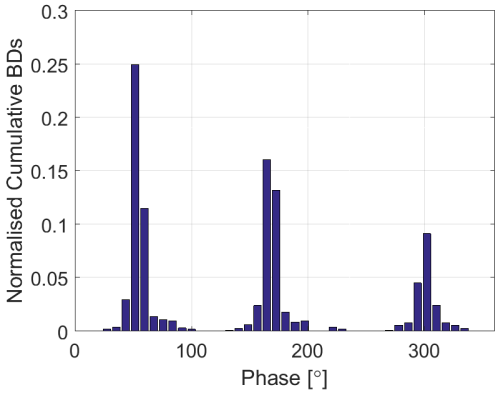

(b) ϕ_{BD}.

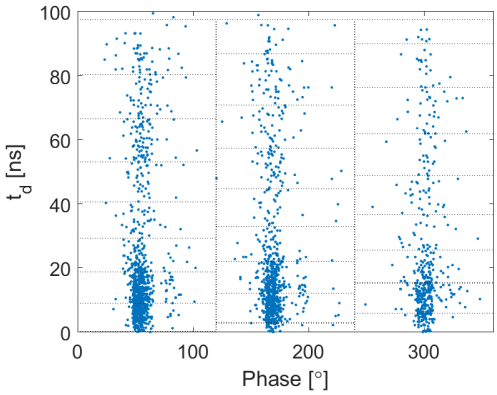

(c) Time-of-propagation vs ϕ_{BD}.

Figure 7.14: Breakdown distributions for the CLIC-G Open structure for the conditioning on Xbox 2. The top-left figure depicts a histogram of the breakdown locations across the structure where the ratio of breakdowns is plotted against the cell number. The top-right figure displays the histogram of the phase difference for the breakdown events where the ratio of breakdowns is plotted against the phase difference in degrees. The bottom figure plots the breakdown position within the structure, expressed as a time-of-propagation in ns, against the phase difference of the breakdown in degrees [67].

gradient and BDR, discernible by the steps in the gradient curve. Increased shielding on the bunker, applied after 600 million pulses, allowed the resumption of power increments towards 100 MV/m. After reaching the desired 100 MV/m at 800 million pulses, the structure was operated at a constant gradient and conditioned down to a low BDR. At 1.05 billion pulses, a BDR of $< 1.5 \times 10^{-5}$ bpp/m was achieved, at this point the structure conditioning was concluded. The achieved gradient of 100 MV/m with a 200 ns pulse is comparable to the gradient achieved by other CLIC prototype structures up to this time, demonstrating the validity of the fabrication technique.

7.3.2 Breakdown Distribution

After conditioning, the breakdown distributions were analysed to understand the limiting factors of the design [77]. Figure 7.14a displays the breakdown distribution in the CLIC-G Open after conditioning, translated into a cell number and normalised to the total number of breakdowns. Breakdowns occurred predominantly towards the first cells of the structure. Figure 7.14b depicts the ϕ_{BD} distribution which appeared in the typical three peaks separated by 120° the cause of which was discussed previously. Figure 7.14c illustrates the time-of-propagation plotted against ϕ_{BD} which describes a structure predominantly undergoing RF breakdown in a few adjacent irises at the input of the structure. Understanding this extreme inhomogeneity in the breakdown distribution will be key to improving the next iteration of a structure constructed from the milling of two halves.

7.3.3 Post-Test Analysis

After removing the CLIC-G Open from Xbox-2, the mildly radioactive structure was stored for several months where it remained in a nitrogen environment to prevent surface degradation. Figure 7.15 describes the structure's nomenclature and areas surveyed in the post-test analysis. To begin, S-parameter and bead-pull measurements were performed to evaluate the change in electric field profile due to the high power testing. In contrast to previous high gradient structures, the CLIC-G Open demonstrated nearly no change in the electric field distribution (amplitude and phase advance per cell) and only slight changes in the S-parameters for the input and output coupler, see Figure 7.16. Before the structure underwent cutting, a borescope was used to observe any visible physical damage. Pictures from the borescope revealed that the breakdown induced damage was towards the start of the structure (Figure 7.17). To allow closer examination the structure was cut using Electron Discharge Machining (EDM) and divided into several sections which included; two halves cut through the brazing material (Cut 1) for cells 1 to 13, two halves for cells 14 to 19 (Cut 2), and the rest of the structure remained intact. A

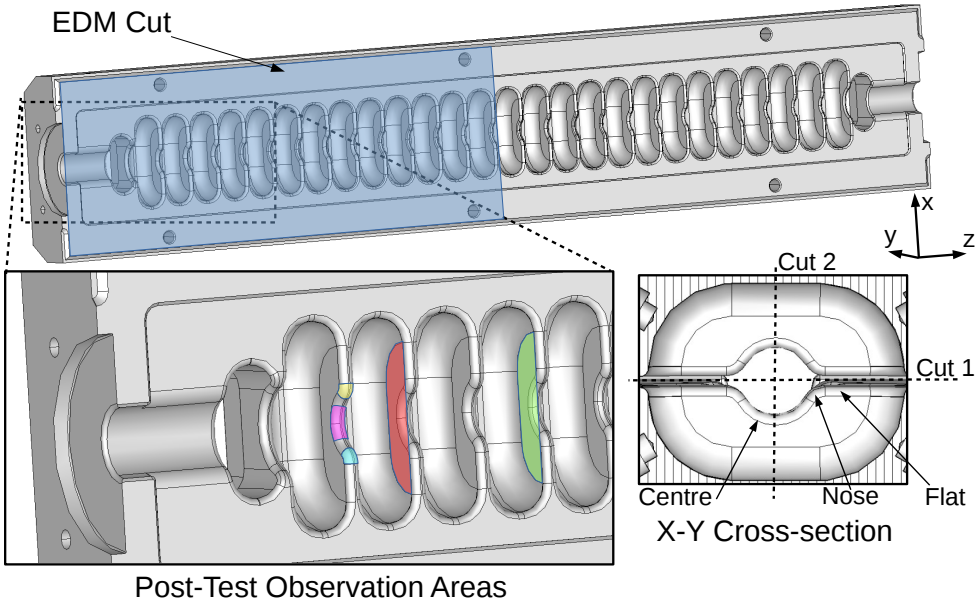

Figure 7.15: Diagram of a half of the CLIC-G open structure demonstrating the EDM cut in blue. Post-test observations with a borescope looked at the Iris 2 (red) and Iris 4 (green) before cutting. After cutting, SEM images of the first iris looked at the left (yellow) and right (cyan) nose, and the center (magenta). An X-Y cross-section demonstrating structure nomenclature [67].

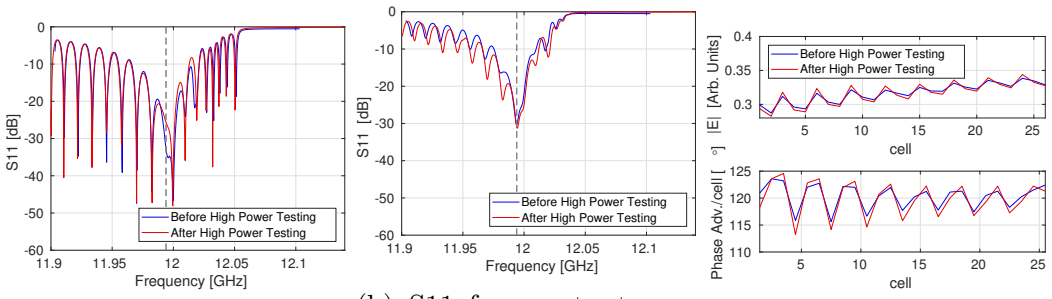

(a) S11 from input coupler. (b) S11 from output coupler. (c) E Field distribution.

Figure 7.16: A comparison of the RF parameters before and after high power testing. The left and middle plots illustrate the reflection from the input and output coupler, respectively, plotted in dB against the RF driver frequency in GHz for before (blue) and after (red) high power testing. The right-hand figure displays both the amplitude and phase advance of the electric field along the structure plotted against the cell number for before (blue) and after (red) high power testing [67].

photograph of the half section containing cells 1 to 13 is displayed in Figure 7.18. Marked in a blue box is an issue which came to light after the structure was cut. During the brazing procedure, the brazing alloy leaked from the joint into the RF region of the structure. This material reached within 200 μm of the cell edge. A scanning electron microscope (SEM) was used to analyse the effect of the leak on the structure performance. Images of the surface, shown in Figure 7.19, demonstrate the breakdown density on the centre and nose sections of the cell. Breakdowns oc-

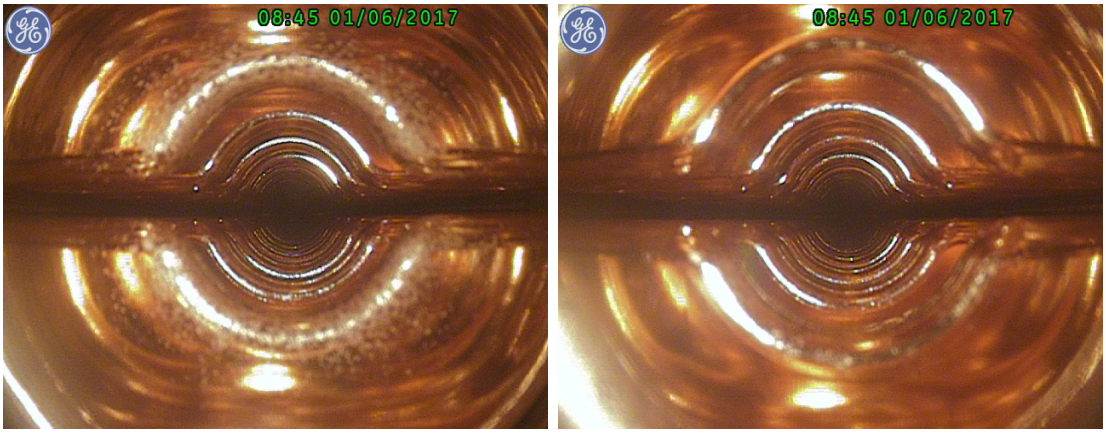

(a) Iris 2. (b) Iris 4.

Figure 7.17: Borescope images from the structure after conditioning. The location of the irises is described in Figure 7.15 [67].

curred primarily on the nose section with only a few visible marks on the centre section. Overlaying the surface E and S_c field profiles, it is found that the breakdowns are most likely to occur around the area with the greatest E or S_c. Due to the similarities of the field profiles, the exact cause of the breakdowns could not be determined. Comparing the breakdown densities of the two opposing nose sections demonstrated similar numbers for the two sided. Given this, it is found that the breakdowns' preference for the first few cells was not related to the brazing filler leak. In Section 6.3.2, sporadic jumps in the radiation were demonstrated to occur throughout the conditioning of a structure. These jumps were postulated to be the result of the RF breakdowns emitting molten copper leading to the formation of new emission sites. These SEM images of the iris illustrate the existence of these breakdown sites where the molten copper is visible around the edges of the craters.

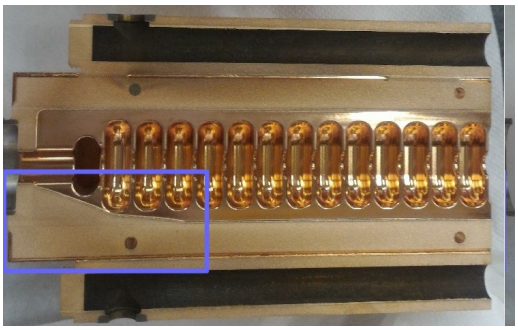

Figure 7.18: Leaked brazing material visible at the input of the structure circled in blue where the dull section is visible to overlap the corner [67].

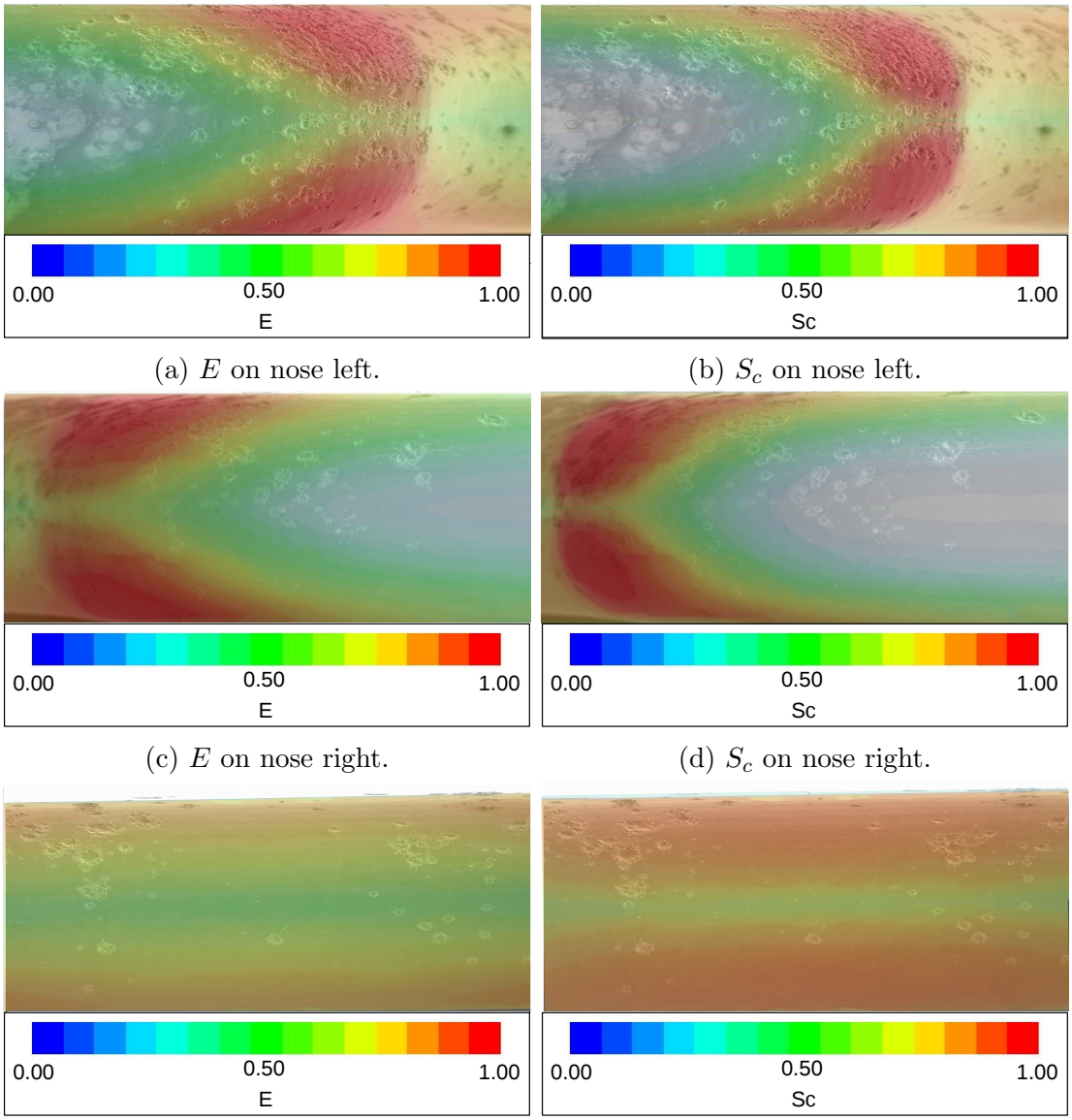

(a) E on nose left.

(b) S_c on nose left.

(c) E on nose right.

(d) S_c on nose right.

(e) E on centre.

(f) S_c on centre.

Figure 7.19: Scanning electron microscope images of various segments along the first iris. Overlaid is a field map of the surface electric field (E) and local power flow (S_c) for a comparison of the breakdown location to the field strength. The location of each scan is described in Figure 7.15 [67].

7.4 HOM Damped Structure with SiC

In comparison to the TD26CC R05 N3, the TD24 R05 SiC N1 (Figure 7.20) is an older CLIC RF design. Novel to this prototype is the addition of SiC HOM damping material [93]. The aim of testing this structure is to understand the behaviour of the SiC material within the HOM dampers at high gradients and to measure whether it affects operation at low BDRs.

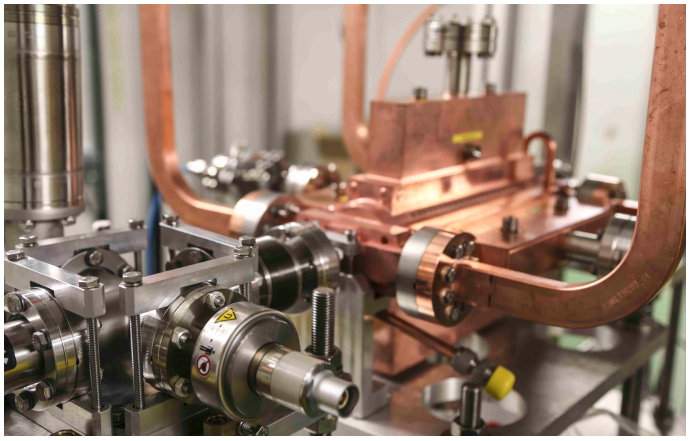

Figure 7.20: A photograph of the first structure installed on Xbox 3, the TD24 R05 SiC N1.

7.4.1 High Power Testing

The final stage of the commissioning of Xbox 3 was the addition of the accelerating structures. First to be tested was the TD24 R05 SiC N1 which was installed on Line 1 of Xbox 3. The complete high power conditioning history of this structure is illustrated in Figure 7.21 which will be referred to throughout the following description below. Conditioning began with a repetition rate of 150 Hz, which was the first time a CLIC structure had been tested at such a high repetition rate. At first, the structure appeared to be impeded in its conditioning given that in the first 200 million pulses the gradient reached only 45 MV/m. This conditioning rate was well below the rate previously observed on other accelerating structures. After an investigation into the rate of conditioning it was postulated that the conditioning algorithm was retarding the progress of conditioning, as discussed in Section 5.3.3. From 200 million pulses, the BDR limit was increased to 10^{-4} bpp, the conditioning

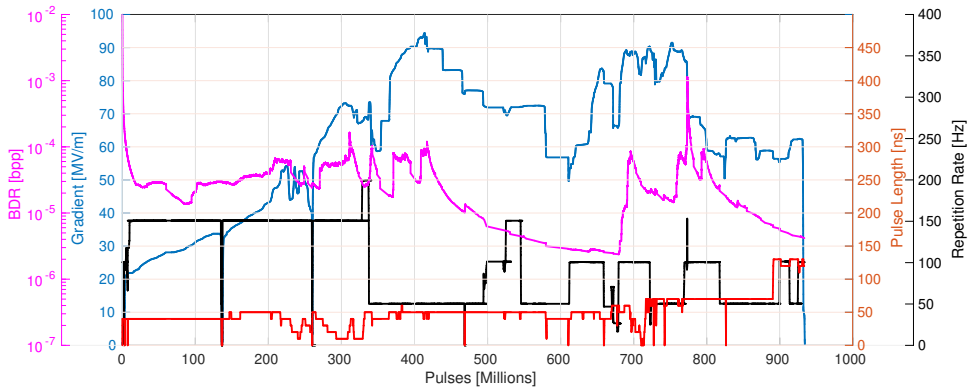

Figure 7.21: The entire high power conditioning history of the TD24 R05 SiC tested using Line 1 of Xbox 3. The plot depicts the gradient (blue), the pulse length (red), the repetition rate in Hz (black) and the breakdown rate (magenta) on the y-axis plotted against the total number of pulses on the x-axis.

rate was observed to increase from then forth. In the original design of Xbox 3, the pulse compressors were chilled using 2.4 kW temperature regulating chillers. After a short period operating at 200 Hz, it was observed that these chillers could no longer sufficiently displace the heat for stable operation, even if the rate was retuned to 150 Hz, therefore the repetition rate was reduced to 50 Hz at 340 million pulses (refer to Section 5.3.4). Accelerating structures must run at the correct frequency as variations not only lead to the variations in dark current capture, as discussed in Chapter 6 but also affect the synchronicity of the beam and RF. For the remainder of the conditioning, the repetition rate was increased whenever the pulse compressors were able to operate with a stable temperature. At 420 million pulses the structure reached 95 MV/m for the 50 ns pulse. At this point one of the klystrons of Xbox 3 was found to have a discontinuity in its power transfer curve, discussed in Section 5.3.1. This resulted in the structure experiencing breakdown clusters caused by a faulty power ramp. It was decided that the klystron required a replacement and that the structure should be pulsed at a constant power with the klystron operating far from this discontinuity in its power transfer curve. At 610 million pulses, the high power testing of the structure resumed with the new klystron, after testing at low power between 580 to 610 million pulses. At 700 million pulses, the structure once again reached 90 MV/m. The pulse compressor and load continued to condition shown as power drops throughout the conditioning history. An error in the LLRF software controlling the trigger phase delay sent the power intended for Line 2, which during this time was operating at a larger peak power, to Line 1. The result was that the SiC structure experienced transit increases in peak power up to 10 MW greater than intended. This event can be observed as the sharp increase in BDR at 770 million pulses. After this event, the structure developed a hot-cell where breakdowns occur repeatedly at a single location and the gradient could not be recovered. Despite efforts to recover the conditioning state, the structure had to be removed.

7.4.2 Breakdown Distribution

The breakdown distributions presented in Figure 7.22 are indicative of the turbulent conditioning history of the structure. Plotting the distribution of the breakdown location, using the previous described method of translating the measured time-of-propagation into a position, presented no clear evidence for a strong breakdown excess at a particular point within the structure (Figure 7.22a). Small peaks of excess breakdowns were evident at the input and output of the structure. To understand the likely cause, the time-of-propagation was plotted against the pulse number, shown in Figure 7.22b. It is evident that the breakdowns were evenly distributed, with only a small excess towards the end of the structure which occured at the start high power testing. Between 480 and 680 million pulses, the power was reduced

which led to few breakdowns occurring during this period. At 680 million pulses, the power returned to approximately 90 MV/m and therefore the BDR started to increase at which point a small excess of breakdowns was identified at the start of the structure. After an algorithm problem sent too much power into the structure, all breakdowns were found to occur overwhelmingly at the beginning of the structure.
The behaviour of measured ϕ_{BD} for the breakdowns revealed an unusual distribution with six dominant peaks (Figure 7.22c). Such structure in the distribution was unexpected and therefore an explanation was required. Plotting the time-of-propagation

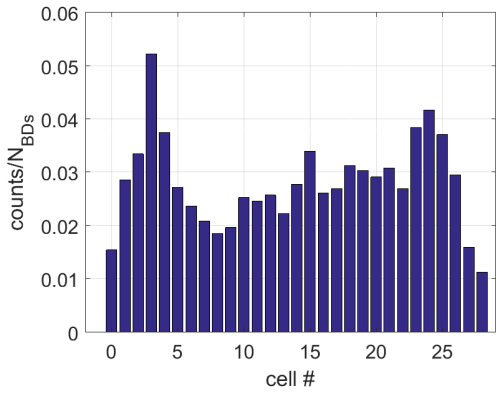

(a) Breakdown distribution.

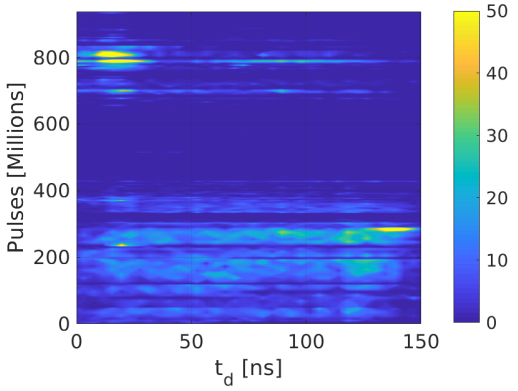

(b) Time-of-propagation vs pulses.

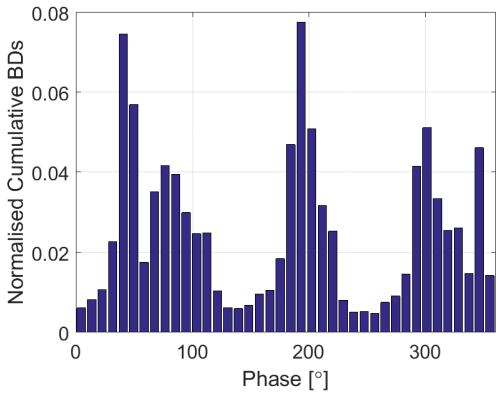

(c) ϕ_{BD}.

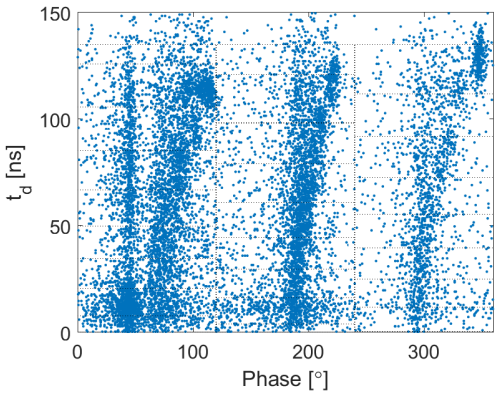

(d) Time-of-propagation vs ϕ_{BD}.

Figure 7.22: Breakdown distributions for the TD24 R05 SiC N1 structure for the conditioning on Xbox 3 Line 1. The top-left figure depicts a histogram of the breakdown locations across the structure where the ratio of breakdowns is plotted against the cell number. The top-right figure illustrates the evolution of these breakdowns' locations over the conditioning by plotting the time-of-propagation value, in ns, against the number of pulses, and displaying it as a density map. The colour map illustrates the density of breakdowns in the area during that period of conditioning. The bottom-left figure displays a histogram of the phase difference for the breakdowns during the conditioning by plotting the ratio of breakdowns against the phase difference, in degrees. The bottom-right figure plots the breakdown position within the structure, expressed as a time-of-propagation in ns, against the phase difference of the breakdown in degrees.

against ϕ_{BD}, as presented in Figure 7.22d, a distinct curvature in the breakdown event clusters was found. This curvature was proposed to be the result of the detuning of the accelerating cells from their nominal frequency and therefore leading to a variation in the phase advance. In Chapter 6 it was demonstrated that the resonant frequency was dependent on the temperature of the structure (refer to Section 6.4.1). Close inspection of the run log revealed that the structure testing had been undertaken at 3°C above the nominal operating temperature resulting in a detuning of 600 kHz from the nominal frequency. This detuning explained the curvature but did not explain the straight distributions overlapped the curved distributions. These were found to be the result of secondary breakdowns which occurred after the high power pulsing was interlocked for ~ 3 s and therefore the structure had time to cool to the nominal temperature [82]. Once cooled, the structure returned to its nominal operational frequency and the distribution of breakdowns appeared as straight clusters, as observed in the diagram. These variations in the operational temperature of the SiC structure were not visible through the measured bunker radiation as the gradient in the SiC structure was consistently the lowest and therefore produced the lowest levels of dark current induced radiation.

7.5 Brazed CLIC Structures

The Paul Scherrer Institute (PSI), in Villigen Switzerland, has developed a fabrication method for creating accelerating structure for the SwissFEL. Using this technique, they have built a CLIC prototype structure based on the T24 design as was used in the CLIC-G Open structure. In comparison to the typical CLIC structure design, the T24PSI used brazing to join the individual disks each containing an accelerating cell (Figure 7.23a) [83]. Such joining technology provided a significantly cheaper alternative compared to the hydrogen bonding. Along with brazing, the new manufacturing technique includes a new "tuning free" technology where structures are built to the operational frequency without the ability to tune the cells. The aim of creating this structure was to test the applicability of this fabrication technique and therefore used the well established T24 RF design [83].

7.5.1 High Power Testing: Phase 1

Following the installation of the SiC structure on Line 1 of Xbox 3, the T24 PSI N1 was installed on Line 2 to be tested alongside (Figure 7.23b). The T24 PSI N1 and TD24 R05 SiC N1 structures were the first CLIC structures to be tested using a shared vacuum and interlock system. Pulsing began with a BDR limit of 5×10^{-5} bpp at a pulse length of 50 ns, shown in Figure 7.24. Conditioning towards an unloaded accelerating gradient of 100 MV/m was smooth and achieved in ∼100 million pulses. After beginning conditioning at 150 Hz, the first attempt to run at 200 Hz occurred

(a) RF cell design. (b) Photograph of PSI on Xbox 3.

Figure 7.23: A photograph of the PSI structure installed on Xbox 3 along with the RF design of a single cell [83].

at 150 million pulses. Unfortunately the higher gradient and repetition rate led to greater power dissipation in the pulse compressor, whose chillers were unable to displace the heat efficiently enough to remain at a stable temperature. Anticipating that this would become a significant problem, with further increases in the peak power and pulse length required, the repetition rate was reduced to 50 Hz. Up to 150 million pulses, the radiation safety threshold outside the bunker was exceeded in two instances which led to the requirement of a power reduction, depicted at 50 and 110 million pulses. It can be observed that the radiation only limited the conditioning for a short period in these instances in comparison to the events during the conditioning of the TD26CCR05 and T24 Open structures. This resulted from an improved understanding of the cause of the radiation and how to minimise its

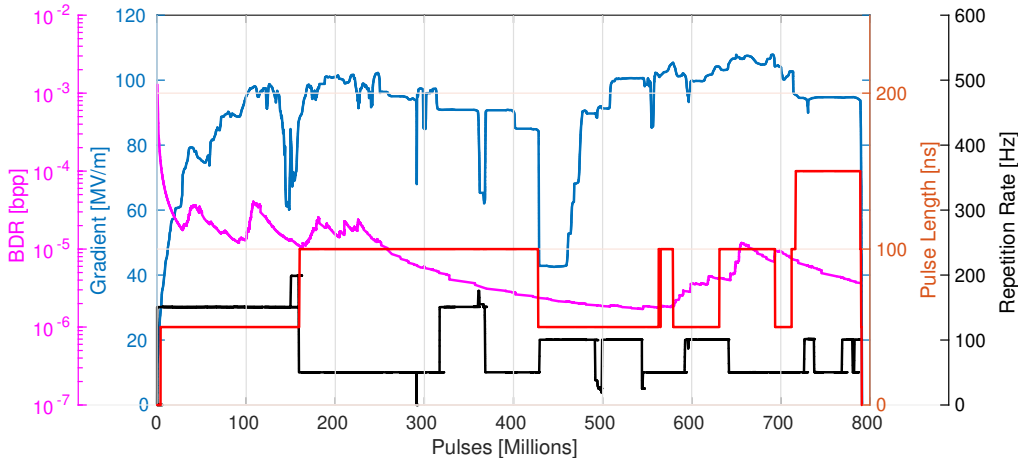

Figure 7.24: Phase 1 of the conditioning of the T24 PSI N1 structure in Xbox 3 Line 2. The plot depicts the gradient in MV/m (blue), the pulse length in ns (red), the pulse repetition rate in Hz (black) and the breakdown rate in bpp (magenta) plotted against the number of pulses.

effects as detailed in Chapter 6.

At 150 million pulses, the second pulse length of 100 ns was implemented along with a gradient reduction of $\sim$ 20% to keep a constant BDR. The structure was observed to condition rapidly back to its previous operating point of 100 MV/m. At 250 million pulses, a problem in the klystron impacted upon the conditioning, due to the requirement to operate at reduced and constant power up to 420 million pulses. This was the same issue previously mentioned in the TD24 R05 SiC N1 conditioning description. At 420 million pulses, the klystron was replaced and conditioning was able to be resumed at 450 million pulses after 30 million pulses of low power testing. The original pulse length of 50 ns was set for the resumption of conditioning and the gradient was increased towards 100 MV/m. To test the available power from Xbox 3 with the new klystron, conditioning continued past 100 MV/m up to 108 MV/m. At 630 million pulses, the pulse length was increased to 100 ns and a gradient of 107 MV/m was achieved. At 700 million pulses, it was decided that the pulse length should be increased to 150 ns, unfortunately the power available in Xbox 3 at 150 ns limited the gradient to 93 MV/m. This concluded the conditioning of the structure in Xbox 3. Due to these power limitations of Xbox 3 it was decided that the structure would be moved to Xbox 2 which offered a much greater peak power.

7.5.2 Breakdown Distribution

Before moving the structure to Xbox 2, the breakdown distributions were analysed to search for evidence that the structure was reaching its high gradient limit. The distribution of the breakdowns, presented in Figure 7.25a, demonstrated that the breakdowns occurred throughout the structure with a small excess towards the end of the structure. A narrow cluster of breakdowns at the start of the structure was also observed. To understand this distribution, the time-of-propagation is plotted against the number of pulses for all of the breakdown events (Figure 7.25b). It was found that breakdowns occurred almost homogeneously throughout the structure for the first 215 million pulses. Between 215 and 600 million pulses, the BDR was low while the power was reduced and consequently few breakdowns occurred. After 600 million pulses, the increased gradient led to breakdowns occurring predominantly at the beginning of the structure. This behaviour was attributed to the structure reaching its high gradient limit. As commonly observed during the high power testing of CLIC prototype structures, the ϕ_{BD} distribution appeared in three peaks. As previously mentioned this is known to be caused most likely by the breakdowns occurring at the iris of each cell (Figure 7.25c). Plotting the time-of-propagation against the ϕ_{BD}, it was observed that the structure was well tuned to the operational frequency, determined by the straightness of the three breakdown clusters (Figure 7.25d).

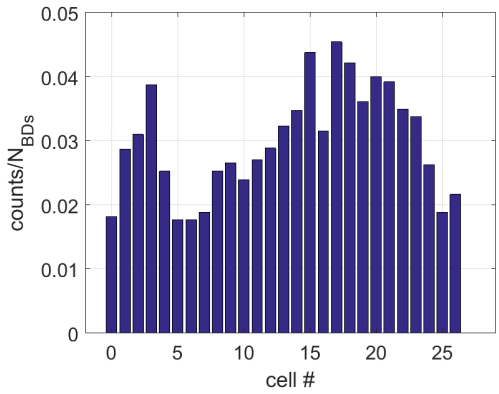

(a) Breakdown distribution.

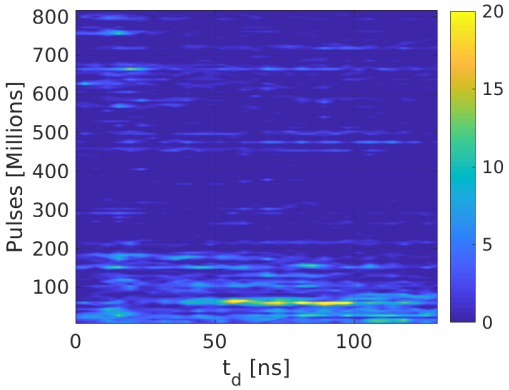

(b) Time-of-propagation vs pulses.

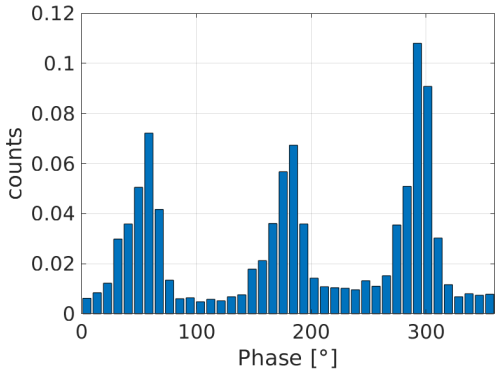

(c) ϕ_{BD}.

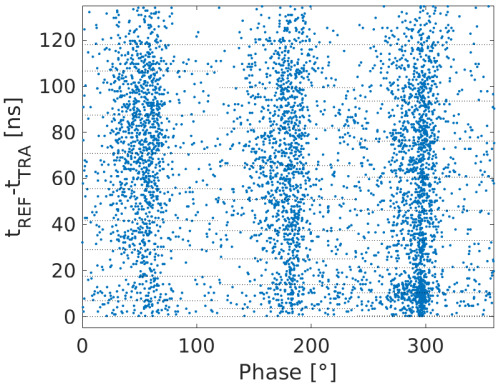

(d) Time-of-propagation vs ϕ_{BD}.

Figure 7.25: Breakdown distributions for the T24 PSI N1 structure for the conditioning on Xbox 3 Line 2. The top-left figure depicts a histogram of the breakdown locations across the structure where the ratio of breakdowns is plotted against the cell number. The top-right figure illustrates the evolution of these breakdowns' locations over the conditioning by plotting the time-of-propagation value, in ns, against the number of pulses, and displaying it as a density map. The colour map illustrates the density of breakdowns in the area during that period of conditioning. The bottom-left figure displays a histogram of the phase difference for the breakdowns during the conditioning by plotting the ratio of breakdowns against the phase difference, in degrees. The bottom-right figure plots the breakdown position within the structure, expressed as a time-of-propagation in ns, against the phase difference of the breakdown in degrees.

7.5.3 High Power Testing: Phase 2

After conditioning for 800 million pulses on Xbox 3, the T24 PSI N1 structure was moved to the Xbox 2 test stand. The choice to move the structure was to exploit the greater peak power available in Xbox 2. At the start of conditioning, the structure was able to begin conditioning at 57 MV/m, as demonstrated in Figure 7.26. Beginning with a pulse length of 50 ns, the structure rapidly reached an unloaded gradient of 100 MV/m in 30 million pulses, using a BDR set point of 5×10^{-5} bpp. The conditioning continued and quickly reached 108 MV/m at 55 million pulses into

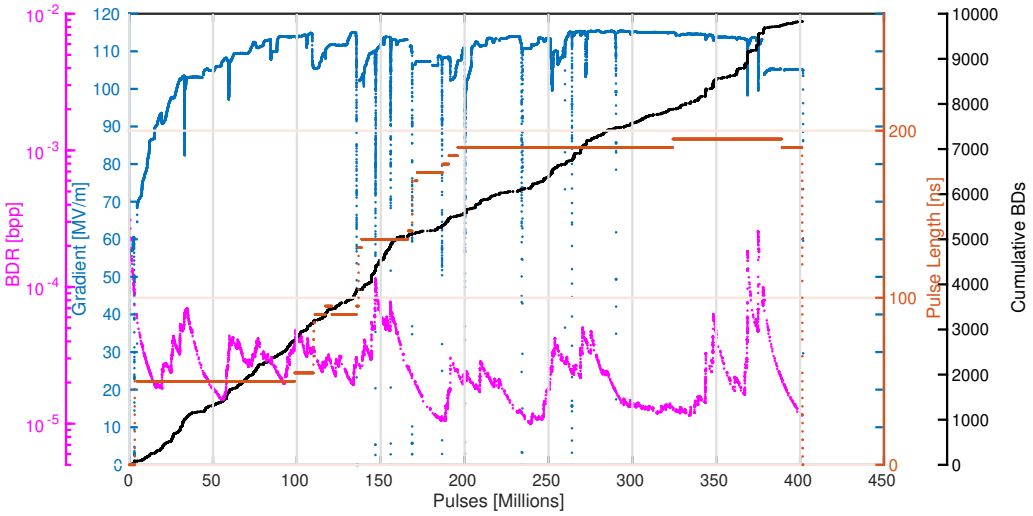

Figure 7.26: Phase 2 of the conditioning of the T24 PSI N1 structure in Xbox 2. The plot depicts the gradient in MV/m (blue), the pulse length in ns (red), the cumulative breakdowns (black) and the breakdown rate (magenta) plotted against the number of pulses.

second phase of the conditioning. The conditioning rate was observed to reduce, as the structure entered the previously unexplored field regime above 108 MV/m. After achieving an average gradient of 113 MV/m at 120 million pulses, the pulse length was increased to 100 ns and the gradient reduced to keep a constant BDR. Conditioning to 113 MV/m at the longer pulse length progressed rapidly and was achieved in only another 30 million pulses. This was repeated for a 150 ns pulse length where the structure was again able to achieve an accelerating gradient of 113 MV/m. At 200 million pulses into the conditioning, the pulse length was set to 200 ns. After 300 million pulses the gradient reached 113 MV/m before it was left to operate at a constant gradient and pulse length. It was observed that the BDR was not reducing as expected, only reducing to 5×10^{-5} bpp/m and for this reason, the gradient was reduced to 105 MV/m at 380 million pulses. It was decided that the structure had reached its high gradient limit and that some damage to the structure may have been preventing it from conditioning to lower BDRs. The structure was therefore removed from Xbox 2.

7.5.4 Breakdown Distribution

Examining the breakdown distribution along the structure for the second phase of conditioning, it was found that the breakdowns occurred predominantly at the input of the structure, as had been observed towards the end of Phase 1 (Figure 7.27a). The time-of-propagation plotted against the number of pulses illustrated that the breakdowns began with a similar distribution to that measured in the high power testing on Xbox 3. At 110 million pulses into the conditioning, it was found that

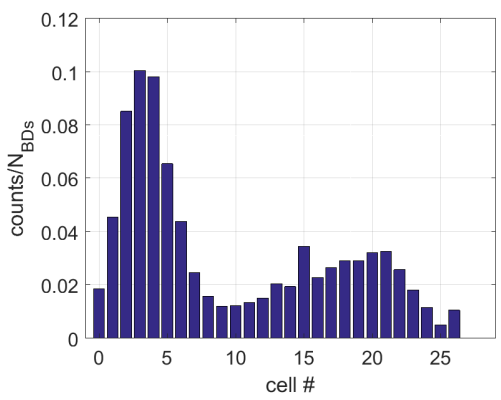

(a) Breakdown distribution.

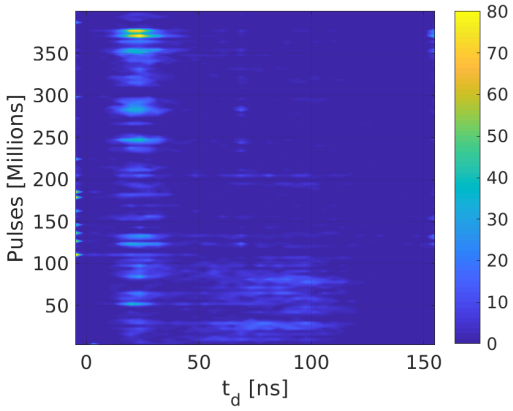

(b) Time-of-propagation vs pulses

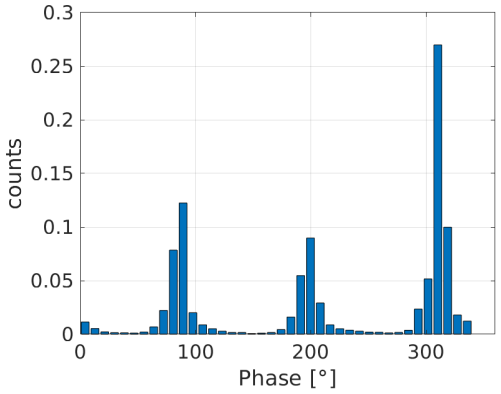

(c) ϕ_{BD}.

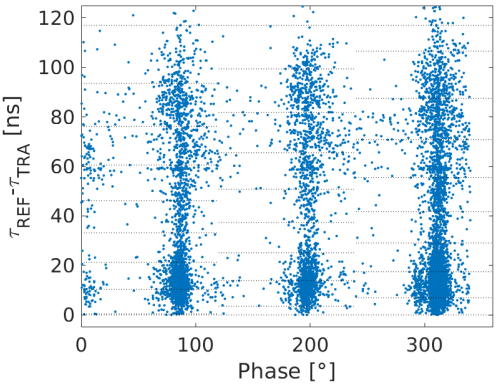

(d) Time-of-propagation vs ϕ_{BD}.

Figure 7.27: Breakdown distributions for the T24 PSI N1 structure for the conditioning on Xbox 2. The top-left figure depicts a histogram of the breakdown locations across the structure where the ratio of breakdowns is plotted against the cell number. The top-right figure illustrates the evolution of these breakdowns' locations over the conditioning by plotting the time-of-propagation value, in ns, against the number of pulses, and displaying it as a density map. The colour map illustrates the density of breakdowns in the area during that period of conditioning. The bottom-left figure displays a histogram of the phase difference for the breakdowns during the conditioning by plotting the ratio of breakdowns against the phase difference, in degrees. The bottom-right figure plots the breakdown position within the structure, expressed as a time-of-propagation in ns, against the phase difference of the breakdown in degrees.

when the structure exceeded this gradient the breakdowns began to occur primarily at the start of the structure. Breakdowns continued to occur around this location until the conditioning was concluded (Figure 7.27b).

The two plots of the ϕ_{BD} distribution (Figure 7.27c) and the time-of-propagation against ϕ_{BD} diagram (Figure 7.27d) were found to have similar characteristics to those measured in Xbox 3. This demonstrates that the structure remained well tuned after its move to the Xbox 2 test stand.

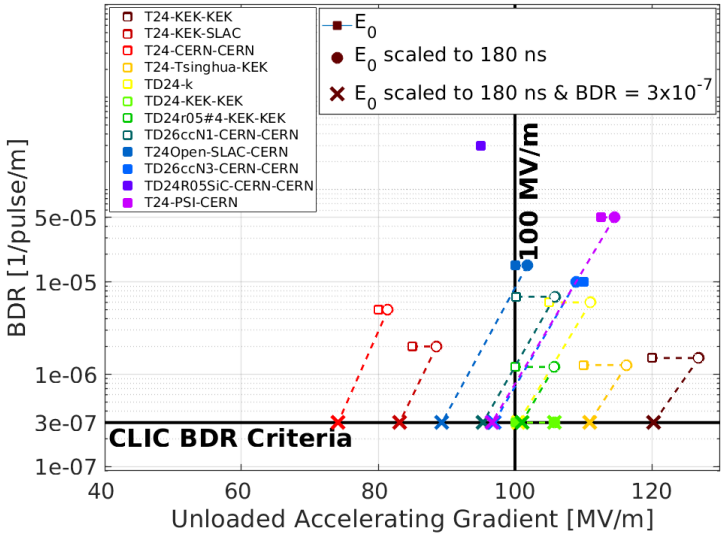

Figure 7.28: A comparison of the testing results present in this thesis to past results from CERN, SLAC and KEK. On the y-axis is the breakdown rate, in bpp/m, plotted against the achieved unloaded accelerating gradient in MV/m. The three marker types are the operational gradient (square), operational gradient normalised to nominal pulse length (circle) and operational gradient normalised to nominal pulse length and breakdown rate (cross). Each colour represents a different prototype structure with the legend indicating the "Prototype name-Fabricated by-Tested by". The unfilled and filled markers represent the structures tested prior to this thesis and in this thesis, respectively.

7.6 Review of Structure Performance

In Table 7.3, the high power testing results from the four structure tests are displayed. Reassuringly three of the four structures exceeded the 100 MV/m unloaded gradient barrier with the fourth failing due to a software malfunction. A comparison of these structure results to previous testing is presented in Figure 7.28. On reaching their high gradient limit, all structures began to breakdown towards the first few cells of the structure. This will need to be considered in the RF design of the next generation of prototype. For the TD26CC R05 N3 structure, the high

Table 7.3: Summary of the testing results from the four structures tested. Results demonstrate the maximum operational gradient achieved. †The TD24 R05 SiC N1 developed a hot-cell and was therefore required to be removed. TD24 R05 SiC N1 is not normalised as it was not deemed a successful test.

Structure	Gradient [MV/m]	Pulse Length [ns]	BDR [bpp/m]
TD26CC R05 N3	110	170	2×10^{-5}
CLIC-G Open	100	200	1.5×10^{-5}
TD24 R05 SiC N1 †	95	50	4×10^{-4}
T24 PSI N1	113	200	5×10^{-5}

power testing caused a 1 MHz detuning of the structure. In comparison, the CLIC-G Open retained its RF properties after 1.05 billion pulses which makes the fabrication technique favourable given the long term operation plans of CLIC.

7.7 Testing of Techniques for Large Scale RF Conditioning Programme for the CLIC

The results, presented in this chapter, have shown that the conditioning of a single accelerating structure commonly takes several hundred million pulses to complete. At the nominal CLIC repetition rate of 50 Hz, this equates to several months of high power testing. In the CLIC-380 design, the main linac is comprised of ∼28 000 accelerating structures and therefore optimising the efficiency of structure conditioning is crucial [9]. The current strategy to condition structures involves conditioning them to the nominal gradient at a constant pulse length then repeating the process at longer pulse lengths, all with a constant BDR [95]. Once the gradient and pulse length are achieved, the structure is left to condition down to the nominal BDR of 3×10^{-7} bpp/m [9]. The following section investigates several procedures which aim to make the conditioning of thousands of accelerating structures more efficient. To initiate the discussion, an investigation into the rate of conditioning will be conducted. This aims to understand how long a single structure requires to reach the nominal CLIC gradient, pulse length and BDR. Following are studies of gradient recovery after exposure to air and the effects of pulse repetition rate. These tests aim to understand the feasibility of a large scale conditioning programme where structures are conditioned in a cascade of test facilities like Xbox 3 then subsequently installed in the main linac. Finally an investigation into a common practice of gradient recovery after breakdown is performed to understand whether this method of recovery, which limits the ultimate luminosity of CLIC, is required for stable, high gradient operation.

7.7.1 Rate of Conditioning

The BDR set point during conditioning, commonly set to $\sim 2.5 \times 10^{-4}$ bpp/m, is three orders of magnitude above the nominal maximum BDR for CLIC. To determine the time required to reach an acceptable BDR, the following section will investigate the BDR reduction trend for structures pulsing at a constant gradient and pulse length. Figure 7.29 displays the BDR reduction for the high power testing of the CLIC-G Open and TD26CC R05 N3 structures each of which were tested on Xbox 2 [67]. The steady decay of the BDR followed an inverse power law and decreased by approximately an order of magnitude per decade though experienced transient jumps in the BDR during breakdown clusters. A strategy to reduce the

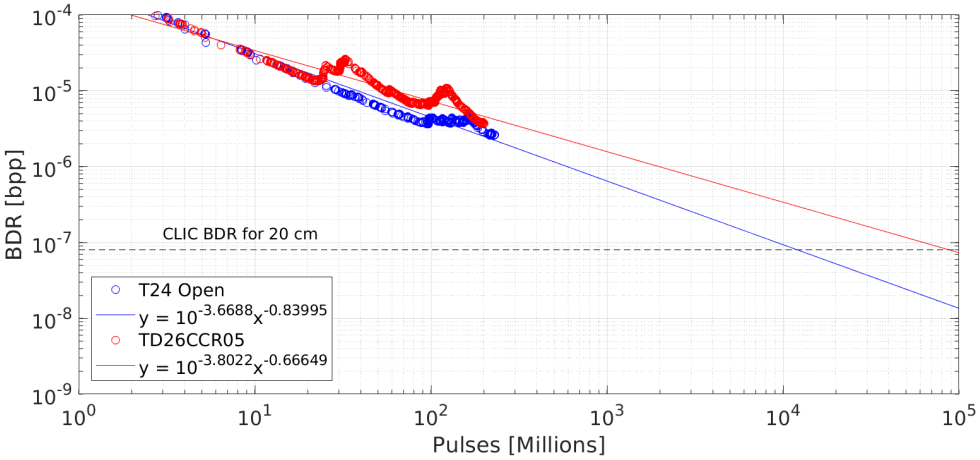

Figure 7.29: Measurement of the BDR in bpp for the CLIC-G Open (blue, circle) and the TD26CCR05 N3 (red, circle) plotted against the number of pulses for a constant pulse length and input power. Power law trend lines are fitted to the data with the corresponding colour of the data points. A horizontal dashed line illustrates the ultimate BDR required for CLIC nominal operation. [57].

time required for conditioning is to increase the repetition rate of the conditioning, which has now been demonstrated as feasible in Section 7.4 and 7.5. Another option is the concept of conditioning the structures prior to their installation into the main linac which will be discussed below. The following discussion may be found in reference [57] which is included in its entirety in Appendix C.

7.7.2 Gradient Recovery After Exposure to Air

Although appearing an attractive option, the in situ conditioning of all of the ∼28 000 structures, required for the main linac, may not be practical. For this reason, it has been suggested that structures may be conditioned in separate test stands before their installation into the main linac [85]. An attraction of the Xbox 3 test stand is that it can operate with a pulse repetition rate up to 200 Hz and therefore offers the possibility of faster conditioning in comparison to Xbox 1 and 2. For the conditioning of the T24 PSI N1 and N2 prototypes, both of the structures began conditioning in Xbox 3 after which they were moved to Xbox 2 to complete their conditioning. During the transition from Xbox 3 to Xbox 2, the structures were exposed to air for a period of 1-2 days [57].

The first phase of conditioning in Xbox 3 and second phase of conditioning in Xbox 2 are demonstrated for the T24 PSI N1 and N2 structures in Figures 7.30a and 7.30b, respectively, overlaying the two phases of conditioning. At the start of the second phase of conditioning, it was observed that the structures began operation at 57 MV/m and 40 MV/m for the N1 and N2, respectively. Two dashed tangent lines demonstrate the approximate rate of conditioning at 70 MV/m. It was found that

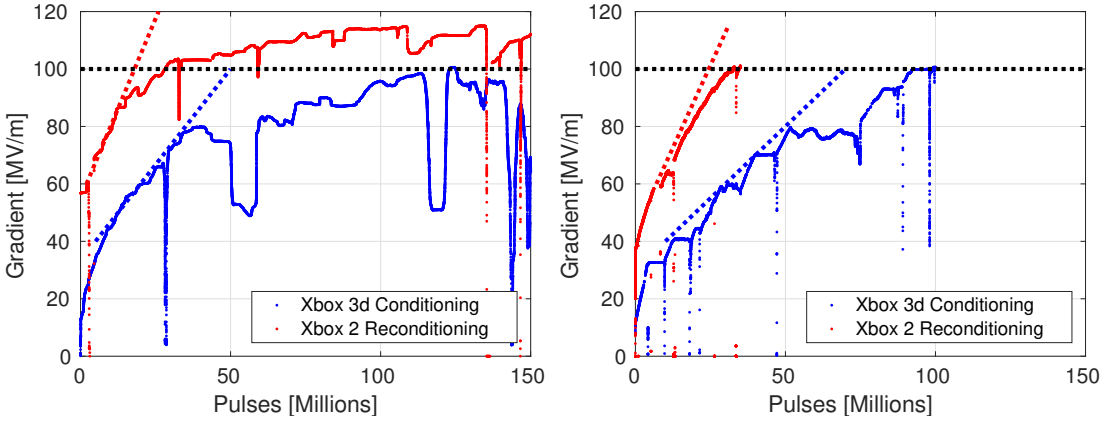

(a) T24 PSI N1. (b) T24 PSI N2.

Figure 7.30: Conditioning and reconditioning curves of the two T24 PSI prototypes N1 and N2. The two graphs plot the gradient, in MV/m, on the y-axis against the number of pulses on the x-axis for the first conditioning of the structure on Xbox 3 (blue) and the reconditioning on Xbox 2 (red) [57].

the conditioning rate was 2.5 and 2.3 times greater at 70 MV/m for the second phase of conditioning of the N1 and N2 structures, respectively, compared to that of the structure yet to be exposed to high power testing (Phase 1). Phase 1 of the conditioning for each structure took approximately the same number of pulses (100 million) to reach 100 MV/m, after adjusting for the power drops in the N1's conditioning resulting from radiation issues (refer to Section 7.5). For the previously conditioned structures (Phase 2), the 100 MV/m unloaded gradient was achieved in approximately 25-30 million pulses. Given the higher initial gradient and larger conditioning rate, it was concluded that the conditioning state had been partially retained in the structure, despite the exposure to air. Such results open the idea of conditioning structures before installation into the main linac [57].

7.7.3 Pulse Repetition Rate vs BDR

In the proposed method to condition accelerating structures before they are installed in the main linac, it has been suggested that pulsing would operate at a repetition rate well above the CLIC's nominal 50 Hz to reduce the required conditioning time. Increasing the repetition rate increases the average power dissipated in the structure and it is important to understand how this affects the BDR. Using the TD24 R05 SiC N2 and the T24 PSI N2, pulsing at constant power and pulse length was performed at three pulse repetition rates. Figure 7.31 displays the cumulative breakdowns for 82 million pulses at these three pulse repetition rates, the results of which are summarised in Table 7.4. For the TD24 R05 SiC N2, the BDR at 25 Hz and 100 Hz appeared to decrease despite the quadrupling of the average power. For 200 Hz pulsing, the BDR remained the same as the 100 Hz repetition rate within

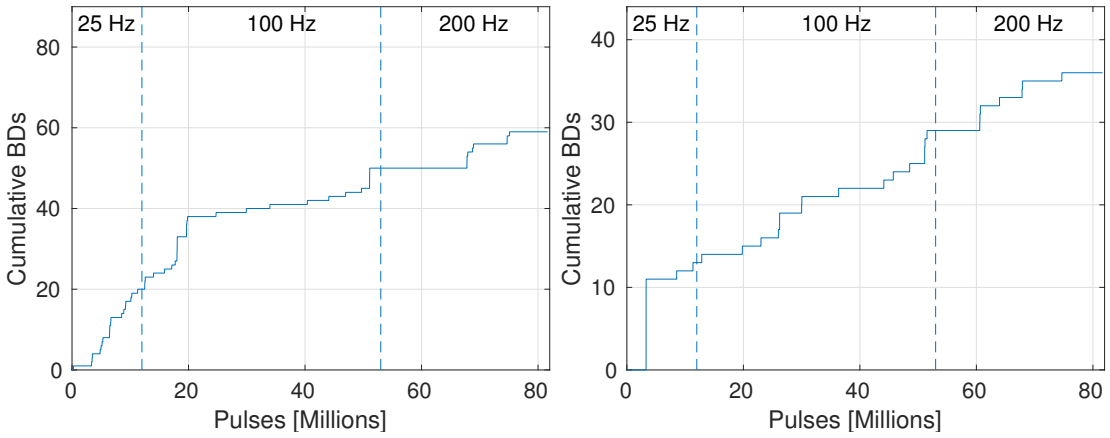

(a) T24 PSI N2. (b) TD24 R05 SiC N2.

Figure 7.31: Measurement of dependence of the BDR on the pulse repetition rate for the T24 PSI N2 and the TD24R05SiCN2. The plots illustrate the cumulative breakdowns plotted against the number of pulses. The vertical dashed lines illustrate the change in the pulse repetition rate with repetition rate of each region included through an annotation. [57].

Table 7.4: A summary of the results for the BDR dependence on the pulse repetition rate [57].

Structure	Rep. Rate [Hz]	BDR [bpp]	Uncertainty [bpp]
TD24R05 SiC N2	25	1.08×10^{-6}	$\pm 3 \times 10^{-7}$
	100	3.9×10^{-7}	$\pm 1 \times 10^{-7}$
	200	2.4×10^{-7}	$\pm 9 \times 10^{-8}$
T24 PSI N2	25	1.66×10^{-6}	$\pm 4 \times 10^{-7}$
	100	7.317×10^{-7}	$\pm 1 \times 10^{-7}$
	200	3.1×10^{-7}	$\pm 1 \times 10^{-7}$

statistical uncertainty. The BDR on the T24 PSI N2 began at the higher BDR of 1.66×10^{-6} bpp at 25 Hz, expected to be the result of the initial change in power. Subsequent pulsing at 100 and 200 Hz found that the BDR decreased most likely due to conditioning. Despite the increase in power dissipation, the operational temperature does not change during operation at higher repetition rate. This is the result of the high thermal conductivity of the copper and the power capacity of the thermal regulating chillers. If the repetition rate was increased to where the average power dissipated in the structure exceeded the power capacity of the chiller, then problems including those mentioned in Chapter 6 would occur. In summary the increase in average power dissipated on the surface of the structure offered no evidence of an increase in the BDR [57].

7.7.4 Gradient Recovery After Breakdown

It has become common practice during the operation of the X-band test stands to interlock the RF power for ~ 3 s after a breakdown, before recommencing pulsing

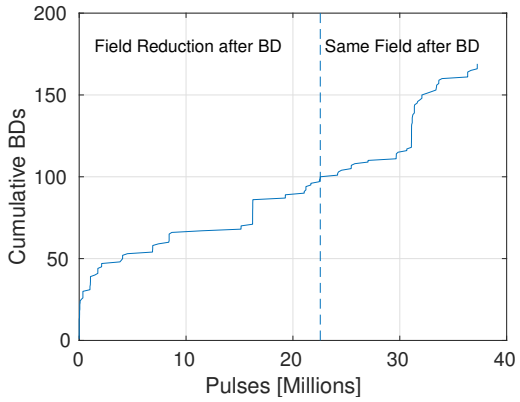

Figure 7.32: Cumulative breakdowns for a period of conditioning plotted against the number of pulses. The vertical dashed line separates the region where field reduction after breakdown was and was not used during operation [57].

at a reduced input power and steadily returning to the set level over a few hundred pulses. This reduction in power aims to reduce the likelihood of a follow-up breakdown. In typical operation a reduction in field after RF breakdown is undesirable as it will affect the luminosity through an increase in the effective downtime of the machine. During testing of the TD26CC R05 N3 structure, modifications to the algorithm allowed continuous pulsing after a breakdown event, with the interlock and field reduction to be enabled only after two consecutive breakdown pulses. Figure 7.32 displays the cumulative breakdowns for high power operation with and without this field reduction. Adopting the new conditioning algorithm did not appear to affect the BDR though further testing will be necessary to determine the long-term feasibility of this operating strategy [57].

7.8 Summary

Four unique CLIC accelerating structure prototypes were tested at high power with the aim of determining the reproducibility of generating unloaded accelerating gradients above 100 MV/m. Three of the four accelerating structures were able to achieve an accelerating gradient of at least 100 MV/m. One such structure was a prototype based on the CLIC baseline RF design. After 900 million pulses, the structure was able to achieve an unloaded gradient of 110 MV/m for a 170 ns RF pulse and conditioning down to a BDR of 2×10^{-5} bpp/m. Unfortunately measurements of the RF parameters before and after the high power testing concluded that the structure had detuned 1 MHz from its nominal RF frequency most likely due to the high power operation. Despite this, the TD26CC R05 N3 achieved the highest accelerating gradient ever produced in a HOM damped CLIC accelerating structure [66]. A vastly different accelerating structure was tested with the aim of determining the feasibility of a novel fabrication technique where an entire ac-

celerating structure is manufactured through the milling of two halves which are subsequently joined through brazing. The structure underwent high power testing for 1.05 billion pulses and achieved an unloaded gradient of 100 MV/m at a BDR of 1.5×10^{-5} bpp/m with a 200 ns pulse. These results verified the feasibility of this fabrication technique and measurements of the RF properties before and after high power testing demonstrated little change, making the technique even more desirable. High power testing on Xbox 3 began with a structure prototype aiming to test the use of SiC for HOM damping at high power and a low BDR. An error in the code led to the premature removal of the structure. Despite this, the structure was still able to operate with an unloaded accelerating gradient of 95 MV/m with a 50 ns pulse length although the BDR was limited to 4×10^{-4} bpp/m. The second structure to be installed on Xbox 3 was a prototype fabricated at the Paul Scherrer Institute using another unique fabrication technique aimed at reducing fabrication costs. High power testing of the structure reach 107 MV/m with a 100 ns pulse length of Xbox 3 although due to power constraints the structure was moved to Xbox 2. The structure continued with conditioning surpassing its previous operational point with ease, going on to achieve 113 MV/m with a 200 ns pulse length and at a BDR of 5×10^{-5} bpp/m.

Results from these and other high power tests were used to investigate possible conditioning strategies for CLIC. Such strategies are crucial for the cost and time efficiency of the commissioning CLIC. Conditioning the accelerating structures in situ whilst installed in the main linac would require in the best case scenario several months of conditioning if pulsed at the nominal repetition rate of 50 Hz, although this can occur in parallel to beam commissioning. Conditioning structures at a higher repetition rate in separate test stands and then installing them into the main linac has been demonstrated as a possible solution to reduce the overall conditioning time. Results demonstrated that higher repetition rate conditioning did not lead to a higher BDR and that the conditioning state was partially maintained in a structure when moved between test stands after an exposure to air. This opens up the option of conditioning structures before installation. Finally, algorithmic reductions of the field strength after RF breakdowns aimed to prevent further RF breakdowns during conditioning though this technique is not desirable for an operational CLIC. Initial tests demonstrated that the continuation of pulsing after an RF breakdown is possible without a noticeable BDR increase.

Chapter 8

Conclusions and Future Work

Achieving accelerating gradients of 100 MV/m in RF linear accelerating structure presents a significant challenge due to high field effects such as RF breakdown and field emission. This thesis has presented an investigation into these phenomena offering further insight into their impact on the operation of accelerating structures and high power testing facilities. Motivating this work was the goal of achieving reliable operation of accelerating structures at ∼100 MV/m, as has been proposed for Compact Linear Collider.

8.1 A Novel X-band Test Stand

A novel high power X-band test stand was commissioned at CERN to increase the facility's high gradient testing capabilities. Using a combination of RF pulse weaving and pulse compression, the new test stand could deliver high power RF pulses at repetition rates up to 200 Hz and test multiple accelerating structures in situ. Operation at these high repetition rates was limited by the heat dissipated within the pulse compressors, though this was subsequently addressed through an upgrade to the cooling capacity of Xbox 3. Ultimately, RF pulses were reliably delivered at up to 150 Hz at a peak power of ∼44 MW for a pulse length of 50 ns and ∼34 MW for a pulse length of 200 ns.

8.2 Field Emission Capture Phenomenology

When operating at the nominal accelerating gradient of 100 MV/m, the surface electric fields in the CLIC accelerating structures can easily exceed 200 MV/m. These intense surface electric fields lead to the field emission of electrons which may be captured in the oscillating electromagnetic fields and propagate through the structure as a "dark current". It was the aim of this work to contribute to the understanding of this field emission capture with the objective of reducing its effects on CLIC and the high gradient test stands. A series of measurements found that

the radiation resulting from this dark current reduced during the conditioning of accelerating structure although experienced transient increases of almost an order of magnitude. Strategically positioned radiation shielding was vital to minimise the effects of this radiation on local instrumentation. It was observed that a significant fraction of the radiation was emitted from captured dark currents colliding with the downstream Faraday cup rather than being expelled from the accelerating structure. With this finding, the shielding was rearranged and able to reduce the overall radiation level within the bunker by approximately an order of magnitude. During the conditioning of the CLIC-G Open structure, the radiation was found to vary with the operational temperature of the structure. Interpretation of this finding using a simplified one dimensional model revealed that the capture of field-emitted electrons was dependent on the RF phase velocity, which could be varied through a change to the accelerating structure temperature or RF driver frequency. A series of measurements found this variation in the dark current intensity to be $\pm \sim 20\%$ for a ± 1 MHz shift in the RF driver frequency. Simulations of the capture of field emitted electrons, performed using a three dimensional RF and particle simulation, obtained similar results validating the capture model.

8.3 High Gradient Testing and Analysis

High power testing of four prototype accelerating structures was conducted using Xbox 2 and the newly commissioned Xbox 3. Three of the four accelerating structures tested with high power RF pulses were able to operate at an unloaded accelerating gradient of at least 100 MV/m. One of these accelerating structures, designed to the most recent CLIC baseline RF design specifications, was able to operate at an unloaded accelerating gradient of 110 MV/m for a 170 ns RF pulse with a BDR of 1.5×10^{-5} bpp/m. This is presently the highest accelerating gradient achieved in a HOM damped accelerating structure. Along with this, a novel accelerating structure fabricated through the milling of two complete structure halves was the first of its kind to be fabricated and tested at high power. The accelerating structure was able to operate at an unloaded accelerating gradient of 100 MV/m with a 200 ns RF pulse and BDR of 2×10^{-5} bpp/m. The new fabrication technique is an attractive option given it offers a significant reduction in the number of pieces required for assembly to just two, as well as offering the opportunity to use various joining technologies. Finally, an accelerating structure fabricated through the brazing of individual accelerating cells was the first produced using this method which aimed at operating at 100 MV/m. The structure conditioned to an accelerating gradient of 113 MV/m for a 200 ns RF pulse although high gradient operation appeared to have damaged the structure and the BDR only reduced to 5×10^{-5} bpp/m.

8.4 Future Work

The peak power which could be achieved by Xbox 3 was limited to $\sim$ 60% of the design specifications at the required pulse length of 200 ns. Overcoming this limitation will be the crucial next step for Xbox 3 to ensure accelerating structures can be tested to high power without the need to move to Xbox 2. Current plans include upgrading the 6 MW klystrons to 8 MW klystrons which is postulated to increase the peak power to $\sim$45 MW for a 200 ns pulse, given the current power losses and pulse compression ratio. A further upgrade to the cooling capacity would be required in order to operate with the higher power klystrons at 200 Hz.
Measurements of the variation of the field emission capture with the RF driver frequency and structure temperature observed a large variation, from 12 to 28%/MHz, in the measured results for the three accelerating structure. This variation was unable to be explained but it is hypothesised to be the result of the location of the emitters on the irises. The next step should include repeating the simulations for emission areas at different locations on the iris. Another area of interest is the energy spectrum of the dark current which was found by the simulation. Using the spectrometer on the X-band test stands, the spectrum of the dark current should be investigated to compare to the simulations.
The next prototype of the CLIC-G Open is currently being manufactured. This structure will have identical RF geometry to that tested in this thesis but be fabricated from a hard CuAg alloy and joined using electron beam welding. The choice of a hard copper alloy resulted from extensive testing by SLAC which had demonstrated that hard copper performed better at high gradients than soft copper [89, 90]. A second T24PSI had started its high power testing in 2018 and will conclude by late 2018. The high gradient performance of the two T24 PSI structures will be compared to determine the reproducibility of the high gradient results achieved by the prototype. A comparison of their RF properties before and after high power testing should also be performed to further the understand of the effects of high power RF testing on the RF properties of the accelerating structures.

Appendices

Appendix A

SLED Type-I Pulse Compressor

First described in 1974, the SLED Type 1 Pulse Compressor is a dual cavity passive RF unit which increases the peak power of an RF pulse. Energy conservation dictates that one cannot receive more power output than is input into a passive system, though the peak power can be increased at the expense of pulse length. Using two high quality factor cavities (Q = 180 000), the pulse compressor stores energy inside these cavities and through manipulation of the phase is able to instantaneously output up to 9 times the power. Figure A.1 will be used to describe the mechanism of pulse compression. To begin one can start at the RF input to the SLED at the start of the RF pulse (0 μs in Figure A.1a and 1 in Figure A.1b)

1. RF Pulse enters the pulse compressor (1) and splits in half at the hybrid (2) with each half arriving at the iris of its respective cavity (3). The signals at the two respective irises are 90° out of phase due to the hybrid.

2. RF signals reaching the iris (3), partially reflect with 180° phase difference but also partially transmit through to begin to fill the cavity.

3. Signals reflected from the irises (3) approach back towards the hybrid's coupling region (2). These signals encounter the hybrid for a second time, constructively interfering at the RF output and cancelling at the RF input preventing reflections. Before any fields are present in the cavities (0 μs) the output field's amplitude is approximately that of the input (ignoring resistive losses and the small amount beginning to fill the cavities).

4. RF power stored in the cavities begins to leak out of the cavity as they fill (0 to 1.5 μs in dashed black line). These leaked RF signals are 180° out of phase with those reflected from the irises. As a result the total voltage output begins to drop as the leakage increases (0 to 1.5 μs in solid red line). Overcoupling of the cavities means the power loss inside the cavities is less than the power loss to the external circuit. This allows an output power greater than the input

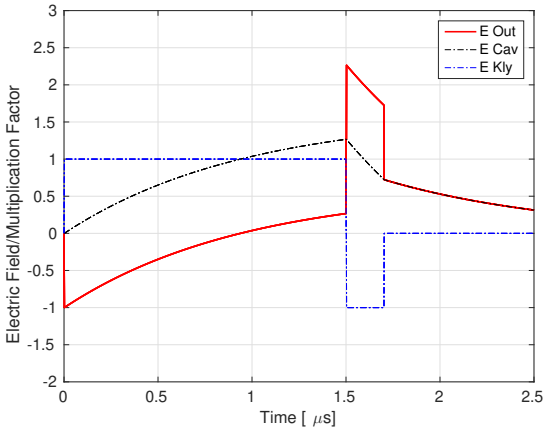

(a) T24 PSI N1

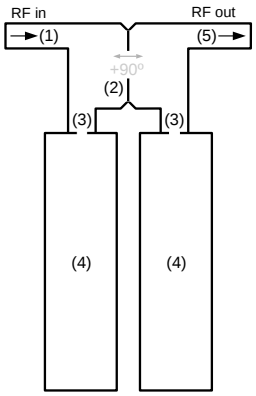

(b) T24 PSI N2

Figure A.1: A description of the pulse compressor where (1) is the input of the RF, (2) is the hybrid's coupler port, (3) is the cavities irises, (4) are the cavities, and (5) is the output RF.

power once filled (observed to be passing beyond this point at ∼0.95 μs). Although the power can not exceed the input total power from the klystron due to conservation laws.

5. Once the leakage power from the cavity has surpassed the input, the RF input into the SLED is flipped 180° (1.5 μs dashed blue line). At this point, the signals reflecting from the iris become in phase with the cavity leakage and the SLED output power jumps (Solid red at 1.5 μs). A phase flip less than 180° followed by a phase ramp over the pulse length allows a flat output pulse.

6. After the designated pulse length time, the RF from the klystron is turned off. Visible at 1.7 μs, the output of the SLED can be observed to drop significantly. However the output does not go to zero as excess stored energy in the SLED continues to leak from the output.

Appendix B

Derivation for the Capture Threshold of Dark Current for a Variation in Phase Velocity

B.1 Motivation

The following derivation is from the CERN Accelerator School in 1994 and was used as the basis for creating Equation 6.2.

B.2 Capture Threshold Equation

One can define the longitudinal field experienced by a particle at phase angle ϕ as:

$$E_z = E_0 \sin \phi. \tag{B.1}$$

If this particle has a velocity v the difference in path length of the RF wave and the particle is given by the difference in their velocity or:

$$dl = (c - v)dt, \tag{B.2}$$

where c is the speed of light and dt is the change in time. Such a length difference can also be expressed as a phase difference as the particle slips out of phase with the RF written as:

$$dl = \frac{\lambda_g}{2\pi} d\phi, \tag{B.3}$$

where λ_g is the wavelength of the RF. Combining Equation B.2 and B.3 one gets:

$$\frac{d\phi}{dt} = \frac{2\pi c}{\lambda_g}(1 - \beta), \tag{B.4}$$

where $\beta = v/c$. The equation of motion for a particle due to this RF is given by

$$\frac{d}{dt}(mv) = m_0 c \frac{d}{dt}\left[\frac{\beta}{\sqrt{1-\beta^2}}\right] = eE_0 \sin\phi, \tag{B.5}$$

where m_0 is the rest mass of the particle, e is the charge of the particle. One can define a new variable α such that:

$$\beta = \cos\alpha. \tag{B.6}$$

Equation B.5 therefore becomes:

$$\frac{d\alpha}{dt} = \frac{eE_0}{m_0 c}\sin\phi sin^2\alpha. \tag{B.7}$$

Expanding $\frac{d\phi}{dt}$ one can find:

$$\frac{d\phi}{dt} = \frac{d\phi}{d\alpha}\frac{d\alpha}{dt}. \tag{B.8}$$

Therefore using Equations B.7 and B.8 is can be found that:

$$-\sin\phi d\phi = \frac{2\pi}{\lambda_g}\frac{m_0 c^2}{eE_0}\frac{(1-cos\alpha)}{\sin^2\alpha}d\alpha, \tag{B.9}$$

Integrating over the LHS and RHS of Equation B.9 gives:

$$\cos\phi_1 - \cos\phi_0 = \frac{2\pi}{\lambda_g}\frac{m_0 c^2}{eE_0}\left[\tan\frac{\alpha_1}{2} - \tan\frac{\alpha_0}{2}\right], \tag{B.10}$$

Recalling the trigonometric relations one can write:

$$\tan\frac{\alpha}{2} = \left(\frac{1-\cos\alpha}{1+\cos\alpha}\right)^{1/2} = \left(\frac{1-\beta}{1+\beta}\right)^{1/2}. \tag{B.11}$$

Substituting in these relations Equation B.10 is rewritten as:

$$\cos\phi_0 - \cos\phi_1 = \frac{2\pi}{\lambda_g}\frac{m_0 c^2}{eE_0}\left(\frac{1-\beta_0}{1+\beta_0}\right)^{1/2}. \tag{B.12}$$

The LHS of Equation B.12 is known to have a maximum value of 2 therefore it can be found that:

$$E_0 \geq \frac{\pi}{\lambda_g}\frac{m_0 c^2}{e}\left(\frac{1-\beta_0}{1+\beta_0}\right)^{1/2}. \tag{B.13}$$

This relation demonstrates that the gradient for capture must be greater than the RHS. Recalling that the 1 is the velocity difference of the RF which was set

to c and β_0 is the particle velocity. These can be set to variable and remove the normalisation to the speed of light to give Equation 6.2.

Appendix C

Published Work

C.1 Lead Author Publications

C.1.1 Peer Reviewed Journal Articles

1. Theodoros Argyropoulos, Nuria Catalan-Lasheras, Alexej Grudiev, Gerard Mcmonagle, Enrique Rodriguez-Castro, Igor Syrachev, Rolf Wegner, Ben Woolley, Walter Wuensch, Hao Zha, Valery Dolgashev, Gorden Bowden, and Andrew Haase, Thomas Geoffrey Lucas, Matteo Volpi, Daniel Esperante-Pereira, Robin Rajamki (alphabetical order and by institution), Design, fabrication and high-gradient testing of an X-band, travelling-wave accelerating structure milled from copper halves, Phys. Rev. Accel. Beams 21, 061001 (2018).
   DOI: `https://doi.org/10.1103/PhysRevAccelBeams.21.061001`

2. Thomas Geoffrey Lucas, Theodorous Argyopolous, Mark James Boland, Nuria Catalan-Lasheras, Roger Paul Rassool, Claudio Serpico, Matteo Volpi, Walter Wuensch, Dependency of the Capture of Field Emitted Electron on the Phase Velocity of a High-Frequency Accelerating Structure, Nuclear Inst. and Methods in Physics Research, A 914C (2019) pp. 46-52.
   DOI: `https://doi.org/10.1016/j.nima.2018.10.166`

C.1.2 Non-Peer Reviewed Conference Proceedings

1. T.G. Lucas, N. Catalan-Lasheras, A. Grudiev, T. Lefevre, G. McMonagle, J. Paszkiewicz, V. del Pozo Romano, I. Syratchev, A. Vnuchenko, M. Volpi, B. Woolley, W. Wuensch, R. Zennaro, P.J. Giansiracusa, R.P. Rassool, C. Serpico, M.J. Boland, *Initial Testing of Techniques for Large Scale RF Conditioning for the Compact Linear Collider*, IPAC Vancouver 2018. `http://accelconf.web.cern.ch/AccelConf/ipac2018/`

C.1.3 Technical Notes

1. Thomas Geoffrey Lucas, Matteo Volpi, Paul Giansiracusa, Roger Paul Rassool, Theodoros Argyropoulos, Hikmet Bursali, Nuria Catalan-Lasheras, Alexej Grudiev, Gerard Mcmonagle, Igor Syrachev, Rolf Wegner, Ben Woolley, Walter Wuensch, Daniel Esperante-Pereira, Mark James Boland, High Power Testing of a Prototype CLIC structure: TD26CC R05 N3, CLIC-Note-1080 `http://cds.cern.ch/record/2642425`

C.2 Co-Author Publications

C.2.1 Non-Peer Reviewed Conference Proceedings

1. M. Volpi, N. Catalan-Lasheras, A. Grudiev, T.G. Lucas, G. McMonagle, J. Paszkiewicz, V. del Pozo Romano, I. Syratchev, A. Vnuchenko, B. Woolley, W. Wuensch, P.J. Giansiracusa, R.P. Rassool, C. Serpico, M.J. Boland,*High Power and High Repetition Rate X-band Power Source Using Multiple Klystrons*, IPAC Vancouver 2018. `http://accelconf.web.cern.ch/AccelConf/ipac2018/`

2. N. Catalan-Lasheras, H. Damerau, R. Gerard, V. del Pozo Romano, A. Grudiev, G. McMonagle, J. Pasckiewicz, S.Pitman, A. Solodko, I. Syratchev, B. Woolley, W. Wuensch, A. Vnuchenko, T. Lucas, M. Volpi *High Power Conditioning of X-band RF Components*, IPAC Vancouver 2018.

3. P.J. Giansiracusa, T.G. Lucas, M. Volpi, R.P. Rassool, M.J. Boland,G.S. LeBlanc, *Applications of a Distributed Beam Loss Monitor at the Australia Synchrotron*, IPAC Vancouver 2018. `http://accelconf.web.cern.ch/AccelConf/ipac2018/`

4. A. Vnuchenko, D. Esperante Pereira, S. Benedetti, N. Catalan Lasheras, A. Grudiev, B. Koubek, S. Pitman, G. McMonagle, I. Syratchev, B. Woolley, W. Wuensch, T. Lucas, M. Volpi, A.Faus Golfe, High Gradient Performance of an S-Band Backward Traveling Wave Accelerating Structure for Medical Hadron Therapy Accelerator. `http://accelconf.web.cern.ch/AccelConf/ipac2018/`

5. R. Zennaro, H. Blumer, M. Bopp, T. Garvey, L. Rivkin, N. Catalan-Lasheras, A. Grudiev, G. McMonagle, A. Solodko, I. Syratchev, R. Wegner, W. Wuensch, T. G. Lucas, M. Volpi, T. Argyropoulos, D. Esperante-Pereira. High Power Tests of a Prototype X-Band Accelerating Structure for CLIC. IPAC 2017. `http://accelconf.web.cern.ch/AccelConf/ipac2017/`

6. N. Catalan Lasheras, A. Grudiev, G. Mcmonagle, I. Syrachev, B. Woolley, W. Wuensch, H. Zha, G. Bowden, V. Dolgashev, A. Haase, T. Argyropou-

los, J. Giner Navarro, D. Esperante Pereira, R. Rajamaki, X. Stragier, P. J. Giansiracusa, T. G. Lucas, M. Volpi. Fabrication and High Gradient Testing of an Accelerating Structure Made from Milled Halves. Linac16. https://frib.msu.edu/misc/linac2016/index.html

C.2.2 Technical Notes

1. Updated baseline for a staged Compact Linear Collider, edited by P.N. Burrows, P. Lebrun, L. Linssen, D. Schulte, E. Sicking, S. Stapnes, M.A. Thomson, CERN2016004 (CERN, Geneva, 2016), http://dx.doi.org/10.5170/CERN-2016-004

C.2.3 Conference and Invited Talks

Conference and Workshop presentation performed by the Author:

1. Poster at IPAC 2018.
2. Talk at CLIC workshop 2018.
3. Talk at HG workshop 2017.
4. Talk at CLIC workshop 2017.
5. Talk at Linear Collider Workshop 2016.
6. Talk at CWRF 2016.
7. Poster at IBIC 2015.

C.3 Publication Examples

The following are the full texts of the publications resulting from or related this work.

PHYSICAL REVIEW ACCELERATORS AND BEAMS **21,** 061001 (2018)

Editors' Suggestion

Design, fabrication, and high-gradient testing of an *X*-band, traveling-wave accelerating structure milled from copper halves

Theodoros Argyropoulos, Nuria Catalan-Lasheras, Alexej Grudiev, Gerard Mcmonagle, Enrique Rodriguez-Castro, Igor Syrachev, Rolf Wegner, Ben Woolley, Walter Wuensch, and Hao Zha
European Organisation for Nuclear Research (CERN), 1211 Geneva, Switzerland

Valery Dolgashev, Gorden Bowden, and Andrew Haase
SLAC, Menlo Park, California 94025, USA

Thomas Geoffrey Lucas* and Matteo Volpi
University of Melbourne, Parkville 3010, Australia

Daniel Esperante-Pereira
Instituto de Fisica Corpuscular (IFIC), Valencia, Spain

Robin Rajamäki
Aalto University, 02150 Espoo, Finland

(Received 9 February 2018; published 7 June 2018)

A prototype 11.994 GHz, traveling-wave accelerating structure for the Compact Linear Collider has been built, using the novel technique of assembling the structure from milled halves. The use of milled halves has many advantages when compared to a structure made from individual disks. These include the potential for a reduction in cost, because there are fewer parts, as well as a greater freedom in choice of joining technology because there are no rf currents across the halves' joint. Here we present the rf design and fabrication of the prototype structure, followed by the results of the high-power test and post-test surface analysis. During high-power testing the structure reached an unloaded gradient of 100 MV/m at a rf breakdown rate of less than 1.5×10^{-5} breakdowns/pulse/m with a 200 ns pulse. This structure has been designed for the CLIC testing program but construction from halves can be advantageous in a wide variety of applications.

DOI: 10.1103/PhysRevAccelBeams.21.061001

I. INTRODUCTION

In order to optimize the performance and cost of the Compact Linear Collider (CLIC), a significant effort is being placed into the development of high gradient normal conducting accelerating structures. The structures for CLIC are designed to operate at 11.994 GHz with an unloaded accelerating gradient of 100 MV/m, an rf pulse length of 240 ns with a 180 ns flat-top, and a breakdown rate (BDR) lower than 3×10^{-7} breakdowns/pulse/m. Fabricated from copper, the structures are manufactured through a combination of precision turning and milling of the individual accelerating cell disks. The numerous individual disks in CLIC structures are generally joined together through diffusion bonding [1,2].

Here we introduce an alternative approach to assembling the structure from individual disks. The novel technique uses precision milling to fabricate structure halves from copper blocks. This accelerating structure design builds upon previous work of an accelerating structure made from quadrants [3], as well as the power extraction and transfer structures for CLIC's drive beam which are constructed from octants [1]. The new assembly method gives a number of advantages compared to traditional disk-based structures, providing the motivation for this study. Particularly notable are: a reduction of the number of precision pieces, freedom of choice in joining technology since there are no rf currents flowing through the metal-to-metal joint, the use of unique geometry for higher order mode damping, the ability to perform bead-pulling

*Corresponding author.
thomas.geoffrey.lucas@cern.ch

measurements before brazing, and an overall reduction of the total manufacturing cost [4].

In this paper we present the rf design and fabrication of the structure, followed by the high-power testing and post-test analysis. Known as CLIC-G-Open, the tapered (constant gradient), traveling-wave structure consists of 24 regular cells and 2 matching cells for the input and output couplers. This design was based on the CLIC-G (T24) which had been tested at high gradients and low breakdown rate [1]. Mechanical design and fabrication was undertaken at SLAC after which the structure was shipped to CERN for high power testing where the structure was installed on CERN's X-band Test Stand, Xbox-2 [5].

II. REGULAR CELL GEOMETRY

The starting point of the structure began with the well tested CLIC-G structure design which operates with 120° phase advance per cell [1]. Figure 1 illustrates the introduction of a gap between the two halves of the structure to avoid unbrazed metal-to-metal contacts. The 1 mm gap is cut off at the working frequency to minimize fields leaking towards brazed surfaces and thus reducing the effects of imperfections of brazing fillets on

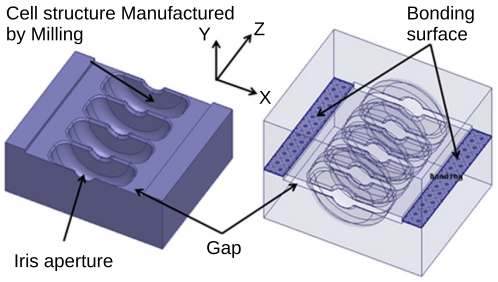

FIG. 1. The HFSS design of the structure demonstrating the structure half on the left and how each half will be joined together [7,9].

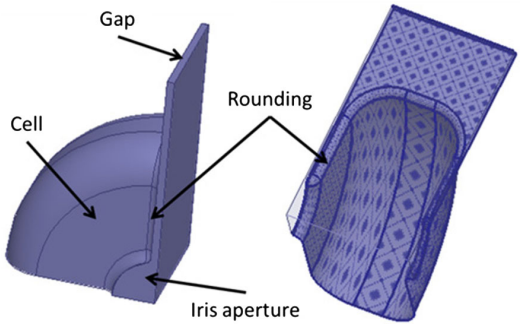

FIG. 2. HFSS model of a single cell quarter, a flatbed region representing gap added to house the metal joining surface [7,9].

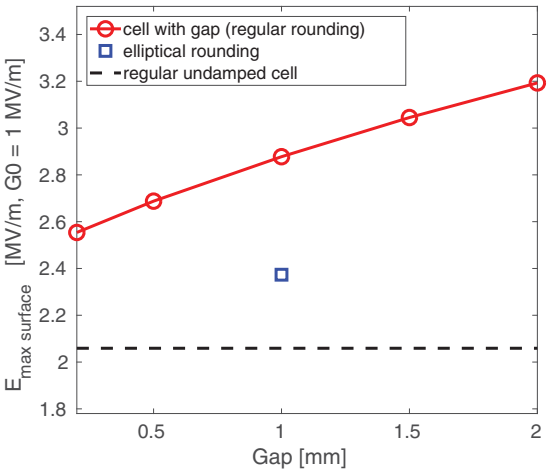

(a) Peak Surface Electric Field.

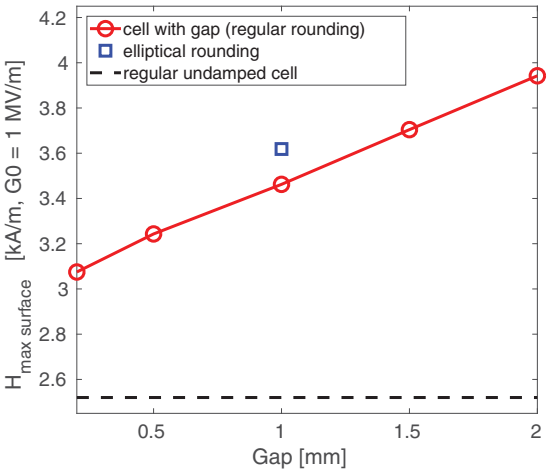

(b) Peak Surface Magnetic Field.

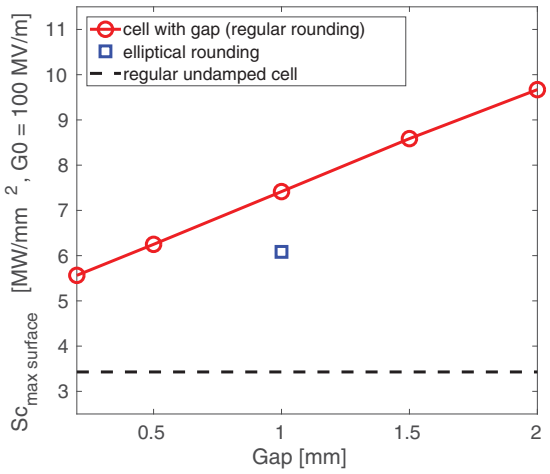

(c) Peak Surface S_c.

FIG. 3. Surface field simulations for the CLIC-G-OPEN design compared to the CLIC-G structure. [9].

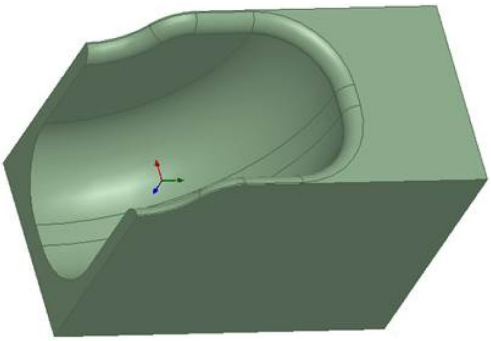

(a) Elliptical Rounding

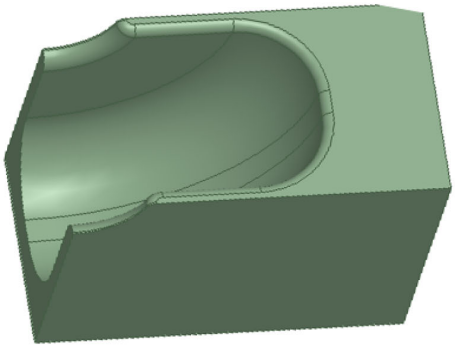

(b) Regular Rounding.

FIG. 4. Rounding profile used on the CLIC-G-OPEN compared to previous CLIC structures [7].

rf performance. We note that a similar approach could be used to reduce trapping of long-range wakefields in the structure [6]. We determined the optimal gap size and other parameters using Ansys' HFSS to model a quarter cell [7], shown in Fig. 2. The addition of this gap into a closed geometry was expected to increase surface fields. A simulation of the surface fields for various gap widths, featured in Fig. 3, indicated that a greater gap size led to

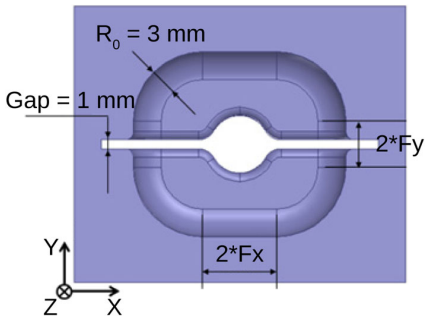

FIG. 5. A cross section of the cell geometry with parameters F_x and F_y which represent size of the flat region of the racetrack design [9].

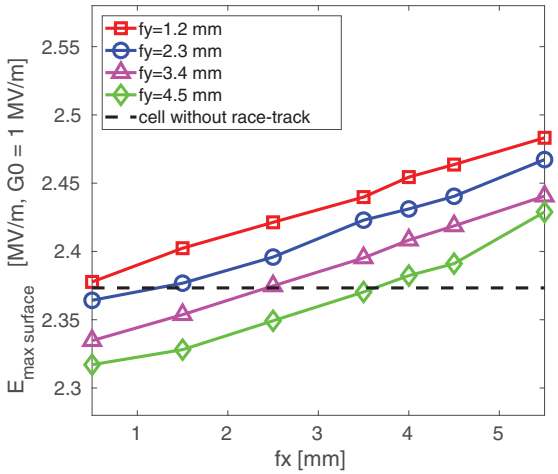

(a) Peak Surface Electric Field.

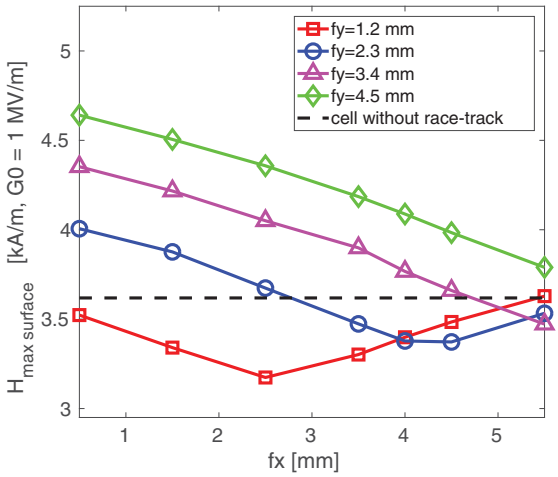

(b) Peak Surface Magnetic Field.

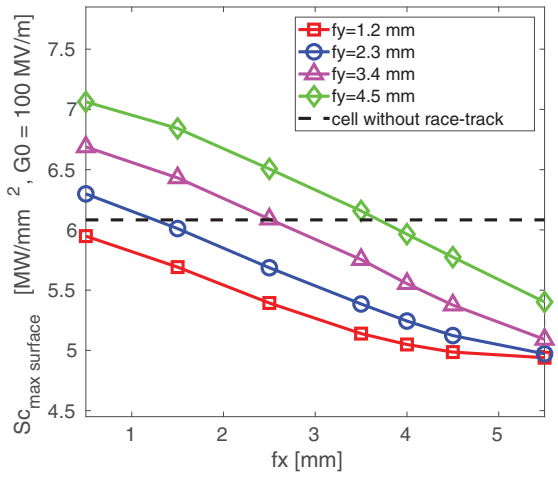

(c) Peak Surface S_c.

FIG. 6. Optimization of the straight sections, F_x and F_y, in the racetrack geometry. [9].

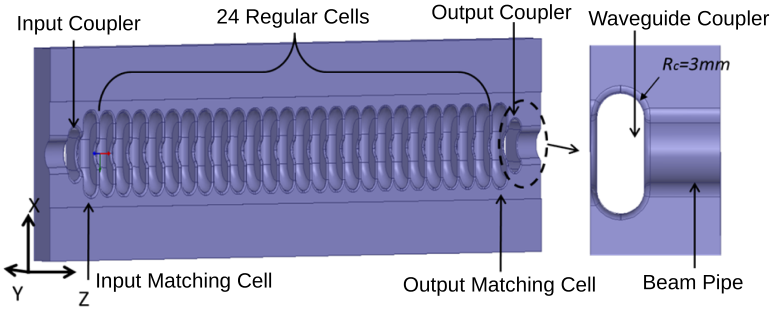

FIG. 7. CLIC-G-OPEN structure half with 24 regular cells and 2 matching cells. The waveguide coupler is also displayed on the right [11].

an increase in peak electric (E) and magnetic (H) fields, and modified Poynting vector (S_c). S_c is closely related to local power flow [8] which is one of the main field quantities which is minimized, along with the surface electric and magnetic fields, during the design and optimization of high-gradient structures.

Figure 6 in [10] depicts a copper pulse heating sample with damage due from the exposure to extremely high electromagnetic fields. During the high power test, the sample was a part of the cavity as show in Fig. 4 in [10]. In this particular experiment, there was a gap between the sample and the cavity body approximately 25 microns wide. Since the mode in the cavity is of type TE, it was expected that there would be no field in the gap, and therefore no damage beyond radius of 2.5 cm. As seen on Fig. 6 in [10], there is obvious damage beyond edge of the cavity in the "no field" area. In the following tests the pulse-heating cavity was re-designed to eliminate the gap. With this experience in mind, we selected the gap in CLIC-G-Open to be significantly larger than 25 microns. We use 1 mm gap as a compromise between increasing the surface fields and degrading high power performance due to the small gap.

Elliptical rounding on the edges, the profile of which is demonstrated in Fig. 4, was used to simplify the fabrication process by permitting the use of a single rounding profile for each cell. Figure 3 also compares the surface fields with (blue square) and without a new elliptical edge rounding technique at the chosen gap size. Peak surface E fields and S_c decreased 17.5% and 18%, respectively, under the new rounding in comparison to the regular rounding at the expense of a 4.4% increase in the maximum surface H field.

The cross-sectional profile of the CLIC-G-Open structure is illustrated in Fig. 5. The lengths of the horizontal and vertical flat sections are defined as F_x and F_y, respectively. Optimization of the peak surface fields, for various values of F_x and F_y are depicted in Fig. 6. It can be seen that to minimize the peak S_c one can increase F_x and decrease F_y, and consequently also reduces the peak H field. We chose the value $F_y = 1.2$ mm as this minimizes the peak H field and S_c. F_x was chosen to be 4.0 mm as a compromise between the peak H fields and S_c.

III. FULL STRUCTURE GEOMETRY

A tapered structure with 24 regular cells, 2 matching cells and waveguide couplers was generated from the optimized single cell geometry. Figure 7 demonstrates the HFSS design of the structure half and the waveguide coupler. Waveguide couplers on the CLIC-G-Open are double fed and manufactured through precision milling, with internal edges possessing a 3 mm rounding. A comprehensive list of the structure parameters is detailed in Table I together with the parameters of the undamped CLIC-G structure used as the basis for the design [11].

IV. STRUCTURE FABRICATION AND TUNING

A prototype of the CLIC-G-Open design was fabricated at SLAC using precision milling on copper blocks. A full structure, as well as a single structure half, was produced and is seen in Fig. 8. In preparation for the brazing the rf

TABLE I. Structure parameters for the CLIC-G-Open structure compared to the CLIC-G structure [11]. All values are normalised to an unloaded gradient of 100 MV/m.

Parameter	CLIC-G Open	CLIC-G
Unloaded Gradient [MV/m]	100	100
Input/output iris radii [mm]	3.15/2.35	3.15/2.35
Group velocity normalized to the speed of light (c) [%c]	1.99/1.06	1.79/0.91
Shunt impendence [MΩ/m]	107/137	116/150
Peak input power [MW]	44.5	37.5
Filling time [ns]	49	57
Maximum E-field [MV/m]	268	222
Maximum S_c [MW/mm^2]	5.16	3.51
Maximum pulsed surface heating for a 200 ns pulse [K]	25	14

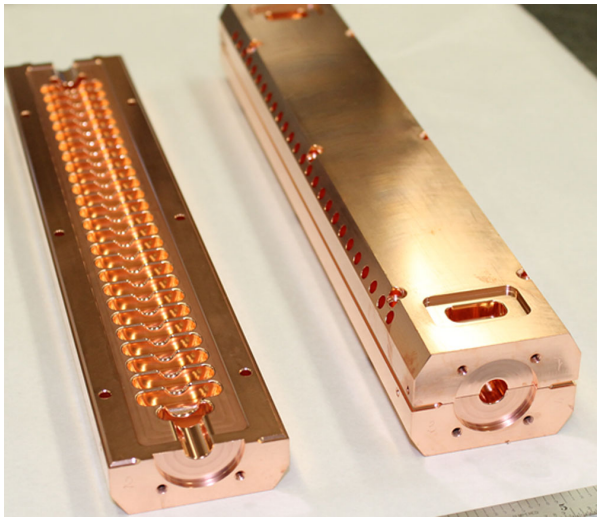

FIG. 8. Photos of the CLIC-G-OPEN after milling and after installation [11].

flanges were plated in copper and chemical etching for 30 sec removed undesirable surface structures. After cleaning, a pre-brazing beadpull measurement was performed to verify structure's dimensions. The pre-brazing beadpull was enabled by the structure design. As no rf currents flow through the joint, the rf parameters of the halves clamped are very similar to that of the brazed structure. This is not possible with the structure made from disks. Finally, atmospheric pressure hydrogen brazing adhered the two halves using a Cu-Au alloy brazing filler.

After brazing, the structure was tuned using non-resonant bead-pulling technique [12]. A comparison of the S-parameters for the brazed structure before and after tuning, as well as the results from the bead-pull measurements, are exhibited in Fig. 9. A good field flatness and low phase advance spread of $120° \pm 2°$ was achieved after tuning. Ultimately, the structure was fired in an ultra-high vacuum at 550°C for over eight hours to asymptote the pressure at temperature.

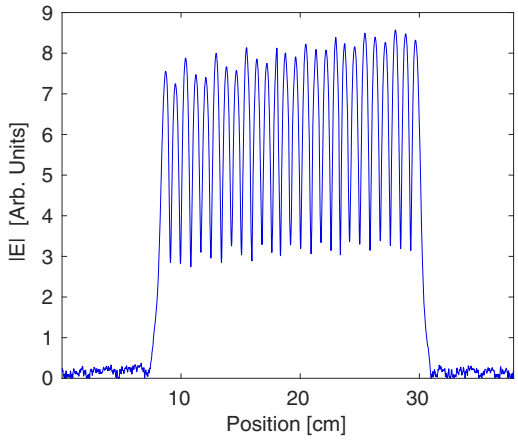

(a) On-axis electric field amplitude.

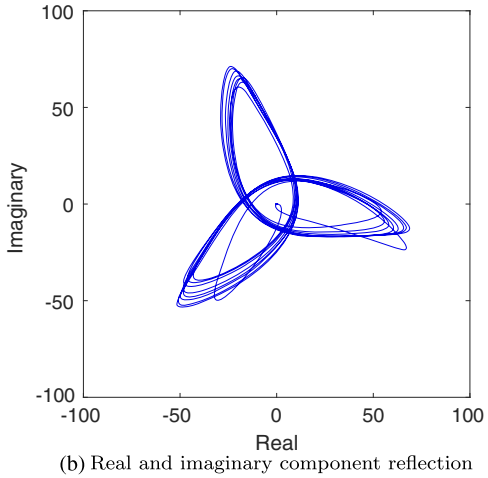

(b) Real and imaginary component reflection from bead-pull measurements.

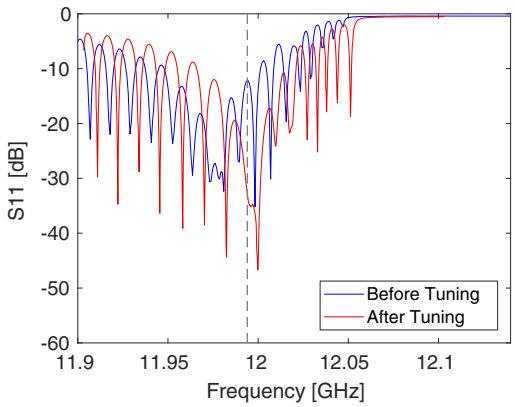

(c) S11 input from coupler as brazed and final.

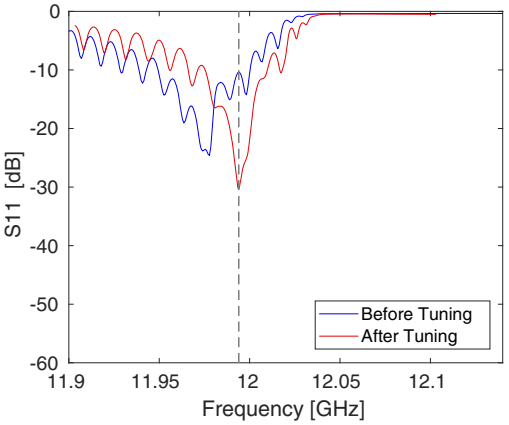

(d) S11 from output coupler as brazed and final.

FIG. 9. S-parameters and results from bead-pull measurement of the brazed structure before and after tuning [11].

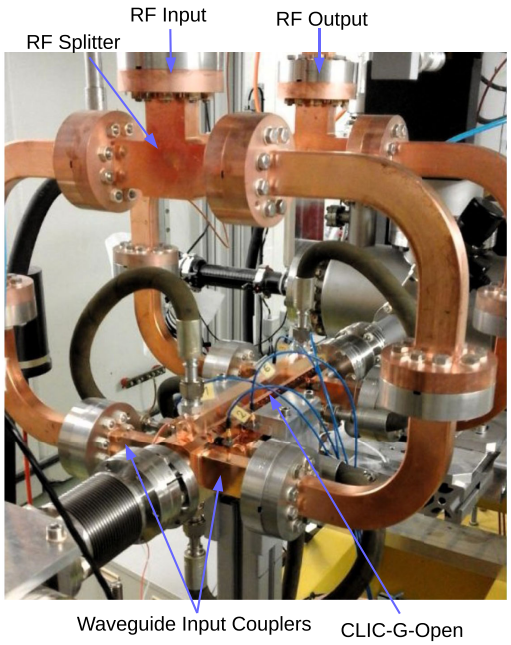

FIG. 10. Photos of the CLIC-G-OPEN after milling and after installation [11].

V. HIGH POWER TESTING

Following tuning, the structure was shipped to CERN where high power testing was conducted on the Xbox-2 X-band test stand (Fig. 10). First commissioned in 2012, Xbox-2 is the second X-band test stand at CERN. The CLIC-G-Open structure was the second structure conditioned at this test stand following a crab cavity test [13]. Based on the same high power infrastructure as Xbox-1 [14], Xbox-2 uses a 50 MW CPI

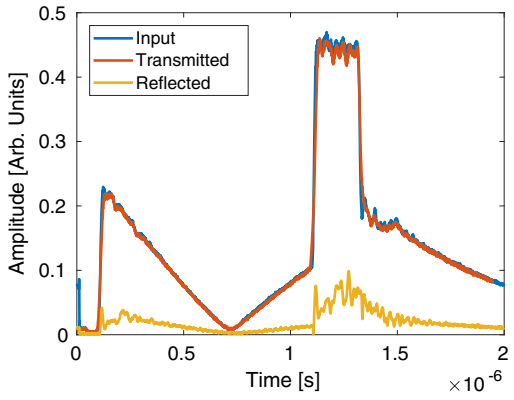

(a) Normal Pulse

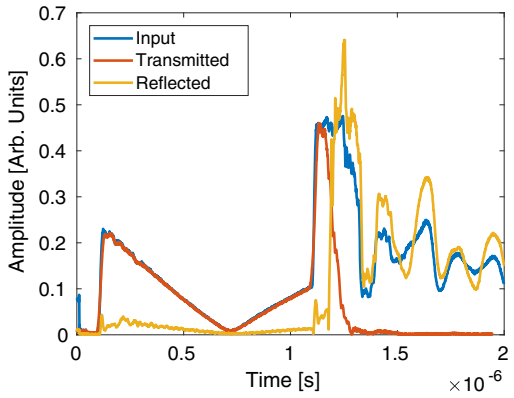

(b) Breakdown Pulse

FIG. 11. Example of the rf signals for the input, transmitted, and reflected signals.

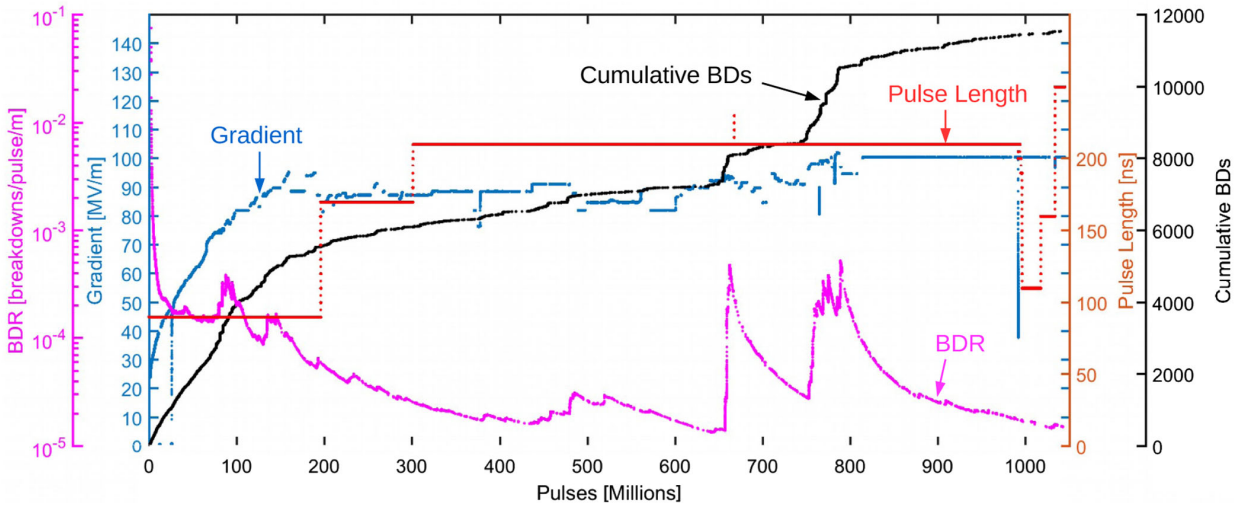

FIG. 12. Summary of the CLIC-G-Open high power test history.

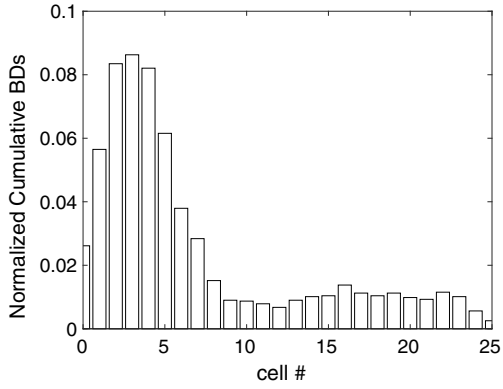

(a) Breakdown distribution along the structure.

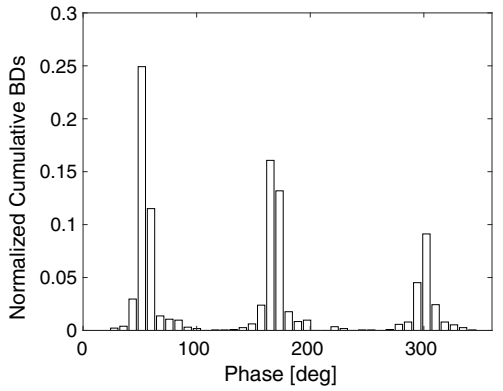

(b) Phase differential from input to reflected RF signals.

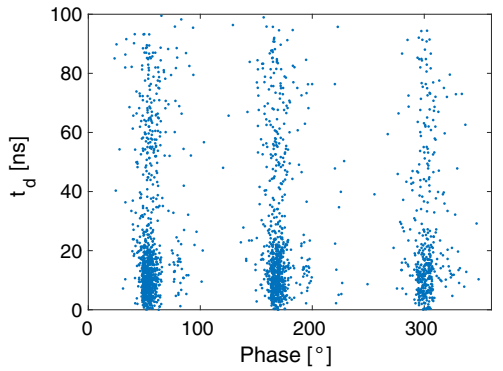

(c) Breakdown distribution along the structure vs phase differential from input and reflect RF signal. Grid lines demonstrate the cell boundaries.

FIG. 13. Breakdown distributions inside the structure normalized to the total number of breakdowns.

klystron and Scandinova modulator with a maximum pulse length of 1.5 μs operating at 50 Hz. Further amplification was achieved through the use of a SLED-I pulse compressor. The pulse compressor can be fully detuned using mechanical pistons for instances where the additional amplification is not required.

For diagnostics of the rf signals, 50 dB directional couplers installed on the waveguide network at the input and output of the structure allow for the measurement of the incident, transmitted, and reflected rf signals from the structure. These signals, along with DC signals from two Faraday cups placed upstream and downstream, were used for breakdown diagnostics, including breakdown location. Understanding the distribution of breakdowns within the structure is key to understanding the performance of a structure and the limiting factors in its design. A time-of-propagation method is used to find the location of a breakdown using the rising edge of the reflected signal and falling edge of the transmitted signal. Figure 11 displays an example of an rf pulse with and without a breakdown. The real-time system used a threshold detector on the rf and DC signals to trigger during a breakdown event, logging the breakdown event and two pulses before the breakdown as reference signals. Controlling the conditioning of the structure was an algorithm originally written for Xbox-1 in 2013 [14–16]. Pulsing began in September of 2015 and by the end of high power testing the structure had undergone 1.05 billion pulses and 11 700 breakdowns. Figure 12 summarizes the history of the structure's high power testing. At the beginning of the conditioning process, the breakdown rate (magenta) was kept at a constant 2.5×10^{-4} breakdowns/pulse/m. Once reaching an unloaded gradient of 95 MV/m (blue) at 150 million pulses, radiation emitted from the structure exceeded the maximum safety limit outside the bunker. As the input power to the structure could not be increased until this issue was solved, the structure ran at a reduced and constant gradient of 90 MV/m. This began at 150 million pulses with the first pulse length of 90 ns where the structure continued to condition, demonstrated by the decreasing trend in the breakdown rate seen up to 200 million pulses. Conditioning of the structure led to a reduction in radiation and allowed the pulse length to be increased, without surpassing the maximum radiation safety limit, firstly to 160 ns at 200 million pulses. From 300 million pulses onwards the final pulse length of 200 ns was set. Various experiments were performed investigating the relation between power and BDR, seen as steps in the power. Increased shielding on the bunker, applied after 600 million pulses, allowed the resumption of power increments towards 100 MV/m. Once reaching the desired 100 MV/m, at 800 million pulses, the structure ran with constant gradient and conditioned down to a low breakdown rate. At 1.05 billion pulses, a breakdown rate of $< 1.5 \times 10^{-5}$ breakdowns/pulse/m was achieved at which time the structure conditioning

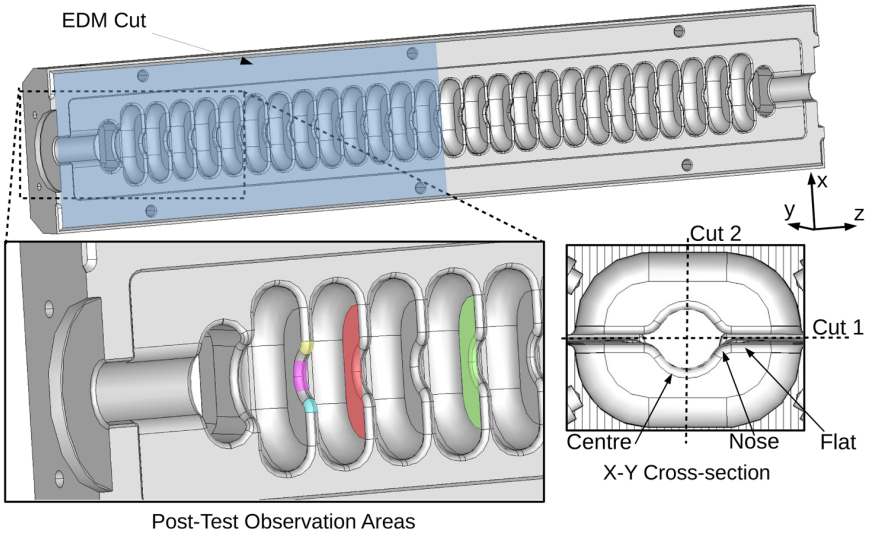

FIG. 14. Diagram of a half of the CLIC-G-OPEN structure demonstrating the EDM cut in blue. Post-test observations with a borescope looked at the iris 2 (red) and iris 4 (green) before cutting. After cutting, SEM images of the first iris looked at the left (yellow) and right (cyan) nose, and the center (magenta). An X-Y cross section demonstrating structure nomenclature.

was concluded. The achieved gradient of 100 MV/m with a 200 ns pulse is comparable to the gradient achieved by other structures up to this time, demonstrating the validity of the fabrication technique.

After conditioning, the breakdown distributions were analyzed to understand the limiting factors of the design [17]. Figure 13(a) displays the breakdown distribution in the CLIC-G-Open after conditioning, translated into a cell number and normalized to the total number of breakdowns. Breakdowns occurred predominantly toward the input of the structure.

Measuring the phase of the incident and reflected rf signals gives breakdown location information due to the known phase advance per cell. For CLIC structures, the phase advance is 120° per cell which means that the breakdowns can be diagnosed to location within a 3 cell segment which repeats throughout the structure as the phase wraps upon itself. Figure 13(b) demonstrates that the breakdown distribution appeared as three peaks for the measured phase difference.

Plotting the phase difference against the positional distribution, Fig. 13(c) illustrates a structure predominantly undergoing rf breakdown in a few adjacent irises at the input of the structure. Understanding this nonuniform breakdown distribution is key to improving the next iteration of a structure designed from halves.

VI. POST-TEST SURFACE EXAMINATION

After removing the structure from Xbox-2, the structure was stored as a radioactive material for several months remaining in a nitrogen environment to prevent surface degradation. Figure 14 describes the structure's nomenclature and areas surveyed in the post-test analysis. To begin, S-parameter and bead-pull measurements were performed to evaluate the change in rf properties due to the high power testing. In contrast to most other high gradient structures, the investigated CLIC-G-Open demonstrated nearly no change in the electric field distribution (amplitude and phase advance per cell) and only slight changes in the S-parameters for the input and output coupler, see Fig. 15.

Before the structure underwent cutting, a borescope was used to observe any visible physical damage. Pictures from the borescope signified that the breakdown induced damage was towards the start of the structure (Fig. 16). For closer examination the structure was cut using electron discharge machining (EDM) and divided into several sections; two halves cut through the brazing material (Cut 1) for cells 1 to 13, two halves for cells 14 to 19 (Cut 2), and the rest of the structure remained intact.

A photo of the half section containing cells 1 to 13 is displayed in Fig. 17. Marked in a blue box is an issue which came to light after the structure was cut. During the brazing procedure, brazing alloy leaked from the joint into the rf region of the structure. This material reached within 200 μm of the cell edge. To determine the effect of the leak on the structure performance the halves were observed with a scanning electron microscope (SEM). Images of the surface, seen in Fig. 18, demonstrate the breakdown density on the center and nose sections of the cell. Breakdowns occurred primarily on the nose section with only a few visible marks on the center section. Overlaying the surface E field and S_c we find that the breakdowns are most likely

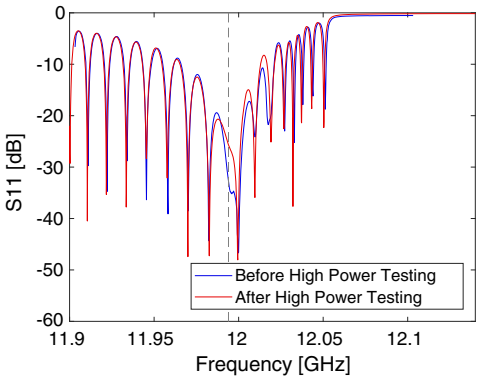

(a) S11 from input coupler.

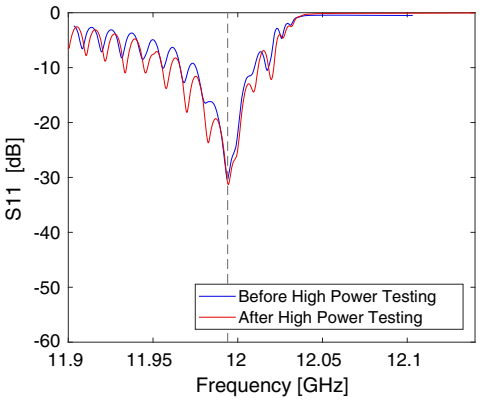

(b) S11 from output coupler.

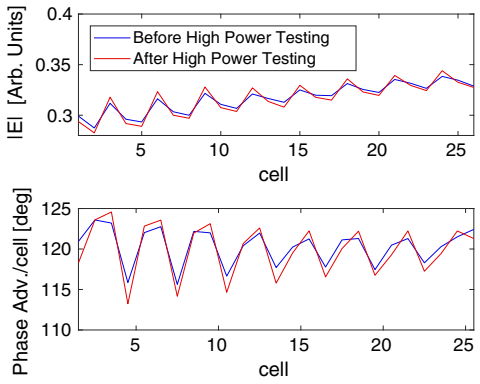

(c) Electric field amplitude and phase distributions.

FIG. 15. A comparison of the rf tests before and after high power testing.

to occur around the area with the greatest E or S_c though due to the similarities on the field profiles we are unable to distinguish which was the cause. Comparing the breakdown densities of the two opposing nose sections demonstrated similar numbers for the two sided. Given this, we found that the breakdowns preference for the first few cells was not related to the brazing filler leak.

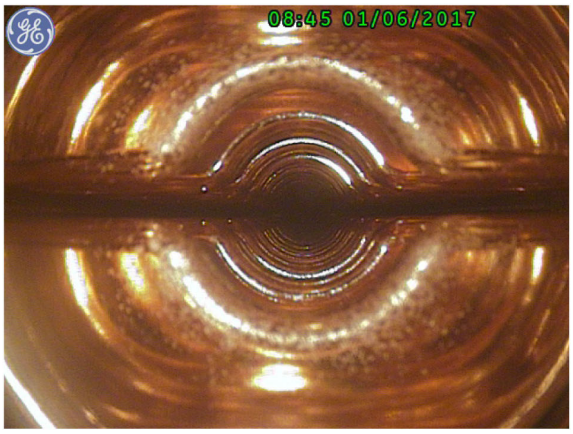

(a) Iris 2

(b) Iris 4

FIG. 16. Borescope images from the structure after conditioning. The location of the irises is described in Fig. 14.

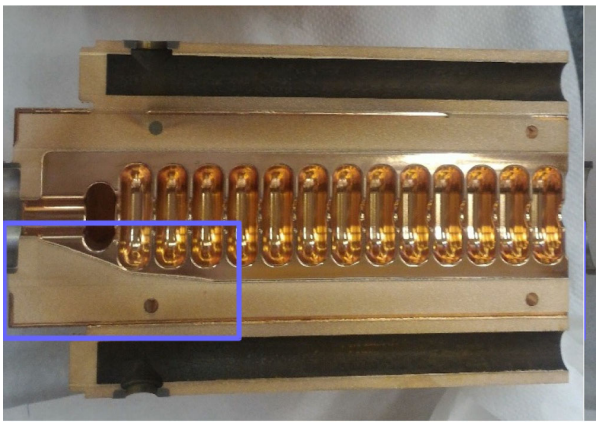

FIG. 17. Leaked brazing material visible at the input of the structure circled in blue.

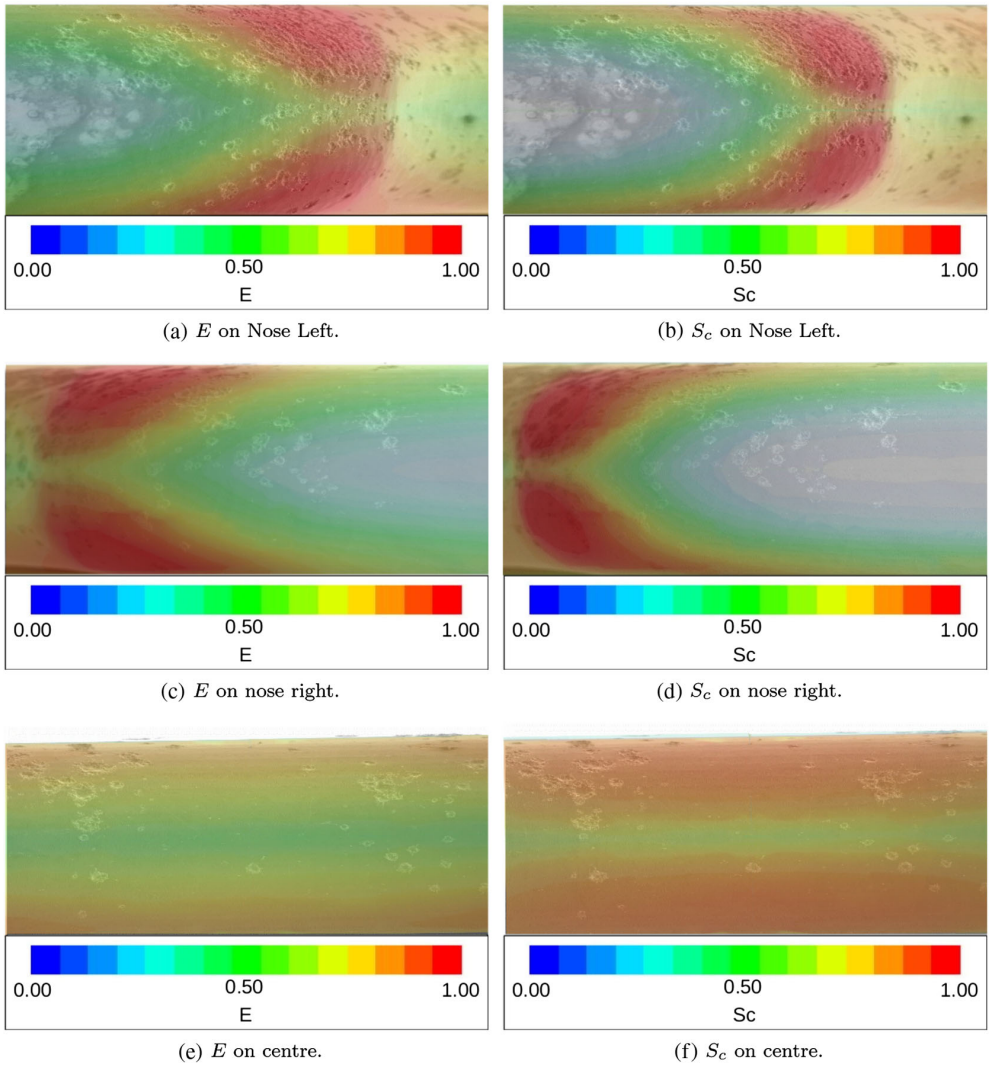

(a) E on Nose Left. (b) S_c on Nose Left.

(c) E on nose right. (d) S_c on nose right.

(e) E on centre. (f) S_c on centre.

FIG. 18. Scanning electron microscope images of various segments along the first iris. Overlaid is a field map of the surface electric field for a comparison of the breakdown location to the field strength. The location of each scan is described in Fig. 14.

VII. CONCLUSION

A prototype for an 11.994 GHz CLIC structure made through a novel fabrication technique has been designed, fabricated and tested in a collaborative effort between CERN and SLAC. With the aim of a more cost-effective fabrication, the structure is designed to be manufactured from two milled halves and brazed together. Testing of the structure at high power was performed at CERN's Xbox-2 where the structure underwent high power testing for 1.05 billion pulses. Ultimately an unloaded gradient of 100 MV/m at a BDR of 1.5×10^{-5} breakdowns/pulse/m was achieved with a 200 ns pulse which is comparable to other CLIC structures. Breakdown distributions were found from analyzing the waveforms during testing. These distributions demonstrated a dominance of breakdowns towards the start of the structure which was confirmed with a post-test analysis. Post-test rf measurements demonstrated that the rf properties were very similar before and after high power testing. Observations of the structure found brazing filler leaked around the input cells of the structure though it was determined that this did not affect the breakdown distribution. The next generation of the CLIC-G-OPEN is being built. This structure will have identical rf geometry but be made from a hard CuAg alloy and joined using electron beam welding. The choice of a hard copper alloy results from extensive testing which has demonstrated that hard copper performs better at high gradients than soft copper [10,18].

ACKNOWLEDGMENTS

The authors would like to sincerely thank the structure production teams at CERN and SLAC for their essential contributions to the preparations and follow up of this experiment.

[1] M. Aicheler *et al.*, A Multi-TeV Linear Collider Based on CLIC Technology, Repotr No. CERN 2012-007.

[2] J. W. Wang, J. R. Lewandowski, J. W. Van Pelt, C. Yoneda, G. Riddone *et al.*, Fabrication technologies of the high gradient accelerator structures at 100 MV/m range, in *Proceedings of the International Particle Accelerator Conference, Kyoto, Japan* (ICR, Kyoto, 2010).

[3] T. Abe, Y. Arakida, T. Higo *et al.*, Basic Study on high gradient accelerating structure at KEK/NEXTEF, *12th Annual Meeting of Particle Accelerator Society of Japan*, http://www.pasj.jp/web_publish/pasj2015/proceedings/index.html.

[4] A. Solodko, X-band accelerating structure fabrication in the perspective of mass production and cost optimization, Talk at LCWS 2017, 2017, Strasbourg (unpublished).

[5] B. Woolley, *High Power X-band RF Test Stand Development and High Power Testing of the CLIC Crab Cavity*, Lancaster University, United Kingdom (Lancaster University, 2015).

[6] S. Doebert *et al.*, High power test of an X-band slotted iris acccelerating structure at NLCTA, in *Proceedings of the 22nd Particle Accelerator Conference, PAC-2007, Albuquerque, NM* (IEEE, New York, 2007).

[7] Ansys HFSS, http://www.ansys.com.

[8] A. Grudiev, S. Calatroni, and W. Wuensch, New local field quantity describing the high gradient limit of accelerating structures, Phys. Rev. ST Accel. Beams **12**, 102001 (2009).

[9] H. Zha, A. Grudiev, and V. Dolgashev, RF Design of the CLIC structure prototype optimized for manufacturing from two halves, IPAC15, Richmond, USA, in *Proceedings of the 6th International Particle Accelerator Conference* (Jacow, Richmond, 2015).

[10] L. Laurent, S. Tantawi, V. Dolgashev, C. Nantista, Y. Higashi, M. Aicheler, S. Heikkinen, and W. Wuensch, Experimental study of rf pulse heating, Phys. Rev. ST Accel. Beams **14**, 041001 (2011).

[11] N. Catalan *et al.*, Fabrication and high gradient testing of an accelerating structure made from milled halves, in *Proceedings of the 28th Linear Accelerator Conference* (Jacow, East Lansing, 2016).

[12] C. W. Steele, A non-resonant perturbation theory, IEEE Trans. Microwave Theory Tech. **14**, 70 (1966).

[13] B. Woolley *et al.*, High gradient testing of an X-band crab cavity at XBOX2, IPAC15, Richmond, USA, in *Proceedings of the 6th International Particle Accelerator Conference* (Jacow, Richmond, 2015).

[14] N. Catalan-Lasheras *et al.*, Experiences operating an X-band high-power test stand at CERN, IPAC14, Dresden, Germany, in *Proceedings of the 5th International Particle Accelerator Conference* (Jacow, Dresden, 2014).

[15] National Instruments, http://www.ni.com.

[16] A. Degiovanni *et al.*, High-gradient test results from a CLIC prototype accelerating structure: TD26CC, IPAC14, Dresden, Germany, in *Proceedings of the 5th International Particle Accelerator Conference* (Jacow, Dresden, 2014).

[17] A. Degiovanni *et al.*, Diagnostics and analysis techniques for high power X-band accelerating structures, LINAC14, Geneva, Switzerland, in (Jacow, Geneva, 2014).

[18] E. I. Simakov *et al.*, Advances in high gradient normal conducting accelerator structures, Nucl. Instrum. Methods Phys. Res., Sect. A, DOI: 10.1016/j.nima.2018.02.085 (2018).

Nuclear Inst. and Methods in Physics Research, A 914 (2019) 46–52

Contents lists available at ScienceDirect

Nuclear Inst. and Methods in Physics Research, A

journal homepage: www.elsevier.com/locate/nima

Dependency of the capture of field emitted electron on the phase velocity of a high-frequency accelerating structure

Thomas Geoffrey Lucas [a,*], Theodorous Argyopolous [b], Mark James Boland [d], Nuria Catalan-Lasheras [b], Roger Paul Rassool [a], Claudio Serpico [c], Matteo Volpi [a], Walter Wuensch [b]

[a] University of Melbourne, Parkville 3010, Australia
[b] CERN, Geneva, Switzerland
[c] Elettra-Sincrotrone Trieste S.C.p.A., Trieste, Italy
[d] University of Saskatchewan, Saskatoon, Canada

ARTICLE INFO

Keywords:
Linear accelerators
Dark current
High gradient
X-band
Compact linear collider
Radiation

ABSTRACT

Surface electric fields within high gradient linear accelerators can exceed 200 MV/m and lead to field emitted (FE) electrons entering the structure. When the accelerating field conditions permit, these FE electrons can become captured in the RF fields and be transported through the accelerating structure as a dark current. Understanding the capture and transport of these FE currents in high frequency linear accelerators, and at accelerating gradients well above the capture threshold, is important for the operation of CERN's X-band test stands and other high gradient linear accelerators. Such dark current leads to a background radiation, which dictates shielding requirements and can damage adjacent instrumentation, as well as a background current within the structure, which can affect beam diagnostics and in the most extreme cases can cause transverse kicks on bunches. The capture of field emitted electrons is described analytically in a one dimensional approximation and is then evaluated numerically for a test structure geometry. A particular focus for the analysis is how the interaction varies with phase velocity. We demonstrate how the phase velocity varies with respect to the nominal driver frequency and structure operational temperature. Measurements on the X-band test stands at CERN demonstrate that the capture increases 12%–28% for a 1 MHz increase in the driver frequency. A three dimensional RF and particle simulation found a similar order of magnitude result for a 1 MHz increase corrborating the measurements.

1. Introduction

RF accelerating structures for the Compact Linear Collider (CLIC), and other high gradient applications, will operate with surface fields in excess of 200 MV/m [1–4]. At these surface field strengths, the spontaneous emission of electrons, known as "field emission", and subsequent capture in accelerating fields results in a propagating current [5]. For high power testing and operation of accelerating structures, this propagating current determines the background radiation dose received by local instrumentation and influences the radiation shielding requirements for experiments [6]. The current which propagates along the structure also affects beam diagnostics and in extreme cases can lead to transverse kicks on bunches [7].

Nominally, the loaded accelerating gradient and operating frequency of CLIC is 100 MV/m and 11.994 GHz for a 3 TeV version where this is reduced to 75 MV/m for the 380 GeV first stage. For this frequency, the capture threshold for an electron at rest is 64 MV/m [8], and therefore well below the operational accelerating gradient. In the following paper, we investigate an observed dependency of the propagating current on the operational phase velocity of the high frequency CLIC structures. Using conditions given in [8], we investigate the effects of how small variations in the nominal RF frequency and structure temperature affect phase velocity and therefore field emission capture. Measurements of the propagating current's dependency on phase velocity were performed on CERN's X-band test stands and then corroborated through a series of simulations using the CST Microwave and Particle Studio packages [9].

2. X-band test stands at CERN

Development of high gradient normal conducting accelerating structures is important for the feasibility of next generation linear colliders [10]. In an effort to understand the operation and reproducibility of high gradient accelerating structure, CERN has commissioned three individual X-band test stands which can test structure at high power. The three test stands, named Xbox 1, Xbox 2 and Xbox 3, generate high

* Corresponding author.
E-mail address: t.lucas@student.unimelb.edu.au (T.G. Lucas).

https://doi.org/10.1016/j.nima.2018.10.166
Received 20 August 2018; Received in revised form 18 October 2018; Accepted 22 October 2018
Available online xxxx

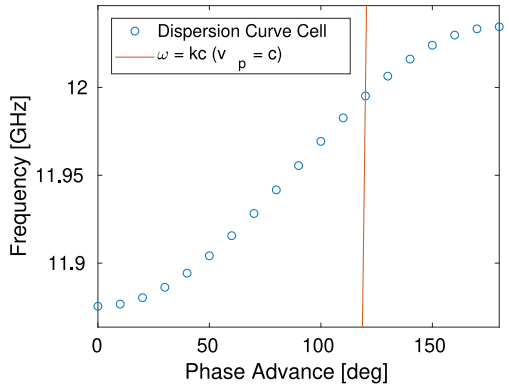

Fig. 1. Operational points on the dispersion curve for the TD26CC middle cell.

power RF pulses using X-band modulators and klystrons which operate up to 50 MW for Xboxes 1 and 2, and 6 MW which are combined to 12 MW for Xbox 3 [11–15]. After compression, using a SLED Type I RF pulse compressor, the power systems deliver above 120 MW up to 50 Hz for Xbox 1 and 2, and up to 50 MW up to 200 Hz per line for XBox 3 to the structure [12]. This high power RF produces unloaded accelerating gradients in excess of 100 MV/m, several times that seen in S-band linear accelerators, commonly used in electron linacs. Resulting from the high power RF are peak surface electric fields of approximately 200 MV/m for CLIC structures for the nominal unloaded accelerating gradient [4]. These high surface fields lead to the field emission of electrons. The emitted current density of these electrons, first described by Fowler and Nordeim in [5], is given by

$$j_F = 1.54\times10^{-6}10^{4.52\phi^{-0.5}}\frac{\beta^2E(t)^2}{\phi} \times\exp\left(-\frac{6.53\times10^9\phi^{1.5}}{\beta E(t)}\right)[\mathrm{A\ m^{-2}}] \quad (1)$$

where ϕ is the work function of copper in eV, β is the field enhancement factor, and $E(t)$ is the electric field strength at the time of emission in V/m [5,16].

With such high accelerating gradients, field emitted electrons can be captured and begin to propagate along the structure known as a dark current. The condition for capture of these electrons is well known and the same as those for the electrons intended for acceleration. This condition is that the gradient is great enough such that a stationary electron can accelerate to stay synchronous with the oscillating RF field. Given a phase velocity of c, this threshold in MV/m is given by

$$E_0 \geq \frac{1.6}{\lambda} \quad (2)$$

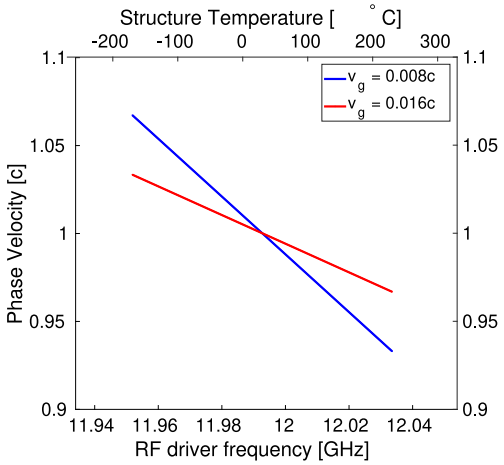

Fig. 3. Variation in the radiation due to the change in structure temperature.

where λ is the RF wavelength in metres [17]. This equation demonstrates that the capture gradient increases inversely to the RF wavelength and therefore is greater in higher frequency linear accelerators.

3. Phase velocity dependence of dark current

In Eq. (2) the threshold gradient for the capture of field emitted electrons in a linear accelerator was described for the special case of the RF phase velocity being equal to c. A more general equation for capture can be written for the case of a varying phase velocity (v_p) as

$$E_0 \geq \frac{\pi m_0c^2}{\lambda e}\left(\frac{v_p - v_0}{v_p + v_0}\right)^{\frac{1}{2}}, \quad (3)$$

where m_0 is the mass of an electron, e is the electron charge magnitude, and v_0 is the velocity of the electrons [8]. Such a relation demonstrates that a reduction in the phase velocity reduces the required gradient for capture of low energy electrons. To understand how the phase velocity varies with the operational parameters we begin with the definitions of phase velocity and group velocity as

$$v_p = \frac{\omega}{k}, \quad (4)$$

and

$$v_g = \frac{d\omega}{dk}, \quad (5)$$

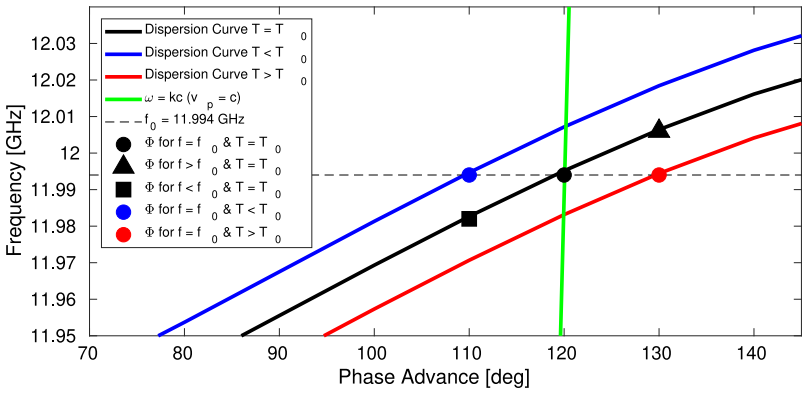

Fig. 2. Operating modes for three structure temperatures and three RF driver frequencies.

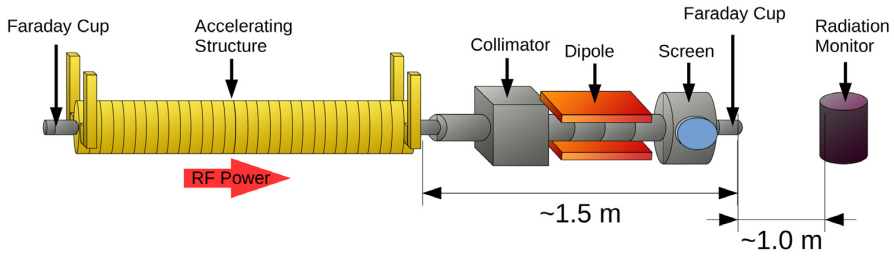

(a) Xbox 2 and spectrometer.

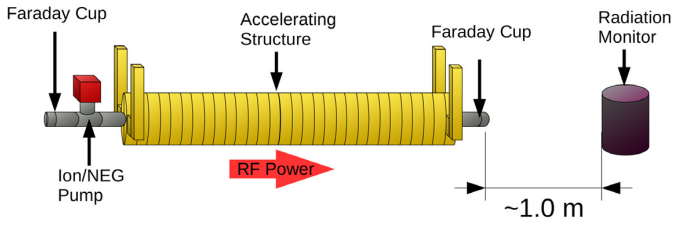

(b) Xbox 3.

Fig. 4. Experimental setup for the measurement of the dependence of dark current on the RF driver frequency and structure temperature using a radiation monitor.

respectively, where ω is the RF driver frequency and $k = 2\pi/\lambda$ is the wavenumber [17]. We see that the phase velocity can be varied through a change in ω (See Fig. 1). Differentiating Eq. (4) against ω gives the variation in phase velocity with respect to RF driver frequency as

$$\frac{dv_p}{d\omega} = \frac{1}{k} - \frac{\omega}{k^2}\frac{dk}{d\omega} \tag{6}$$

$$= \frac{1}{k}\left(1 - \frac{\omega}{k}\frac{1}{v_g}\right) \tag{7}$$

$$= \frac{\lambda}{2\pi}\left(1 - \frac{v_p}{v_g}\right). \tag{8}$$

Setting the synchronicity condition as c we find

$$dv_p = \frac{\lambda}{2\pi}\left(1 - \frac{c}{v_g}\right)d\omega. \tag{9}$$

This gives the relation between the variation in the phase velocity and driver frequency set value. From this relation we find that an increase in the driver frequency results in a decrease in the phase velocity, given typical group velocity (v_g) values for CLIC structures are well below c and given the structures are a forward travelling wave design, where the group velocity travels in the same direction as the phase velocity. For a backward travelling wave structure, the group velocity travels in the opposite direction of the phase velocity therefore an increase in the driver frequency results in an increase in the phase velocity, according to Eq. (9).

Equivalent to a variation in the RF driver frequency, a shift in the resonant frequency (ω_r) can also vary the phase velocity. Such a shift in ω_r can be achieved through a variation in the structure's operating temperature which causes thermal expansion/contraction of the structure, and therefore changes the radius of the structure's cells. The variation in the resonant frequency for a given temperature change is given as

$$\frac{d\omega_r}{dT} = -\alpha\omega_r, \tag{10}$$

where α is the thermal expansion coefficient which for copper is 17×10^{-6} K^{-1} and $\omega_r = 2\pi f_r$ is the resonant frequency ($f_r = 11.994$ GHz) in rad/s. For a 1 °C increase in the structure temperature, we see a 203 kHz decrease in f_r. In Eq. (10) we see that the change in temperature varies the resonant frequency ω_r rather the driver frequency ω. To demonstrate how $d\omega_r$ is related to $d\omega$ Fig. 2 displays the operating points for three structure temperatures and three driver frequencies. It can seen that for the phase velocity ($v_p \propto f/\phi$) an increase in the structure temperature, which Eq. (10) explains is a decrease in the resonant frequency, is equivalent to an increase in the driver frequency. From these diagrams we find that an increase in ω_r is the equal to a reduction in ω such that

$$d\omega = -d\omega_r. \tag{11}$$

Substituting Eqs. (10) and (11) into Eq. (9) we get the change in the phase velocity with respect to structure temperature change as

$$dv_p = \frac{\lambda}{2\pi}\left(1 - \frac{c}{v_g}\right)\alpha\omega_r dT. \tag{12}$$

We find that an increase in the structure temperature similarly increases the phase velocity. In Fig. 2 we plot 5 points on a dispersion curve to demonstrate Eqs. (9) and (12). At the nominal driver frequency and structure temperature (●) we see that the phase velocity is $v_p = c$ as it lies on the green line, recalling $v_p \propto \omega/\Phi$ where Φ is the phase advance per cell. For an increase in the structure temperature (●) or an increase in the driver frequency (▲) we find the operational point is below the $\omega = kc$ line and therefore $v_p < c$. Conversely, for a decrease in the structure temperature (●) or a decrease in the driver frequency (■) we find $v_p > c$.

To understand the scales required for a noticeable variation in v_p, we plot the phase velocity normalised to the speed of light against the structure temperature and driver frequency in Fig. 3 for a group velocity of $0.008c$ and $0.016c$. These group velocity values are the maximum and minimum values within the iris-tapered CLIC baseline structure design [1]. The change in the phase velocity is $0.082\%c$/MHz and $0.164\%c$/MHz for a group velocity of $0.016c$ and $0.008c$, respectively.

Table 1
RF pulse parameters for three structures under test on the two test stands.

Test stand	Structure	Power [MW]	Gradient [MV/m]	Pulse Length [ns]	Rep. Rate [Hz]
Xbox 2	TD26CC R05	43	100	170	50
Xbox 3	TD24 R05 SiC	17	64	50	50
Xbox 3	T24 PSI	33	94	200	50

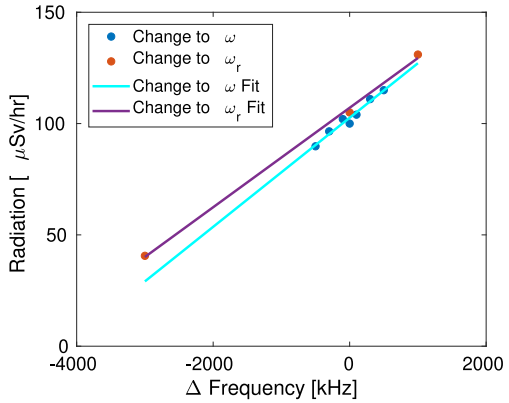

(a) TD26CC R05 N3

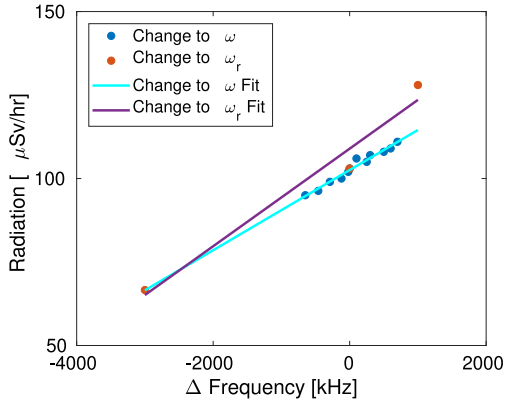

(b) T24 PSI

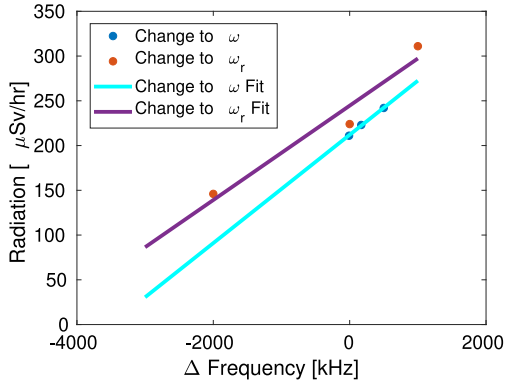

(c) TD24 R05 SiC

Fig. 5. Change in Radiation measured inside the bunker vs the change in the structure temperature and driver frequency.

Recalling Eq. (3) we saw that a decrease in the phase velocity reduces the required gradient for the capture of field emitted electrons. In summary we can state that: *The capture likelihood of field emitted electrons will increase when there is an increase in driver frequency or an increase in structure temperature due to a reduction in phase velocity, and vice versa.*

4. Measurements of dark current capture changes with phase velocity

First observations of a notable variation in the dark current level occurred by chance due to a malfunctioning structure temperature regulating chiller, during the conditioning of a test structure made from halves [18]. The incident led to a radiation safety threshold being exceeded and tripping an interlock. During this time it found that there was a strong correlation between the structure temperature and radiation outside the bunker. Testing of the dark current capture dependence on the phase velocity was performed on CERN's X-band test stands and came at a later date using three accelerating structures that were under high power testing at the time.

The RF driver frequency and structure temperature were varied for a constant peak power, pulse length and pulse repetition rate to measure the variation of steady state dark current [6]. Table 1 depicts the RF pulse parameters used for the testing on the three structures. The experimental setup of the dark current measurements for the structures installed on Xbox 2 and Xbox 3 are illustrated in Figs. 4a and 4b, respectively. The dark current measurements were performed indirectly using an ionisation chamber radiation monitor which tracked the radiation dosage at the end of the structure, known to be caused by dark current incident with the Faraday cup [6]. Between the measurements of each structure, the radiation monitor was aligned to be directly downstream of the structure under test and approximately 1 m from the end of the beamline. The spectrometer set up on Xbox 2 had its collimator and screen completely retracted during the measurement [19]. The choice of using the radiation monitor to measure dark current was due a poorly aligned Faraday cup in Xbox 2, after the spectrometer, consequently leading to poor signal strength. We will refer to the change in structure temperature as a shift in resonant frequency from here onwards, and calculate the equivalent frequency shift using Eq. (10). This will allow an easy comparison for the two operational parameter changes. Radiation measurements were performed at structure resonant frequency shifts of −3 MHz (−2 MHz for TD24 R05 SiC), 0 MHz, and +1 MHz. Likewise, radiation measurements were performed for a variation in the klystron driver frequency. Such variations in the driver frequency were restricted to ±1 MHz due to the bandwidth limitation of the klystron. In Fig. 5 we plot these radiation measurements for a given RF driver or resonant frequency shift, and fit each with a linear regression. For an increase in the RF driver and equal magnitude decrease in resonant frequency (structure temperature increase), we see an increase in the radiation level within the bunker. The vertical offset between the temperature and frequency measurements resulted from RF breakdowns causing new baseline dark current levels. When taking the driver frequency (ω) fit values we see that a 24.5%/MHz, 28.67%/MHz, and 12.64%/MHz shift in the radiation levels for the TD26CC, TD24SiC, and T24PSI, respectively. This increase in dark current for an increase in driver frequency and decrease in resonant frequency (increase in structure temperature) is what is expected from Eqs. (9) and (12) supporting the change in phase velocity as the mechanism for the dark current variation.

5. A three-dimensional simulation of dark current capture changes with phase velocity

To further study the effects of phase advance on field emitted current capture simulation have been made using CST Microwave and Particle Studio [9]. Calculating the entire structure geometry for RF fields and particle simulations required too much computation power to make it feasible. Instead, to obtain the electric and magnetic field distributions, we began with the eigenmode solver and a single cell geometry. The middle cell from the TD26CC R05 structure, currently the CLIC baseline structure, was used for the single cell geometry [4]. In this cell, the iris radius is 2.75 mm resulting in a group velocity of around $0.012c$. For the boundary conditions we started with $\Phi = 2\pi/3$ (120°) mode, as

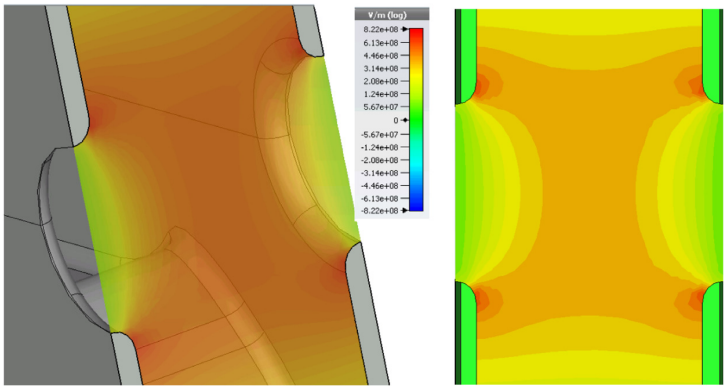

Fig. 6. Eigenmode Solution for the TD26CC R05 cell.

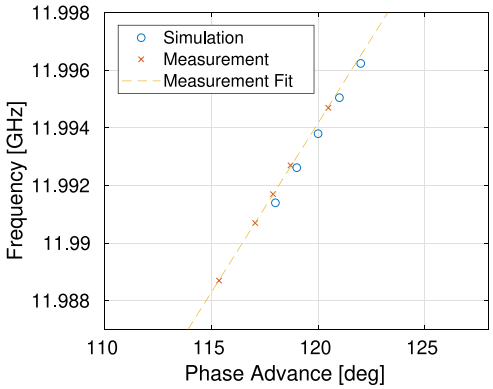

Fig. 7. Dispersion curve for the eigenmode solutions from the RF simulation overlaid on the RF measurements.

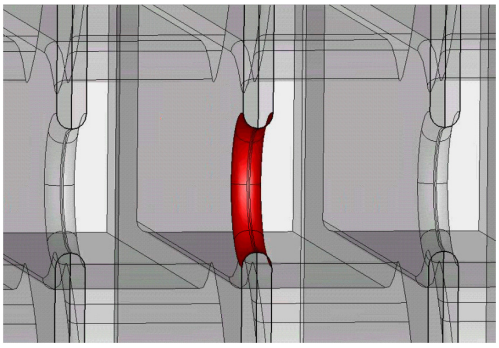

Fig. 8. Iris emission area used in the PIC solver.

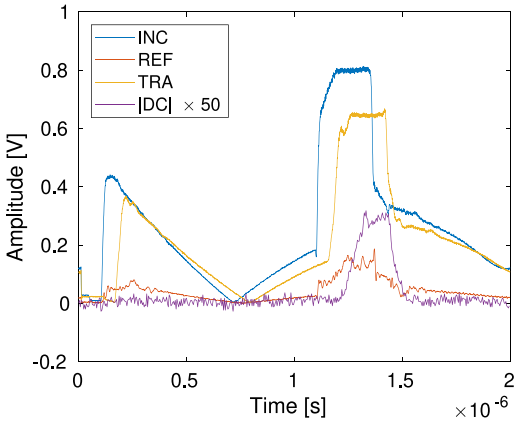

Fig. 9. Sample incoming (INC), reflected (REF), and transmitted (TRA) RF waveforms along with the downstream Faraday cup signal (DC).

used in the CLIC design, then solved the E and H fields for a single cell (Fig. 6). Surface electric fields are seen to be greatest near the iris and therefore are expected to be main source of field emitted electrons [5]. Running the eigenmode solver for various Φ values allowed a change in the frequency of the cell. In Fig. 7, the five points on the dispersion curve are plotted for different Φ values on the single cell geometry. The phase and group velocity is found using Eqs. (4) and (5), setting $k = \Phi/L_{cell}$ where L_{cell} is the cell length. These give the phase velocity and group velocity as $v_p = c$ and $v_g = 0.011998c$, respectively, which agrees well with the expected value. A non-perturbative bead-pull measurement gave the electromagnetic field distributions along the structure which demonstrated good agreement with the simulation [20,21].

For the particle model, a 48 cell model was assembled to understand the upstream and downstream behaviour of a 24 cell structure [7]. From Floquet's Theorem, we find that for infinitely repeating coupled cells electromagnetic fields in each cell differ by only a phase difference [8]. Based on this, the single cell electromagnetic fields were imported into each of the adjacent cells with the appropriate phase advance for the given RF driver frequency (119° for 11.9926 GHz, 120° for 11.9938 GHz, and 121° for 11.995 GHz). Using the single cell geometry and its electromagnetic field solutions for each of the 48 cells allows the structure to act as a constant gradient structure, although the structure lacks the iris tapering seen in the structures under test. This simplified geometry was used to reduce the computational time of the simulation.

Two dimensional monitors at each iris measured the properties of particles emitted from the centre of the 48 cells. The idea of using this symmetry for upstream and downstream behaviour of a full structure model was exploited in [7]. As the source of the particle, we set the iris as the emission area where the fields are greatest (Fig. 8) and therefore the field emitted current density is greatest. To find the density of field emitted electrons, the emission area used the Fowler–Nordheim model described in Eq. (1). By setting the total area of the iris as the emitter, early simulations found that the downstream current is well beyond that measured. Emitters in structures are known to be microscopic in nature and therefore their area vastly smaller than the area of the iris [16]. For the model we add an emitter density factor to determine the effective area of the emitter(s). Measurements in X-band test stands

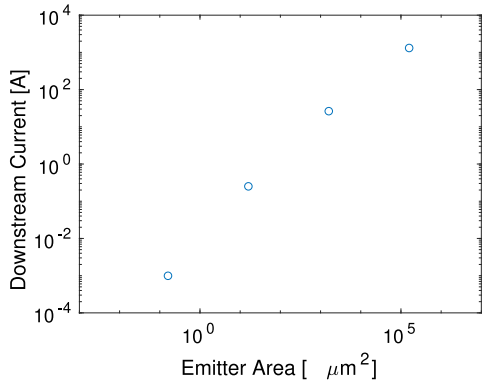

Fig. 10. Scan of the effective area of emission for the iris.

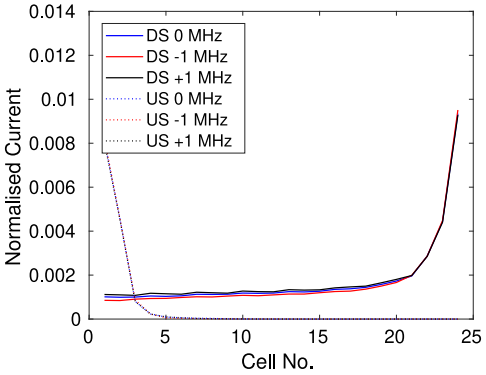

(a) Per Cell

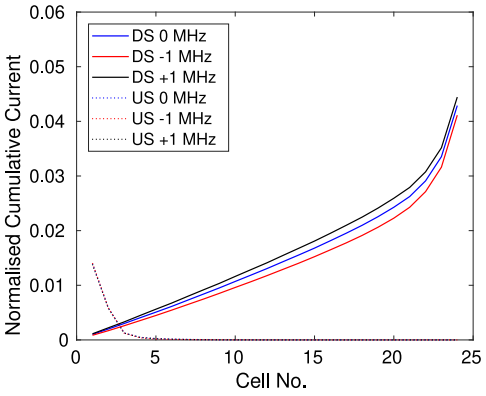

(b) Cumulative

Fig. 11. Results of dark current capture for PIC simulation.

at CERN demonstrate downstream currents in the hundreds of microamp to milliamp regime (Fig. 9). Fig. 10 plots the downstream current against the effective area of the emitter and shows that the effective area size is from 0.01 to 1 μm^2. We take the upper limit of the emitter size and spread the effective emitter area homogeneously across the entire iris as it is yet known how the emitter's position on the iris affects the capture of dark current. The scaled emission current density (j'_F) used for the final simulation is given by multiplying the current density (j_F) by the ratio of the effective emitter area to the iris area such that

$$j'_F = \frac{A_{emitter}}{A_{iris}} j_F, \tag{13}$$

where $A_{emitter}$ is the effective area of the emitter and A_{iris} is the area of the iris. In the emission model we chose a field enhancement factor β of 30, a typical value measured in experiments, and the work function for copper to be 4.5 eV [22].

6. Simulation results

To investigate the changes in captured dark current, Fig. 11 displays the capture efficiency from each cell. Plotting the capture as a percentage for each cell (Fig. 11a), as well as an accumulation along the structure towards each respective output (Fig. 11b), the capture efficiency is seen to increase for a greater frequency RF driver as seen in measurements. Simulations demonstrated that particles emitted later in the RF oscillation are captured for higher driver frequencies whereas they slip from the bucket at lower driver frequencies. This effect is therefore seen for the field emitted particles which have undergone capture, which is important for our analysis of the simulations. In Figs. 6 and 8 of [7] it was shown that the low energy particles in the cells far downstream predominantly were not measured in the Faraday cups as these particles were not captured well enough for transmission through the beam pipe, housing the vacuum system, and on to the Faraday cup. These low energy particles are seen as the jump in transmission downstream in cells 21 to 24 of Fig. 11a. Taking this into account, our analysis looked at the particles arriving downstream of the structure which are known to have been captured (cells 1 to 20), and therefore likely to arrive at the Faraday cup due to their lower emittance and greater longitudinal momentum. From cells 1 to 20, the cumulative capture for the nominal driver frequency is 0.0243 compared to 0.0259 for +1 MHz and 0.0223 for −1 MHz. This accounts for an average of 8.05%/MHz change in the capture of the dark currents with respect to the driver frequency change for 20 cells. In Fig. 12 we compare these simulation results to the measurement results from Fig. 5 where we use the change in driver frequency. We find a similar magnitude change in the dark current between the simulation and measured results for the T24 PSI structure. The large difference between the T24 PSI structure and the other two structures is yet to be understood and will be studied in future investigations. It is expected by the authors that the difference may be caused by the location of the emitter on the iris.

7. Conclusion

X-band test stands operating at CERN operate with surface fields in excess of 200 MV/m leading to the emission and capture of field emitted electrons. A simplified one dimensional model demonstrated that the capture of these field emitted electrons was dependent on the driver frequency as well as the structure temperature, which shifted the structure's resonant frequency. This dependence was explained to be the result of a shift in the phase velocity of the RF fields. Measurements of the dependency on the X-band test stands at CERN demonstrated a strong variation in the measured dark current for a small variation in the driver frequency. Simulations of the capture of dark current also found this dependency and obtained similar variations in the capture likelihood as the measurements performed.

Acknowledgements

The authors would sincerely like to acknowledge the help of the radiation protection group at CERN for their assistance during these measurements. We would also like to thank Thibaut Lefevre and Andrea Latina for their support and input.

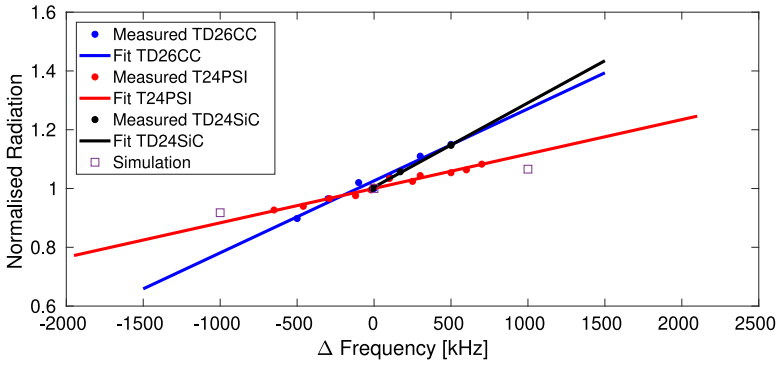

Fig. 12. A comparison of the simulated and measured radiation within the bunker for the three structure seen in Fig. 5 and normalised to the radiation measured at the nominal frequency.

References

[1] M. Aicheler, et al., A Multi-TeV Linear Collider Based on CLIC Technology, CERN 2012-007.

[2] S. Benedetti, A. Grudiev, A. Latina, High gradient linac for proton therapy, Phys. Rev. Accel. Beams 20 (2017) 040101.

[3] S. Benedetti, et al., Fabrication and testing of a novel S-Band backward travelling wave accelerating structure for proton therapy linacs, in: 28th Linear Accelerator Conference, East Lansing.

[4] A. Grudiev, W. Wuensch, Design of an X-band Accelerating STructure for the CLIC main Linac, in: Proceedings of LINAC08, Victoria, BC, Canada.

[5] R.H. Folwer, L. Nordheim, Electron emission in intense electric fields, Proc. R. Soc. Lond. Ser. A Math. Phys. Eng. Sci. 119 (1928) 173.

[6] N.V. Mokhov, I.L. Rakhno, N.A. Solyak, A. Sukhanov, Igor S. Tropin, Dark Current and Radiation Shielding Studies For The ILC Main Linac, arXiv:1705.02363 [physics.acc-ph].

[7] Karl L. F. Bane, et al., Dark currents and their effect on the primary beam in an X-band linac PRAB, 064401, 2005.

[8] CERN Accelerator School, 1992.

[9] CST STUDIO SUITE, 2018.

[10] W. Wuensch, High Gradient X-band Technology: From TeV colliders to light sources and more, CERN courier, April 2018, volume 58 number 3.

[11] N. Catalan-Lasheras, et al., Experience Operating an X-band High-Power Test Stand at CERN. http://accelconf.web.cern.ch/accelconf/IPAC2014/papers/wepme016.pdf.

[12] B. Woolley, High Power X-band RF Test Stand Development and High Power Testing of the CLIC Crab Cavity, Lancaster University, United Kingdom, 2015.

[13] M. Volpi, et al., High Power and High Repetition Rate X-band Power Source Using Multiple Klystrons. http://ipac2018.vrws.de/papers/thpmk104.pdf.

[14] N. Cataln Lasheras, et. al., Experience Operating an X-band High-Power Test Stand at CERN, 5th International Particle Accelerator Conference, Dresden, Germany, 15 - 20 Jun 2014, 2288.

[15] N. Cataln Lasheras, et. al., Commissioning of XBox-3: A very high capacity X-band test stand, in: 28th Linear Accelerator Conference, East Lansing, Michigan, 25 - 30 Sep 2016, TUPLR047.

[16] J.W. Wang, G.A. Loew, Field Emission and RF Breakdown in High-Gradient Room-Temperature Linac Structures. SLAC-PUB-7684, 1997.

[17] Wangler, RF Linear Accelerators, Wiley, 1998.

[18] T. Argyropoulos, et al., Design, fabrication, and high-gradient testing of an X-band, traveling-wave accelerating structure milled from copper halves, Phys. Rev. Accel. Beams 21 (2018) 061001.

[19] M. Jacewicz, et al., Spectrometers for RF breakdown studies for CLIC, Nucl. Instrum. Methods Phys. Res. A 828 (2016) 63–71.

[20] C.W. Steele, A non-resonant perturbation theory, IEEE Trans. Microw. Theory Tech. 14 (2) (1966) 70–74.

[21] Rolf Wegner, RF Tuning of 12SWV18026-01CSCC (TD26 CC N3) https://edms.cern.ch/document/1626878/1.

[22] W. Wuensch, CLIC Accelerating Structure Development Proceedings of EPAC08, Genoa, Italy.

CERN – EUROPEAN ORGANIZATION FOR NUCLEAR RESEARCH

CLIC – Note – 1080

HIGH POWER TESTING OF A PROTOTYPE CLIC STRUCTURE: TD26CC R05 N3

Thomas Geoffrey Lucas[1], Matteo Volpi[1], Paul Giansiracusa[1], Roger Paul Rassool[1], Theodoros Argyropoulos[2], Hikmet Bursali[2], Nuria Catalan-Lasheras[2], Alexej Grudiev[2], Gerard Mcmonagle[2], Igor Syrachev[2], Rolf Wegner[2], Ben Woolley[2], Walter Wuensch[2], Daniel Esperante-Pereira[3], Mark James Boland[4]

[1]University of Melbourne, Parkville 3010, Australia
[2]European Organisation for Nuclear Research (CERN)
[3]Instituto de Fisica Corpuscular (IFIC), Valencia, Spain
[4]University of Saskatchewan, Saskatoon, Canada

CERN-ACC-2018-0030
19/09/2018

Abstract

Testing of high gradient accelerating structure prototypes for the Compact Linear Collider is ongoing at CERN. High power testing of the baseline structure CLIC-G, also known as TD26CC R05, from the most recent concept design review was conducted on CERN's second X-band test stand, Xbox 2. Several months of conditioning resulted in an ultimate unloaded gradient of 110 MV/m, the highest achieved for a structure with higher-order mode damping, with a 170ns flat-top RF pulse and operating with a breakdown rate of 2 ×10−5 breakdowns/pulse/metre. Investigations of the breakdown distribution demonstrated homogenous breakdown behaviour throughout the structure when fields were below 110 MV/m. After high power testing, a measurement of the RF parameters of the structure illustrated a significant change in the S-parameters consequential of a detuning of the cells, equating to a 1 MHz shift in the frequency.

Geneva, Switzerland
19 September 2018

High Power Testing of a Prototype CLIC structure: TD26CC R05 N3

Thomas Geoffrey Lucas,* Matteo Volpi, Paul Giansiracusa, and Roger Paul Rassool
University of Melbourne, Parkville 3010, Australia

Theodoros Argyropoulos, Hikmet Bursali, Nuria Catalan-Lasheras, Alexej Grudiev, Gerard Mcmonagle, Igor Syrachev, Rolf Wegner, Ben Woolley, and Walter Wuensch
European Organisation for Nuclear Research (CERN)

Daniel Esperante-Pereira
Instituto de Fisica Corpuscular (IFIC), Valencia, Spain

Mark James Boland
University of Saskatchewan, Saskatoon, Canada

(Dated: 18 April 2017)

Testing of high gradient accelerating structure prototypes for the Compact Linear Collider is ongoing at CERN. High power testing of the baseline structure CLIC-G* , also known as TD26CC R05, from the most recent concept design review was conducted on CERN's second X-band test stand, Xbox 2. Several months of conditioning resulted in an ultimate unloaded gradient of 110 MV/m, the highest achieved for a structure with higher-order mode damping, with a 170 ns flat-top RF pulse and operating with a breakdown rate of 2×10^{-5} breakdowns/pulse/metre. Investigations of the breakdown distribution demonstrated homogenous breakdown behaviour throughout the structure when fields were below 110 MV/m. After high power testing, a measurement of the RF parameters of the structure illustrated a significant change in the S-parameters consequential of a detuning of the cells, equating to a 1 MHz shift in the frequency.

I. INTRODUCTION

High gradient testing of accelerating structures for the Compact Linear Collider (CLIC) is ongoing at CERN's X-band test stands. Current testing involves structures designed around the CLIC-G (3 TeV) design. Three prototypes using the CLIC-G* (TD26CC) design, with internal edge rounding of 0.5 mm (R05), were produced at CERN for the purpose of understanding their high power performance. Below we will review the high power testing of one of these structure demonstrating the achieved unloaded gradient and pulse length, as well as reviewing the RF breakdown behaviour within the structure. Following that we will discuss the RF parameter of the structure after high power testing, investi-

* Corresponding Author thomas.geoffrey.lucas@cern.ch

gating structure RF property changes possibly caused by high power operation.

II. STRUCTURE OVERVIEW

Submitted as the baseline structure for CLIC 3 TeV design in the most recent Concept Design Report, the TD26CC structure has an operational frequency of 11.994 GHz and a phase advance per cell of $2\pi/3$ [1]. Tapering of the irises offers a constant gradient across the 26 regular cells, once one accounts for beam loading. Two additional coupling cells, designed using the compact coupler design, input the high power RF [2]. Achieving the 100 MV/m loaded gradient requires a peak power of 61.3 MW [1]. For machining purposes the inner edges of these structures' cells are rounded with a regular rounding profile and 0.5 mm diameter. Three iterations of this design were produced at CERN, the structure in question was the third to be produced (N3) and second to be tested at high power.

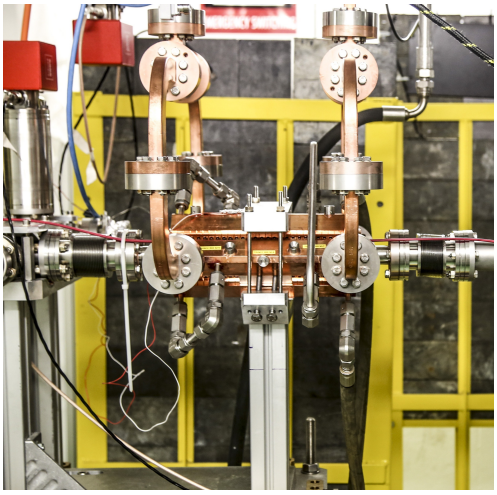

FIG. 1. The TD26CCR05 N3 installed on the Xbox 2 X-band test stand.

III. CONDITIONING HISTORY

Commencing in December of 2015, the TD26CC R05 N3 structure was installed on Xbox 2. Commissioned in 2014, Xbox 2 is the second X-band test stand at CERN (Figure 1). The infrastructure of Xbox 2 have been extensively reviewed in [3]. The RF conditiong history is depicted in Figure 2 which will be used to describe the entire history in detail below. RF Conditioning began with a short 70 ns RF pulse length (red), the BDR limit of the conditioning algorithm was set to 8×10^{-5} breakdowns per pulse (bpp) for 50 million pulses in which the structure conditioned to 60 MV/m, where the unloaded gradient is depicted in blue. It was found that a greater BDR limit led to periods of clustered breakdowns seen in the BDR's variation of 60% (magenta). This was considered undesirable for the structure and the BDR limit was reduced to 3×10^{-5} bpp, seen clearly in the gradient reduction of the cumulative breakdowns plot(black). Continuing to condition, the structure reached 105 MV/m after 300 million pulses. Investigations into the power curves observed an uncharacteristically linear behaviour and further investigations found that this was the result of the conditioning algorithm retard-

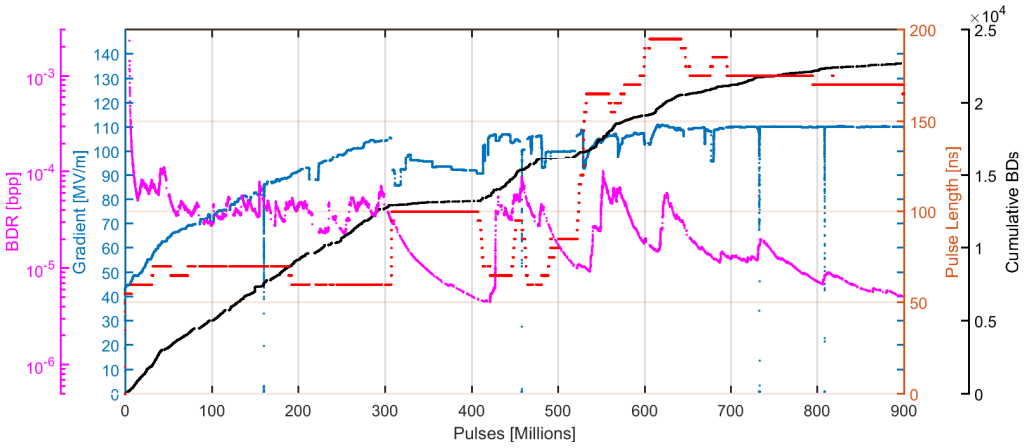

FIG. 2. Conditioning history of the TD26CCR05 N3 structure in Xbox 2.

ing progress [4]. At 105 MV/m, and just above 300 million pulses, the safe limit of radiation outside the test bunker was exceeded and temporarily prevented further increases in the power. During these periods, where power changes were not permitted, a test of the gradient dependence of the BDR was performed. During this time, the pulse length was set to the second pulse length of 100 ns to increase the BDR, allowing the increase in the number of breakdowns and therefore improving statistics. Scanning through peak electric fields of 187.5 MV/m followed by 182.6 MV/m and 180.25 MV/m, the BDR depedency is seen in Figure 3. Past tests have found a dependence of E^{30} which fits well within the error bars of the measured values [5].

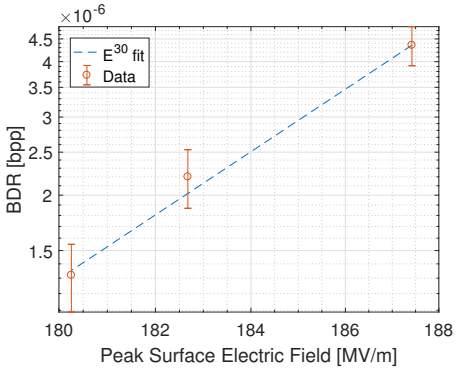

FIG. 3. Test of the BDR dependency on the surface electric field.

At 415 million pulses into the high power testing, the structure resumed power ramping with the RF pulse parameters set to those used at 300 million pulses. Between 415 and 500 million pulses, the structure was pushed to an unloaded gradient of 107 MV/m, at this time it was found that a reflection from the structure caused an undesirable peak in the pulse's flat top. It was determined that this peak came from a reflection from the start of the structure which interfered with the klystron pulse and led to excess power being extracted from the klystron [7]. A change to the phase profile allowed the pulse amplitude to be flattened. At 540 million pulses, a new pulse length and shape was estalished to

4

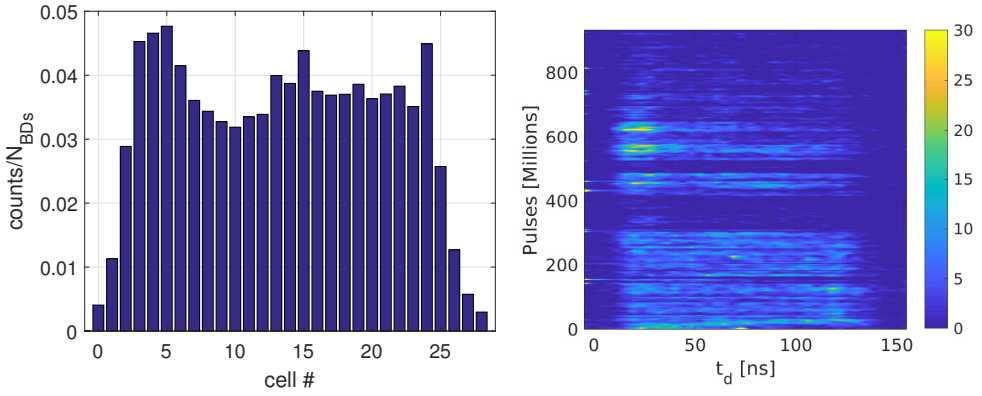

(a) Cumulative Breakdown Distribution.

(b) Breakdown distribution per day.

FIG. 4. Breakdown distibution along the structure.

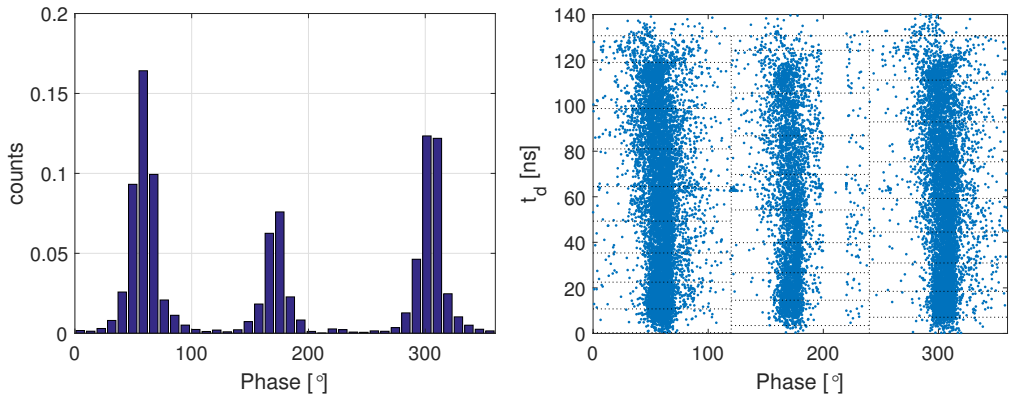

(a) Phase differential for breakdowns.

(b) Phase differential vs breakdown position.

FIG. 5. RF breakdown distribution in the structure.

flatten the pulse by reducing the reflection from the start of the structure. Up to 600 million pulses, the structure was pulsed with a "CLIC-like" pulse shape with a power ramp at the start of the pulse and a 160 ns pulse flat top [8]. Conditioning was able to reach 113 MV/m though an excess of breakdowns at the beginning of the structure was observed and will be elaborated on in the coming setion.

At 600 million pulses the structure was increased to a 200 ns pulse and ran with the undesirable peak in the otherwise flat pulse. From 650 to 700 million pulses, the pulse shape was changed to a CLIC pulse, totalling 240 ns with 180 ns flat-top [8]. This allowed testing with the nominal CLIC pulse shape while removing the undesirable peak in the pulse. Setting the unloaded gradient to a constant 110 MV/m, the structure ran with the intention of reducing the BDR for the last 200 million pulses.

A small change in the pulse length is seen at 800 million caused by a reconfiguration of the phase control after a power outage. At the end of conditioning, the CLIC-G* had reached 110 MV/m with 170 flat top and a breakdown rate of 4×10^{-6} bpp, equivalent to 2×10^{-5} breakdowns/pulse/metre, which is the highest gradient achieved on a higher order mode damped CLIC structure.

IV. BREAKDOWN DISTRIBUTION

An analysis of the breakdown distributions revealed further information about the structure's performance. Figure 4(a) depicts the breakdown distribution within the structure plotted against the cell number. A close to flat distribution demonstrated the health and field flatness of the structure as the breakdowns are expected to occur more frequently in regions of greater surface electric field strength [5, 6]. A small peak developed at the start of the structure which required further investigation. To understand the excess breakdowns at the start of the structure we plot the breakdown distribution against the number of pulses of conditioning (Figure 4(b)). For the first 300 million pulses of conditioning the breakdowns were evenly distributed across the structure. From 300 to 415 million pulses, the structure ran at a reduced power due to the radiation outside the bunker exceeding the maximum safe level. After 415 million pulses, the structure continued with another power reduction occuring at 475 million pulses. Resuming the RF conditioning after 540 million pulses, the gradient was increased to the 113 MV/m which resulted in an excess of breakdowns in the start of the structure. A reduction in power reduced the total number of breakdowns though the breakdowns continued to predominantly occur at the input of the structure. These results led to the conclusion that once a breakdown site is developed due to excessive fields it will remain despite the field reduction. Looking at the phase distribution, the expected three peaks occured in accordance with the peak surface fields occuring at the iris each separated by 120° (Figure 5(a)) [10]. When plotting the phase difference against the breakdown position a small curvature is visible in the three vertical clusters. This curvature is indicative of cell detuning which can occur during transport but also may result from high power operation(Figure 5(b)).

V. RF TESTING AFTER HIGH POWER

After the structure was removed from the test stand it was taken for low power testing. For long term operation, it is important to understand changes in the structure's RF parameters due to high power operation. In Figure 6 the reflection from the input and output ports are displayed before (labelled "after tuning") and after high power testing. Before testing the structure can be seen to be well tuned to the oper-

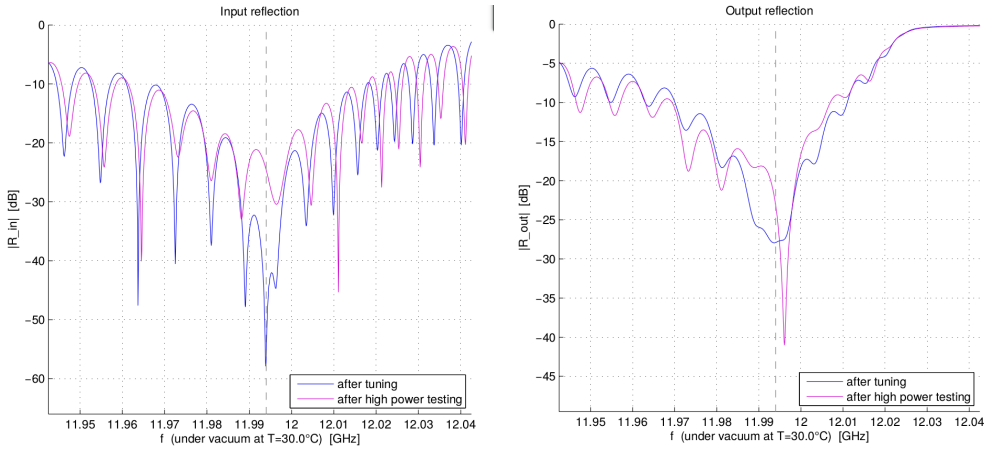

(a) Input coupler reflection.

(b) Output coupler reflection.

FIG. 6. S-parameter measurements of the structure before and after high power testing.

ational frequency of 11.994 GHz with a reflection from the input coupler of −58 dB. After the RF conditioning, the reflection at the operational frequency of 11.994 GHz can be seen to jump to −26 dB. Using a non-perturbative beadpull method the cell detuning due to high power could be determined. In Figure 7(a) we observe an average frequency change of about 1 MHz (corresponding to 1° in phase advance) [9]. Such significant detuning resulted in a significant change in electric field profile's amplitude and phase, seen in Figures 7(b) and 7(c), as the standing wave ratio increased. The variance of the field amplitude and phase can be seen to increase after high power testing. It has been previously observed that structures field properties change after high power testing and this provides further evidence supporting the detuning of structures due to RF conditioning.

VI. CONCLUSION

A CLIC baseline structure operating at 11.994 GHz underwent high power testing at CERN's X-band test stand (Xbox 2). After 900 million pulses the structure was able to achieve an ultimate unloaded gradient of 110 MV/m for a 170 ns RF pulse and conditioning down to a BDR of 2×10^{-5} breakdowns/pulse/metre. Breakdown distributions along the structure demonstrated that the breakdowns occured homogeneously across the structure before occurring predominantly at the beginning of the structure when the gradient was pushed above 110 MV/m. Testing of the structures field distribution and S-parameters after high power testing illustrated significant detuning, averaging 1 MHz over the structure, expected to be the result of high power testing.

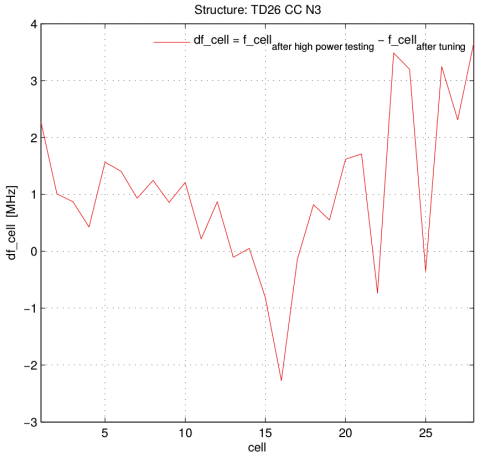

(a) Electric field profile along the structure.

(b) Cell detuning along the structure.

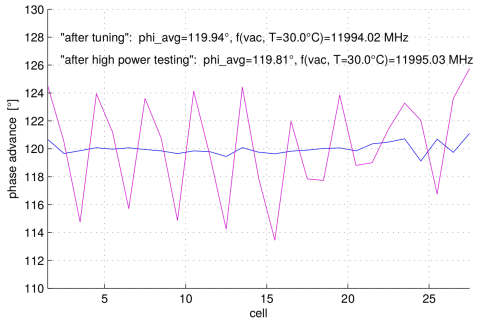

(c) Phase advance per cell.

FIG. 7. Electric field properties along the structure before and after high power testing.

[1] M. Aicheler et al., A Multi-TeV Linear Collider Based on CLIC Technology, CERN 2012-007.

[2] A. Grudiev and W. Wuensch, Design of the CLIC Main Linear Accelerating structure for the CLIC conceptual Design report. In Proceedings of Linear Accelerator Conference LINAC2010, Tsukuba, Japan. https://accelconf.web.cern.ch/accelconf/LINAC2010/papers/mop068.pdf.

[3] B. Woolley(2015), High Power X-band RF Test Stand Development and High Power Testing of the CLIC Crab Cavity, Lancaster University, United Kingdom.

[4] T.G. Lucas, et al., Initial Testing of techniques for Large Scale RF Conditioning for the Compact Linear Collider, IPAC 2018, Vancouver.

[5] A. Grudiev, S. Calatroni, and W. Wuensch, New local field quantity describing the high gradient limit of accelerating structures, Physics Review Special Topics- Accelerators and Beams, 12, 102001, (2009).

[6] K. Nordlund and F. Djurabekova, Defect model for the dependence of breakdown rate on external electric fields, Phys. Rev. ST Accel. Beams 15, 071002 (2012)

[7] M. Volpi, et al., High Power And High Repetition Rate X-band Power Source using Multiple Klystrons, IPAC 2018, Vancouver.

[8] Alexej Grudiev, Oleksiy Kononenko Pulse Shape Optimization for the Beam Loading Compensation in CLIC Main Linac. Talk at 4th Annual X-band Structure Collaboration Meeting, May 3-5, 2010.

[9] C. W. Steele, A non-resonant perturbation theory, Microwave Theory and Techniques. IEEE Transactions, 14(2), 70-74. (1966)

[10] A. Degiovanni et al., Diagnostics and analysis techniques for high power X-band accelerating structures, LINAC14, Geneva, Switzerland, 2014.

9th International Particle Accelerator Conference IPAC2018, Vancouver, BC, Canada JACoW Publishing
ISBN: 978-3-95450-184-7 doi:10.18429/JACoW-IPAC2018-THPMK103

INITIAL TESTING OF TECHNIQUES FOR LARGE SCALE RF CONDITIONING FOR THE COMPACT LINEAR COLLIDER

T.G. Lucas[1] *, N. Catalan-Lasheras, A. Grudiev, T. Lefevre, G. McMonagle, J. Paszkiewicz[2]
V. del Pozo Romano, I. Syratchev, A. Vnuchenko[3], M. Volpi[1], B. Woolley, W. Wuensch
European Organisation for Nuclear Research (CERN)
R. Zennaro, Paul Scherrer Institute, Villigen, Switzerland
P.J. Giansiracusa, R.P. Rassool, University of Melbourne, Parkville, Australia
C. Serpico, Elettra-Sincrotrone Trieste S.C.p.A., Basovizza, M.J. Boland
University of Saskatchewan, Saskatoon, Canada
[1]also at University of Melbourne, Parkville, Australia
[2]also at University of Oxford, Oxford, United Kingdom
[3]also at IFIC, Valencia

Abstract

Nominal operating conditions for the Compact Linear Collider (CLIC) 380 GeV requires 72 MV/m loaded accelerating gradients for a 180 ns flat-top pulse. Achieving this requires extensive RF conditioning which past tests have demonstrated can take several months per structure, when conditioned at the nominal repetition rate of 50 Hz. At CERN there are three individual X-band test stands currently operational, testing up to 6 structures concurrently. For CLIC's 380 GeV design, 28,000 accelerating structures will make up the main linac. For a large scale conditioning programme, it is important to understand the RF conditioning process and to optimise the time taken for conditioning. In this paper, we review recent X-band testing results from CERN's test stands. With these results we investigate how to optimise the conditioning process and demonstrate the feasibility of pre-conditioning the structures at a higher repetition rate before installation into the main linac.

INTRODUCTION

In preparation for the 380 GeV Compact Linear Collider (CLIC), testing of X-band high gradient accelerating structures is ongoing at CERN. Before injection of the first bunches, the high gradient accelerating structures require RF conditioning to achieve the 72 MV/m loaded gradients. The testing programme at CERN has continued with the CLIC-G (3 TeV) based structures where structures are conditioned in excess of 100 MV/m. This is in order to complete this study and allowing the results from the tested structures to be compared to existing benchmark data. In the past, conditioning of the structures has taken several months per structure [1]. In the CLIC-380 design, approximately 28,000 structures make up the main linac and therefore optimising the efficiency of structure conditioning is crucial [2].

Determining an optimal conditioning strategy is an important priority for the CLIC accelerating structure development programme. The current strategy involves conditioning to nominal gradient at a constant pulse length then repeating the process at longer pulse lengths, all with a constant BDR [3]. Once the gradient and pulse length are achieved, the structure is left to condition down to the nominal BDR of 3×10^{-7} breakdowns/pulse/m [2]. The BDR set point during conditioning, generally around 2.5×10^{-4} breakdowns/pulse/m, is three orders of magnitude above the nominal minimum BDR. To determine the time it will take to reach the acceptable BDR level, we investigate the BDR decay trend for structures pulsing at a constant gradient and pulse length. Figure 1 displays the BDR decay of the T24 Open and TD26CCR05 structure each tested on the Xbox 2 X-band test stand [4]. The steady decay of the BDR follows an inverse power law and decreases by approximately a factor of ten per decade though experiences transient jumps in the BDR during breakdown clusters. A possible strategy to reduce the time required for conditioning is to increase the repetition rate of the conditioning and also to pre-condition the structures before installation into the main linac. Below we will investigate the feasibility of this high repetition rate pre-conditioning from test results performed on CERN's X-band test stands.

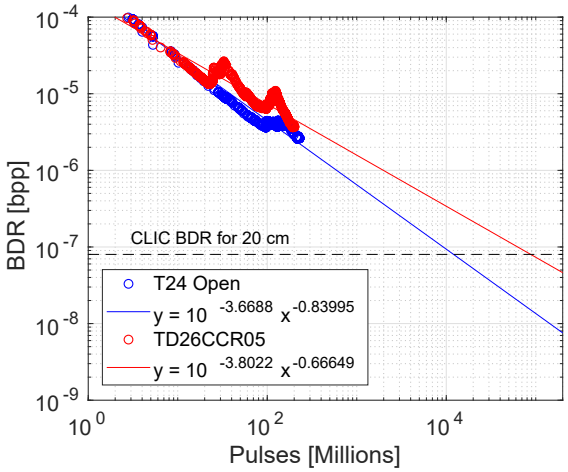

Figure 1: BDR decay rate during conditioning for the TD26CC R05 and T24 Open structures.

* thomas.geoffrey.lucas@cern.ch

9th International Particle Accelerator Conference IPAC2018, Vancouver, BC, Canada JACoW Publishing
ISBN: 978-3-95450-184-7 doi:10.18429/JACoW-IPAC2018-THPMK103

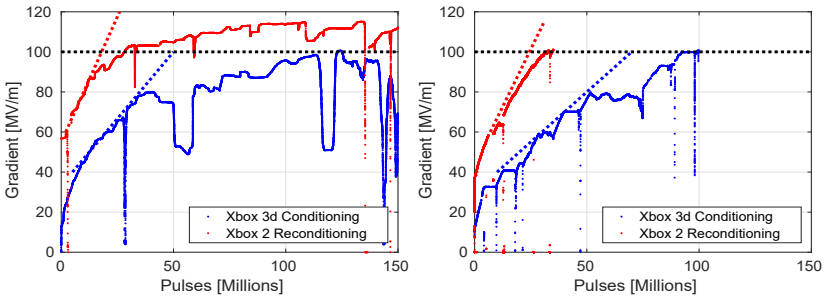

Figure 2: A comparison of the conditioning of the T24 PSI N1 (left) and N2 (right) structures which each started the first phase of conditioning in Xbox 3 which subsequently continued in Xbox 2. Tangent lines compare the conditioning rate at 70 MV/m.

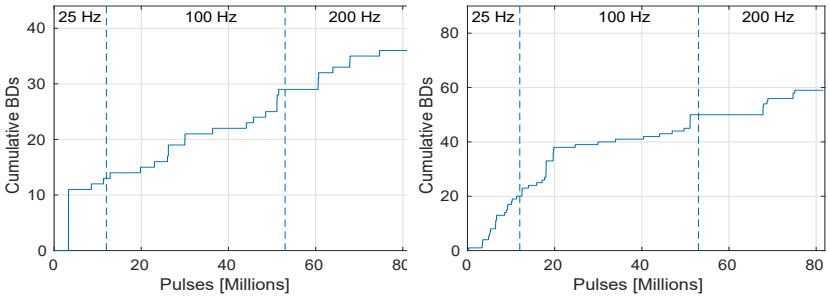

Figure 3: Cumulative breakdowns during conditioning of the T24 PSI (left) and TD24 SiC (right) at 25, 100, and 200 Hz.

GRADIENT RECOVERY AFTER EXPOSURE TO AIR

With 28,000 individual structures and a nominal repetition rate of 50 Hz, conditioning of the structure installed in the main linac isn't the most efficient method of conditioning. It has been suggested that structures may be pre-conditioned in separate test stands before installation into the main linac [5]. For the conditioning of the T24 PSI N1 and N2 prototypes, the structures began conditioning in Xbox 3. The Xbox 3 test stand can operate with a pulse repetition rate up to 400 Hz and therefore offers the possibility of faster conditioning. Each structure was able to achieve an unloaded gradient of 100 MV/m, before being limited by the achievable power of Xbox 3 [6, 7]. Subsequently the structures were moved to Xbox 2, which can operate with a much greater input power than Xbox 3, where they continued and concluded their conditioning.

In Fig. 2, the first phase of conditioning in Xbox 3 and second phase of conditioning in Xbox 2 are demonstrated for the T24 PSI N1 and N2 structure, separating, by overlaying the two phases of conditioning. At the start of the second phase of conditioning, we observed that the structures could begin conditioning at 57 MV/m and 40 MV/m for the N1 and N2, respectively. Two dashed tangent lines demonstrate the appoximate rate of conditioning at 70 MV/m. It was found that the conditioning rate was 2.5 and 2.3 times greater at 70 MV/m for the second phase of conditioning compared to that of the structure yet to see high power (first phase). For the structures in phase 1, the conditioning took approximately the same number of pulses (100 million) to reach 100 MV/m, after adjusting for the power drops on the N1's phase 1 conditioning at 50 and 115 million pulses resulting from radiation issues. For the previously conditioned structures, phase 2, the 100 MV/m unloaded gradient was achieved in approximately 25-30 million pulses. Given the higher initial power and steeper conditioning curve, and that the structures reached the 100 MV/m in fewer pulses, we found that the conditioning is partially retained in the structure, despite the exposure to air.

PULSE REPETITION RATE VS BDR

The klystrons in Xbox 3 can operate at pulse repetition rates up to 400 Hz, allowing pulsing of the each line up to 200 Hz [8]. For pre-conditioning of the structures, it has been proposed that pulsing would operate at repetition rates well above the nominal CLIC parameters to reduce the

Table 1: BDR measured for the SiC structure for variations in the pulse repetition rate.

Structure	Rep. Rate [Hz]	BDR [bpp]	Uncertainty [bpp]
SiC N2	25	1.08×10^{-6}	$\pm 3.0 \times 10^{-7}$
	100	3.9×10^{-7}	$\pm 9.7 \times 10^{-8}$
	200	2.4×10^{-7}	$\pm 9.12 \times 10^{-8}$
PSI N2	25	1.66×10^{-6}	$\pm 3.73 \times 10^{-7}$
	100	7.317×10^{-7}	$\pm 1.34 \times 10^{-7}$
	200	3.1×10^{-7}	$\pm 1.03 \times 10^{-7}$

9th International Particle Accelerator Conference IPAC2018, Vancouver, BC, Canada JACoW Publishing
ISBN: 978-3-95450-184-7 doi:10.18429/JACoW-IPAC2018-THPMK103

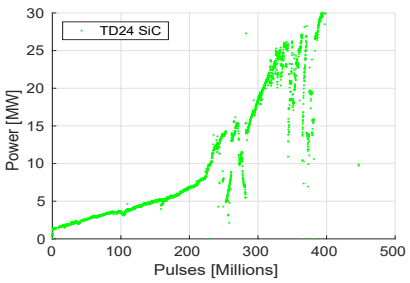

Figure 4: Conditioning curve of the TD24 R05 SiC whose progress was limited due to the algorithm.

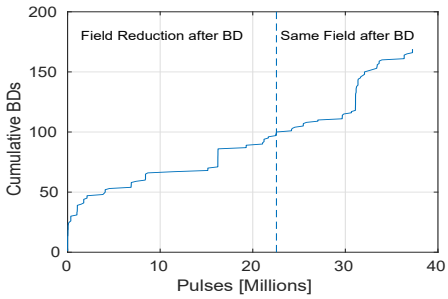

Figure 5: Cumulative Breakdown curve for operation with and without field reduction after breakdowns.

required conditioning time. Increasing the repetition rate increases the average power dissipated in the structure and it is important to undestand how this affects the BDR. Using the damped Silicon Carbide (SiC) structure and the undamped PSI structure, pulsing at constant power and pulse length was performed at three pulse repetition rates. Figure 3 displays the cumulative breakdowns for 82 million pulses. Summarising the results, Table 1 displays the measured BDR for the three repetition rates. For the SiC structure, the BDR at 25 Hz and 100 Hz appeared to decrease despite the increased average power. For 200 Hz pulsing, the BDR remained the same as the 100 Hz repetition rate within statistical uncertainty. The BDR on the PSI structure began at the higher breakdown rate of 1.66×10^{-6} bpp at 25 Hz, expected to be the result of the initial change in power. Subsequent pulsing at 100 and 200 Hz continued to decrease in BDR due to conditioning. With the increase in average power, there was no evidence of a BDR increase for a pulse repetiton rate change.

LIMITED RATE OF CONDITIONING DUE TO ALGORITHM

Conditioning in the X-band test stands is controlled by an algorithm previously described in [3]. Checking the BDR every 180 seconds, the power increases in 10 kW steps when the BDR is below the selected setpoint. The rate of power increase is dependent on the BDR limit, the loop length, and the power step size. During the conditioning of the first structure on Xbox 3, it was observed that the rate of RF conditioning was unusually slow and linear in comparison to past structures [1]. Figure 4 displays the conditioning of the TD24R05 SiC N1 structure. For the first 200 million pulses with an increment loop length of 30,000 pulses, power step of 10 kW, and BDR limit of 3×10^{-5} bpp, it can be seen that the increase in power is 7 MW over 200 million pulses. At 200 million pulses, the BDR limit was changed to 1×10^{-4} bpp and a loop length of 7500 pulses. A clear increase in the rate of conditioning is visible with the distinct curvature of RF conditioning. This demonstrates the algorithm's ability to limit the progress of the structure's conditioning. The drops at 250 and 350 million pulses are the result of conditioning of the waveguide network.

RECOVERY AFTER BREAKDOWN

After breakdown events in the X-band test stands, it has become common practice to interlock briefly before recommencing pulsing at a reduced input power then steadily returning to the set power level after a few hundred pulses. This reduction in power is meant to reduce the likelihood of a follow-up breakdown. For CLIC, this reduction in field after a breakdown is undesirable as it will affect the luminosity of the machine by increasing the downtime due to RF breakdown. During testing of the TD26CCR05 structure, modifications to the algorithm allowed continuous pulsing after a breakdown event, with the interlock and field reduction to be enabled only after two consecutive breakdown pulses. Figure 5 displays the cumulative breakdowns for the normal conditioning algorithm and for the running without this field reduction. Switching to this new conditioning algorithm didn't appear to affect the BDR though further testing will be necessary to determine the long-term feasibility of this pulsing strategy.

CONCLUSION

A structure conditioning strategy for the high gradient accelerating structures of CLIC is crucial for cost minimisation. Conditioning the structures while installed in the main linac will require several months of RF conditioning, if pulsed at the nominal repetition rate, although this can occur in parallel with beam commissioning. Preconditioning structures at a higher repetition rate in separate test-stands and then installing them into the main linac has been demonstrated as a possible solution to reduce the overall conditioning time. Results demonstrated that higher repetition rate conditioning didn't lead to a higher breakdown rate and conditioning was partially maintained in a structure when moved between test-stands. This opens up the option for pre-conditioning structures before installation. If the structure conditions faster than the algorithm increases the input RF power, the conditioning is retarded by the algorithm. Finally, algorithmic reductions of the field strength after RF breakdowns aimed to prevent further RF breakdowns during conditioning, though this technique isn't desirable for an operational CLIC. Initial tests demonstrated that the continuation of puls-

9th International Particle Accelerator Conference IPAC2018, Vancouver, BC, Canada JACoW Publishing
ISBN: 978-3-95450-184-7 doi:10.18429/JACoW-IPAC2018-THPMK103

ing after an RF breakdown is possible without a noticeable BDR increase.

REFERENCES

[1] A. Degiovanni *et al.*, "Comparison of the conditioning of high gradient accelerating structures", *PRAB 19*, 032001 (2016).

[2] M. Aicheler *et al.*, "A Multi-TeV Linear Collider Based on CLIC Technology", CERN 2012-007.

[3] N. Catalan-Lasheras *et al.*, "Experience Operating an X-band High-Power Test-stand at CERN", in *Proc. IPAC14*, Dresden, Germany, Jun. 2014.

[4] N. Catalan *et al.*, "Fabrication and High Gradient Testing of an Accelerating structure made from Milled Halves", in *Proc. LINAC 2016*, East Lansing, MI, USA, Sep. 2016.

[5] P. Burrows, W. Wuensch and T. Argyopoulos. *High-gradient X-band RF technology for CLIC and beyond*. ICHEP 2016 Chicago, USA.

[6] R. Zennaro *et al.*, "High Power Tests of a Prototype X-Band Accelerating Structure for CLIC", in *Proc. IPAC17*, Barcelona, Spain, 2017.

[7] M. Volpi *et al.*, "High Power and High Repetition Rate X-band Power Sources Using Multiple Klystrons", presented at IPAC18, Vancouver, April-May 2018.

[8] N. Catalan Lasheras, *et al.*, "Commissioning of Xbox 3: A Very High Capacity X-band RF Test Stand", in *Proc. LINAC 2016*, East Lansing, MI, USA, Sep. 2016.

9th International Particle Accelerator Conference IPAC2018, Vancouver, BC, Canada JACoW Publishing
ISBN: 978-3-95450-184-7 doi:10.18429/JACoW-IPAC2018-MOPML043

HIGH GRADIENT PERFORMANCE OF AN S-BAND BACKWARD TRAVELING WAVE ACCELERATING STRUCTURE FOR MEDICAL HADRON THERAPY ACCELERATORS

A. Vnuchenko, D. Esperante Pereira, Instituto de Física Corpuscular (IFIC), Valencia, Spain
S. Benedetti, N. Catalan Lasheras, A. Grudiev, B. Koubek, S. Pitman[1], G. McMonagle,
I. Syratchev, B. Woolley, W. Wuensch, CERN, Geneva, Switzerland
T. Lucas, M. Volpi, the University of Melbourne, 3010 Melbourne, Australia
A.Faus Golfe, LAL, Univ. Paris-Sud and Paris-Saclay, CNRS/IN2P3, Orsay, France
[1]formerly at The Cockcroft Institute, Daresbury, UK

Abstract

The high-gradient performance of an accelerating structure prototype for a medical proton linac is presented. The structure was designed and built using technology developed by the CLIC collaboration and the target application is the TULIP (Turning Linac for Proton therapy) proposal developed by the TERA foundation. The special feature of this design is to produce gradient of more than 50 MV /m in low-β accelerating structures (v/c=0.38). The structure was tested in an S-band test stand at CERN. During the tests, the structure reached over above 60 MV/m at 1.2 μs pulse length and breakdown rate of about $5x10^{-6}$ bpp. The results presented include ultimate performance, long term behaviour and measurements that can guide future optimization.

INTRODUCTION

The development of low-β high-gradient (HG) accelerating structures is one of the main requirements for implementation of compact and cost-effective hadron linacs for medical applications. Cancer therapy accelerator need to reach the full penetration depth of the human body and thus provide particle beams with energies in the range 70-230 MeV for protons and 100-400 MeV/nucleon for carbon ions.

To accelerate effectively to higher energies, a HG S-band structure has been designed and manufactured at CERN. An overview of the 3 GHz Backward Travelling Wave (BTW) structure, currently under test, is given in [1].

This accelerating structure is proposed as part of the TULIP project [2], a single room proton therapy facility. The prototype has been designed to accelerate protons with an energy of 70 MeV. Composed of 12 equal length RF cells, totally 189.84 mm in length, the structure has 10 regular cells and two coupling cells, whose aperture diameter is 5mm. Main parameters of the structure are shown in Table 1.

HG operation of RF cavities is limited by undesired RF breakdowns (BD) which may cause beam losses, cavity surface damage, radiation and vacuum deterioration. A maximum breakdown rate (BDR) of the order of 10^{-6} bpp/m is usually required in a hadron therapy linac in order to guarantee an acceptable number of BDs throughout the whole treatment session.

The main goal of this study is to define the HG limits of S-band cavities in terms of BDR. In this paper we present test and data analysis of the structure which includes the BD localisation within the structure and the study of BDR dependence on the RF fields and pulse parameters.

Table 1: Main Parameters of the Accelerating Structures

Operation frequency	2.9985 GHz
Number of RF cells	12
Geometric β – RF Ph. Adv.	0.38 – 150 deg
Max Es/Ea	3.9
Pin @ 50 MV/m	20.16 MW
Pout @ 50 MV/m	11.24 MW
Filling time	220 ns
Group velocity (first/last)	0.39 / 0.21 %c

HIGH POWER TEST SET-UP

The first high-power test of the BTW structure is being performed at the S-band test facility at CERN. The accelerating structure is located in the CTF2 bunker and powered by a 43 MW S-band klystron via WR-284 waveguide lines. The klystron is protected against reflected power by a high power circulator. A schematic of the high-power components of the test facility is shown in Fig. 1.

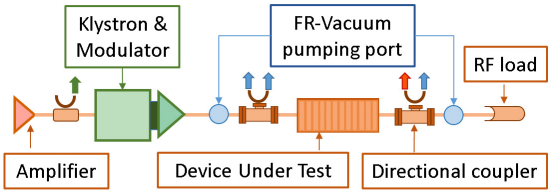

Figure 1: Schematic layout of the test setup.

Presently, the klystron MKS07 previously used in CTF3 is used to delivers RF pulses with a maximum length of 5 μs at a repetition rate of 50 Hz.

Directional couplers situated at the input and output of the structure, are used to measure the incident, reflected and transmitted RF signals. Faraday cups are placed in the upstream and downstream directions along the structure's

9th International Particle Accelerator Conference IPAC2018, Vancouver, BC, Canada JACoW Publishing
ISBN: 978-3-95450-184-7 doi:10.18429/JACoW-IPAC2018-MOPML043

beam axis to measure dark current and detect BD events in the structure. The structure is connected to an ion pump and dedicated chiller unit to adjust the cooling water temperature. An additional sensor is installed to measure the surface temperature of the structure.

The control and acquisition system are based on National Instruments electronics. A PXI real-time system performs the acquisition of RF, vacuum, temperature and water cooling signals. The detection of BD events in the structure using the acquired signals and the final data storage. The RF signals from the directional couplers are digitised in a NI-5761 ADC installed on the PXI crate and they are used as feedback to the power fed to the system. The operation of the test stand is controlled and interfaced by a simplified version of the Xbox-2 LabVIEW software [3]. In Fig. 1, the arrows show the signals that are sent to the NI PXI crate for acquisition and analysis. A photograph of the experimental setup is shown in Fig. 2.

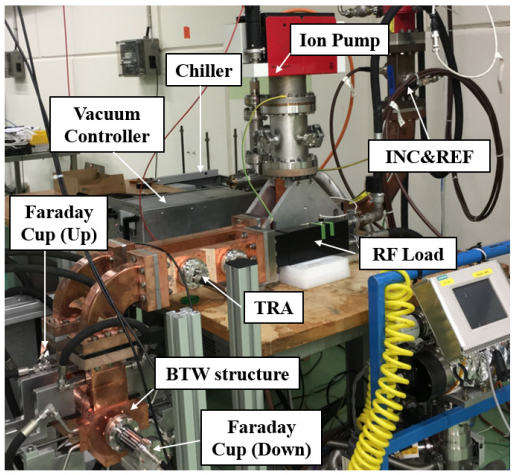

Figure 2: Picture of the test bench at S-box. Structure, diagnostics, vacuum and cooling system are labelled.

HIGH POWER MEASUREMENT

The conditioning algorithm developed on the Xboxes, was also used to test the BTW structure [4, 5]. The conditioning is carried out by increasing the input power level in a controlled manner while limiting itself by BDR of about $3x10^{-5}$ BDs per pulse. A small initial pulse width was used to avoid damaging the structure. The pulse length has been gradually increased from 350 ns up to 1.2 µs.

The plot in Fig. 3 represents the accelerating gradient (blue) and the cumulative number of breakdowns (red) with respect to the number of triggered pulses, at the different pulse lengths indicated on top.

The BTW structure achieved a maximum gradient above 60 MV/m with 1.2 µs pulses. The typical pulse length for medical accelerators is 2.5 µs flat-top with rise time equal to filling time of the structure. Therefore, further testing of the structure with a longer pulse length has a significant interest.

The structure is still conditioning and more data is being collected to increase the statistics and measure BDR at longer pulses.

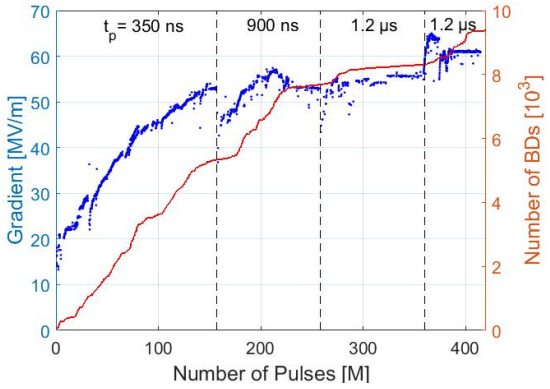

Figure 3: Conditioning history of a BTW prototype tested at Sbox.

BD localisation

The threshold detection of the reflected signal from the structure and the dark current signals, measured from the upstream and downstream Faraday cups are used to determine if a BD has occurred. The shape of these signals during a BD and the previous pulse is shown in Fig. 4

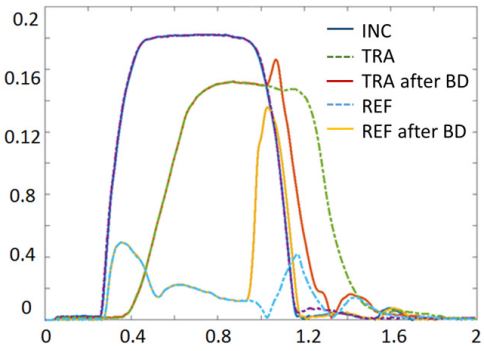

Figure 4: BD incident (INC), reflected (REF) and transmitted (TRA) RF signals in the structure during the conditioning phase with comparison to a nominal pulse before the BD event, for an RF pulse length 900 ns (amplitude of signal versus time (µs)).

The data collected by the acquisition system is analysed offline in order to characterize the behaviour of the structure. The group velocity profile of the structure used to translate the time into a measure of the length travelled by the RF wave [6]. The difference in timing between the transmitted and reflected signals have been used for BD cell localization. This measurement allows determination of the spatial distribution of the BDs along the multiple cells of the structure (see Fig. 5). We aim for the earliest detection of a 'hot spot', where BDs predominantly occur

9th International Particle Accelerator Conference IPAC2018, Vancouver, BC, Canada JACoW Publishing
ISBN: 978-3-95450-184-7 doi:10.18429/JACoW-IPAC2018-MOPML043

at a single point in the structure and can lead to the deterioration of the structure's performance.

The results show that the BDs are distributed along the structure according to the design features. Indeed group velocity has a strong reduction between the input and output of the structure of a factor of two. A 'hot spot', where excessive BDs are initiated, is observed at cell number 5. Continuous monitoring of BDs localisation is required to avoid damage of the cell.

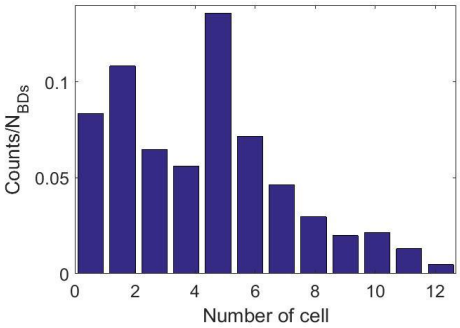

Figure 5: BD location in the RF structure.

Dark Current Measurement

A unique feature of this structure is that it is both high gradient, with surface fields in excess of 200 MV/m, and low beta. Consequently there may be differences in captured field emission current compared to high-gradient, high-beta structures and field emission is being studied closely. Field emission induced radiation can become an important issue for shielding in a medical facility.

During operation of the structure, field emission currents varied over time. Higher values are observed at initial conditioning of the structure due to imperfections on the surface that can lead to enhanced field emission. To quantify the quality of the surface of the structure, a power scan measuring radiation and the dark current level were performed by a radiation monitor and Faraday cup (see Fig 6).

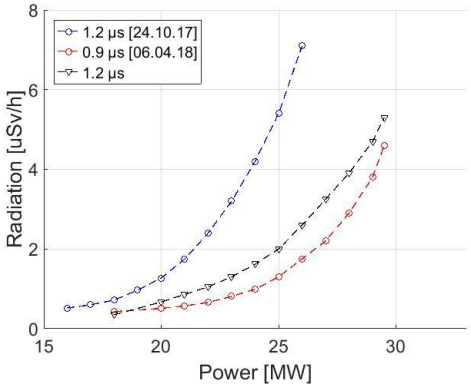

Figure 6: Dependence of radiation level on power during conditioning.

The amplitude of the dark current emitted from the structures follows the Fowler-Nordheim dependence on the surface electric fields after fitting the field enhancement factor β [7]. For BTW structures β is around 35 – 45 as shown in Figure 7. This value of β is similar to that of Xband accelerating structures tested at CERN.

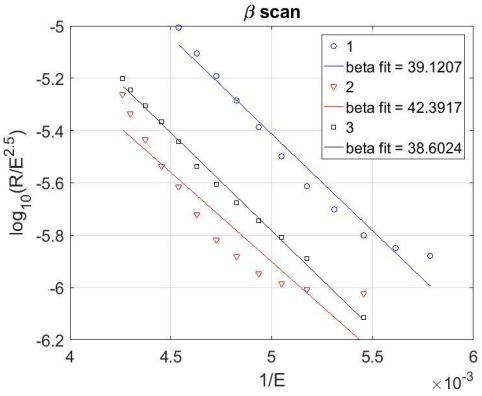

Figure 7: Linear fit of the Fowler-Nordheim formula.

BDR evaluation

The performance of the accelerating structures is assessed by the BDR. This parameter changes over time as structure conditions and has a strong dependence on the accelerating gradient and the pulse length. The reduction of the BDR measured for a certain field level indicates the conditioning status of the cavity. The BDR decay was measured for a peak power corresponding to 60 MV/m close to the limiting value. Fig. 8 shows the measurement during which the BDR dropped to 4×10^{-6} bpp. In this way, we can estimate the asymptotic value of the BDR in a conditioned structure.

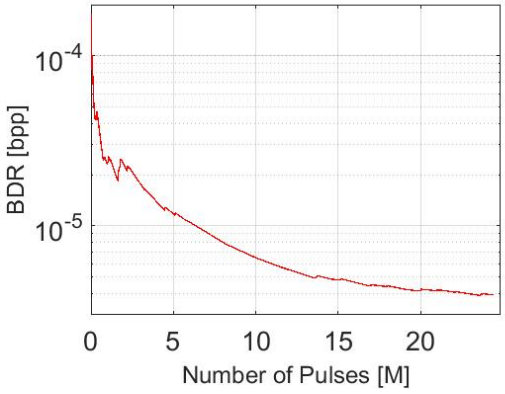

Figure 8: BDR with respect to the accumulated number of pulses during conditioning with constant power. Accelerating gradient is around 60 MV/m.

CONCLUSION

A unique high-gradient, low-beta structure is being tested in the Sbox at CERN. This structure is reaching an accelerating gradient never achieved so far in low beta RF structures. Accelerating gradient is currently above 60

9th International Particle Accelerator Conference IPAC2018, Vancouver, BC, Canada JACoW Publishing
ISBN: 978-3-95450-184-7 doi:10.18429/JACoW-IPAC2018-MOPML043

MV/m at 1.2 μs pulse length with BDR about 2.5×10^{-5} bpp/m. The testing of the structure continues with a longer pulse width.

REFERENCES

[1] S. Benedetti, A. Grudiev, A. Latina, *Phys. Rev. Accel. Beams,* vol. 20, p. 040101, 2017.

[2] A. Degiovanni *et al.*, "Design of a fast-cycling high-gradient rotating linac for proton therapy", in *Proc. 4th Int. Particle Accelerator Conf. (IPAC'13)*, Shanghai, China, 2013.

[3] B. J. Woolley, "High Power X-band RF Test Stand Development and High Power Testing of the CLIC Crab Cavity", Ph.D thesis, Lancaster University, 2015.

[4] N. Catalan-Lasheras, A. Degiovanni, S. Doebert, W. Farabolini, J. Kovermann, G. McMonagle, B. Woolley, and J. Tagg, "Experience Operating an X-Band High-Power Test Stand at CERN", in *Proc. 5th Int. Particle Accelerator Conf. (IPAC'14)*, Dresden, Germany, 2014.

[6] A. Degiovanni, S. Doebert, W. Farabolini, I. Syratchev, W. Wuensch, J. Giner Navarro, J. Tagg and B. Woolley. "Diagnostics and analysis techniques for high power X-band accelerating structures", In *Proc. LINAC'14*, Geneva, Switzerland, pp. 490-492, 2014.

[7] J. W. Wang and G. A. Loew, "Field emission and RF breakdown in high-gradient room-temperature linac structures". SLAC PUB 7684, Oct. 1997.

9th International Particle Accelerator Conference IPAC2018, Vancouver, BC, Canada JACoW Publishing
ISBN: 978-3-95450-184-7 doi:10.18429/JACoW-IPAC2018-THPMK104

HIGH POWER AND HIGH REPETITION RATE X-BAND POWER SOURCE USING MULTIPLE KLYSTRONS

M. Volpi[1*], N. Catalan-Lasheras, A. Grudiev, T.G. Lucas[1], G. McMonagle, J. Paszkiewicz[2]
V. del Pozo Romano, I. Syratchev, A. Vnuchenko[3], B. Woolley,
W. Wuensch, European Organisation for Nuclear Research (CERN)
P.J. Giansiracusa, R.P. Rassool, University of Melbourne, Parkville, Australia
C. Serpico, Elettra-Sincrotrone Trieste S.C.p.A., Basovizza
M. J. Boland, Canadian Light Source and Department of Physics and Engineering Physics, University of Saskatchewan, Canada
[1]also at University of Melbourne, Parkville, Australia
[2]also at University of Oxford, Oxford, United Kingdom
[3]also at IFIC, Valencia

Abstract

In July 2016, the first X-band test facility operating with two interwoven RF pulses produced from 6 MW klystron was commissioned at CERN. Outputting up to 49 MW after pulse compression [1], the new test stand allows testing of two structures concurrently with a combined repetition rate of up to 400 Hz. Commissioning of two of the four lines has been completed and testing of high gradient accelerating structures for the Compact Linear Collider has commenced. Operations have been ongoing for more than a year, where dedicated control algorithms have been developed to conditioning the structure and to keep the pulse compressors tuned. Significant progress has been made in understanding the conditioning of two structures that are sharing an interlock and vacuum system. The higher pulse repetition rate has demonstrated a significantly reduction in the time required to condition accelerating structures.

INTRODUCTION

The Compact Linear Collider (CLIC) [2] project at CERN has led to the development of numerous high-gradient X-band accelerator technologies. Such advancements are attracting great interest from the light source and medical communities where linear accelerators are foreseen as the next generation of accelerators. Critical to CLIC's development of high-gradient X-band technology has been an investment in test stands, which allowed investigations of the complex, multi-physics effects that affect high-power behavior in operational structures.

Increasing the number of available testing slots is important because within the CLIC project there is an extensive program aiming to test 40 structures by 2019. CERN has built three test facilities called Xbox 1, Xbox 2, and the newest and subject of this report, Xbox 3 [3].

Xbox 1 and Xbox 2 use similar technologies to the original klystron-based test facilities in Japan and the US. These use costly, high peak power, 50 MW klystrons which require modulators capable of producing up to 450 kV. However, Xbox 3 uses twin low peak power, 6 MW klystrons. High peak powers are achieved by combining the output power of these klystrons and using pulse compression. This process allows the production of 47 MW for a 200 ns pulses at much higher repetition rates than would be possible with the single, 50 MW klystrons used in previous Xboxes.

CLIC prototype structures require 40–50 MW of RF power to reach a unloaded gradient of 100 MV/m. High-gradient accelerating structures take several hundred millions pulses to condition to nominal operating conditions [4]. It is therefore advantageous to make testing facilities that can pulse at high repetition rates, in order to reduce the time needed to condition structures.

In this paper, we will describe the combination scheme used in Xbox 3 and the experience of commissioning [5–7] the facility under high power.

XBOX 3 LAYOUT

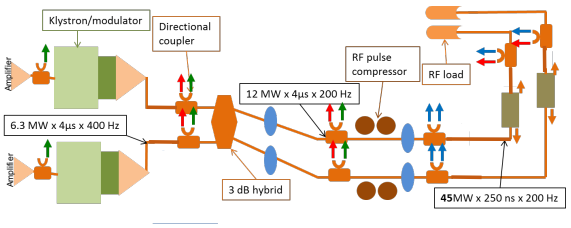

Figure 1: Schematic of the high power RF network of half the Xbox 3 facility.

Depicted in Figure 1 is the layout of one half of the Xbox 3 waveguide network. To achieve the peak power necessary, two klystrons are combined through a hybrid and subsequently compressed using a SLED-I pulse compressor (PC). The pulse repetition rate of each klystron can be increased up to 400 Hz. The whole system counts two symmetric layouts with a total of four test stands, consequently each test stand can operate up to 200 Hz.

The Low Level RF and control system is based on a National Instruments PXI crate. Each pair of klystrons shares

* matteo.volpi@cern.ch

9th International Particle Accelerator Conference IPAC2018, Vancouver, BC, Canada JACoW Publishing
ISBN: 978-3-95450-184-7 doi:10.18429/JACoW-IPAC2018-THPMK104

one PXI crate and controller. The RF drive signals are produced using NI 5793 IQ generators. Due to inherent nonlinearities in the klystrons, they are run in saturation and the power controlled by changing the drive signal.

After the hybrid combination each line has a PC, test slot for the device under test and an RF stainless steel load to terminate the waveguide network. Directional couplers are placed at critical locations in the network for monitoring purposes. Vacuum pumping ports complete the network. There are several control loops controlling the stability of the RF power distributed to the waveguide network. Pulse-by-pulse changes can be made to the drive signal which allows the two test slots to operate independently. Sharing an interlock system, for safety reasons, an interlock in one line arrests the RF pulsing in both lines.

Breakdown rate (BDR [8]) of the structure has been demonstrated that is not affected by the previous history like power pulse ramping after a BD. That means in the next future we can still pulsing in one line if the BD/interlock happen in the other line [4].

COMMISSIONING

Initial pulsing was performed at a low repetition rate to check the performance of the subsystems, after that the repetition rate was increased to 200 Hz in each line.

An algorithm [9] was developed to flatten the pulse compressor's output pulse. Changes to the slope of the pulses flat-top can be performed through the cavities' temperature controller or by manipulating the input pulse's phase profile. By changing the input phase profile the response will be immediate. The algorithm uses a simple feedback loop and fitting the flat-top with a 5th order polynomial (Fig. 2 [9]).

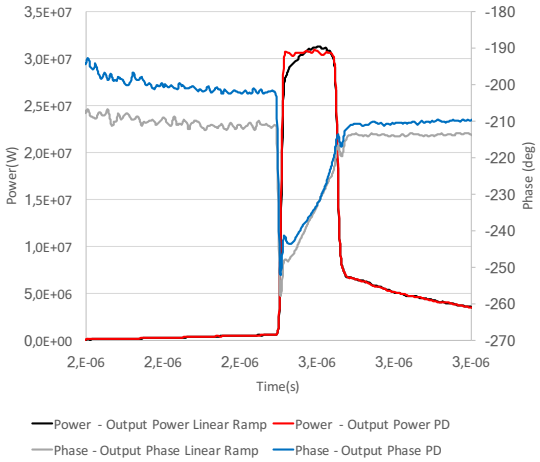

Figure 2: Power and phase of the incident and compressed pulses when tuned using the pulse flattening algorithm.

A frequency shift due the phase ramp (line blue of Fig. 2) have been observed that provoke an increase of the the dark current [10]. Thanks to the phase algorithm, Xbox 2 is running with a flat phase (Fig. 3). Flat phase is mandatory for injected bunches and it also decrease the radiation level on the structure. No correlation between BDR and flat phase have been observed.

Figure 3: Flat top pulse compressor with flat phase.

Xbox 3 uses Toshiba E37113 klystrons and ScandiNova K1 modulators which can each produce up to 5 µs pulses with 6 MW of peak power. At high repetition rate, greater than 200 Hz, the waveguide temperature increases up to the interlock limit (55°C). A dedicated cooling system based on clamps was design and installed to allow pulsing below the interlock limit. Any change in the average RF power (such as pulsing interruption due to an RF breakdown) caused the PC to cool and, as a result, detune. A frequency shift algorithm was added to the RF control GUI to tune the PCs after an RF interlock. The algorithm uses transmitted phase to choose the frequency shift as shown in Fig. 4. When the PC is perfectly tuned, the phase is exactly 180° at the minimum point of the transmitted power is zero. This occurs when the RF power leaking from the cavities begins to exceed the input power. Over tuned cavities mean that the filling phase shift is negative so that the phase flip is smaller than the desired value of about 180°, while under tuned means that the filling phase shift is positive so that the phase flip is larger than the desired value of 180°. A shift of drive frequency up to ±1 MHz can be applied to tune the PC instantaneously without waiting for temperature stabilisation. Within this range the klystrons are still stable, 1 MHz corresponds to about 5°C. The frequency shift algorithm is activated until the temperature of the cavities reach the working temperature stabilized with high power chillers.

Calibration of the entire RF system from waveguide to detector is very important, in order to reduce uncertainty in the RF measurements. There are several stages needed in order to fully calibrate the RF network. RF signal cables are split and sent to the low level RF diagnostic crate for down-mixing/log detection and simultaneously to a calibration system. Due to the temperature difference between summer and winter two sets of attenuation constants have been measured, where positive shift of 0.15 dBm is observed in summer.

9th International Particle Accelerator Conference IPAC2018, Vancouver, BC, Canada JACoW Publishing
ISBN: 978-3-95450-184-7 doi:10.18429/JACoW-IPAC2018-THPMK104

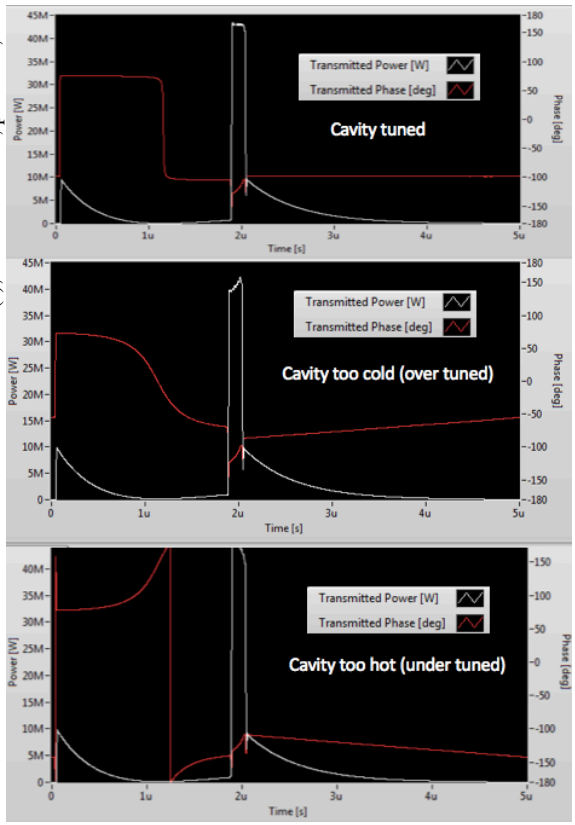

Figure 4: Simulation of tune/detuned cavity.

REFLECTION INTERFERENCE

In Xbox 2, it was observed that an interference from breakdown reflection resulted in up to a 40% increase in the input power (Fig. 5).

Xbox 2 and Xbox 3 have approximately 10 metres of waveguide that gives around 150 ns of delay minimum. If a BD occurs at the start of the structure and at the start of the pulse, the reflected signal from the structure can be interact in constructive way with itself. If the high power RF pulse is longer more than 150 ns the pulse can reenter the klystron and constructive interfere with the end of the same pulse (Figure 6).

This same effect is also observed as a small amplitude blip in the incident RF pulse flat-top. A correction in the phase program allows flattening of the pulse though this brings further challenges through a discontinuity in the incident phase. A more permanent solution to this is to have long waveguides. At least 15 meters in the CLIC design. This will of course lead to greater power loss compared to a shorter waveguide. No impact on the BDR is observed despite the structure seeing more power.

CONCLUSION AND ONGOING WORK

The commissioning of the most recent X-band test facility at CERN has been completed. The combination of two low

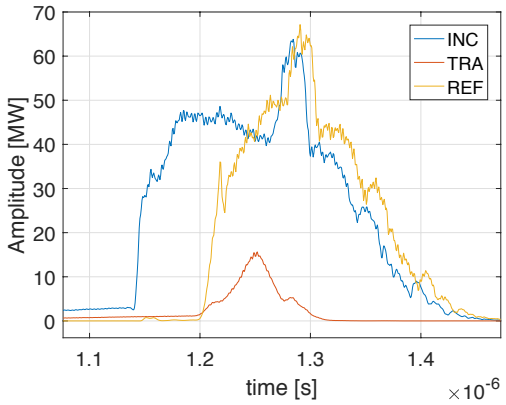

Figure 5: BD reflection interference.

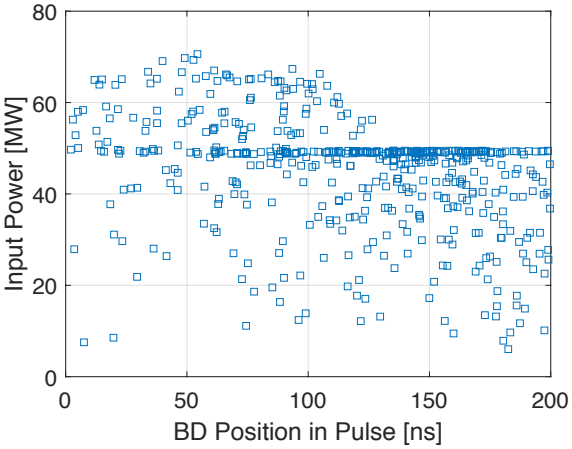

Figure 6: Power peak BD position in pulse.

power RF sources into two separate high power testing slots has been successfully demonstrated. New algorithms and new effects due to the peculiarities of this system have been observed and studied. Four CLIC prototype structures have already been tested in line 3 and 4 of Xbox 3.

In March of 2018, we installed a new klystrons in line 1 and 2. These lines are currently used to test RF components [11] such as 3D printed loads, a high power phase shifter, and variable power splitter. After testing the RF components the lines will be commissioned in the same way of line 3 and 4 with CLIC prototype structures. The high repetition rate of Xbox 3 is already showing the significantly reduced time needed to condition accelerating structures as shown in [4, 12].

REFERENCES

[1] Z. D. Farkas *et al.*, "SLED: A method of doubling SLAC's energy," in *Proc. 9th Int. Conf. on High Energy Accelerators*, SLAC, 1974.

[2] "A Multi-TeV linear collider based on CLIC technology: CLIC Conceptual Design Report," edited by M. Aicheler *et al.*,

9th International Particle Accelerator Conference IPAC2018, Vancouver, BC, Canada JACoW Publishing
ISBN: 978-3-95450-184-7 doi:10.18429/JACoW-IPAC2018-THPMK104

CERN-2012-007.

[3] B. Woolley *et al.,* "High Power X-Band Generation Using Multiple Klystrons and Pulse Compression," in Proc. IPAC17, Copenhagen, Denmark, 2017.

[4] T. G. Lucas, Results and Observations from High Gradient X-band Tests at CERN, peesented at IPAC2018, Vancouver, Canada, 2018.

[5] J. Kovermann *et al.,* "Commissioning of the First Klystron based X-Band Power Source at CERN," in Proc. IPAC2012, New Orleans, LA, USA, May 2012.

[6] N. Catalan-Lasheras *et al.,* "Experience Operating an X-band High Power Test Stand at CERN", in Proc. IPAC2014, Dresden, Germany, June 2014.

[7] N. Catalan Lasheras *et al.,* "Construction and commissioning Xbox 3: a very high capacity X-band test stand," in *Proc. 2016 IEEE Power Modulator and High Voltage Conference,* San Francisco, USA.

[8] W. Wuensch *et al.,* "Statistics of vacuum breakdown in the high-gradient and low-rate regime," *Phys. Rev. ST Accel. Beams* vol. 20, p. 011007, Jan 2017.

[9] B. Woolley *et al.,* "Control and performance improvements of a pulse compressor in use for testing accelerating structures at high power," *Phys. Rev. Accel. Beams* 20, 101001, 2017.

[10] T. G. Lucas, "Dark Current frequency dependence: measurement and simulation", CLIC workshop, CERN, 2018.

[11] N. Catalan Lasheras *et al.,* "High Power Conditioning of X-band RF Components", presented at IPAC2018, Vancouver, Canada, 2018.

[12] Zennaro, R *et al.,* "High Power Tests of a Prototype X-Band Accelerating Structure for CLIC", in *Proc. IPAC2017,* Copenhagen, Denmark, May 2017.

9th International Particle Accelerator Conference IPAC2018, Vancouver, BC, Canada JACoW Publishing
ISBN: 978-3-95450-184-7 doi:10.18429/JACoW-IPAC2018-WEPMF074

HIGH POWER CONDITIONING OF X-BAND RF COMPONENTS

N. Catalan-Lasheras, H. Damerau, R. Gerard, V. del Pozo Romano, A. Grudiev, G. McMonagle, J. Paszkiewicz, S.Pitman, A. Solodko, I. Syratchev, B. Woolley, W. Wuensch, CERN, 1211 Geneva, Switzerland
A. Vnuchenko, IFIC, 46980 Valencia, Spain
T. Lucas, M. Volpi, the University of Melbourne, 3010 Melbourne, Australia

Abstract

As part of the effort to qualify CLIC accelerating structures prototypes, new X-band test facilities have been built and commissioned at CERN in the last years. In this context, a number of RF components have been designed and manufactured aiming at stable operation above 50 MW peak power and several kW of average power. All of them have been tested now in the X-band facility at CERN either as part of the facility or in dedicated tests. Here, we describe shortly the main design and manufacturing steps for each component, the testing and eventual conditioning as well as the final performance they achieved.

INTRODUCTION

CERN has recently invested in developing X-band technology to test CLIC accelerating structure prototypes. A total of four independent testing facilities with a capacity to test up to six structures simultaneously has been built and is now fully operational [1,2]. The power supplied by these facilities is in the order of tens of megawatts even for very short pulses (ns). Considerable effort has gone into designing, manufacturing and testing X-band components capable of sustaining such high power. The design and manufacture of high-power broadband loads, bi-directional couplers, splitters, hybrids, variable power attenuator and phase shifters can be found in [3]. In this paper, we will report briefly the performance of some of these components in low and high power measurements. A second section will be dedicated to the pulse compressor and the operational results in the X-band testing facilities. The last section is dedicated to recent developments in loads produced by additive manufacturing and their performance at high power.

X-BAND COMPONENTS

A number of new X-band components has been designed by the CLIC collaboration and manufactured in industry in small series. They are now in operation in the test facility at CERN or in other collaborating institutes. High power loads and 3dB splitters have been described in [3]. Since a waveguide bi-directional coupler and pumping port have been added to the catalogue of high power X-band components available under the CERN open hardware license [4]. They are made out of milled oxygen-free copper and stainless steel parts joined by brazing. The main RF parameters measured during production are shown in Table 1 together with the maximum power during operation of the test facility. This power value has been reached with a 50 to 200 ns pulse and does not seem to depend on repetition rate. High power loads have reached 31 MW at 50 Hz and 30 MW at 200 Hz depending only on the power and attenuation from the upstream structure. None of these components is currently limiting the power delivered by the facility.

Table 1: Main parameters for each component type as measured during acceptance. Red lines are design values.

High power loads 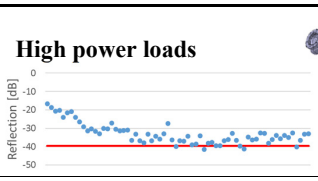 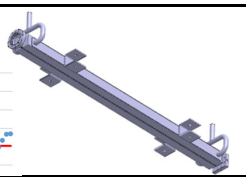	
# of units	66
Reflection [dB] *(from later production)*	-36±2.8
P_{ave} in operation [kW]	0.81
P_{max} in operation [MW]	31
Pumping ports 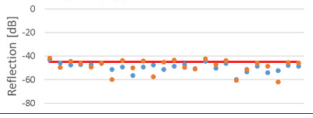 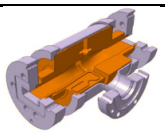	
# of units	30
Reflection [dB]	-49±5
Transmission [dB]	(-0.05, -0.08)
P_{max} in operation [MW]	56
3 dB Splitters 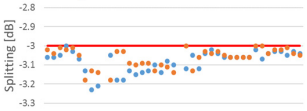 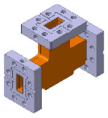	
# of units	41
Reflection [dB]	-47±6
Splitting [dB]	-3.02±0.05
P_{max} in operation [MW]	56
Bi-Directional couplers 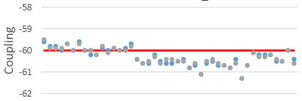 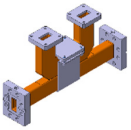	
# of units	67
Coupling [dB]	-60±0.4
Directivity [dB]	-27.9±2.4
P_{max} in operation [MW]	56

9th International Particle Accelerator Conference IPAC2018, Vancouver, BC, Canada JACoW Publishing
ISBN: 978-3-95450-184-7 doi:10.18429/JACoW-IPAC2018-WEPMF074

X-BAND SLED PULSE COMPRESSOR

Pulse Compressor

The pulse compressor designed and manufactured for the X-band test facility at CERN consists of two resonant cavities operating at the $H_{0.1.32}$ mode coupled through a double height hybrid [5]. Machining tolerances of the internal cylindrical geometry are on the order of 40 microns. The cavities are machined out of a single cylinder of OFE copper with a groove in the outside face for cooling. A mode converter and a coupling segment are brazed at the entrance of the cavity. A stainless steel jacket and vacuum manifolds are brazed to the outside copper surface. Tuning of each individual cavity is achieved through the manual machining of a fixed piston, which closes the volume of the cavity. After this, a double height hybrid is connected between the cavities which finishes the pulse compressor. Final tuning of the pulse compressor as a whole can be done by changing the temperature of the cooling water.

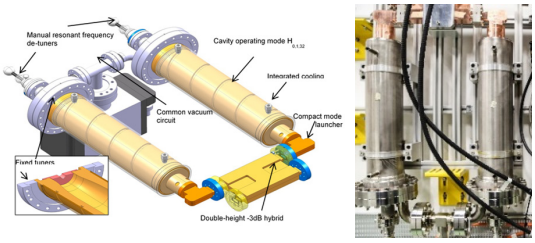

Figure 1: SLED pulse compressor 3D drawing (left) and as installed in the X-band facilities at CERN (right).

Pulse Compressor Commissioning

After tuning, the first pulse compressor was installed in the test facility known as Xbox2. A rectangular pulse is produced by the klystron on the order of 1 µs with a maximum power of 50 MW. During the typical conditioning of a structure, the pulse length to the structure is varied from 50 to 100, 150 and 200 ns by using the pulse compressor. At fixed pulse width, the power and thus gradient is ramped until reaching the nominal values for this structure. Data from Figure 2 are extracted from the successful conditioning of a structure in Xbox2.

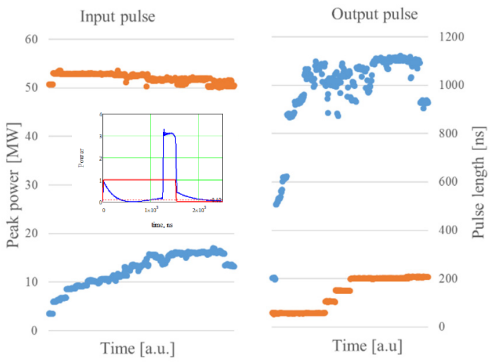

Figure 2: Peak power (blue) and pulse length (orange) before and after the pulse compressor during conditioning of a structure. On the insert, the shape of the incoming pulse (red) and the resulting output pulse (blue).

The compression factor is defined as the ratio between the input and output pulse lengths and it is a parameter of the system. The timing and shape of the phase flip are tuned to get a flat pulse of the required length. The gain, defined as the peak power ratio between compressed and uncompressed pulses, is given by the characteristics of the pulse compressor and ranges from 3 and 4 depending on the compression factor. The net power efficiency of the pulse compressor depends also on the compression factor and gain. As the pulse gets narrower or taller, the area under the $P(t)$ curve before and after the usable pulse becomes more important. For Xbox2, the energy in the compressed pulse is between 15 and 60 % of that in the original pulse and it can be easily calculated as the ratio between gain and compression ratio.

Taking the data from another run, a similar analysis has been done for the data relative to the pulse compressor in the test facility known as Xbox3. In this facility, the klystron pulse is longer and the peak power smaller (12 MW for a maximum pulse length of 2.5 µs). The pulse compressor for both test facilities shares the same design with small variations in the coupling to optimize to the longer input pulse.

Figure 3 shows gain vs. compression factor for both pulse compressors. For Xbox3 pulse compressors, we have chosen to operate at a gain value between 4 and 5 and very large compression factor (13 to 47) to reach peak power values on the order of 45 MW. The price to pay is a reduced power efficiency of between 10 and 25%.

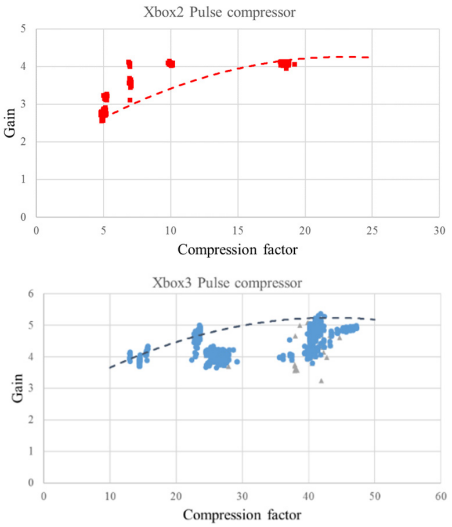

Figure 3: Gain as a function of compression factor for Xbox2 (top, red) and Xbox3 (bottom, blue). The dashed line represents the values calculated from low power measurements.

9th International Particle Accelerator Conference IPAC2018, Vancouver, BC, Canada JACoW Publishing
ISBN: 978-3-95450-184-7 doi:10.18429/JACoW-IPAC2018-WEPMF074

3D PRINTED LOADS

In order to benefit from the recent advances in 3D printing technology, RF loads have been designed to be produced by additive manufacturing. This technology is not presently suited for copper but can be used on other conductive materials like aluminium, titanium or stainless steel. Titanium produces accuracy and roughness of around ±50 µm which makes it unsuitable for other components. Two kind of dry RF loads have been designed and manufactured and were recently tested in the CERN X-band facility.

Compact Load

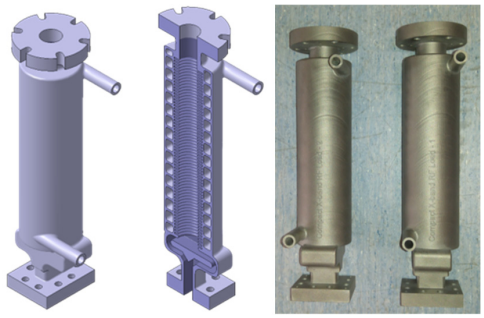

Figure 4: Compact load mechanical design and finished product printed from titanium at CERN.

The first load is a compact all-metal RF load based on a corrugated waveguide [6]. After some unsuccessful trials in industry, one example of this type was printed out of Titanium at CERN. The load was vacuum tight and the measured reflection was considered acceptable. It was installed in Xbox3 for dedicated high power tests. We observed that, unlike an accelerating structure, a breakdown in the load is only visible through vacuum activity as no significant reflected power is measured from the load. We did reach the maximum power under the condition of having a maximum vacuum level of 10^{-8} mbar in the load by increasing both pulse length and repetition rate. We observe that the power in the load is limited by a combination of peak power and average power (cf. Figure 5). The load can be used at relatively high peak power by keeping the average power low or at a considerable average power by keeping the peak power low. From the two points above the curve taken at a vacuum of $5 \cdot 10^{-8}$ mbar, we see that working at a higher vacuum level will shift the curve to higher power.

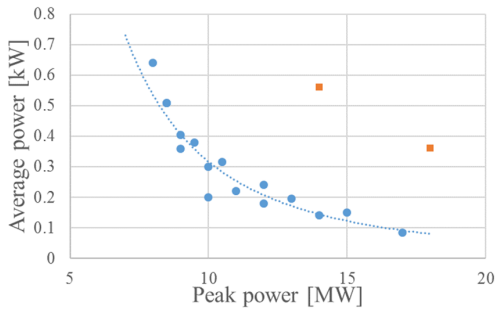

Figure 5: Power parameter space for the operation of the compact load measured at a vacuum level of 10^{-8} mbar. The two points in orange were measured allowing the vacuum in the load to degrade to $5 \cdot 10^{-8}$ mbar.

Spiral Load

A radically different design for a 3D printed load can be seen in Figure 6. This load is a tapered waveguide spiralling inwards for compactness. Vacuum pumping holes and water cooling are integrated in the spiral [7].

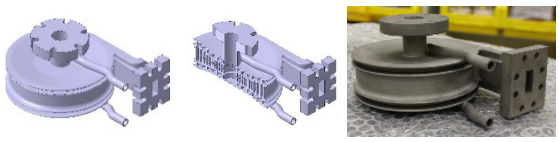

Figure 6: Spiral load RF and mechanical design and the final item manufactured out of Titanium at CERN.

A first load was manufactured in stainless steel and showed very high reflection during RF low power tests. The load was cut longitudinally by EDM and traces of material were seen inside the load traversing the waveguide. After mechanically removing this material, the two halves were mechanically clamped and RF tests showed a net improvement on the reflection, albeit not to the required value. A second unit has since been produced in a company and a third at CERN both made of titanium. This last load was installed in Xbox3 for a dedicated test of the performance. Breakdowns in this load are clearly visible through reflected power and the vacuum levels were good after a short time. We operated the load at pulse length of 50-200 ns and up to 200 Hz repetition rate. The load does not seem to have an intrinsic limitation. We tested up to the maximum available power in the line which was 35.5 MW peak power for 50 ns and 25 MW for 200 ns pulses always at 200 Hz. The maximum average power put into the load was 2.1 kW. A test of the second unit plus an improved version of the load is still pending.

CONCLUSION

The experience of testing CLIC prototypes has allowed the development of RF X-band components capable to perform in high power. They have now been validated through routine operation at high gradient and are available for use and manufacture under the terms of the open hardware license at CERN [4]. Besides the ones described in this paper, variable power splitters and phase shifters are currently under test and will be reported in the future.

REFERENCES

[1] N. Catalan Lasheras *et al.*, "Commissioning of XBox-3: A very high capacity X-band test stand*", in Proc. of 28th Linear Accelerator Conference*, East Lansing, Michigan, Sep 2016, pp.TUPLR047

[2] Matteo Volpi *et al.*, "High power and high repetition rate x-band power source using multiple klystrons", Presented at IPAC'18, Vancouver, May 2018, paper THPMK104 .

[3] M. Filippova, V. Soldatov, A. Solodko, G. Riddone, I. Syratchev, "Engineering design and fabrication of X-Band components", *Proc. of IPAC'11*, San Sebastian, Spain, Sep 2011, pp.MOPC052

9th International Particle Accelerator Conference IPAC2018, Vancouver, BC, Canada JACoW Publishing
ISBN: 978-3-95450-184-7 doi:10.18429/JACoW-IPAC2018-WEPMF074

[4] Open hardware license CERN Open Hardware License (OHL), https://kt.cern/open/, retrieved on 11.4.2018

[5] B. Woolley, I. Syratchev and A. Dexter, "Control and performance improvements of a pulse compressor in use for testing accelerating structures at high power", in *PRAB*, Vol. 20, p. 101001, 2017.

[6] Design *of compact high power RF components at X-band*. A. Grudiev CLIC note 1067

[7] G.L. D'Alessandro, "Development of x-band high-power RF load for CLIC applications using additive manufacturing techniques", Rep. CERN-THESIS-2015-315, CLIC-Note-1061

9th International Particle Accelerator Conference IPAC2018, Vancouver, BC, Canada JACoW Publishing
ISBN: 978-3-95450-184-7 doi:10.18429/JACoW-IPAC2018-THPML130

APPLICATIONS OF A DISTRIBUTED BEAM LOSS MONITOR AT THE AUSTRALIAN SYNCHROTRON

P. J. Giansiracusa*, T. G. Lucas, M. Volpi, R. P. Rassool,
The University of Melbourne, Melbourne, Australia
G. S. LeBlanc, The Australian Synchrotron, Clayton, Australia
M. J. Boland, Canadian Light Source and Department of Physics and Engineering Physics,
University of Saskatchewan, Canada

Abstract

A distributed beam loss monitoring system, based on Cherenkov silica fibres, has been installed at the Australian Synchrotron. The fibres are installed parallel to the beam pipe and cover the majority of the length of the injection system and storage ring. Relativistic charged particles from beam loss events that have a velocity above the Cherenkov threshold produce photons in the fibres. These photons are then guided along the fibres to detectors outside of the accelerator tunnels. Originally the system was installed to determine its suitability for measuring losses at a future linear collider, such as the Compact Linear Collider, with single pass 150 ns bunch trains. This work builds on these results and attempts to use the system to measure loss locations with a circulating beam.

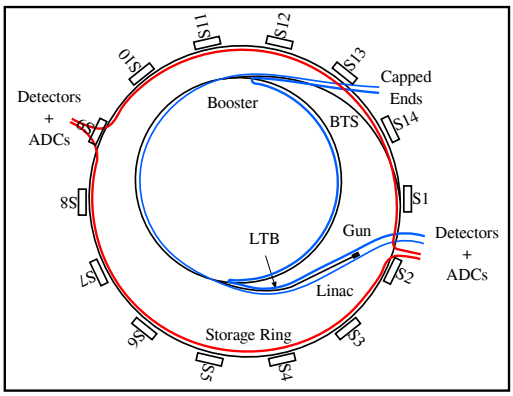

Figure 1: The locations of the fibres installed at the Australian Synchrotron. The red and blue lines how the position of the fibres installed on the storage ring and injection system respectively. Only a short section of the BTS transfer line is left uncovered.

INTRODUCTION

Beam loss monitors are essential for protection and efficient operation of particle accelerators [1]. A distributed beam loss monitoring system has been installed at the Australian Synchrotron. It consists of several silica fibres running parallel to the beam pipe that detect beam losses via the Cherenkov mechanism. Relativistic charged particles from beam loss events that have an energy above the Cherenkov threshold, $E_k > 186$ keV for $e\pm$ [2], produce optical photons in the fibres. These photons are then guided along the fibres to detectors outside of the accelerator tunnels. Originally the system was installed to determine the suitability of optical fibres for measuring losses at a future linear collider and its damping rings with single pass 150 ns bunch trains [3, 4, 5].

This work attempts to adapt the system and determine its suitability for measuring loss locations at a circular accelerator with circulating beam. In particular it is anticipated that the system can be used to determine the location of steady state losses and as a post mortem system to identify the dominant loss locations after beam dump events. The preliminary results of this investigation are presented here.

EXPERIMENTAL SETUP

The Australian Synchrotron is a 3rd generation light source. An injection system consisting of a thermionic electron gun, 100 MeV LINAC, a 3 GeV booster synchrotron and two transfer-lines, the LINAC to booster (LTB) and the booster to storage ring (BTS), provide beam to the storage ring. The storage ring is 216 m in diameter and a beam energy of 3 GeV is maintained with 500 MHz RF. In user beam operation 300 of the 360 RF buckets are filled with a nominal total current of 200 mA. Arbitrary fill patterns and signal bunch operation are also possible. The storage ring consists of 14 sectors each with a double bend achromat cell and a straight section [6].

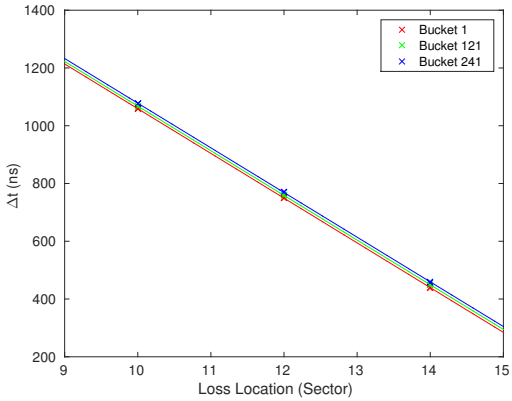

Figure 2: The target bucket's effect on the measured time difference, Δt, between the primary and reflected signal. For clarity the results for bucket 1 and bucket 241 have been offset by -10 and 10 ns respectively. It can be seen that changing the target bucket has no effect on the measured Δt.

* pgia@student.unimelb.edu.au

9th International Particle Accelerator Conference IPAC2018, Vancouver, BC, Canada JACoW Publishing
ISBN: 978-3-95450-184-7 doi:10.18429/JACoW-IPAC2018-THPML130

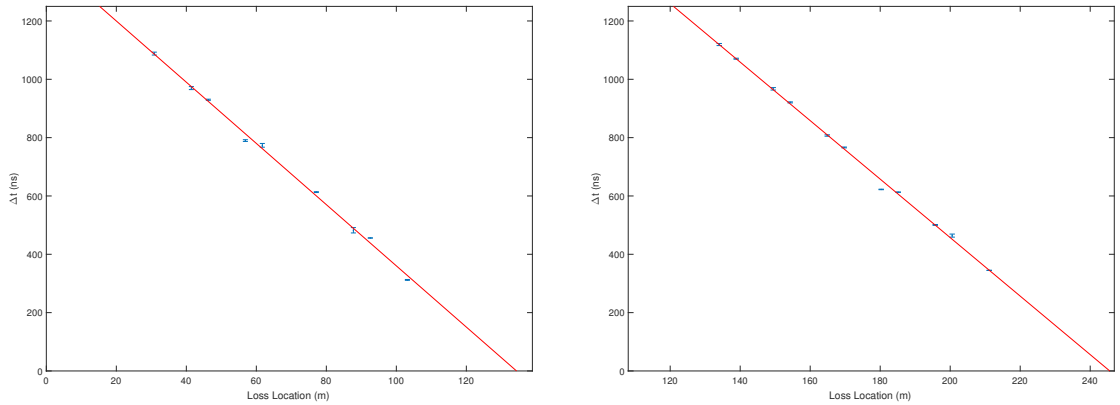

Figure 3: The measured Δt for each valve in the storage ring. Locations are given relative to the first valve in sector 1. The left plot shows the results for the fibre covering sectors 2 to 9 and the right shows the fibre covering sectors 9 to 2. The red lines show the lines of best fit. Deviations from the red lines are attributed to the physical placement of the fibres, often it was not possible to place them directly on the beam pipe.

Four 125 m silica fibres are installed such that they run on the inside of and parallel to the beam pipe and cover the majority of the system, as shown in Fig. 1. Insertion devices are installed in sectors 2, 3, 5, 8, 12, 13 and 14 and RF cavities, in sectors 6 and 7, and the fibres are routed around these as best as possible. Each fibre is made up of 245 μm silica (SiO_2), 200 μm core and 45 μm cladding, coated in a light tight sheath and then covered by a protective nylon jacket. Light is collected by Silicon photo-multipliers (SPMs) at all four ends of the two storage ring fibres, and at only one end of the injection system fibres. The unused ends are capped, to ensure no external light can leak in. The fibres have a refractive index of n=1.47 in the visible spectrum, thus the speed of signal in the fibre is v=c/n or approximately 2/3 the speed of light. As such the beam generating the losses is faster than the signal in the fibres, so signals at the downstream end are likely to pile up therefore all of the measurements in this work were preformed using signals recorded at the upstream end of the fibres. Signals produced by the SPMs are digitised with various analogue to digital converters (ADCs) at 2 GS/s and 8 bits or better.

To accurately test and calibrate the system a reliable method of generating losses at known fixed locations is required. This was done using beam scrapers and vacuum gate valves that can be used to block the path of the beam. The scrapers are located in sector 11 and the vacuum gate valves are two per sector in the storage ring and at several locations along the injection system. The locations of these devices are known to millimetre accuracy.

RESULTS AND PROCEDURE

Previous measurements of loss location made use of the event generation and timing system to determine the time of flight of events in the fibre with respect to the firing of the gun. This approach works well for leading edge measurements of first pass signals. However, it is based on the assumption that the target bunch in the train is producing the first loss seen by the detectors. So, if the loss is produced by a bunch other than the target bunch the reconstructed loss location is out by the time difference between the target bunch and the loss generating bunch. This effect in highlighted in the time resolution measurements in [3], where losses at the scrappers were induced by targeting different RF buckets to produce loss signals with different times of flight. Thus, a measurement method is required, that allows the loss location to be tied to a position along the fibre independent of RF bucket producing the loss and event system used to trigger the detectors.

Several methods of determining the loss location based solely on the observed signals in the fibre are under investigation. Here the results for a single method is presented, the measurement of the the time difference between the primary loss signal and its reflection from the opposite end of the fibre. It was found that the measured time difference, hereafter referred to as Δt, gave a result that was only dependant on the loss location. However, requiring the detection of the reflected signal results in a significantly lower sensitivity, limiting the systems use to large loss events or steady state processes where multiple signals can be averaged. To test for independence, losses were generated at three valves, in sectors 10,12 and 14, using a single bunch and targeting three different RF buckets, 1, 121 and 241, at each location. The resultant signals were digitised and the Δt was determined for each combination of valve and bucket by defining both a threshold and time window after the leading edge of the primary signal. Figure 2 shows the results of this test. For clarity the results corresponding to buckets 1 and 10 have been offset by 10 ns and -10 ns respectively. It can be seen that changing the target bucket has no apparent effect on the measured Δt at each location.

Following the successful test a calibration mapping loss location to the measured Δt was produced for entire storage ring that will be used to determine the location of unknown

9th International Particle Accelerator Conference IPAC2018, Vancouver, BC, Canada JACoW Publishing
ISBN: 978-3-95450-184-7 doi:10.18429/JACoW-IPAC2018-THPML130

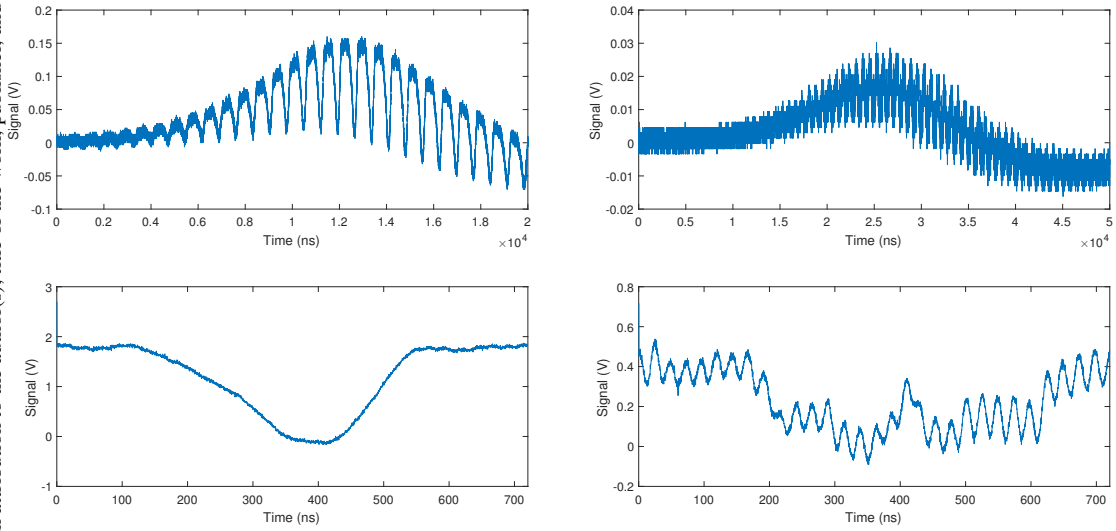

Figure 4: Examples of the beam dump signals captured using the distributed beam loss monitors. The upper two plots show the raw loss signals and the lower two plots show their corresponding turn by turn sum for user beam and single bunch fills on the left and right respectively.

losses. To do so each vacuum valve along the path of the beam was inserted in turn, several valves had to be skipped for various reasons, and targeted with a single bunch. The results for the fibres covering sectors 2 to 9 and 9 to 2 are shown in Figure 3 on the left and right respectively. A line of best fit is shown, it can be seen that some data points do not quite fall on the line. Since the valve locations are well known these small deviations are attributed to the routing of the fibre around various devices as mentioned earlier. Therefore, rather than use the fitted lines as the calibration, the measured loss locations are taken as known and a linear interpolation between any two points will be used to determine the loss location of unknown events.

After calibration, attempts were made to measure the dominant loss locations of a beam dump event. A reliable method of triggering a beam dump was required to do so. This was achieved by tripping the orbit interlock system which turns off the storage ring RF in the event the beam is deemed unstable by the BPM system. Rather than kicking the beam to trigger the interlock, which was found to be unreliable, a BPM offset parameter was set out of range tripping the orbit interlock and dropping the RF on command. Low stored currents of 4 mA for single bunch and 20 mA for multi-bunch were used to expedite testing and minimise radiation produced. The ADCs were set to trigger on the beam loss signal and the sample length recorded was adjusted to capture the entire loss event, which was found to occur over approximately 50 turns for multi-bunch and 70 for single bunch. Figure 4 shows two of the captured beam dump signals. As expected the signals show a clear periodic structure at the revolution frequency. Summing turn by turn reveals the steady-state loss pattern but blurs the finer details present in the raw waveforms. Current work is focused on developing a technique to better understand the observed waveforms and characterise and pair peaks in these and other waveforms where loss signals from multiple locations are present.

CONCLUSION

It has been shown that the time difference between the primary loss signal and its reflection in Cherenkov beam loss fibres provide a means of accurately determining loss locations along the length of an accelerator, which is independent of the triggering system and does not require knowledge of which bucket it producing the loss. A calibration mapping Δt to loss location for storage ring has been produced. Attempts at measuring the dominant loss locations of a beam dump have been made but as of yet have been unsuccessful. Further work is required to correctly characterise and pair primary and reflected peaks when multiple loss signals are present in the waveform.

ACKNOWLEDGEMENTS

The authors would like to acknowledge the CERN Instrumentation team, particularly Dr. Barbara Holzer, Dr. Eduardo Nebot Del Busto and Maria Kastriotuo, who developed and installed the original fibre system at the Australian Synchrotron that this work is built on. Also thank you to the operators of the Australian Synchrotron for their help and willingness to generate losses. And thank you to Eugene Tan and Dr. Rohan Dowd for the helpful discussions.

REFERENCES

[1] Kay Wittenburg, “Beam loss monitors”, CAS 2008, CERN Accelerator School: Beam Diagnostics, Volume CERN-2009-005, pp. 294.

9th International Particle Accelerator Conference IPAC2018, Vancouver, BC, Canada JACoW Publishing
ISBN: 978-3-95450-184-7 doi:10.18429/JACoW-IPAC2018-THPML130

[2] Jacobus Willem van Hoorne. *Cherenkov Fibers for Beam Loss Monitoring at the CLIC Two Beam Module*. Tech. rep. 2012.

[3] E Nebot Del Busto et al. "Position resolution of optical fibre-based beam loss monitors using long electron pulses." In: *Proc. IBIC15* (2015), pp. 580–584.

[4] EB Holzer et al. *Measurement of Beam Loss at the Australian Synchrotron*. Tech. rep. CERN-BE-2014-010. Geneva: CERN, Sept. 2014. URL: http://cds.cern.ch/record/1973063.

[5] Maria Kastriotou et al. "An optical fibre BLM system at the Australian Synchrotron Light Source." In: *5th Int. Beam Instrumentation Conf.(IBIC'16), Barcelona, Spain, Sept. 13-18, 2016*. JACOW, Geneva, Switzerland. 2017, pp. 670–673.

[6] JW Boldeman and D Einfeld. "The physics design of the Australian synchrotron storage ring." In: *Nuclear Instruments and Methods in Physics Research Section A: Accelerators, Spectrometers, Detectors and Associated Equipment* 521.2-3 (2004), pp. 306–317.

THPIK097 Proceedings of IPAC2017, Copenhagen, Denmark

HIGH POWER TESTS OF A PROTOTYPE X-BAND ACCELERATING STRUCTURE FOR CLIC*

R. Zennaro, H. Blumer, M. Bopp, T. Garvey, L. Rivkin,
Paul Scherrer Institut, 5232 Villigen PSI, Switzerland
N. Catalan-Lasheras, A. Grudiev, G. McMonagle, A. Solodko, I. Syratchev, R. Wegner,
B. Woolley, W. Wuensch, CERN, Geneva, Switzerland
T. G. Lucas, M. Volpi, University of Melbourne, Australia
T. Argyropoulos, D. Esperante-Pereira, University of Valencia, Spain

Abstract

We present the design, construction and high-power test of an X-band radio-frequency accelerating structure, built as a prototype for the CERN LInear Collider (CLIC) study. X-band structures have been attracting increasing attention in recent years with applications foreseen in the domains of compact free electron lasers, medical accelerators and as diagnostics for ultra-short (femtosecond) electron bunches (when used in deflecting mode). To date, the main motivation for developments in this field has been as accelerating structures for linear colliders such as CLIC. In the context of a CERN/PSI collaboration we have built a prototype structure based on an existing CERN design, but with some modification, and following, as closely as possible, the realization and vacuum brazing techniques employed in the production of the C-band structures for the Swiss Free Electron Laser, SwissFEL. We will present the basic design of the structure and describe the fabrication process. The results of high power conditioning of the structure at CERN on an X-box test stand, to assess conditioning times, accelerating field and measure breakdown rates, will also be presented.

INTRODUCTION

The production of 120 C-band accelerating structures for SwissFEL provided PSI with the opportunity to develop a strong expertise in the field of travelling wave structures [1]. Although the nominal gradient for SwissFEL is 28.5 MV/m, the PSI recipe for structure production may be of interest also for high gradient performance. During high power test a two-meter long C-band structure reached gradients exceeding 50 MV/m [2]. These results together with the "tuning free" technology developed at PSI made it interesting, for high gradient studies, to produce two X-band T24 prototypes using this technique. T24 is one of the most well tested designs for CLIC and it is the ideal candidate for a comparative study on performance [3]. These test structures also allow us to compare the vacuum brazed technology applied by PSI to the diffusion bonding, which is presently used by CERN for the CLIC structures [4, 5].

* This work was partially funded by an SNF FLARE grant 20FL20_147463

STRUCTURE PRODUCTION

The mechanical design is very similar to that of the SwissFEL C-band structure, with the main difference being the input/output couplers which are of the mode launcher type as for many CLIC test prototypes. All cups and the two couplers were produced by the company VDL [6]. The inner profiles of the cups are all well within the specified tolerances (±2 µm) and the average surface roughness (Ra) is below 20 nm. The cups have been vacuum fired at 400 °C for two hours before brazing in order to remove residual oxidation. The cooling circuits are integrated in the cups whose external diameter was reduced from 110 mm to 90 mm because of the different RF frequency. Because of this modification the pre-brazing stacking was not possible with the robot employed for SwissFEL structures. Instead manual stacking was employed. The stacking is based on a pre-heating (ΔT=50 °C) shrink-fit design. The final straightness after brazing is better than 10 microns. The RF design had to be slightly modified to adapt it to the PSI mechanical design which is based on copper disks with one half cell machined on each side in order to have the brazing plane in the middle of the cell as shown in Figure 1.

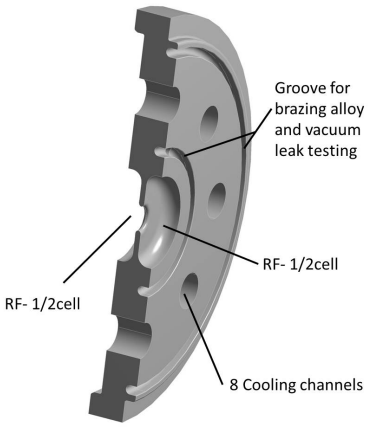

Figure 1: View of a section of one cell.

This solution allows one to have double rounding of the cells and to prevent the braze alloy from flowing into the structure through capillary action. This design is possible thanks to the absence of any tuning feature. The double

Proceedings of IPAC2017, Copenhagen, Denmark THPIK097

rounding allows also a larger Q factor of the cells. The basic parameters of T24 PSI prototype are shown in Table 1. Two brazing gaps house the copper-silver brazing wire. Sharp edges in the cells stop the melted brazing material from flowing into the cells and the size of the brazing gap has been experimentally optimised to provide the best reproducibility of the brazing material distribution. Air channels allow one to check for vacuum tightness after brazing.

Table 1: Cavity Parameters

Frequency (GHz)	11.9944
Number of accelerating cells	24(2)
Phase advance/cell (°)	120
Iris aperture diameter $a_{in,out}$ (mm)	6.30,4.70
Iris thickness $t_{in,out}$ (mm)	1.67, 1.00
Group velocity $vg_{in,out}$ (%c)	1.8, 0.9
Quality factor $Q_{in,out}$	7250, 7615
Filling time (ns)	59
Input power for 100 MV/m (MW)	37.5

LOW POWER MEASUREMENTS

Bead pulling and S-parameters measurements were performed at CERN. The structure, as shown in Figure 2, was mounted vertically and the nylon wire for the bead pulling was inserted from the top without risk of touching the irises. During measurements the structure was constantly under dry nitrogen flow.

Figure 2: Structure ready for vertical bead-pulling.

Given that the structure does not have any possibility of tuning it was vital to fabricate it at the exact operating frequency. The input match shown in Figure 3 is -31 dB. The operating temperature is 35.5 °C, 2.5 °C more than the design value (33 °C). The field along the structure, as shown in Figure 4 has a small standing wave component, probably due to a mismatch of the last two cells.

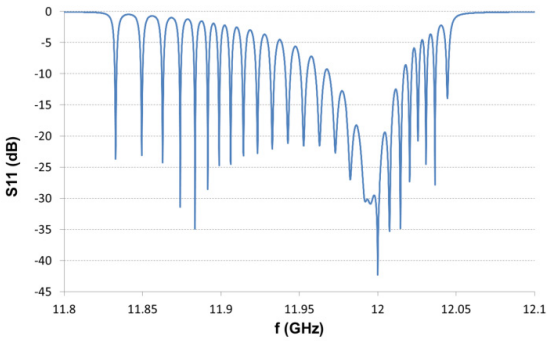

Figure 3: Reflected power to the input, S11 is equivalent to -31 dB at the equivalent working frequency in vacuum (11.9944 GHz).

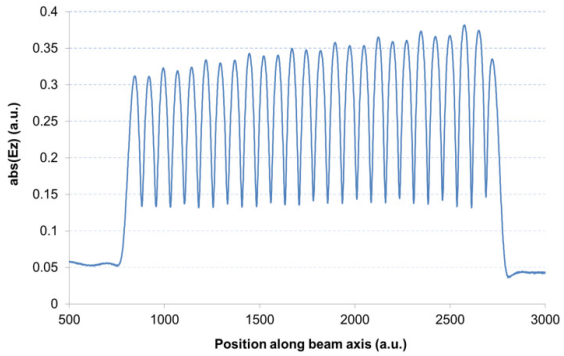

Figure 4: Bead pulling results: electric field on axis (arbitrary scale) along the structure, input on the left.

HIGH POWER MEASUREMENTS

Following the low power testing, the structure was installed on one of the test slots CERN's most recent X-band test stand, XBOX3 (Figure 5) [7-9].

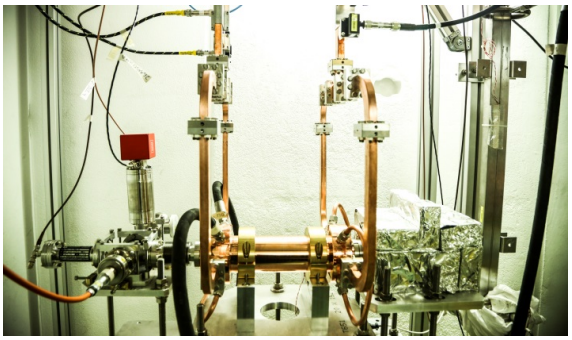

Figure 5: Structure installed in XBOX3.

XBOX3 is a unique development in X-band testing capabilities with two 6 MW Toshiba klystrons [10] combined to create the pulse to feed the SLED pulse compressor. The relatively low peak power klystrons allow for higher repetition rates, up to 400 Hz, which allows the T24 PSI manufactured structure to be tested at 100 and 150 Hz at various stage of conditioning. This compares to

ISBN 978-3-95450-182-3

the standard 50 Hz testing of previous test stands Xbox 1 and 2. Similar to past structures, the structure's conditioning was algorithmically set to keep a constant BDR of $5*10^{-5}$ bpp (breakdowns per pulse) while varying the input power accordingly. Figure 6 demonstrates the structure conditioning history to date, scaled to the CLIC nominal operating parameters (10^{-6} BDR with 200 ns pulse length) using standard scaling low [11]. The structure has run continuously for three weeks, or approximately 180 million pulses, and reached 100 MV/m average gradient at the first pulse length of 60 ns pulse. A comparison to a previously conditioned TD26CCR05 structure demonstrates the similarity in the conditioning of the structure to a standard bonded structure.

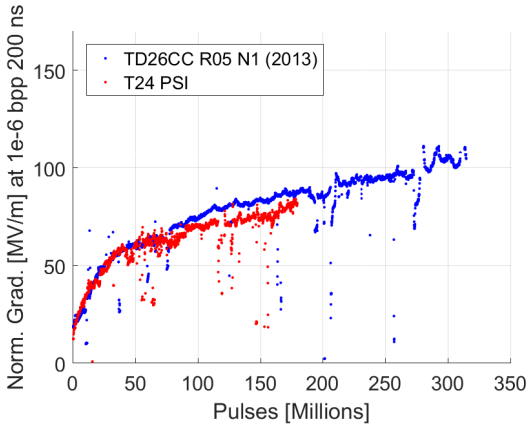

Figure 6: Structure conditioning history.

Quantifying the quality of the surface of the structure is done through a power scan measuring the dark current level on a radiation monitor. The field enhancement factor β, in the Fowler Nordheim Equation [12] is obtained by a simple linear fitting as shown in Figure 7.

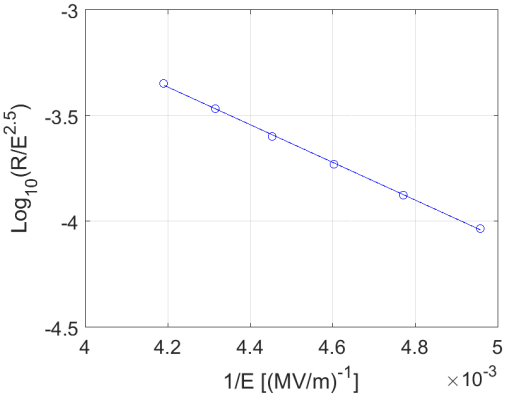

Figure 7: Linear fit of the Fowler Nordheim; R (Radiation) is proportional to the dark current.

The measured β value is 31 and is consistent with previous bonded structures demonstrating the high surface quality achieved in fabrication.

CONCLUSION

Developments in vacuum brazing at PSI for SwissFEL have led to a whole new structure production technique. Based on the T24 CLIC structure design, PSI designed and fabricated a new brazed structure for the high gradient application of CLIC. Initial conditioning has demonstrated the new structure performance with comparable results to previous structure produced through standard bonding. After twelve days of testing the structure has reached the 100 MV/m average gradient and is currently running at 150 ns pulse length.

REFERENCES

[1] J.-Y. Raguin, M. Bopp, A. Citterio, and A. Scherer, "The SwissFEL C-band accelerating structure: RF design and thermal analysis", in *Proc. LINAC'12*, Tel-Aviv, Israel, Sep. 2012, pp. 442-444.

[2] R. Zennaro, J. Alex, A. Citterio, and J.-Y. Raguin, "Measurements and high power test of the first C-band accelerating structure for SwissFEL", in *Proc. LINAC'14*, Geneva, Switzerland, Aug.-Sep. 2014, pp. 333-335.

[3] R. Zennaro *et al,.* "Design and fabrication of CLIC test structures", in *Proc. LINAC'08*, Victoria, BC, Canada, 2008, pp. 533-535.

[4] A. Solodko *et al.,* "Novel manufacturing concepts for 12 GHz high gradient accelerating structures", presented at IPAC'17, Copenhagen, Denmark, paper THPAB039, this conference.

[5] A. Xydou *et al.*, "Production of CLIC accelerating structures using diffusion bonding at very high temperature", Int. Journal of Mettalurgical and Materials Science and Engineering (IJMMSE); vol. 6, no. 2, Apr. 2016.

[6] `http://www.vdlgroep.com`

[7] N. Catalan Lasheras *et al.*, "Commisioning of XBOX3: a very high capacity X-band RF test stand", in *Proc. LINAC'16*, East-Lansing, MI, USA, Sep. 2016, pp. 569-572.

[8] A. Degiovanni *et al.,.*"Comparison of the conditioning of high gradient accelerating structures", P*hys. Rev. Accel. Beams*, vol. 19, p. 032001, 2016.

[9] B.J. Woolley *et al,.* "High power x-band generation using multiple klystrons and pulse compression", presented at IPAC'17, Copenhagen, Denmark, paper THPIK095, this conference.

[10] `http://www.toshiba-tetd.co.jp/eng/tech/klystron.htm`

[11] A. Grudiev, S. Calatroni, and W. Wuensch, *Phys. Rev. ST Accel. Beams*, vol. 12, p. 102001, 2009.

[12] R.H. Fowler and L. Nordheim, *Proc. Royal Society A*; vol. 119, p. 173, London, UK, 1928.

FABRICATION AND HIGH-GRADIENT TESTING OF AN ACCELERATING STRUCTURE MADE FROM MILLED HALVES

N. Catalan Lasheras, A. Grudiev, G. Mcmonagle, I. Syrachev, B. Woolley, W. Wuensch, H. Zha, CERN, Geneva, Switzerland
G. Bowden, V. Dolgashev, A. Haase, SLAC, Menlo Park, CA 94025, USA
T. Argyropoulos[1], J. Giner Navarro[1], D. Esperante Pereira[1], IFIC (CSIC-UV), Valencia, Spain
R. Rajamaki, Aalto University, Espoo, Finland
X. Stragier[1], Eindhoven Technical University, Eindhoven, Netherlands
P. J. Giansiracusa, T. G. Lucas, M. Volpi[1], University of Melbourne, Melbourne, Australia
[1]also at CERN, Geneva, Switzerland

Abstract

Accelerating structures made from parts which follow symmetry planes offer many potential advantages over traditional disk-based structures: more options for joining (from bonding to welding), following this more options for material state (heat treated or not) and potentially lower cost since structures can be made from fewer parts. An X-band structure made from milled halves, and with a standard benchmarked CLIC test structure design has been fabricated and high-gradient tested above 95 MV/m.

INTRODUCTION

The development of the high-gradient normal conducting accelerating structures has a strong influence on both performance and cost of the Compact Linear Collider (CLIC). As a consequence, significant effort has been invested in the optimization of the structures, while maintaining the CLIC performance requirements. The latter are defined by a loaded accelerating gradient of 100 MV/m, pulse length of around 200 ns and breakdown rate (BDR) of 10^{-7} 1/pulse/m [1].

The CLIC accelerating structures operate at 11.994 GHz and are made from copper. They are usually manufactured by precision turning and milling of individual cells, and combined with precision milling for complex parts such as RF power couplers. These multiple parts and auxiliary components such as cooling pipes, tuning pins and flanges are bonded into a complete structure [2]. An alternative approach is the use of precision milling to cut cells into metal blocks that comprise halves of the complete structure [3]. This novel accelerating structure design and assembly gives a number of advantages compared to traditional structures. In particular, reduction of the number of precision pieces per structure to two, free choice of joining since there are no RF currents flowing through the metal-to-metal joint and an overall reduction of the total fabrication and handling cost.

In this paper we describe the RF design, fabrication, tuning and high-power testing of a prototype accelerating structure, T24-open, milled out of two halves and brazed together. It is a full tapered structure which includes 24 regular traveling wave cells and 2 matching cells and works at a $2\pi/3$ phase advance per cell. Each regular cell uses the same iris dimensions as the CLIC-G structure [4]. One of the main motivations for this work is to study the high gradient performance of accelerating structures made with novel manufacturing methods.

RF DESIGN

The RF design and optimization of the structure is described in [3]. The geometry is optimized to simplify the machining process, as well as to reduce the maximum surface electric and magnetic fields and the local modified Poynting vector (S_c) [5]. Therefore, a racetrack profile with 1 mm gap and an elliptical rounding of the irises is selected for the geometry of single cells. The commercial finite element code HFSS [6] was used for the simulations.

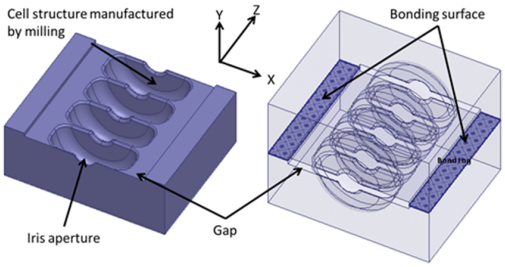

Figure 1: Manufacturing accelerating structure by milling on two halves of copper plate (HFSS model [6]).

The full tapered structure (Fig. 2) uses a so called waveguide coupler, with matching transitions to standard WR-90 waveguides. These are on-axis double-feed and can be manufactured by milling. The matching cell uses same geometry parameters as its neighbor regular cell except for the matching iris aperture. Dimensions are well tuned to minimize the reflection among the cells. The RF parameters of the full tapered structure are listed in Table 1 together with those of the CLIC-G undamped T24 structure.

STRUCTURE FABRICATION AND TUNING

The prototype T24-open structure, shown in Fig. 3, was machined at SLAC.

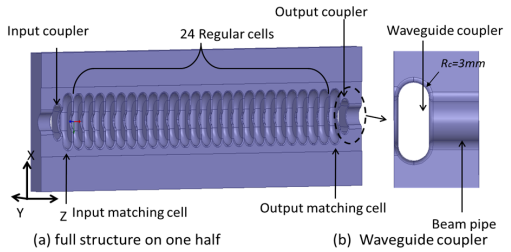

Figure 2: Model of the full tapered structure.

Table 1: RF parameters of full tapered structure

	T24-open	**CLIC-G T24**
Unloaded Gradient [MV/m]	100	100
Input/output radii [mm]	3.15/2.35	3.15/2.35
Group velocity [%c]	1.99/1.06	1.79/0.91
Shunt impedance [MΩ/m]	107/137	116/150
Peak input power [MW]	44.5	37.5
Filling time [ns]	49	57
Maximum E-field [MV/m]	268	222
Maximum Sc [MW/mm^2]	5.16	3.51
Maximum pulse heating temperature [K]	25	14

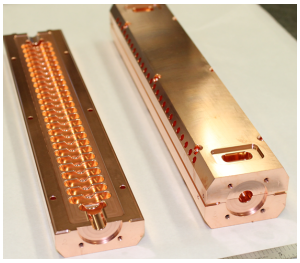

Figure 3: Structure and half structure prototype.

A pre-brazing RF test was performed to check the on-axis field profile and S-parameters. After the RF properties were verified, all parts received standard processing including polishing and Cu plating of the RF flanges, chemical cleaning, atmospheric pressure hydrogen brazing with Cu-Au alloys. The halves were cleaned with the standard SLAC procedure developed for the processing of high-gradient X-band accelerators with chemical etch time limited to 30 seconds. A more detailed description of the process can be found in reference [7]. After the structure was brazed, bead-pull measurements were carried out to determine the field profile along the structure. The results of the field pattern are presented in Fig. 4, while Fig. 5 shows the S-parameters before and after the tuning. The structure was successfully tuned, showing good field flatness and a cell to cell phase advance of 120 °±2 °. After tuning the structure was vacuum fired in an Ultra-High-Vacuum furnace at 550 °C for pressure asymptote at temperature, for more than 8 hours.

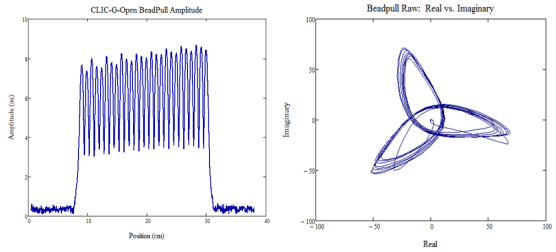

Figure 4: Bead-pull measurement results of the structure after tuning. Left: the on-axis field amplitude, right: polar plot of the bead-pull data.

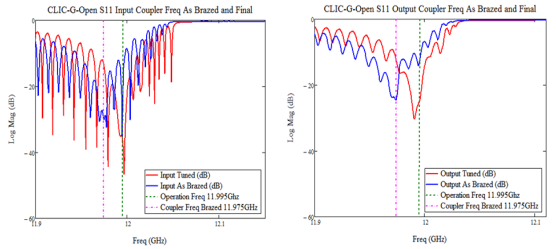

Figure 5: Input (left) and output (right) S-parameters of the brazed structure before (blue) and after (red) tuning.

HIGH-POWER-TESTING

The structure was shipped to CERN where it was installed in the Xbox-2 test stand (Fig. 6) in order to test its high-gradient performance. Xbox-2 is the second generation of the CLIC high-power klystron-powered test stand at CERN based on the same infrastructure design as in Xbox-1 [8]. Improvements include an upgraded control system, a more compact waveguide network and a new pulse compressor. This new pulse compressor can be fully detuned through the use of mechanical pistons. T24-open is the second structure that is tested in Xbox-2 after the crab cavity [10].

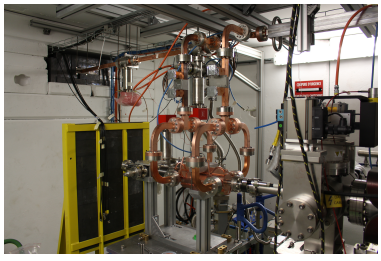

Figure 6: T24-open structure installed in Xbox-2.

The conditioning process followed that of the TD26CC at Xbox-1 in 2013 [9] and was computer controlled using the algorithm described in [8]. The structure history is summarized in Fig. 7. The power was ramped while maintaining a constant BDR of 3×10^{-5} bpp. An initial pulse width of 100 ns was used up to the gradient of 95 MV/m. Although, the structure was being well conditioned towards the tar-

get of 100 MV/m with a low and decreasing BDR (around 5×10^{-6} bpp), the operation was restricted by radiation interlocks due to bunker shielding issues. A pulse width of 155 ns was then chosen but the maximum reachable power was again limited by the radiation. Nevertheless, during that constant power run the BDR was decreasing, implying that the structure continued to condition. Finally, a pulse width of 200 ns was selected and different experiments at lower power were carried out [11] until the shielding problem was solved. Presently, the bunker shielding is enhanced and the conditioning towards the 100 MV/m is resumed. The change in the target power can be seen in Fig. 7 by the increase of the slope of the accumulated breakdowns.

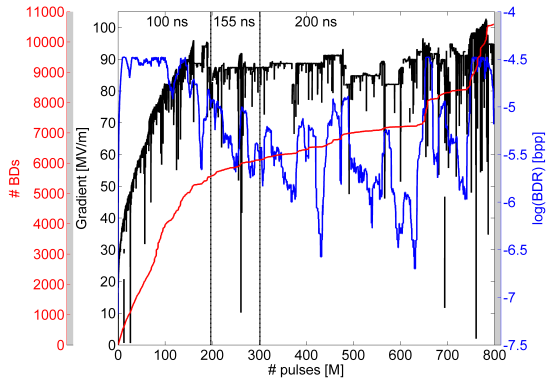

Figure 7: Summary of the T24-open test history.

The overall conditioning process of the T24-open is shown in Fig. 8, where the normalized modified Poynting vector is plotted together with different disk-based damped CLIC prototypes. The normalization was carried out using the empirical formula [5]:

$$BDR \propto S_c^{15}\tau^5, \quad (1)$$

where S_c is the modified Poynting vector and τ is the pulse width. There is a very good agreement between the different conditioning curves as expected from [5], meaning that the structure conditioned steadily throughout the run.

The detection and positioning of the RF breakdowns is done by acquiring the incident, transmitted and reflected RF signals, measured with RF directional couplers that are placed in the input and output of the structure. In addition, the signals of the Faraday cups upstream and downstream are also used to indicate the breakdown occurrence. Threshold detection on the reflected signal from the structure and the dark current signals are used to establish if a breakdown has occurred.

The position of each breakdown was determined using the timing of breakdown-induced features in incident, transmitted and reflected RF signals. The analysis followed is the same as the one presented in [12]. A histogram of the breakdown distribution inside the structure during the run of March 2016 is shown in Fig. 9. The edge method [12] was

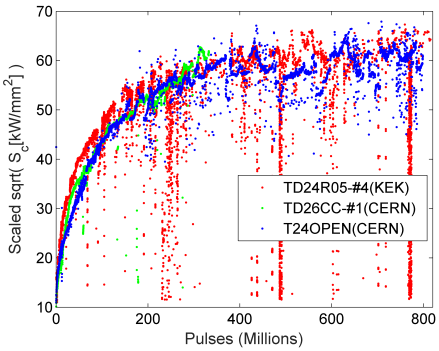

Figure 8: S_c normalized to τ=200 ns and BDR=10^{-6} bpp/m, for different accelerating structures. T24-open (blue color) is compared to different disk-based damped CLIC prototypes.

used where the position is calculated from the difference between the falling edge of the transmitted power (t_{TRA}) and the rising edge of the reflected power (t_{REF}). A slight excess of breakdowns is observed in the beginning of the structure but there is no evidence of the development of any 'hot' cell. The analysis is on-going.

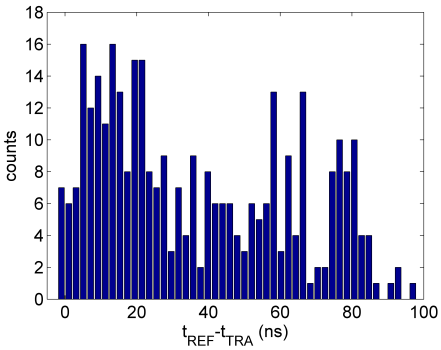

Figure 9: Breakdown distribution inside the structure during the run in March 2016 as a function of the time delay between the reflected and transmitted RF signals.

CONCLUSION

A novel CLIC prototype accelerating structure , T24-open, milled out of two halves and brazed together has been designed, successfully fabricated and tuned. Currently, T24-open is under high-power testing in the Xbox-2 test stand at CERN. The conditioning process of the structure is comparable with that of the disk-based CLIC prototypes. It reached an accelerating gradient of 95 MV/m with a relatively small BDR of around 5×10^{-6} bpp, but restricted by radiation interlocks due to bunker shielding issues. This problem is now fixed and the conditioning towards the 100 MV/m is resumed.

REFERENCES

[1] M. Aicheler et al., "A Multi-TeV Linear Collider Based on CLIC Technology," CERN 2012-007.

[2] J. W. Wang, J. R. Lewandowski, J. W. Van Pelt, C. Yoneda, G. Riddone, et al., "Fabrication technologies of the high gradient accelerator structures at 100 MV/m range," IPAC10, Kyoto, Japan, 2010.

[3] V. Dolgashev, A. Grudiev, H. Zha, "RF Design of the CLIC structure prototype optimized for manufacturing from two halves," IPAC15, Richmond, USA,2015.

[4] A. Grudiev, W. Wuensch, "Design of the CLIC main linac accelerating structure for CLIC Conceptual Design Report," LINAC10, Tsukuba, Japan, 2010.

[5] A. Grudiev, S. Calatroni and W. Wuensch, "New Local Field Quantity Describing the High Gradient Limit of Accelerating Structures," Phys. Rev. ST Accel. Beams 12, 102001 (2009).

[6] Ansys HFSS, `http://www.ansys.com`

[7] V. Dolgashev et al., "Building open traveling wave accelerating structures," talk on HG2015, Beijing, China, 2015.

[8] N. Catalan-Lasheras et al., "Experiences Operating an X-Band High-Power Test Stand at CERN," IPAC14, Dresden, Germany, 2014.

[9] A. Degiovanni et al., "High-gradient test results from a CLIC prototype accelerating structure: TD26CC," IPAC14, Dresden, Germany, 2014.

[10] B. Woolley et al., "High gradient testing of an X-band crab cavity at XBOX2," IPAC15, Richmond, USA, 2015.

[11] T. Argyropoulos, J. Giner-Navarro, "High-power test of a structure built from halves," talk on HG2016, Argonne, USA, 2016.

[12] A. Degiovanni et al., "Diagnostics and analysis techniques for high power X-band accelerating structures," LINAC14, Geneva, Switzerland, 2014.

Bibliography

[1] Veksler, V I, A new method of acceleration of relativistic particles, J. Phys. 9 (1945) pp.153-158.

[2] G. Arduini, et al., Electron-positron collisions at 209 GeV in LEP, PACS2001. Proceedings of the 2001 Particle Accelerator Conference (Cat. No.01CH37268) DOI: 10.1109/PAC.2001.987514.

[3] First 13 TeV Collisions: Reporting from the CCC (CERN Bulletin). URL: http://cds.cern.ch/journal/CERNBulletin/2015/22.

[4] J. Schwinger, On Radiation by Electrons in a Betatron, A Quantum Legacy, pp. 307-331 (2000). URL: https://doi.org/10.1142/9789812795694_0015.

[5] Julian Schwinger, On the Classical Radiation of Accelerated Electrons, Phys. Rev. 75, 1912 (1949). URL: https://doi.org/10.1103/PhysRev.75.1912.

[6] BSM physics at CLIC - CLICdp Collaboration (Simoniello, Rosa for the collaboration) In the proceeding of the international conference of high energy physics, Chicago, USA (2016). URL: https://cds.cern.ch/record/2230934/files/ICHEP2016_153.pdf

[7] Minutes of the Meeting of September 19-21, 1946 at New York Phys. Rev. 70, 784 Published 1 November 1946. URL: https://doi.org/10.1103/PhysRev.70.784.2

[8] B. Barish, International Linear Collider, Talk at APS Meeting. URL: https://www.aps.org/meetings/multimedia/april2007/upload/E4_2.pdf

[9] M. Aicheler et al., A Multi-TeV Linear Collider Based on CLIC Technology, Geneva : CERN, 2012. - 841 p. URL: https://cds.cern.ch/record/1500095

[10] J. D. Lykken, Beyond the Standard Model. URL: https://arxiv.org/abs/1005.1676

[11] Bhat, et al. Proton-proton and electron-positron collider in a 100 km ring at Fermilab, arXiv:1306.2369 [physics.acc-ph]. URL: https://arxiv.org/pdf/1306.2369.

[12] FCCs: Future Circular Colliders. Talk at "Futur de la physique des particules". (2015)

[13] M Bicer, First Look at the Physics Case of TLEP, arXiv:1308.6176 [hep-ex]. URL: https://arxiv.org/pdf/1308.6176.pdf

[14] Palmera and Long, Muon Accelerators for Particle Physics. URL: http://map.fnal.gov/

[15] Updated baseline for a staged Compact Linear Collider, edited by P.N. Burrows, P. Lebrun, L. Linssen, D. Schulte, E. Sicking, S. Stapnes, M.A. Thomson, CERN2016004 (CERN, Geneva, 2016), URL: http://dx.doi.org/10.5170/CERN-2016-004

[16] S. Doebert, RF Power Production at CTF3. Talk at X-band structure collaboration meeting, SLAC USA (2006).

[17] R. Bossart et al. CTF3 Design Report. URL: http://cds.cern.ch/record/559331

[18] I. syratchev, RF Power Production at the Two Beam Test Stand at CERN, in the proceedings of the linear accelerator conference, Tel-Aviv, Israel (2012).

[19] K. Anthony, First phase of CLIC R&D complete, CERN Bulletin Issue: 47/2012 and 48/2012, Mon 19 Nov 2012.

[20] PhD Thesis: Jorge Giner Navarro(2016), Breakdown studies for high gradient RF warm technology in: CLIC and hadron therapy linacs, University of Valencia, Spain.

[21] D. Schulte and I. Syratchev, Beam Loading Compensation in the Main Linear of CLIC, In the proceedings of the 20th International Linear Accelerator Conference, Monterey, CA, USA, 21 - 25 Aug 2000, pp.e-proc. MOA04

[22] PhD Thesis: B. Woolley (2015), High Power X-band RF Test Stand Development and High Power Testing of the CLIC Crab Cavity, Lancaster University, United Kingdom.

[23] D. Sprehn, A. Haase, A. Jensen, E. N. Jongewaard, C. D. Nantista, et al. A 12 GHz 50 MW klystron for support of accelerator research. Proceedings of IPAC2010, Kyoto, Japan, (2010)

[24] A. Degiovanni et al. High-Gradient Test Results froma CLIC Prototype. In the proceedings of the International Particle Accelerator Conference (2014). URL: http://accelconf.web.cern.ch/accelconf/ipac2014/papers/wepme015.pdf

[25] B. Woolley et al., High gradient testing of an X-band crab cavity at XBOX2, In the proceedings of the International Particle Accelerator Conference (2015), Richmond, USA, 2015.

[26] C.G. Limborg-Deprey, et al. Commissioning of the X-band Test Area at SLAC, in the Proceedings of LINAC2012, Tel-Aviv, Israel (2012). URL: http://accelconf.web.cern.ch/accelconf/linac2012/papers/mopb029.pdf

[27] S. Matsumoto et al. NEXTEF : 100MW X-Band Test Facility in KEK. In the Proceedings of EPAC08, Genoa, Italy. URL: https://accelconf.web.cern.ch/accelconf/e08/papers/wepp096.pdf

[28] Xbox Status Update CLIC Project Meeting April 2018 URL: https://indico.cern.ch/event/721644/contributions/2966594/attachments/1636625/2611452/CLIC_Project_Meeting_19_04_2018.pdf

[29] A. Solodko, X-band Structure manufacturing and tests, Talk at the CLIC workshop 2017.

[30] W. Herr and B. Muratori, Concept of luminosity URL: https://cds.cern.ch/record/941318/files/p361.pdf

[31] C. Rossi, Design Choices for the Klystron and Drive Beam Based CLIC Main Linac Modules. Talk at Linear Collider Workshop 2017.

[32] I. Syratchev, High efficiency klystron technology Talk at HG2017 (2017).

[33] L. Strahinja, Higgs physics at CLIC, 38th International Conference on High Energy Physics 3-10 August 2016, Chicago, USA URL: https://arxiv.org/pdf/1610.00628.pdf

[34] G. Degrassi,S. Di Vita, J Elias-Miro, et al. J. High Energ. Phys. (2012) 2012:98. URL: https://doi.org/10.1007/JHEP08(2012)098.

[35] Classical Electrodynamics, Jackson, John Wiley & Sons 1999.

[36] RF Linear Accelerators, T. Wangler, Wiley 1998.

[37] Introduction to linear accelerators, Mario Weiss. CERN Document Server. https://cds.cern.ch/record/261732/files/p913.pdf

[38] Cavity Types, F. Gerigk. ArXiv:1111.4897v1. https://arxiv.org/pdf/1111.4897.pdf

[39] W. K. H. Panofsky, Linear Accelerator Beam Dynamics, University of California Report UCRL-1216, Berkeley, USA (1951).

[40] Linear Accelerators, Lapostolle and Septier, North-Holland Publishing Company, 1970.

[41] R.H Folwer and L Nordheim, *Electron Emission in Intense Electric Fields*, Proc. R. Soc. A 119, 173 (1928).

[42] J. W. Wang and G. A. Loew, Field Emission and RF Breakdown in High-Gradient Room-Temperature Linac Structures. SLAC-PUB-7684, 1997.

[43] A. Palaia, et al. Effects of RF Breakdown on the Beam in the Compact Linear Collider Prototype Accelerator Structure. Phys. Rev. ST Accel. Beams 16, 081004 (2013).

[44] PhD Thesis: Kyrre Ness Sjobaek (2016), Avoiding vacuum arcs in high gradient normal conducting RF structures, University of Oslo.

[45] A. Grudiev, S. Calatroni, and W. Wuensch, New local field quantity describing the high gradient limit of accelerating structures, Phys. Rev. ST Accel. Beams 12, 102001 (2009).

[46] S. Doebert, et al. High gradient performance of NLC/GLC X-band accelerating structures. Proceedings of the IEEE Particle Accelerator Conference, Knoxville (2005).

[47] K. Nordlund and F. Djurabekova, Defect model for the dependence of breakdown rate on external electric fields, Phys. Rev. ST Accel. Beams 15, 071002 (2012)

[48] PhD Thesis: D.P. Pritzkau, RF pulsed heating. Stanford University, USA (2001).

[49] M. Aicheler, TD18 post-mortem summary. Oral presentation at CLIC RF Structure Development Meeting, 2011.URL: `http://indico.cern.ch/event/106251/`

[50] W. Wuensch, Observations About RF Breakdown From the CLIC High-Gradient Testing Program. AIP Conference Proceedings, 877(1):1521, 2006. DOI: 10.1063/1.2409116.

[51] J. Alberto Rodriguez, CLIC structure testing results, Talk at HG2006.

[52] A. Grudiev, RF design and parameters of 12 GHz TD24-vg1.8-disk, CERN EDMS, CERN, Geneva (2010). URL: `https://edms.cern.ch/file/1070498/1/TD24_vg1p8_disk.pdf`

[53] A. Fiebig and Ch. Schieblich, A SLED Type Pulse Compressor with Rectangular Pulse Shape. In the proceedings of European Particle Accelerator Conference, Nice, France (1990), pp.937-939.

[54] N. Catalan-Lasheras, et al., High Power Conditioning of X-band RF Components, In the proceedings of the internation particle accelerator conference, Vancouver, Canada (2018).

[55] L. Bertolini, Talk at The US Particle Accelerator School: Non-evaporable Getter Pumps June 10-14 (2002). URL: `http://uspas.fnal.gov/materials/02Yale/06_Non-EvapGetter.pdf`

[56] M. Volpi, et al. High Power and High Repetition Rate X-band Power Source Using Multiple Klystrons. In the proceedings of the internation particle accelerator conference, Vancouver, Canada (2018). URL: `http://ipac2018.vrws.de/papers/thpmk104.pdf`

[57] T.G. Lucas, et al., Initial Testing of techniques for Large Scale RF Conditioning for the Compact Linear Collider, In the proceedings of the internation particle accelerator conference, Vancouver, Canada (2018). URL: `http://ipac2018.vrws.de/papers/thpmk103.pdf`

[58] A. Degiovanni, et al. *Comparison of the conditioning of high gradient accelerating structures*, Phys. Rev. Accel. Beams 19, 032001 (2016).

[59] N V. Mokhov, et al. Dark Current and Radiation Shielding Studies for the ILC Main Linac, arXiv:1705.02363 [physics.acc-ph]. URL: `https://arxiv.org/abs/1705.02363`.

[60] K. L. F. Bane, et al. *Dark currents and their effect on the primary beam in an X-band linac* Phys. Rev. ST Accel. Beams, 064401 (2005)

[61] Wilson R.G. , J. Appl. Phys. 37 2261 (1966).

[62] Fomenko V S, Handbook of Thermionic Properties (1966).

[63] M. Kastriotou, et al. An Optical Fibre BLM system for the Australian Synchrotron Light Source. In the Proceedings of IBIC2016, Barcelona, Spain. URL: `http://accelconf.web.cern.ch/AccelConf/ibic2016/papers/wepg20.pdf`.

[64] I. Tamm, I. Frank, Coherent radiation of fast electrons in a medium, in: Dokl. Akad. Nauk SSSR, Volume 14, pp 107-112.

[65] M. Jacewicz et al., Spectrometers for RF breakdown studies for CLIC, Nuclear Instruments and Methods in Physics Research A 828 (2016) 6371.

[66] T. G. Lucas, et al. High power testing of a prototype clic structure: TD26CC R05 N3 - CERN-ACC-2018-0030.

[67] T. Argyropoulos, et al. Design, fabrication, and high-gradient testing of an X-band, traveling-wave accelerating structure milled from copper halves Phys. Rev. Accel. Beams 21, 061001 (2018).

[68] T. Argyropoulos, T. G. Lucas, J. Giner Navarro, C. Serpico, M. Volpi, B. Woolley. Talk at CLIC workshop 2017.

[69] T. G. Lucas, et al. Dependency of the capture of field emitted electron on the phase velocity of a high-frequency accelerating structure, Nuclear Inst. and Meth. in Physics Research Section A: Accelerators, Spectrometers, Detectors and Associated Equipment, Volume 914, 2019, Pages 46-52, ISSN 0168-9002, URL: https://doi.org/10.1016/j.nima.2018.10.166.

[70] CERN Accelerator School 1992.

[71] CST STUDIO SUITE 2018.

[72] A. Grudiev and W. Wuensch, Design of an X-band Accelerating STructure for the CLIC main Linac, Proceedings of LINAC08, Victoria, BC, Canada

[73] C. W. Steele, A non-resonant perturbation theory, Microwave Theory and Techniques. IEEE Transactions, 14(2), 70-74, (1966).

[74] R. Wegner, RF Tuning of 12SWV18026-01CSCC (TD26 CC N3) EDMS CERN, Geneva. URL: https://edms.cern.ch/document/1626878/1

[75] W. Wuensch, CLIC Accelerating Structure Development In the Proceedings of European Particle Accelerator Conference, Genoa, Italy (2008).

[76] PhD thesis: J.W.Kovermann (2010), Comparative studies of high-gradient RF and DC breakdown, RWTH Aachen University.

[77] A. Degiovanni et al., Diagnostics and analysis techniques for high power X-band accelerating structures, I the proceedings of LINAC, Geneva, Switzerland (2014).

[78] A. Palaia et al. Diagnostics of RF breakdowns in High Gradient Accelerating structures, SLAC-PUB-16089. URL: http://www.slac.stanford.edu/cgi-wrap/getdoc/slac-pub-16089.pdf

[79] A. Grudiev and W. Wuensch, Design of the CLIC Main Linear Accelerating structure for the CLIC conceptual Design report. In Proceedings of Linear Accelerator Conference LINAC2010, Tsukuba, Japan. URL: `https://accelconf.web.cern.ch/accelconf/LINAC2010/papers/mop068.pdf`.

[80] A. Grudiev and O. Kononenko, Pulse Shape Optimization for the Beam Loading Compensation in CLIC Main Linac. Talk at 4th Annual X-band Structure Collaboration Meeting, May 3-5, 2010.

[81] T. Abe, et al. Basic Study on High Gradient Accelerating Structure at KEK/NEXTEF,14th Annual Meeting of Particle Accelerator Society of Japan, 2017, Japan.

[82] W. Wuensch, et al. Statistics of Vacuum Breakdown in the High-Gradient and Low-Rate Regime. Phys. Rev. Accel. Beams 20, 011007 (2017).

[83] R. Zennaro, et al. *High Power Tests of a Prototype X-Band Accelerating Structure for CLIC*. In the proceedings of the international particle accelerator conference, Barcelona, Spain (2017).

[84] W. Wuensch, A Review of Vacuum Breakdown in High-Gradient Accelerators, Published in the 28th International Symposium on Discharges and Electrical Insulation in Vacuum (2018). URL: `https://doi.org/10.1109/DEIV.2018.8537005`

[85] P. Burrows, W. Wuensch and T. Argyopoulos. *High-gradient X-band RF technology for CLIC and beyond*. ICHEP 2016 Chicago, USA.

[86] H. Weise, High Gradient Superconducting RF Structures, Proc. of the XIX International Linear Accelerator Conference, Chicago, IL, Aug. 23-28, 1998, p. 674. URL: `https://accelconf.web.cern.ch/accelconf/l98/PAPERS/WE1002.pdf`

[87] The International Linear Collider Volume 2 - Physics, arXiv:1306.6352 [hep-ph]. URL: `https://arxiv.org/pdf/1306.6352`

[88] L. Laurent, et al., Experimental study of rf pulse heating, Phys. Rev. ST Accel. Beams 14, 041001 (2011).

[89] V. Dolgashev, Progress on High-Gradient Structures, AIP Conference Proceedings 1507, 76 (2012). DOI: 10.1063/1.4773679.

[90] E. I. Simakov et al., Advances in high gradient normal conducting accelerator structures, Nucl. Instrum. Methods Phys. Res., Sect. A, DOI: 10.1016/j.nima.2018.02.085 (2018).

[91] M. Dal Forno, Design of a high power TM01 mode launcher optimized for manufacturing by milling SLAC-PUB-16902. URL: https://www.slac.stanford.edu/pubs/slacpubs/16750/slac-pub-16902.pdf

[92] Linear Collider School, Fuji, Japan (2016).

[93] T. Pieloni and R. Zennaro, Absorbers Materials for HOM Damping in CLIC PETS and Accelerating Structures, Talk at CLIC workshop 2009.

[94] National Instruments, URL: http://www.ni.com

[95] N. Catalan-Lasheras, et al. *Experience Operating an X-band High-Power Test-stand at CERN.* IPAC14

[96] PhD Thesis: Silvia Verdu Andres (2012), High-Gradient Accelerating Structure Studies and their Application in Hadron therapy, University of Valencia, Spain.

[97] W.D.Kilpatrick, Criterion for Vacuum Sparking Designed to Include Both RF and DC, The Review of Scientific Instruments (1957) VCRL-2321